Numerical modelling of an EHL contact undergoing multiple overrollings

Maxence Decote

N° d'ordre NNT: 2024ISAL0096

THESE de DOCTORAT DE L'INSA LYON, membre de l'Université de Lyon

Ecole Doctorale N° 162
Mécanique, Énergétique , Génie Civil et Acoustique (MEGA)

Spécialité/ discipline de doctorat:
Génie Mécanique

Soutenue publiquement le 20/11/2024, par :
Maxence Decote

Numerical modelling of an EHL contact undergoing multiple overrollings

Devant le jury composé de:

CAYER-BARRIOZ	Juliette	Directeur de Recherche	École Centrale de Lyon	Président
ALMQVIST	Andreas	Professeur des Universités	Luleå University of Technology	Rapporteur
MARIAN	Max	Professeur des Universités	Leibniz University Hannover	Rapporteur
FILLOT	Nicolas	Professeur des Universités	INSA de Lyon	Directeur de thèse
BIBOULET	Nans	Maitre de conférence	INSA de Lyon	Invité
RUELLAN	Arnaud	Docteur	SKF Aerospace	Invité

INSTITUT NATIONAL DES SCIENCES APPLIQUÉES LYON

Département de la Formation par la Recherche et des Études Doctorales (**FEDORA**)

Bâtiment Charlotte Perriand 3e étage
17, av. des Arts
69621 Villeurbanne Cédex
fedora@insa-lyon.fr

Référence : TH1152_DECOTE Maxence

L'INSA Lyon a mis en place une procédure de contrôle systématique via un outil de détection de similitudes (logiciel Compilatio). Après le dépôt du manuscrit de thèse, celui-ci est analysé par l'outil. Pour tout taux de similarité supérieur à 10%, le manuscrit est vérifié par l'équipe de FEDORA. Il s'agit notamment d'exclure les auto-citations, à condition qu'elles soient correctement référencées avec citation expresse dans le manuscrit.

Par ce document, il est attesté que ce manuscrit, dans la forme communiquée par la personne doctorante à l'INSA Lyon, satisfait aux exigences de l'Etablissement concernant le taux maximal de similitude admissible.

INSA LYON
Campus LyonTech La Doua
20, avenue Albert Einstein - 69621 Villeurbanne cedex - France
Tél. +33 (0)4 72 43 83 83 - Fax +33 (0)4 72 43 85 00
www.insa-lyon.fr

membre de UNIVERSITÉ DE LYON

Département FEDORA – INSA Lyon - Ecoles Doctorales

SIGLE	ECOLE DOCTORALE	NOM ET COORDONNEES DU RESPONSABLE
ED 206 CHIMIE	**CHIMIE DE LYON** https://www.edchimie-lyon.fr Sec. : Renée EL MELHEM Bât. Blaise PASCAL, 3e étage secretariat@edchimie-lyon.fr	**M. Stéphane DANIELE** C2P2-CPE LYON-UMR 5265 Bâtiment F308, BP 2077 43 Boulevard du 11 novembre 1918 69616 Villeurbanne directeur@edchimie-lyon.fr
ED 341 E2M2	**ÉVOLUTION, ÉCOSYSTÈME, MICROBIOLOGIE, MODÉLISATION** http://e2m2.universite-lyon.fr Sec. : Bénédicte LANZA Bât. Atrium, UCB Lyon 1 Tél : 04.72.44.83.62 secretariat.e2m2@univ-lyon1.fr	**Mme Sandrine CHARLES** Université Claude Bernard Lyon 1 UFR Biosciences Bâtiment Mendel 43, boulevard du 11 Novembre 1918 69622 Villeurbanne CEDEX e2m2.codir@listes.univ-lyon1.fr
ED 205 EDISS	**INTERDISCIPLINAIRE SCIENCES-SANTÉ** http://ediss.universite-lyon.fr Sec. : Bénédicte LANZA Bât. Atrium, UCB Lyon 1 Tél : 04.72.44.83.62 secretariat.ediss@univ-lyon1.fr	**Mme Sylvie RICARD-BLUM** Laboratoire ICBMS - UMR 5246 CNRS - Université Lyon 1 Bâtiment Raulin - 2ème étage Nord 43 Boulevard du 11 novembre 1918 69622 Villeurbanne Cedex Tél : +33(0)4 72 44 82 32 sylvie.ricard-blum@univ-lyon1.fr
ED 34 EDML	**MATÉRIAUX DE LYON** http://ed34.universite-lyon.fr Sec. : Yann DE ORDENANA Tél : 04.72.18.62.44 yann.de-ordenana@ec-lyon.fr	**M. Stéphane BENAYOUN** Ecole Centrale de Lyon Laboratoire LTDS 36 avenue Guy de Collongue 69134 Ecully CEDEX Tél : 04.72.18.64.37 stephane.benayoun@ec-lyon.fr
ED 160 E.E.A.	**ÉLECTRONIQUE, ÉLECTROTECHNIQUE, AUTOMATIQUE** https://edeea.universite-lyon.fr Sec. : Philomène TRECOURT Bâtiment Direction INSA Lyon Tél : 04.72.43.71.70 secretariat.edeea@insa-lyon.fr	**M. Philippe DELACHARTRE** INSA LYON Laboratoire CREATIS Bâtiment Blaise Pascal, 7 avenue Jean Capelle 69621 Villeurbanne CEDEX Tél : 04.72.43.88.63 philippe.delachartre@insa-lyon.fr
ED 512 INFOMATHS	**INFORMATIQUE ET MATHÉMATIQUES** http://edinfomaths.universite-lyon.fr Sec. : Renée EL MELHEM Bât. Blaise PASCAL, 3e étage Tél : 04.72.43.80.46 infomaths@univ-lyon1.fr	**M. Hamamache KHEDDOUCI** Université Claude Bernard Lyon 1 Bât. Nautibus 43, Boulevard du 11 novembre 1918 69 622 Villeurbanne Cedex France Tél : 04.72.44.83.69 hamamache.kheddouci@univ-lyon1.fr
ED 162 MEGA	**MÉCANIQUE, ÉNERGÉTIQUE, GÉNIE CIVIL, ACOUSTIQUE** http://edmega.universite-lyon.fr Sec. : Philomène TRECOURT Tél : 04.72.43.71.70 Bâtiment Direction INSA Lyon mega@insa-lyon.fr	**M. Etienne PARIZET** INSA Lyon Laboratoire LVA Bâtiment St. Exupéry 25 bis av. Jean Capelle 69621 Villeurbanne CEDEX etienne.parizet@insa-lyon.fr
ED 483 ScSo	**ScSo*** https://edsciencessociales.universite-lyon.fr Sec. : Mélina FAVETON Tél : 04.78.69.77.79 melina.faveton@univ-lyon2.fr	**M. Bruno MILLY (INSA : J.Y. TOUSSAINT)** Univ. Lyon 2 Campus Berges du Rhône 18, quai Claude Bernard 69365 Lyon CEDEX 07 Bureau BEL 319 bruno.milly@univ-lyon2.fr

*ScSo : Histoire, Géographie, Aménagement, Urbanisme, Archéologie, Science politique, Sociologie, Anthropologie

Remerciements

En premier lieu je tiens à remercier mes encadrants de thèse Monsieur le Professeur N. Fillot et Monsieur le Docteur G. Morales-Espejel pour la confiance qu'ils m'ont accordé. Je souhaite appuyer mes remerciements envers Pr. N. Fillot pour les nombreuses heures passées à échanger sur ce sujet et pour tous les nombreux précieux conseils distillés durant ces trois années.

Je remercie Messieurs les Professeurs A. Almqvist et M. Marian d'avoir accepté d'être les rapporteurs de cette thèse et d'avoir fait partie du jury. Je remercie aussi Madame le Docteur J. Cayer-Barrioz pour s'être intéressée à ce travail en acceptant de faire partie du jury. Finalement, je remercie aussi Messieurs les Docteurs N. Biboulet et A. Ruellan d'avoir accepté d'être membre du jury.

Je tiens encore à remercier Dr. Biboulet pour m'avoir fait aimer le monde de la lubrification ainsi que le monde de la modélisation numérique ainsi que pour toutes la rigueur qu'il m'a transmit au fils des années à l'INSA de Lyon. Je souhaite aussi remercier Pr. G. Bayada, Dr. P. Vergne et Dr. D. Philippon pour leur disponibilité quand j'ai eu besoin d'eux.

A présent je souhaite remercier les membres du laboratoire qui ont rendu cette aventure très sympathique avec de nombreuses discussions scientifiques, sportives à base de VO_2max, pour les nombreuses blagues... Je tiens particulièrement à remercier Simone et Kévin pour tout ce qui est cité au dessus.

Cela peut paraître étonnant mais je souhaite remercier Monsieur le Docteur F. Chevalier pour l'extrême clarté de son manuscrit de thèse. En effet, ce manuscrit m'a toujours accompagné depuis mon premier jour et je pense l'avoir ouvert quasiment tous les jours.

Mes pénultièmes remerciements vont ma famille pour qui la lubrification d'un contact ElastoHydroDyamique est toujours un peu abstraite mais j'y

travaille encore. Finalement, je remercie Camille, avec qui nous avons fondé une famille dans un premier temps d'êtres à quatre pattes qui d'ailleurs va s'incrémenter même si d'ici quelque mois elle devrait devenir bipède. Peut-être sera t-elle plus réceptive à la lubrification EHD elle...

Abstract

Rolling element bearings (REB) in helicopter gearboxes are essential components that enable the helicopter to fly. A failure of these components can result in severe consequences, such as the crash of the helicopter or ditching while undertaking offshore operations. In excess of 1000 incidents have been attributed to issues with the lubrication system. In the current era, helicopters are required to demonstrate a 30-minutes autorotation capability when confronted with an oil shortage. The objective of this work is to gain a deeper comprehension of the operational capabilities of a REB in the presence of an oil shortage. The ultimate goal is to enhance the run-dry requirement time in the future.

In order to achieve this, this work does not consider a full REB, as this would be computationally intractable. Instead, the investigation is focused on a single contact between a rolling element and a raceway. This work represents the initial stage in the process of developing an understanding of the behaviour of a REB when it is subjected to an oil shortage. The next step would be to extrapolate the behaviour of one contact to the entire REB.

Experimental studies on Loss of Lubricant (LoL) applications (i.e. oil shortages) have yielded two distinct outcomes: the stabilisation and non-stabilisation of the friction coefficient during multiple overrollings. A numerical model enabling the starvation of a Thermo-ElastoHydrodynamic Lubricated (TEHL) contact has been developed with the objective of reproducing the experimental results. An innovative method based on Moving Mesh (MM) is employed to introduce starvation. The numerical model has been validated against existing literature. A comparison with experimental works on oil shortage revealed successful replication of scenarios in which the contact operates for an extended duration without replenishment.

Keywords: Thermal ElastoHydrodynamic Lubrication (TEHL), starvation, Moving Mesh (MM), oil shortage, Loss of Lubricant (LoL).

Résumé

Les roulements à billes sont des éléments cruciaux pour une boîte de vitesse d'hélicoptère, car ils lui permettent de voler. En effet, une défaillance de ces éléments peut entraîner une fin dramatique de l'hélicoptère, comme un crash. Ce travail a pour but de mieux comprendre le fonctionnement d'un roulement à billes dans des conditions de défaillance de lubrification.

Afin de réaliser cela, ce travail ne va pas considérer un roulement entier (trop compliqué). Il va se focaliser sur un contact entre un élément roulant et une bande de roulement. Il constitue une première étape dans la compréhension du fonctionnement d'un roulement à billes en présence d'une panne de lubrification. L'extrapolation des résultats obtenus sur un contact à l'ensemble du roulement serait la prochaine étape.

Des travaux présentent deux comportements différents : la présence de grippage ou un fonctionnement stable. Un modèle numérique permettant de prendre en compte la sous-alimentation dans un contact ElastoHydroDynamique (EHD) (et Thermo-ElastoHydrodynamique (TEHD)) a été développé dans le but de reproduire ces travaux expérimentaux. La sous-alimentation est introduite par le biais d'une méthode innovante faisant appel au maillage mobile. Ce modèle numérique a été confronté avec succès à une référence provenant de la littérature. Par la suite, il a été comparé à des résultats expérimentaux en condition de perte de lubrifiant. Des situations stables dans lesquelles le contact fonctionne durant de nombreuses heures sans ajout de lubrifiant ont été obtenues.

Mots clefs: Lubrification, ElastoHydroDynamique, sous-alimentation, maillage mobile, avarie de lubrifiant, perte de lubrifiant.

List of terms and acronyms

Acronyms

ALE Arbitrary Eulerian Lagragian.

EHL ElastoHydrodynamic Lubrication.

FD finite difference.

FE finite element.

GLS Galerkin Least Squares.

HL Hydrodynamic Lubrication.

JFO Jakobsson-Floberg-Olsson.

LoL Loss of Lubricant.

MLMI Multi-Level Multi-Integral.

MM Moving Mesh.

MTM Mini Traction Machine.

PM Penalty Method.

REB Rolling Element Bearing.

SRR Slide to Roll Ratio.

SUPG Streamline Upwind Petrov–Galerkin.

TEHL Thermal ElastoHydrodynamic Lubrication.

Nomenclature

Domains

Ω	Equivalent solid domain
Ω_L	Lubricant domain
Ω_P	Pressurized domain
Ω_T	Transport domain
$\omega_{t\ell}$	Thin layer domain
Σ	Frontier between Ω_T and Ω_L
Σ^{free}	Free frontier (between of Σ^{inlet} and Σ^{outlet})
Σ^{inlet}	Inlet frontier (partition of Σ)
Σ^{outlet}	Outlet frontier (partition of Σ)
X_{in}	Inlet of Ω_L in the X-direction
X_{out}	Outlet of Ω_L in the X-direction
Y_{out}	Outlet of Ω_L in the Y-direction

Elasticity symbols

$E_\varnothing$	Young modulus of solid $\varnothing$	[Pa]
E_{eq}	Equivalent Young modulus	[Pa]
$\varepsilon_{\varnothing\varnothing}$	Deformation in the $\varnothing\varnothing$-direction	[$\varnothing$]
$f_\varnothing$	Body force in the $\varnothing$-direction	[N $\cdot$ m^{-3}]
Λ	Lamé parameter	[Pa]
μ	Lamé parameter	[Pa]
$\nu_\varnothing$	Poisson coefficient of solid $\varnothing$	[$\varnothing$]
ν_{eq}	Equivalent Poisson coefficient	[$\varnothing$]
ρ_s	Solid density	[kg $\cdot$ m^{-3}]

$\sigma_{\varnothing\varnothing}$	Stress in the $\varnothing\varnothing$-direction	[Pa]
τ_{wave}	Characteristic time	[s]
$\mathfrak{U}$	Elastic deformation containing $u,\ v,\ w$	[m]
u	Elastic deformation in the x-direction	[m]
v	Elastic deformation in the y-direction	[m]
v_p	P wave, longitudinal wave	$[\mathrm{m} \cdot \mathrm{s}^{-1}]$
v_t	S wave, shear wave	$[\mathrm{m} \cdot \mathrm{s}^{-1}]$
w	Elastic deformation in the z-direction	[m]

Fluid symbols

α	Pressure viscosity coefficient	$\left[\mathrm{Pa}^{-1}\right]$
c_f	Friction coefficient	$[\varnothing]$
δ_{id}	Artificial diffusion parameter	$[\varnothing]$
η	Fluid viscosity	$[\mathrm{Pa} \cdot \mathrm{s}]$
η_0	Ambient fluid viscosity	$[\mathrm{Pa} \cdot \mathrm{s}]$
η_e	First-order cross-film lubricant viscosity	$[\mathrm{Pa} \cdot \mathrm{s} \cdot \mathrm{m}^{-1}]$
η'_e	Second-order cross-film lubricant viscosity	$[\mathrm{Pa} \cdot \mathrm{s} \cdot \mathrm{m}^{-2}]$
η_R	Reference fluid viscosity	$[\mathrm{Pa} \cdot \mathrm{s}]$
F	Applied load on the contact	[N]
$f_\varnothing$	External force in the $\varnothing$-direction	$[\mathrm{N} \cdot \mathrm{m}^{-3}]$
h	Film thickness	[m]
h_{00}	Total gap height at $x = y = 0$	[m]
h_c^{ff}	Central film thickness in fully flooded (at $x = y = 0$)	[m]
h_{oil}	Total oil thickness	[m]
ℓ_{oil}	Oil layer	[m]
m	Reduced mass	[kg]
$\mathcal{O}_\varnothing$	Order of discretization of the $\varnothing$ equation	$[\varnothing]$
p	Pressure	[Pa]

$q_\varnothing$	Flowrate in the $\varnothing$-direction	$[\mathrm{m}^3 \cdot \mathrm{s}^{-1}]$
ρ	Fluid density	$[\mathrm{kg} \cdot \mathrm{m}^{-3}]$
ρ_0	Ambient fluid density	$[\mathrm{kg} \cdot \mathrm{m}^{-3}]$
ρ_e	First-order cross film lubricant density integral	$[\mathrm{kg} \cdot \mathrm{m}^{-2}]$
ρ'_e	First-order cross film density-to-viscosity integral	[s]
ρ''_e	Second-order cross film density-to-viscosity integral	$[\mathrm{m} \cdot \mathrm{s}]$
ρ_R	Reference fluid density	$[\mathrm{kg} \cdot \mathrm{m}^{-3}]$
σ_f	Surface tension coefficient	$[\mathrm{J} \cdot \mathrm{m}^{-2}]$
SRR	Slide to Roll Ratio	$[\varnothing]$
$\tau_{\varnothing\varnothing}$	Shear stress in the $\varnothing\varnothing$-direction	[Pa]
τ_0	Eyring shear stress taken at 5 MPa	[Pa]
τ_{dist}	Characteristic time	[s]
θ	Oil ratio	$[\varnothing]$
$u_\varnothing$	Surface velocity of solid $\varnothing$ in the x-direction	$[\mathrm{m} \cdot \mathrm{s}^{-1}]$
u_f	Fluid velocity in the x-direction	$[\mathrm{m} \cdot \mathrm{s}^{-1}]$
u_m	Mean entrainment velocity $\frac{u_1+u_2}{2}$	$[\mathrm{m} \cdot \mathrm{s}^{-1}]$
u_s	Sliding velocity $u_2 - u_1$	$[\mathrm{m} \cdot \mathrm{s}^{-1}]$
$v_\varnothing$	Surface velocity of solid $\varnothing$ in the y-direction	$[\mathrm{m} \cdot \mathrm{s}^{-1}]$
v_f	Fluid velocity in the y-direction	$[\mathrm{m} \cdot \mathrm{s}^{-1}]$
$\omega_\varnothing$	Surface velocity of solid $\varnothing$ in the z-direction	$[\mathrm{m} \cdot \mathrm{s}^{-1}]$

General Symbols

$\hbar$	Element size	$[\varnothing]$
$\vec{n}$	Normal vector (can be dimensionless)	[m or $\varnothing$]
$\vec{n}_\varnothing$	Normal vector in the $\varnothing$-direction (can be dimensionless)	[m or $\varnothing$]
n	Number of overrolling	$[\varnothing]$
t	Time	[s]
x	Coordinate in the rolling direction	[m]

y Coordinate perpendicular to x ..... [m]

z Coordinate perpendicular to x and y in the thickness direction ... [m]

$\ddot{\varnothing}$ Second derivative of $\varnothing$ with respect to time ..... [s^{-2}]

Hertz symbols

a Hertzian half widht of contact ..... [m]

E' Reduced elasticity modulus ..... [Pa]

p_H Hertzian pressure ..... [Pa]

R Reduced radius of curvature ..... [m]

$R_{\varnothing}$ Radius of curvature of solid $\varnothing$ ..... [m]

Loss of Lubricant (LoL) symbols

A_a Area of the annulus on the MTM disc ..... [m^2]

h_{oil}^{ini} Initial oil thickness of the annulus ..... [m]

L_{rw} Half width of the raceway/annulus ..... [m]

m_{oil} Mass of oil deposited on the disc ..... [kg]

R_{ball}^{MTM} Ball radius of the MTM ball ..... [m]

R_{mid}^{disc} Medium radius of the MTM disc ..... [m]

R_{int}^{MTM} Inner radius of the MTM disc ..... [m]

R_{ext}^{MTM} Outer radius of the MTM disc ..... [m]

T_{end}^{ball} Dimensionless time required for the ball to complete a revolution [$\varnothing$]

T_{end}^{disc} Dimensionless time required for the disc to complete a revolution [$\varnothing$]

Moving Mesh (MM) symbols

$\delta_{\varnothing}$ Prescribed displacement of the mesh in the $\varnothing$-direction ..... [$\varnothing$]

$\dot{\Sigma}_n$ Normal velocity of the frontier (can be dimensionless). [$m \cdot s^{-1}$ or $\varnothing$]

Σ_X^{inlet} Dimensionless X position of Σ^{inlet} at $Y = 0$ ..... [$\varnothing$]

Σ_X^{outlet} Dimensionless X position of Σ^{outlet} at $Y = 0$ ..... [$\varnothing$]

$\mathcal{X}$ Dimensionless coordinate (X-direction in the Lagrangian frame) . [$\varnothing$]

XY_{free} Position coordinate vector of Σ^{free} ..... [$\varnothing$]

XY_{inlet} Position coordinate vector of Σ^{inlet} ..... $[\varnothing]$

XY_{outlet} Position coordinate vector of Σ^{outlet} ..... $[\varnothing]$

$\mathcal{Y}$ Dimensionless coordinate (Y-direction in the Lagrangian frame) . $[\varnothing]$

Thermal symbols

$C_{p\varnothing}$ Heat capacity of $\varnothing$ ..... $[\mathrm{J} \cdot \mathrm{K}^{-1}]$

$k_{\varnothing}$ Thermal conductivity of $\varnothing$ ..... $[\mathrm{W} \cdot \mathrm{K}^{-1} \cdot \mathrm{m}^{-1}]$

$\varphi_{\varnothing}$ Heat flux in the $\varnothing$-direction ..... $[\mathrm{kg} \cdot \mathrm{s}^{-3}]$

Q Heat source ..... $[\mathrm{W} \cdot \mathrm{m}^{-3}]$

Q_{comp} Heat source due to compression ..... $[\mathrm{W} \cdot \mathrm{m}^{-3}]$

Q_{shear} Heat source due to shear ..... $[\mathrm{W} \cdot \mathrm{m}^{-3}]$

$\mathbb{T}$ Temperature ..... $[\mathrm{K}]$

$\mathbb{T}_0$ Ambient Temperature ..... $[\mathrm{K}]$

$\mathbb{T}_R$ Reference Temperature ..... $[\mathrm{K}]$

$\mathrm{u}_{\varnothing}$ Velocity in the $\varnothing$-direction ..... $[\mathrm{m} \cdot \mathrm{s}^{-1}]$

$u_{\varnothing}$ Surface velocity of solid $\varnothing$ in the x-direction ..... $[\mathrm{m} \cdot \mathrm{s}^{-1}]$

Dimensionless symbols

$\bar{\alpha}$ Dimensionless piezoviscosity coefficient

β Convection term in diffusive-convective-source shape

dr Parameter enabling stabilisation of the film thickness decay

$\bar{E}_{eq}$ Dimensionless equivalent Young modulus

$\bar{\eta}$ Dimensionless viscosity

$\bar{\eta}_e$ Dimensionless first-order cross-film lubricant viscosity

$\bar{\eta}'_e$ Dimensionless second-order cross-film lubricant viscosity

$\bar{f}_{\varnothing}$ Dimensionless external force in the $\varnothing$-direction

γ Resistance to side flow coefficient

H Dimensionless film thickness

H_{00} Dimensionless total gap height at $X = Y = 0$

H_c Dimensionless central film thickness (at $X = Y = 0$)

H_c^{ff} Dimensionless central film thickness in fully flooded (at $X = Y = 0$)

H_m Dimensionless minimum film thickness

H_{oil} Dimensionless total oil thickness

H_{oil}^{inlet} Dimensionless total oil thickness at the inlet X_{in}

H_{oil}^{ini} Dimensionlness initial oil thickness of the annulus

H_{oil}^{outlet} Dimensionless total oil thickness at the outlet X_{out}

$\bar{\xi}$ Dimensionless diffusive term $\bar{\xi} = \bar{\xi}_{\mathrm{P}} + \bar{\xi}_{id}$

$\bar{\xi}'$ Dimensionless Generalized diffusive term $\bar{\xi} = \bar{\xi}'_{\mathrm{P}} + \bar{\xi}_{id}$

$\bar{\xi}_{\mathrm{P}}$ Dimensionless Poiseuille flux

$\bar{\xi}'_{\mathrm{P}}$ Dimensionless Generalized Poiseuille flux

$\bar{\xi}_{id}$ Dimensionless artificial flux

L Moes dimensionless piezoviscosity parameter

$\bar{\Lambda}$ Dimensionlness Lamé parameter

$\bar{\lambda}$ Dimensionless term within dimensionless Poiseuille flux

$\bar{\ell}_{oil}$ Dimensionless oil layer

M Moes dimensionless load parameter

$\bar{\mu}$ Dimensionlness Lamé parameter

$\mathcal{O}_{\varnothing}$ Order of discretization element of $\varnothing$

Ω_n Dimensionless natural frequency

P Dimensionless pressure

$P^{\star}$ Dimensionless penalty pressure used in PM

P_{inlet} Dimensionless inlet pressure when using PM

Pe Péclet number

Ψ Coefficient handling the initial offset of H_{00}

ψ Monitor the degree of starvation

$\bar{Q}_{\varnothing}$ Dimensionless heat source due to $\varnothing$

$Q_{f\varnothing}$	Dimensionless mass flow rate in the $\varnothing$-direction
$\mathcal{R}_c$	Dimensionless central film thickness reduction
r_0	Dimensionless initial relative oil film thickness
$\bar{\rho}$	Dimensionless density
$\bar{\rho}_e$	Dimensionless first-order cross film lubricant density integral
$\bar{\rho}'_e$	Dimensionless first-order cross film density-to-viscosity integral
$\bar{\rho}''_e$	Dimensionless second-order cross film density-to-viscosity integral
$\bar{\sigma}_f$	Dimensionless surface tension coefficient
$\overline{\mathbb{T}}$	Dimensionless temperature
T	Dimensionless time
T_{end}	Dimensionless time just before dry contact
$\mathcal{U}$	Dimensionless elastic deformation containing U, V, W
U	Dimensionless elastic displacement in the X-direction
V	Dimensionless elastic displacement in the Y-direction
W	Dimensionless elastic displacement in the Z-direction
X	Dimensionless coordinate in the x-direction
Y	Dimensionless coordinate in the y-direction
Z	Dimensionless coordinate in the z-direction

Remark. Symbols that are used once are not printed in this nomenclature. However, their meaning is rigorously stated.

Remark. The end of a hypothesis is marked by the symbol "¶".

Contents

General introduction

The lubrication of machine elements is of great consequence, as it serves to diminish the effects of friction and wear. In certain applications, a failure in the lubrication system can result in a catastrophic outcome.

This is exemplified by the gearbox of a helicopter, which serves as the link between the engine and the blades, enabling the helicopter to fly. The gearbox comprises a variety of components, including gears and bearings, which require lubrication. The present study focuses on bearings. Consequently, in the event of an oil shortage, the duration for which the bearings can perform their primary function (rotation) is of paramount importance. Gearbox lubrication issues have the potential to be problematic during offshore helicopter operations, such as air-sea rescue missions, and may ultimately result in ditching. Indeed, Rashid et al. [114] in 2015 reported 1232 helicopter accidents due to lubrication issues within the helicopter main gearbox (sum of accidents occurring in different countries). Astridge [5] in 1989 identified transmission failure as the third most prevalent issue for helicopters, representing 22 % of all reported issues for helicopters manufactured between 1956 and 1986. In accordance with the regulations set forth by the European Aviation Safety Agency [55], certain categories of helicopters are required to have the capacity to fly for a minimum of 30 minutes in the event of a malfunction in the lubricating system. This is to be achieved by undertaking an autorotation "run-dry requirement". It is anticipated that this period will be extended in the future, thus enabling longer autorotation and more secure offshore helicopter operations. This research represents an initial step in this direction.

The existing literature proposes analytical laws that enable the prediction of film thickness decay. However, none of the aforementioned models is capable of predicting whether the film thickness decay will stabilise, as is

evidenced by experimental findings in the literature. Furthermore, there is no existing numerical study that is exclusively devoted to this phenomenon. Consequently, the forthcoming work will establish a numerical strategy that will enable the reproduction of the experimental works that are present in the literature in order to determine the required ingredient leading to this result.

Chapter 1 presents a review of the existing literature on the subject. The initial step is to introduce Rolling Element Bearing (REB). A review of the lubrication theory reveals that there are two main approaches, namely experimental and numerical. The phenomenon of starvation is examined in great detail. Subsequently, experimental works dealing with starvation as well as related phenomena are presented.

Chapter 2 presents the classical equations that are required in order to solve an ElastoHydrodinamic Lubricated (EHL) problem. In-depth derivations of both the Reynolds equation and the linear elasticity equation are provided. In order to account for the viscosity and density dependencies, different fluid properties laws are provided. Subsequently, the equations required for the resolution of a Thermo-ElastoHydrodinamic Lubricated (TEHL) problem are presented. The lubricated contact problem is normalised. In conclusion, a numerical procedure for solving the lubricated problem is presented.

Chapter 3 introduces the concept of starvation to the classical approach to ElastoHydrodynamic Lubrication (EHL). Two methods for computing starvation are presented. The initial approach is based on the Penalty Method (PM). The second method proposes a novel approach based on a Moving Mesh (MM) strategy. The efficacy of these methodologies was evaluated through a comparative analysis with a benchmark established in the literature. This analysis was conducted in a stationary context, encompassing scenarios with varying degrees of starvation. The two methods are then compared to each other through the use of a transient application, which presents a time-varying quantity of oil upstream of the contact. Finally, an initial transient investigation related to the simulation of a sudden cessation of lubrication, known as “oil-off”, is conducted.

Chapter 4 presents a synthesis of experimental studies on Loss of Lubricant (LoL) applications. Numerical simulations are conducted to enhance comprehension of film thickness decay during a LoL application. Adaptations to the numerical solver are outlined. Isothermal and thermal simulations are evaluated in comparison with experimental outcomes.

Chapter 1

State of the art

In the event of a lubrication issue being encountered with a Rolling Element Bearing (REB), it is of interest to enquire as to the length of time that the bearing can be expected to continue to operate effectively. This question serves as the foundation for this work. The following chapter elucidates the operational principles of a REB, beginning with its constituent components and culminating in an examination of the physical phenomena that are integral to its functionality.

This is followed by a historical overview of the techniques employed for the measurement and numerical analysis of lubrication, which are essential for predicting its behaviour. Thereafter, an experimental procedure called Loss of Lubricant (LoL) of a lubricated contact as well as track replenishment phenomenon are introduced.

1.1 Rolling Element Bearing (REB)

As illustrated in figure 1.1, a REB is comprised of two rings: an outer ring (1), which is typically affixed to a housing, and an inner ring (2), which is usually mounted on a shaft. The two rings are separated by the rolling elements (5). The rolling elements are typically composed of balls or barrels. The rolling elements are in contact with both the inner and outer rings. In

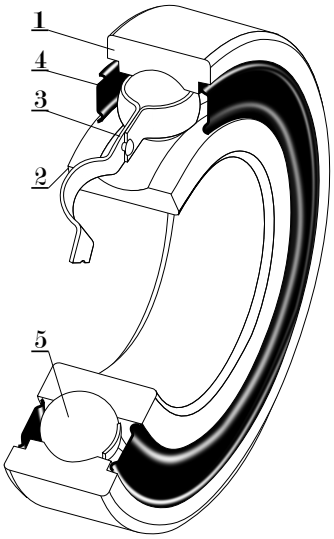

Figure 1.1: Representation of a rolling element bearing in a cut view
Credit: Image from Wikimedia Commons by Silberwolf & Malyszkz – entitled "Radial-deep-groove-ball-bearing din625-t1 2rs 120" – distributed under a CC BY-SA 3.0 licence – modifications: converted in black & white, font has been changed to Modern 20 and characteristic dimensions have been removed

contrast to a sliding contact, as observed in a journal bearing, the rolling elements facilitate a rolling contact (see, e.g. Hamrock et al. [68]). In order to minimise friction and wear, a lubricant is used to separate the surfaces. The lubricant may be either an oil or a grease. Depending on the type of REB, a cage (3) may be present in order to maintain the distance between the rolling elements. Similarly, seals (4) are present with the purpose of protecting the rolling element from external contamination on both sides of the REB, as well as maintaining the lubricant inside the REB.

The objective of a REB is to achieve relative rotation between two elements, thereby optimising precision and minimising power losses [68]. When mounted in pairs, they form a revolute joint, as illustrated in figure 1.2. They are integral to a vast array of mechanical devices, capable of supporting axial and/or radial loads, high-speed rotation, and high temperatures.

It should be noted that not all REB are equipped with seals comparable to those found in a gearbox. In this instance, the gearbox is equipped with a dedicated lubrication system, which is responsible for ensuring the optimal lubrication of the gear contact surfaces. Subsequently, the aforementioned

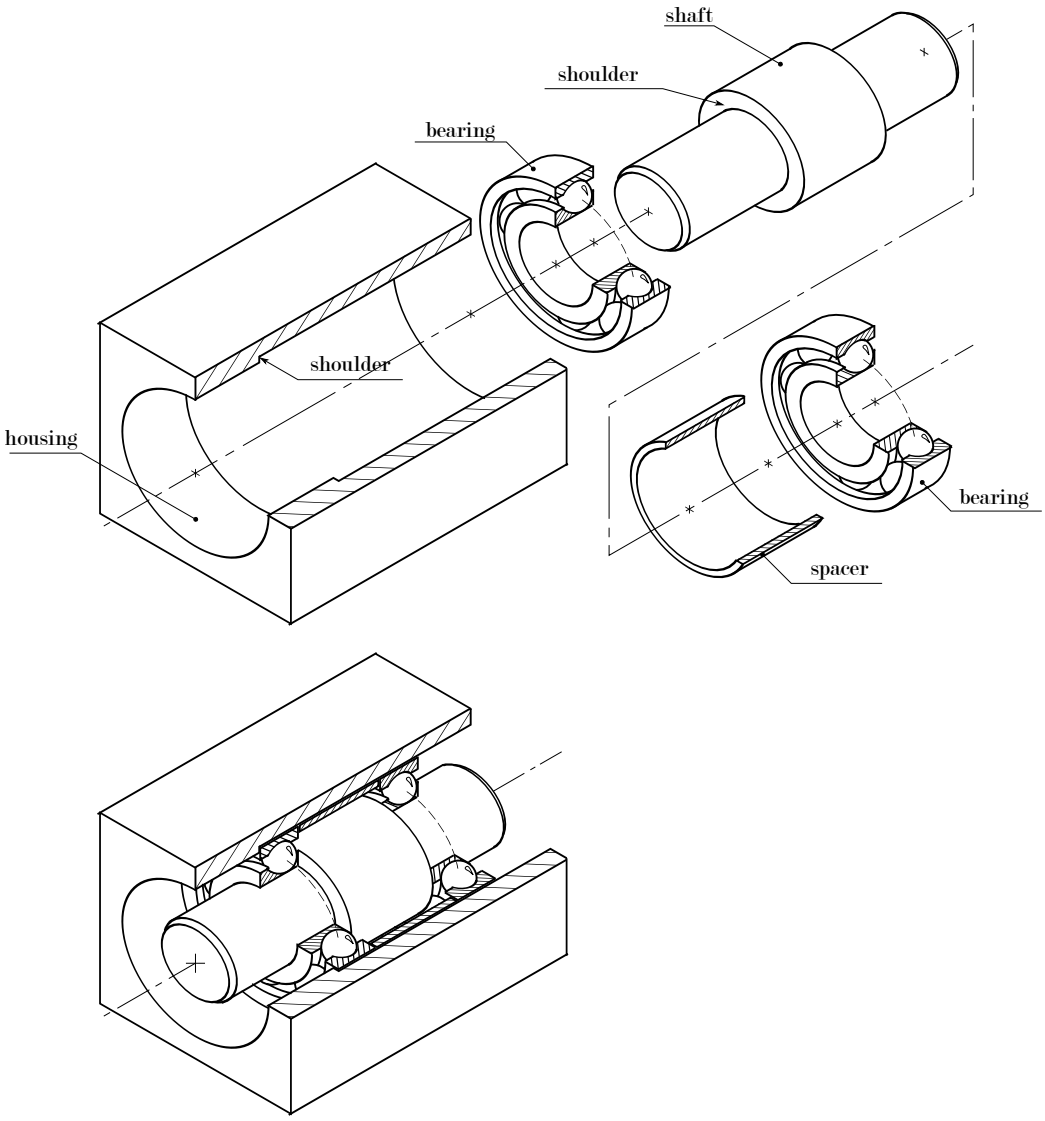

Figure 1.2: Schematic representation of a bearing assembly that realises a revolute joint

Credit: Image from Wikimedia Commons by Cdang – entitled " Assembling of a revolute joint with two ball bearings, and vocabulary (in French)" – distributed under a CC BY-SA 4.0 licence – modifications: converted in black & white, font has been changed to Modern 20 and translated in English

lubricant also serves to lubricate the REB. Figure 1.3 illustrates a technical diagram of a planetary gearbox. The figure illustrates five REB that are not sealed. It can be observed that two radial lip seals are present on both

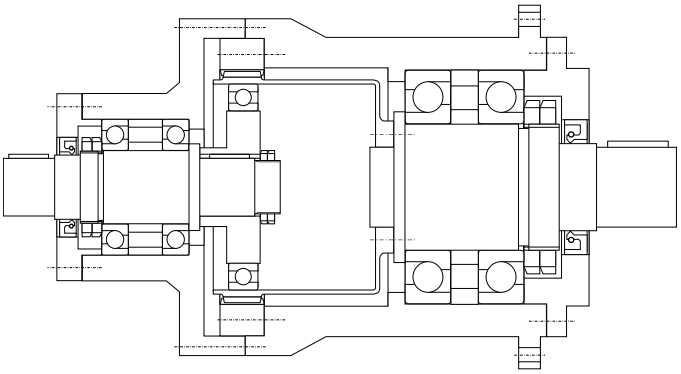

Figure 1.3: Schematic representation of a gearbox comprising multiple bearings

Credit: Image from Wikimedia Commons by Jahobr & Kaboldy – entitled "Cross section of a harmonic drive" – distributed under a CC BY 3.0 licence – modifications: converted in black & white

edges of the gearbox, indicating the presence of lubricant within the internal mechanism. An oil failure mode in this case is that the external device (oil pump) does not ensure the lubrication of the lubricated components. Another potential failure mode is the presence of leakages from the housing. In such situations, the REB has to run with the remaining oil on the raceway. The raceway is the path where the contact between the rolling element and the ring occurs, as illustrated in figure 1.4.

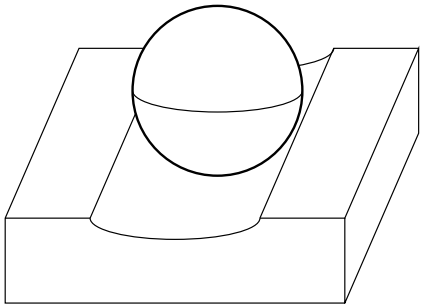

Figure 1.4: Contact between the rolling element and the raceway of a rolling element bearing

A REB is a sophisticated mechanical assembly, the study of which is inherently challenging. Consequently, this work focuses exclusively on the contact between a rolling element and the raceway, with the objective of extrapolating these findings to the entire assembly in due course. The subsequent

sections will therefore examine lubricated contacts in detail.

1.2 Lubrication review

Lubrication constitutes a discipline within the expansive field of Tribology. Fluid lubrication can be achieved through the use of either a gas or a liquid. The separation of the two bodies is achieved by virtue of the pressure exerted by the fluid on the surface between them. Lubrication can be classified as either hydrostatic or hydrodynamic. In hydrostatic lubrication, the pressure is generated by an external device, such as a pump, as seen in hydrostatic bearings used in giant telescopes. In contrast, in hydrodynamic lubrication, the pressure is generated by the entrainment of the fluid into a converging gap, as observed in journal bearings in internal combustion engines, ball bearings, gears, and other similar applications.

1.2.1 Lubrication history

Lubrication has become ubiquitous, as evidenced by its presence in numerous applications, including automobiles (as illustrated by Venner [130]), household appliances (as demonstrated by Zhang et al. [143]), door hinges and locks, and even human joints (as observed by Dowson et al. [48]). The practice of lubrication can be traced back to antiquity, with examples including the use of lard or animal fat for axles chariots and carts, as well as olive oil mixed with limestone powder to achieve a consistency similar to that of grease (see Guay [35]).

The utilisation of lubricants enables a reduction in friction, thereby facilitating the consumption of less energy for the movement of an object. The reduction of friction represents a primary objective for numerous researchers and engineers, who have been engaged in this pursuit for decades. The automobile serves as an exemplar of this phenomenon; according to Holmberg et al. [74], 33 % of the energy in the fuel is lost due to friction. Thus, reducing friction enables a vehicle to traverse a greater distance for a given quantity of fuel, which ultimately translates to reduced costs for consumers at the fuel pump. Furthermore, the carbon footprint of the vehicle per kilometre is reduced. The aforementioned example can be extrapolated to other modes of transportation, including railways, aeronautics, and even bicycles (see, for instance, Aubert et al. [6] or Martin et al. [97]). Additionally, lubrication can mitigate wear, safeguard surfaces against corrosion, prevent galling, and dissipate the heat generated during contact, as outlined by Guay [35].

Conversely, certain applications necessitate high friction, such as in the case of brakes, tyres, clutches, etc.. The function of a brake is to decelerate an object in motion, such as a vehicle. Consequently, the higher the friction, the greater the braking efficiency (see Brunetti et al. [21]). Additionally, the tyre must also generate substantial friction with the road to contribute to the braking process.

In order to gain a deeper comprehension of the lubrication phenomenon and to ascertain the optimal utilisation of such a phenomenon in the future, the theoretical treatment of the action of oils and other viscous fluids to decrease friction and wear between solid surfaces was initiated in the 1880s. In 1882 in the United Kingdom, Tower [125, 126] conducted experimental studies with the objective of enhancing the lubrication of railway axles. In summary, Tower was able to measure the pressure at various points along the railway axle. His findings indicated that the pressure was not constant and could exceed the average pressure required to balance the imposed load. Alternatively, Petrov (cited by Hamrock et al. [70]) reached a similar conclusion through friction measurements in 1883.

In 1886, Reynolds [115] achieved a significant breakthrough in the field of theoretical mechanics by successfully recovering the experimental results originally obtained by Tower [125, 126] through theoretical analysis. This led to the birth of the theory of lubrication. To build pressure and consequently generate lift, Reynolds demonstrated that the gap between solids should form a convergent. He was able to calculate the pressure within railway axles by simplifying the Navier-Stokes equations (see Navier [104] in 1827 and Stokes [122] in 1845) into the so-called Reynolds equation, in which the unknown p represents the pressure field across the contact area. This was done on the assumption that velocity profiles can be expressed as a sum of Poiseuille and Couette flows. The equation is detailed in the second chapter of this manuscript. In the following years, thanks to Reynolds' contribution, researchers and engineers began to study analytically and then numerically a great many liquid-lubricated systems, including thrust and journal bearings (see, for example, Michell [100] in 1929), tooth gears (see Martin [96]), etc.. Nevertheless, for some applications, only considering the Reynolds equation was not sufficient.

1.2.2 ElastoHydrodynamic Lubrication (EHL)

Indeed, in the 1910s, Martin [96] applied the Reynolds equation to tooth gears. However, according to Lugt et al. [94], the theoretical film thickness was found to be significantly smaller than the roughness height. In the

1940s, a couple of decades later, Ertel [53] and his collaborator Grubin [59] developed a model which coupled the Reynolds equation and the elastic deformation equation based on Hertz's [73] theory of contact. They considered the oil as a piezoviscous fluid using the viscosity–pressure law proposed by Barus [10]. The fundamental concept was that a lubricant film acts to separate the surfaces, and the pressure is such that the surfaces deform, as in a dry contact theorised by Hertz [73] in 1896. This work led to the birth of the ElastoHydrodynamic Lubrication (EHL) theory, in whereby Ertel [53] was able to predict more realistic film thicknesses.

EHL is a lubrication regime in which the lubricant pressure is typically of the order of magnitude of the gigapascal. The application of this elevated pressure results in the elastic deformation of the contacting bodies. Consequently, the elastic deformation cannot be disregarded. At elevated pressures, the molecules of a liquid are in closer proximity to one another, resulting in an increase in density. As the distance between molecules is reduced, the strength of their interaction increases, leading to an elevated viscosity (as described by Lubrecht [90]). In the context of EHL conditions, the pressure reaches such an elevated level that there is a considerable increase in viscosity, by a number of orders of magnitude. This lubrication regime is most prevalent when the contacting bodies are non-conformal, as is the case with REB and tooth gears (see figure 1.5). Due to the high pressure, the oil film thickness is very thin, varying between micrometres and hundreds of nanometres. Despite the film thickness being very small, the EHL contact offers a very small friction coefficient, mostly below 1×10^{-2}, as illustrated by Johnson et al. [81] or Spikes [121].

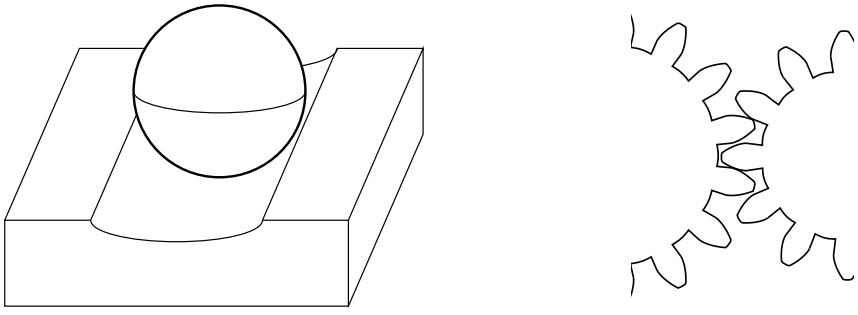

(a) Ball bearing contact (b) Gears

Figure 1.5: Non conformal surfaces leading to EHL contact applications

Experimental techniques

In the present era, an EHL contact can be observed and measured in an experimental setting on a test rig, as well as computed numerically, thanks to a variety of methods, which will be explained in greater detail later on. To illustrate, the "ball-on-disc" test rig, as presented in figure 1.6, enables the measurement of the film thickness of an EHL contact through the utilisation of an interferometric method (see, for example, Hartl et al. [72]), as well as the determination of the friction coefficient. Experimental measurement of film thickness is not the only possibility. Jubault et al. [83] achieved an in situ pressure distribution measurement using Raman microspectrometry and differential colorimetric interferometry. In 2020, Seoudi et al. [120] proposed a methodology for the in situ measurement of pressure and temperature within an EHL contact, based on the photoluminescence properties of non-intrusive quantum dots. The development of test rigs has also permitted the observation of spinning motion, as demonstrated by Dormois et al. [41], as well as truncation, as illustrated by Patrigeon et al. [107].

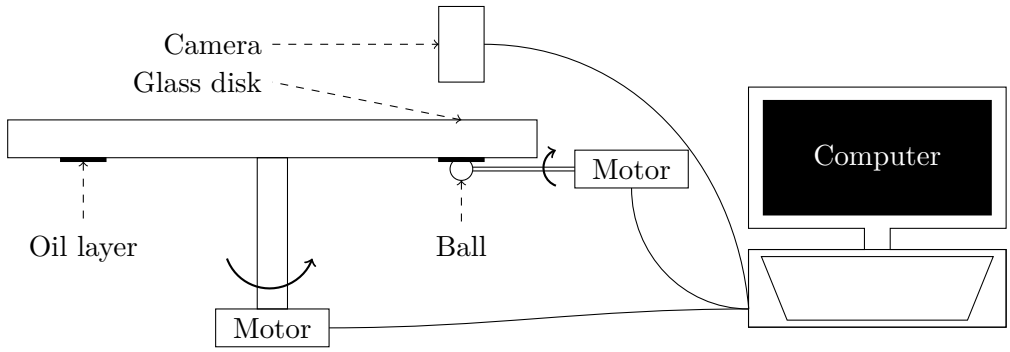

Figure 1.6: Schematic drawing of test rig allowing to observe and measure the film thickness

Numerical models

Including these physical phenomena

- small elastic deformations (larger than the film thickness itself);
- important piezo-viscous effects;

the following paragraphs elucidate the manner in which the outcomes yielded by Ertel [53] and Grubin [59] have been enhanced.

In order to simplify the elastic deformation of the lubricated contact, Ertel [53] employed the concept of dry contact elastic deformation. This indi-

cates that the thickness of the film is constant. Nevertheless, a constant film thickness throughout the entire contact area contravenes the conservation of mass flow rate. The elastic deformation of a dry contact has been calculated by Hertz [73] using the Boussinesq [17] potential theory, also known as the Boussinesq-Cerruti solution (see, for example, Johnson [80]). This theory is predicated on the assumption of a minimal contact area between two elastic solids, which are thus treated as semi-infinite half-spaces. The convolution product, which depends on the pressure field, is used to compute the elastic deformation. Therefore, the elastic deformation computation can be enhanced through the utilisation of the Boussinesq-Cerruti solution, without the necessity of considering the dry pressure field, as proposed by Ertel [53]. An alternative approach to computing elastic deformation is through the resolution of the linear elasticity equation, namely the Navier-Cauchy equation, which was derived by Timoshenko et al. [124]. This equation enables the simulation of a semi-infinite half-space, as well as a finite solid, where phenomena such as truncation may occur.

Furthermore, an enhanced improvement of the result is also directly correlated with an enhanced mathematical representation of the rheological properties of the fluid under diverse conditions.

The viscosity of the fluid is of great consequence with regard to the pressure build-up. In 1893, Barus [10] developed a viscosity-pressure law in the exponential form, which was notable for its simplicity. Nevertheless, the Barus formula tends to over-predict viscosity at high pressure. In 1965, Cheng et al. [28] proposed an extension of the law of Barus [10] to include temperature dependence. In 1966, Roelands [118] proposed a new viscosity-pressure-temperature law in the exponential form. However, it should be noted that the Roelands [118] formulae tend to underestimate viscosity at higher pressure values (see Habchi [62]). The aforementioned viscosity-pressure-temperature laws have not been established on a physical basis; they are purely empirical. In 1955, Williams, Landel, and Ferry [137] put forth a viscosity-pressure-temperature law that was initially situated within the domain of polymer physics. Subsequently, Yasutomi et al. [141] in 1984 proposed an improvement to the WLF law, resulting in the Yasutomi et al. model. The latter model has been further developed by Bair et al. [9] in 2013. As stated by Habchi [62], this enhanced model offers an exceptionally precise representation of the viscosity-pressure-temperature dependence of lubricants. However, the WLF model requires eight parameters to be determined for a given fluid through the use of measurements. In 2019, Bair [7] proposed an alternative, highly accurate model, the Vogel-like thermodynamic scaling model. However, the equation also includes a term that depends on density

and pressure, which must be determined using an equation of state. Similarly, Doolittle [40] in 1951 proposed the Doolittle free-volume model, which also requires the use of an equation of state to determine the density. The Doolittle free-volume model also provides an accurate representation of the viscosity-pressure-temperature dependence of lubricants (see Habchi [62]).

In regard to the fluid density, the most commonly employed equation of state is that proposed by Dowson and Higginson [45] in 1966. Similar to certain viscosity relationships, the Dowson and Higginson equation of state was derived through the fitting of experimental data for a single mineral oil under low pressure and controlled temperature conditions (for further information, please refer to Habchi [62]). The Dowson and Higginson equation is straightforward to employ, necessitating only two parameters (one if an isothermal study is undertaken). However, this equation of state is not applicable to all lubricants. Habchi et al. [63] investigated the influence of the equation of state and demonstrated that the Dowson and Higginson equation underestimates the increase in density with both pressure and temperature. This discrepancy results in a greater film thickness than that predicted by other equations of state. The most accurate representation of the density-pressure-temperature dependence of lubricants is the Tait equation of state (established in 1888), summarised by Dymond et al. [49] (see Habchi [62]). However, this equation of state requires five parameters, which must be determined through experimental measurement. Additionally, a similar equation of state was proposed by Murnaghan [102] in 1944, which also necessitates five input parameters.

Other factors that have not previously been discussed are the thermal contribution and the non-Newtonian behaviour encountered within EHL contact. Indeed, due to the sliding between the two surfaces, considerable shear stress can arise, resulting in thermal dissipation and rheological effects. Rheological effects result in a deviation from the Newtonian law, as outlined by Lubrecht [90], leading to a non-Newtonian behaviour. Non-Newtonian behaviours may manifest in a number of ways, including shear thickening, whereby the viscosity increases with shear, as observed in cornflour, and shear thinning, whereby the viscosity decreases with shear, as seen in blood and toothpaste. A number of models have been developed to represent the non-Newtonian viscosity of a fluid. Examples include the Eyring and Power law models, as discussed by Habchi [62]. Furthermore, thermal dependence is induced by shear, which generates a heat source and a compressive heat source, the latter of which can either warm or cool the fluid and the interacting surfaces. The thermal influence is contingent upon the operational conditions, including the velocity of the solids, their thermal properties, the

presence of a coating, etc.. As both the viscosity and the density are functions of temperature, an increase in temperature results in a decrease in viscosity, which in turn affects the film thickness and the friction coefficient, as evidenced by Amine et al. [3].

In light of the aforementioned concerns, it can be concluded that a numerical solver is the only method capable of solving an EHL problem. The numerical resolution of an EHL contact is not a straightforward process, due to a number of factors. Firstly, an EHL problem is highly non-linear. Secondly, the computational performance of the system is a significant factor.

In 1951, Petrusevich [109] was the first to solve a numerical EHL problem. He demonstrated the existence of a local convergent at the outlet of the EHL contact, as well as a pressure spike, both of which are presented qualitatively in figure 1.7. This figure also shows two deformed solids moving from left to right.

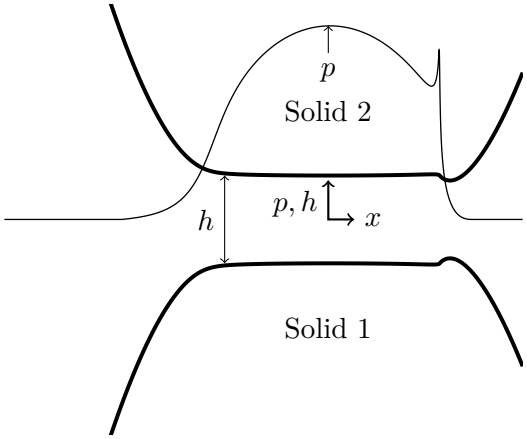

Figure 1.7: Typical result of an EHL contact

As computers became more powerful, the number of numerical solutions increased. For example, Dowson et al. [44] published a solution to the line contact problem (i.e. 1D, cylinder on plane contact) in 1959. A considerable amount of work has been carried out by Hamrock and Dowson [65, 66, 67] in relation to the point contact problem (i.e. 2D contact, sphere-on-plane contact). The work of Hamrock and Dowson is comprehensively summarised by Hamrock et al. [69]. Hamrock and Dowson developed analytical formulae that enable the estimation of minimum and central film thicknesses based on curve fitting of a substantial number of diverse computational cases. Chittenden et al. [33, 34] in 1985 combined the data from Hamrock and Dowson

with their own to encompass a broader range of geometrical configurations, thereby enhancing the analytical formulae.

While the EHL problem has been successfully addressed, the developed algorithms have encountered challenges in addressing more realistic applications, particularly those with high load. The algorithms are based on either an inverse method or a direct method utilising finite difference (FD). The inverse method involves solving the equations separately, with an iterative procedure established between their respective solutions until convergence is attained. The Boussinesq [17] potential theory, which is employed on numerous occasions when computing elastic deformation, is a particularly time-consuming process, rendering the method inefficient. The direct method employs simultaneous solution of the equations, utilising either a Gauss-Seidel relaxation or a Newton-Raphson procedure (see Venner [130]). The Gauss-Seidel relaxation method is unable to converge for high-load applications, and when it does converge, the convergence time is considerable. The Newton-Raphson procedure encounters difficulties due to the full Jacobian matrix, which is a consequence of the elastic deformations contribution computed using Boussinesq [17] potential theory. This results in convergence issues or a lengthy computation time for the algorithms. Consequently, it was not feasible to compute highly loaded cases, and therefore the results from light loads were extrapolated to predict film thickness.

In order to overcome these issues, Lubrecht [91] adapted a multigrid method (see Brandt et al. [18]) for the EHL problem based on FD discretisation in 1987. The method permitted the rapid and robust resolution of the EHL contact problem, thereby enabling the utilisation of a finer grid and, consequently, an enhancement in accuracy. Nevertheless, the application of the Boussinesq [17] equation to compute elastic deformations remained a time-consuming process. Subsequently, Venner [130] in 1991 enhanced the method's robustness through the incorporation of the "line-relaxation scheme", while also accelerating the computation of the elastic deformation based on the work of Brandt et al. [19] through the introduction of the Multi-Level Multi-Integral (MLMI) into the multigrid EHL solver. Based on this method, numerous analytical formulae for predicting film thickness have been presented (see, for example, Nijenbanning et al. [105]). This method enabled the computation of more realistic cases, including heavy-loaded applications and elliptical contacts. Additionally, it facilitated transient computations, which led to the investigation of surface roughness (see Venner et al. [133] or Biboulet [15]) and transient operating conditions (see Messé [99]).

In more recent times, another method to solve the EHL problem has been

developed by Habchi [61] in 2008. This is known as the "full system approach" and is based on the finite element (FE) method. In addition to the aforementioned discretisation, the method differs in terms of the manner in which elastic deformations are computed (Habchi [61] used the linear elasticity equation). The full system approach employs a fully coupled Newton-Raphson algorithm, the disadvantage of which, associated with the full Jacobian matrix, is eliminated by virtue of the modifications introduced by the elasticity deformation equation. In the words of Habchi et al. [64], the full system approach has a time complexity* of $\mathcal{O}(n \ln(n))$, identical to that of the MLMI multigrid EHL solver. The full system approach permitted the consideration of thermal effects† in addition to non-Newtonian fluids‡. Furthermore, full coated applications have been solved with this method (see Habchi [62]). The full system approach also permitted transient computation, enabling the study of, for example, inclusions§ (see Habchi [62]) and the investigation of the effect of spin (see Doki-Thonon [39]).

The aforementioned methods have facilitated a comprehensive investigation and comprehension of the "classical" EHL. Nevertheless, the starved lubricated contact, which represents a subject of significant importance, has yet to be fully explored. This manuscript aims to provide a detailed examination of this particular phenomenon.

1.3 Starvation

1.3.1 Starvation modeling

In lubrication, two regimes of feeding condition are found:

- fully flooded lubrication (see figure 1.8(a));
- starved lubrication (see figure 1.8(b)).

*The time complexity is typically indicated as $\mathcal{O}$(something), where "something" represents the number of costly operations as a function of the problem size. To illustrate, for a problem size of $n = 5$ the computation takes 15 s with a time complexity of $\mathcal{O}(n^2)$ indicating that there are $n^2 = 5^2$ costly operations. For $n = 50$ (a problem size 10 times larger), the computation takes 1500 s (on the same laptop).

†Can be done using MLMI multigrid EHL solver see Liu et al. [89].

‡Can be done using MLMI multigrid EHL solver see Chapkov [27].

§Can be done using MLMI multigrid EHL solver see Biboulet [15].

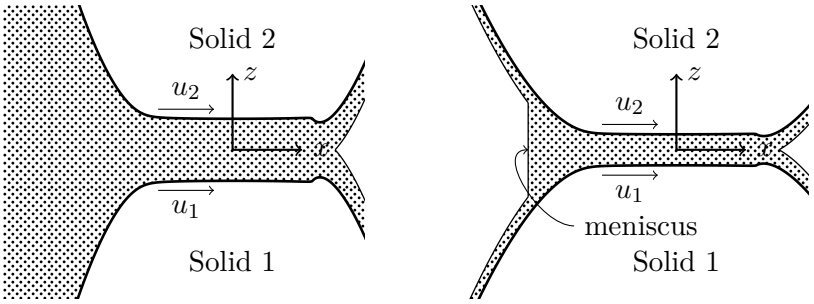

(a) Fully flooded (b) Starved

Figure 1.8: Difference between fully flooded and starved lubricated contacts

The dotted pattern displayed in figures 1.8(a) and 1.8(b) represents the lubricant, which is identified as oil. The distinction between the two lies in the quantity of lubricant present at the inlet of the contact, specifically at the left, upstream. As can be observed in the fully flooded regime, the oil completely fills the gap between the two solids. Figure 1.8(b) illustrates the phenomenon of two oil layers meeting at the inlet of the contact, resulting in the formation of a meniscus. In practice, this configuration also occurs in fully flooded applications, but the meeting point (meniscus) occurs at a much greater distance upstream. The aforementioned meeting point is referred to as the "inlet meniscus". Subsequently, alterations in the quantity of oil available result in corresponding shifts in the location of the inlet meniscus. After a certain position, the inlet meniscus position affects the film thickness (and therefore the load-carrying capacity), as illustrated in figure 1.9. A fully flooded lubricated contact is a contact where a variation of the amount of lubricant (i.e. the position of the inlet meniscus) has no impact on the film thickness. A starved contact differs from a fully flooded contact

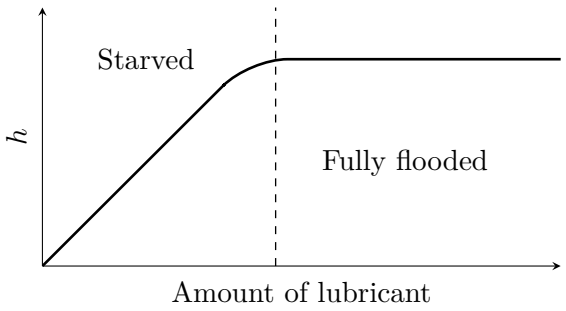

Figure 1.9: Schematic drawing of the evolution of the film thickness at a single point as a function of the feeding condition

in that, in this feeding condition, a change in the amount of lubricant (i.e. the inlet meniscus) modifies the film thickness. Ultimately, as illustrated in figures 1.8(a) and 1.8(b), the occurrence of cavitation can be observed at the outlet of the contact, specifically on the right-hand side, downstream. The phenomenon is caused by a decline in pressure, which leads to the formation of a mixture comprising oil, oil vapour and air.

According to Guangteng et al. [60], most of the REB as well as machine elements are working under starved conditions. Coy et al. [36] conducted measurements of film thicknesses in 1981 and compared the results to the analytical formulae previously mentioned (Hamrock et al. [67]). A satisfactory correlation was observed at low speeds; however, at high speeds, the measured film thicknesses were found to be smaller than the predicted values. The aforementioned gaps were attributed to thermal effects and also kinematic starvation (i.e. starvation generated by high speed conditions). In 1970, Wedeven [135] conducted an experimental investigation of starvation employing optical interferometry, simultaneously observing lubricant supply and contact thicknesses. Wedeven's findings indicated that starvation is directly linked to the inlet meniscus position, which is a consequence of the amount of lubricant entering upstream of the EHL contact.

The phenomenon of starvation has been the subject of modelling for several decades. The classical approaches described above do not take into account the quantity of lubricant available at the inlet of the contact. The contact is considered to be entirely filled with lubricant, such that the inlet meniscus is formed at a considerable distance from the contact. The film formation was theoretically treated by Jakobsson-Floberg-Olsson (JFO) in the 1950s and 1960s, resulting in the JFO theory (see, for example, Braun et al. [20]). They formulated the mass conservation of the fluid on the film formation frontier as well as the film rupture frontier, thereby enabling them to model cavitation as well as proposed by Bayada et al. [11] in 1990 in the framework of Hydrodynamic Lubrication (HL) applications. The position of both frontiers is unknown and depends on the conservation of mass flow rate. The JFO theory has been discussed in detail by Elrod and Adams [52] in 1975 and Bayada et al. [12]. Elrod and Adams [52] proposed an algorithm enabling the resolution of the JFO theory for transient starved HL application using FD. The Elrod and Adams algorithm has been widely used in the context of starved HL applications, for instance in journal bearings, due to its simplicity (see Dowson et al. [46] in 1984 or see Sahlin et al. [119]). At the present time, there are a number of highly efficient solvers in existence which are capable of computing the JFO theory. One such example is the solver developed by Biboulet et al. [16] in 2018.

An attempt to model starved EHL contact was made by Dowson [43] in 1975 using an artificial method. In this situation, the inlet domain computation was deliberately reduced in order to generate starvation (i.e. to prevent a zero pressure gradient at the pressure build-up). In contrast to the fully flooded scenario, the pressure rises from zero, resulting in a non-zero pressure gradient at the inlet meniscus (i.e., the inlet of the computational domain in this case). While this approach enables the simulation of starved conditions, it does not guarantee the conservation of the mass rate of flow.

In 1996, Chevalier [29] conducted pioneering research on starved EHL point contact, as also discussed in [30, 31, 32]. He employed the modified Reynolds equation, as introduced by Bayada et al. [11], in combination with the multigrid MLMI solver. This approach enabled him to compute a number of starved cases by imposing a known quantity of lubricant upstream of the inlet meniscus, the position of which was determined through use of a numerical procedure. His findings were in alignment with those previously reported by Dowson [43] using the artificial method. Nevertheless, when the degree of starvation increased, Chevalier demonstrated that the Dowson method yielded an overestimation of the film thickness. Chevalier proposed a relation for the prediction of film thickness in a starved lubricated case. In order to obtain such a prediction, Chevalier introduced the parameter γ, which is defined as "resistance to side flows". This parameter must be correlated with the fully flooded central film thickness, which can be calculated numerically or using analytical formulae. Furthermore, Chevalier examined the influence of lubricant deficiencies. In this scenario, the lubricant defect was caused by an uneven distribution of lubricant upstream of the inlet meniscus. Ultimately, he devised a formula for the reduction in film thickness in an EHL contact under multiple overrollings, utilising the γ parameter to achieve a more accurate representation of a true bearing. The oil layer thickness at the outer edge of the contact (i.e. downstream) assumes a specific configuration that subsequently influences the following contact, and so forth. Moreover, Chevalier [29] extended his film thickness decay formula in 1996 to encompass the scenario of track replenishment. In the circumstances described by Chevalier, the film thickness decay is observed to become null, reaching a steady value. Consequently, if the steady value is known, Chevalier [29] in 1996 is able to predict the film thickness decay curve until the stabilised value. The veracity of Chevalier's work has been corroborated by means of experimental investigation (see Chevalier et al. [30]). Based on the prediction of the film thickness of a starved EHL contact, Svoboda et al. [123] proposed an experimental approach in 2013 that enabled the measurement of the film thickness by determining the amount of oil available for the contact.

To achieve this outcome, the researchers developed an experimental method comprising a ball-on-disc test rig. An upstream barrel was incorporated to flatten the oil layer. By utilising optical measurement techniques on both the barrel and the ball, the thickness of the oil entering the contact could be quantified. The findings of Svoboda et al. [123] demonstrated a high degree of agreement between the numerical and experimental results.

In addition to the work of Chevalier, Wijnant [136] conducted an investigation in 1998 into a transient starved EHL contact, taking into account the effects of ellipticity. Wijnant made a significant contribution to the field of dynamically loaded EHL contacts, utilising the opportunity to provide a detailed derivation of the transient JFO theory, which led to the result presented by Bayada et al. [12]. Additionally, Wijnant proposed a modification to the dimensionless parameters, enabling a reduction in the number of unknowns in elliptical studies while employing the multigrid MLMI solver.

In 2003, Damiens [37] extended the work of Chevalier to starved elliptical EHL contact, focusing on the formula that allows for the determination of film thickness reduction in the context of successive overrollings. By combining the work of Chevalier and Wijnant and taking into account the enhanced capabilities of computers, Damiens achieved greater precision in determining the parameter γ, which varied between 0.4 % and 20 % compared to the values presented by Chevalier [29] in 1996, depending on the operational conditions. Additionally, Damiens [37] put forth an analytical Ertel [53]-like methodology for quantifying the ejected side flows. As a result of this analytical work, Damiens demonstrated that the closer the inlet meniscus is to the Hertzian area, the smaller the side flows will be. Additionally, Damiens conducted experimental research to corroborate the effectiveness of the formula employed to calculate the reduction in film thickness over multiple overrollings. Furthermore, he took into account the possibility of both oil layers re-entering the contact at different times. This has been achieved theoretically by means of the analytical formula proposed by Chevalier [29]. Damiens was successfully able to formulate the film thickness decay, taking into account the fact that both layers of oil re-enter at different times. In this scenario, the film thickness decay curve exhibits the same slope but a vertical offset with respect to the reference curve where both oil layers re-enter the contact simultaneously. Damiens [37] conducted a parametric study to create a table listing the coefficients required to multiply Chevalier's [29] film thickness decay function in order to generate the desired offset. Furthermore, Kostal et al. [86] in 2017 validated the prediction of a starved film thickness for elliptical contact given by Damiens using the experimental method developed by Svoboda et al. [123].

Popovici [110] conducted similar research to that of Wijnant in 2005, focusing on transient effects in the context of the starved EHL contact. The objective was to investigate the start-up of an EHL contact, assess the influence of impact, and examine the role of surface roughness. This was achieved by employing a numerical approach that incorporated time-dependent varying mass flow rates at the contact inlet and time-varying loads.

In 2009, van Zoelen [127] conducted a study on starvation, examining two distinct phenomena. Firstly, the effect of volumetric external forces (i.e. centrifugal force) on the oil layer (i.e. the layer of oil situated outside a contact, or between two contacts) has been subjected to analytical study. A fourth-order time-dependent differential equation, known as the thin layer equation, has been derived, thereby enabling observation of the behaviour of the oil layer. The aforementioned equation has been derived utilising curvilinear coordinates. Secondly, van Zoelen developed an alternative formulation for evaluating film thickness decay based on side flow fluxes, which differs from the Chevalier and Damiens formulation. This expression does not take into account track replenishment and allows for the prediction of film thickness as a function of time, rather than overrolling. Moreover, this expression does not require the use of γ, as is the case with the Chevalier model. In its original form, the equation representing film thickness decay was developed as a simplified means of determining the transverse thickness distribution at the central contact point. Consequently, the film thickness decay formula is simply the evaluation of the central value of the film thickness, which can be made analytically, whereas the distribution must be determined numerically. The van Zoelen thin layer model and film thickness decay formula have been validated through experimental work (see van Zoelen et al. [129] and van Zoelen et al. [128], respectively). As demonstrated by Lugt et al. [94], the van Zoelen model is more accurate than the Chevalier model in situations of severe starvation. This is because the Chevalier model requires the parameter γ to be determined numerically based on the position of the inlet meniscus. However, when severe starvation occurs, it is challenging to accurately capture the position of the inlet meniscus using current numerical methods. In response to this challenge, Lugt et al. [93] proposed a combined version of both analytical methods to predict film thickness decay.

In a more recent study, Porras Vazquez [111] in 2020 investigated the phenomenon of starvation in the context of spin motion, employing both numerical and experimental approaches. Porras Vazquez did not employ the JFO algorithm for the development of a starvation model. He developed a novel starvation model, which was based on the work of Bayada et al. [13]. Bayada et al. [13] initially proposed a cavitation algorithm utilising a biphasic

approach based on the sound velocity in the fluid to determine the cavitation pressure. Accordingly, the authors introduced a biphasic fluid. When the pressure exceeds the cavitation pressure, the density and viscosity of the mixture are those of a fluid. Otherwise, the density and viscosity are a function of the properties of the oil and the oil vapour. Bayada et al. [13] proposed a starved computation; however, as the model in question considers solely oil and oil vapour, rather than air, it is not applicable to starvation scenarios. Porras Vazquez incorporated air properties into the model originally proposed by Bayada et al. [13] in order to consider starvation. In contrast to the preceding studies, Porras Vazquez did not develop a homemade solver to address a starved lubricated problem. Instead, he employed a FE commercial software to integrate starvation into the full system approach developed by Habchi [61]. Porras Vazquez conducted an experiment in accordance with the method proposed by Svoboda et al. [123] to measure film thickness in the starved condition with the presence of spin. In the absence of spin, the numerical model proposed by Porras Vazquez was validated against experimental data, exhibiting a 5 % variation in central film thickness and a 17 % variation in minimum film thickness. Similarly, Marian et al. [95] employed a FE commercial software to model transient starvation, with the help of a penalised formulation of the JFO theory in 2019.

Moreover, the concept of thermal dependency has been incorporated into the starvation model. To the best of the author's knowledge, Yin et al. [142] are the first to introduce thermal dependency into the study of starved EHL point contact, extending the work previously conducted by Yang et al. [139] on line contact. In order to develop such an algorithm, Yin et al. [142] employed the MLMI multigrid solver. In recent years, a limited number of studies have been conducted on the topic of thermal starvation, with notable contributions from researchers such as Wang et al. [134] and Zhang et al. [144]. A comparison of starved Thermal ElastoHydrodynamic Lubrication (TEHL) contact with isothermal applications reveals that the former returns smaller values for both central and minimum film thicknesses. Yin et al. [142] conducted a parametric study, both thermal and isothermal, with varying oil quantity upstream of the contact. As previously stated, a starved TEHL contact results in a reduction in the values of minimum and central film thicknesses. However, the figure presented in [142] indicates that the inlet meniscus position is in front of its respective isothermal position. This would typically indicate a larger value for the central and minimum film thicknesses, as illustrated in figure 1.9. Furthermore, an increase in the quantity of oil upstream of the contact results in a greater disparity between the thermal and isothermal values in terms of film thickness. These numerical studies

were conducted using FD and the MLMI multigrid solver, in accordance with the JFO theory in the context of starvation.

1.3.2 Loss of Lubricant (LoL)

It can be observed that REB or gears can be either lubricated by means of an external device or possess a self-contained reservoir. The REB serves as an exemplar in this regard. Some REB are equipped with seals and are lubricated only once during the assembly process (see Hamrock et al. [68]). Other REB that does not possess seals are lubricated as a result of splashing (see, for example, Parker [106]). In the aforementioned case, the mechanical component is typically equipped with a lubrication system that facilitates lubricant circulation, as illustrated in section §1.1. A pertinent inquiry pertains to the operational longevity of a sealed bearing, which is capable of functioning for extended periods without interruption, despite the limited quantity of lubricant retained during its assembly. Similarly, it is crucial to understand the bearing's capacity to withstand prolonged operation in the event of an external device malfunction, such as an oil pump failure.

Analytical formulations for this situation were first provided by Chevalier et al. [30] and Damiens [37]. Subsequently, these formulations were used extensively by Querlioz [112] in 2007, with experimental validation. To achieve this, Querlioz deposited a series of oil droplets with the objective of obtaining a known mass of oil on the disc of the Mini Traction Machine (MTM) prior to its operation. Figure 1.10 provides a schematic representation of the MTM, while figure 1.10(b) offers a zoomed-in view of the MTM pot, with the filled dark rectangle indicating the oil layer that has been deposited on the MTM disc. This work may be classified as a LoL application, given that no supplementary oil is introduced into the test rig. Subsequently, she conducted a series of experiments utilising disparate entrainment velocities and oil masses. The setup allowed Querlioz to identify two distinct behaviours in terms of the friction coefficient. The initial outcome, which was anticipated, demonstrated an increase in the friction coefficient in relation to the number of overrollings until a sudden surge at the end, indicating the potential for dry contact, as illustrated in figure 1.11 and called "non-stabilisation". Conversely, at lower speeds, the friction coefficient reached a steady state, called "stabilisation" in figure 1.11. It was proposed by Querlioz that in this situation, replenishment of the track occurred, and that the initial outcome was due to the presence of scuffing, which resulted in a non-stabilised state. To facilitate comparison with the analytical formula, Querlioz proposed a methodology for converting the measured friction coefficient on MTM to

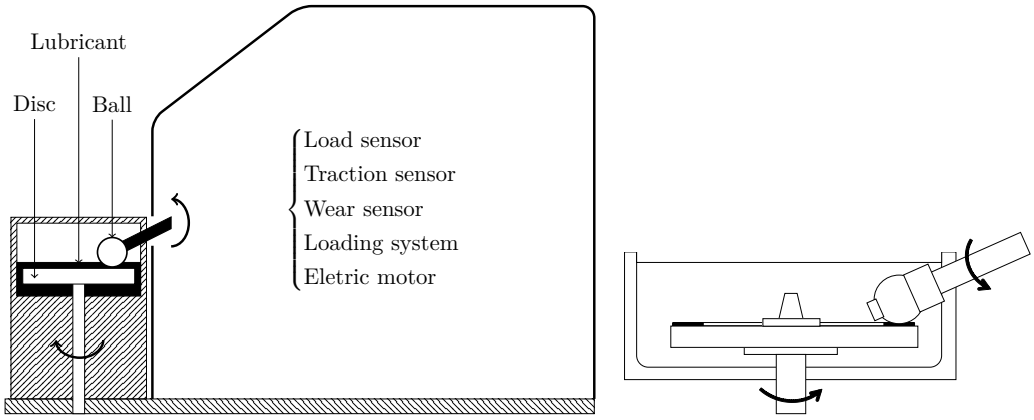

(a) Drawing of a cross section of a MTM (b) Zoom-in the MTM pot

Figure 1.10: Technical drawing of the MTM

central film thickness via a rheological model. This allowed for a comparison of her results with Chevalier' [30] film thickness reduction theory, both with and without consideration of track replenishment. Querlioz then succeeded in matching her experimental results to the analytical formula.

Similarly to Querlioz [112], Popovici [110] and van Zoelen et al. [128] con-

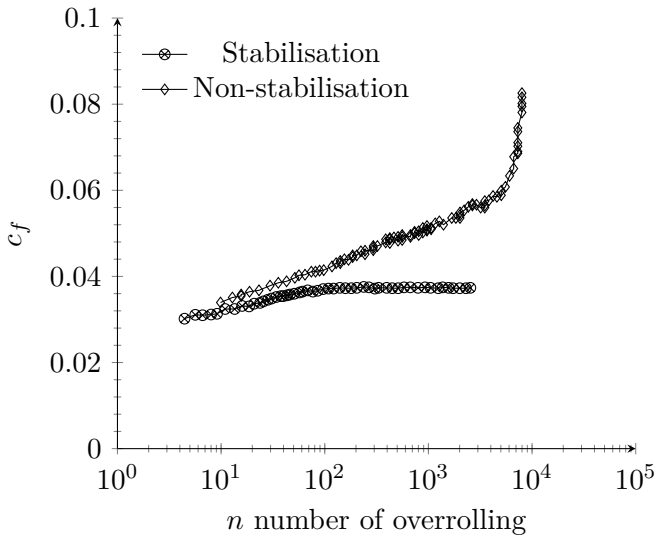

Figure 1.11: Two LoL applications made on MTM with different entrainment velocities leading to two different behaviours (data has been extracted from Querlioz [112] figure using OriginLab® software)

ducted experimental work, measuring both film thickness and the thickness of the oil layer entering the contact. Popovici observed a stabilisation of the film thickness following a number of overrollings at low speed. However, he observed a persistent reduction in film thickness at higher speeds. Nevertheless, the experimental duration was relatively brief (100 overrollings). Van Zoelen et al. [128] demonstrated two distinct categories of experimental LoL applications. Firstly, they observed a gradual decline in film thickness, which reached a stable state when using a ball rolling element. Secondly, when employing an elliptical rolling element, the film thickness decay remained unstable.

In 2017, Riggs et al. [116] conducted a study on the LoL for helicopter gearboxes using a protocol comparable to that employed by Querlioz. A MTM experiment was conducted for a period of 10 min with a lubricant supply in operation. The lubricant supply was then subjected to a sudden interruption. A series of tests were conducted to evaluate the performance of various materials and oils under high-speed and high-load conditions. The aforementioned applications demonstrated scuffing to occur at varying times, relative to the conditions previously outlined. Riggs et al. [117] conducted a similar investigation with the same conditions as those used by Riggs et al. [116], examining the impact of coating in a LoL process. The results demonstrated that the application of coatings can delay the onset of scuffing. Similarly, Anifa Mohamed Faruck et al. [4] examined the performance of diverse aviation industry oils in a LoL test, as Riggs et al. [116] had previously done. Furthermore, Anifa Mohamed Faruck et al. observed the occurrence of scuffing after a specific elapsed time, which was dependent on the oil under examination. Eichler et al. [50] and Mutyala et al. [103] conducted thrust bearing applications with and without coating, measuring torque and temperature. In their applications, the researchers used a minimal quantity of lubricant, immersing the ball bearings in a mixture of lubricating oil and hexane. In a state of rest, the hexane evaporates, leaving a thin layer of oil on the balls. During operation, a pronounced rise in temperature and torque was observed, akin to the findings from the experiments measuring the friction coefficient. In the uncoated case, the temperature and torque exhibited a concurrent increase. With the application of the coating, the temperature exhibited a sudden surge, while the torque did not demonstrate a simultaneous increase. The coating served as a solid lubricant for a period before the torque underwent a sharp rise. The chemical components within the coating and the lubricant play a prominent role in this phenomenon.

This raises the question of why some LoL applications result in steady-state lubricated behaviour, while others exhibit unsteady-state and scuffing

behaviour. A number of parameters appear to exert an influence, including the entrainment velocity, the load, the lubricant and material properties, etc.. As posited by the authors previously referenced, the answer is presumed to hinge on the presence or absence of track replenishment. What, then, is the mechanism behind the occurrence of replenishment in some applications and its absence in others? Can this behaviour be elucidated?

1.3.3 Track replenishment

According to Gershuni et al. [58], track replenishment inside REB appears because the "oil that is pushed to the side by overrolling may flow back into the track behind the contact and contribute to the layer of oil that is fed to the next rolling element ring contact again". The replenishment phenomenon is not straightforward to describe; however, as outlined by Gershuni et al. [58], the factors influencing this process include the viscosity, surface tension and external forces acting on the oil. Nevertheless, for replenishment to occur, the time between successive overrollings must be sufficiently long.

In 1976, Pemberton et al. [108] conducted experimental work which demonstrated the formation of a somewhat butterfly-shaped oil film around the contact, as illustrated in figure 1.12. The presence of the rolling element generates oil ridges downstream of the contact, which then feed the following contact. According to Pemberton et al. [108], those ridges may flow back into the raceway, thereby replenishing the track. However, they observed this behaviour only at low entrainment speeds and noticed that when speed is increased, the ridges do not replenish. They concluded that the replenishment

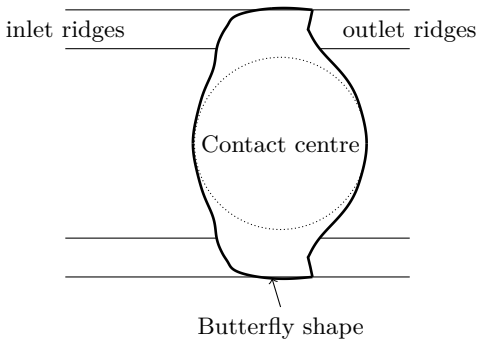

Figure 1.12: Technical drawing of a butterfly oil shape around the EHL contact

time is governed by the oil viscosity.

The phenomenon of track replenishment has also been observed by Hurley et al. [76] in 2000 and Cann [24] in 1996. Both studies were based on the use of grease lubricant. The investigation by Hurley et al. [76] examined the behaviour of the track replenishment in the presence of aged and non-aged grease. The researchers noted a decline in lubricant reflow rates with the aging of grease. This finding led them to hypothesize that an increase in viscosity may be responsible for this observed phenomenon. Furthermore, it was established that the base oil of the grease is the initial component to reflow in the track. Cann [25] posited that the grease in the vicinity of the contact releases its base oil as a consequence of shear degradation. Cann [25] observed the formation of a bulk grease at the edge of the track where the contact occurs. Indeed, it appears that the grease inside the bearing is rapidly ejected to the side of the contact, forming a reservoir. This reservoir bleeds its base oil, which contributes to track replenishment, as explained by Lugt [92]. Currently, surface adaptation is being studied in order to improve the ability to replenish by using, for example, texturations, as presented by Liu et al. [88]. The following paragraphs deal with different works related to track replenishment.

Cann et al. [26] investigated the track replenishment of greases in 1997, and additionally analysed the track replenishment of base oils. A ball-on-disc test was performed, and the film thickness was subsequently measured. The rotation of the ball was monitored, and the disc was driven by the ball. The focus of this work is not the grease, which is therefore not discussed here. However, the experimental work on the base oil is described in detail. A small quantity of oil was deposited on the disc and over 1000 to 2000 overrollings were subsequently completed. The experimental work of Querlioz [112] bears resemblance to this one. Cann et al. [26] presented a base oil film thickness decay during the first 100 revolutions of the disc, after which the film thickness reached a stabilised value. According to Cann et al. [26], this behaviour is due to track replenishment, which they state depends solely on the initial amount of oil available on the track. The experimental results have been compared to Chevalier [29] film thickness decay formula including replenishment, showing good proximity between the two.

In 1999, Jacod et al. [77] conducted a comprehensive investigation into the replenishment of tracks, employing both numerical and experimental methods. A dual experimental approach was employed, with observations made from two distinct vantage points, designated as “out of contact” and “close to contact”. The objective of the out-of-contact experiment was to observe the

behaviour of the oil layer situated downstream of the contact. The thin layer equation, as presented by Pemberton et al. [108], was solved with the inclusion of disjoining pressure and the exclusion of external forces. Subsequently, the investigation was limited to surface tension and disjoining pressure. It was found that both effects were negligible. However, the contribution of disjoining pressure increases with a reduction in film thickness, a phenomenon that has also been demonstrated by Guangteng et al. [60] in 1996. Jacod et al. [77] posit that this phenomenon occurs when the film thickness is so thin that it lacks physical significance. Conversely, the authors examined the vicinity of the contact. They investigated two capillarity pressure-driven track replenishment phenomena, designated as the radial model and the circumferential model. The radial model was found to be insignificant, whereas the circumferential model exhibited a more pronounced effect. The latter model demonstrated that the oil ridges merged with each other downstream of the contact. This phenomenon occurred during a stationary study. According to Jacod et al. [77], the numerical and experimental results exhibited a high degree of proximity.

In 2005, Popovici [110] conducted an experiment to quantify oil replenishment through the measurement of the oil profile. After performing multiple overrollings with a ball-on-disc test rig, he ceased the application and proceeded to measure the oil profile in the transverse direction at various time while the system was at rest. Between two successive measurements, a change in the oil layer profile was observed. Specifically, the curve after two minutes exhibited a flattening.

In 2008, Gershuni et al. [58] proposed a numerical study of track replenishment using the thin layer equation. The context of their study is as follows: the evolution of the oil layer deposited on the outer ring at the exit of one contact was observed. It was assumed that the oil layer presents two ridges downstream of the contact, as observed by Pemberton et al. [108] and illustrated in figure 1.13(a). The outer ring is subjected to a rotary motion with its axis of rotation aligned with the ground. In this application, the centrifugal force acts in the direction of gravity, which should result in the flattening of the oil profile shown in figure 1.13(a). Following the simulation of a range of rotational speeds (and therefore varying centrifugal forces), it was observed that track replenishment did not occur between two overrollings. In the optimal scenario, the replenishment of the track required a time period exceeding 1×10^5 s, given a time interval between two overrollings of only 3 ms. Gershuni et al. [58] defined the replenishment time as the period during which the central oil layer reaches an asymptote. Figure 1.13(b) presents a qualitative representation of the evolution of the application. However, this

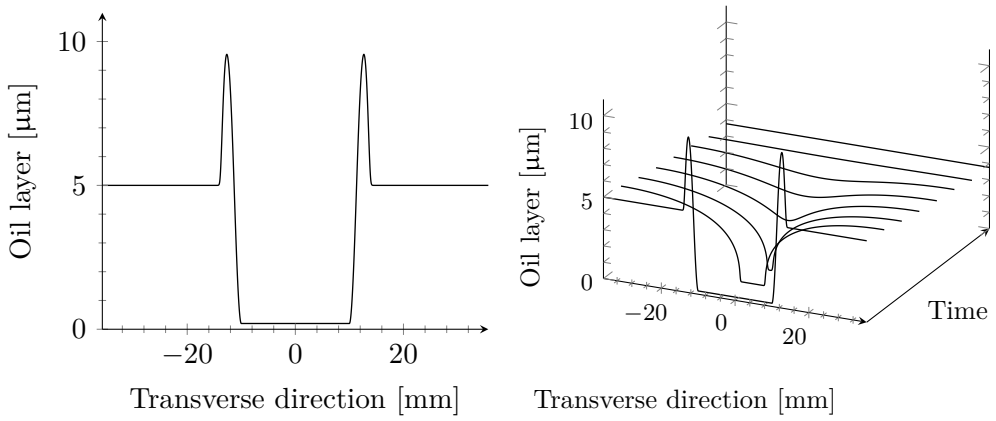

(a) Initial thin layer profile (b) Evolution of the thin layer profile

Figure 1.13: Reproduction of the application presented by Gershuni et al. [58]

application is a particular case and other working conditions may result in the appearance of track replenishment between two successive overrollings. For instance, this may occur when the centrifugal force acts in the tangential direction.

In 2015, Kostal et al. [85] conducted an experimental study on track replenishment utilising oil, with the objective of reproducing the numerical work of Gershuni et al. [58]. The configuration of the test rig differed from that of the numerical case, yet the resulting trends were analogous. One of the experiments conducted was a ball-on-disc test rig. Ten microlitres of oil were deposited on the disc, after which the test rig was run. The ball was then removed from contact with the disc, and the evolution of the oil layer was observed while the disc continued to rotate. The time required for the oil to replenish the track was measured in a similar manner to that described by Gershuni et al. [58]. Replenishment of the track commenced at 3 s and was complete after 8 s. However, this time is still considerably longer than the interval between two overrollings.

In 2015, Ali et al. [2] conducted an experiment to observe the impact of track replenishment on the friction coefficient and film thickness of an elliptical contact. In order to facilitate the observation of the impact of track replenishment on the friction coefficient and film thickness in an elliptical-on-disc contact, an ellipsoid in contact with a slider was employed. This configuration allowed for the flattening of the lubricant layer before its return to the contact, thereby enabling the study of track replenishment. Measurements

were conducted with and without the slider. The presence of the slider then generates track replenishment, thereby enabling the contact to operate in a fully flooded condition through the overrollings. The absence of the slider resulted in an increase in the friction coefficient, without the stabilisation observed in the experimental time frame. Furthermore, the effect of viscosity on these applications was investigated. It was observed that a more viscous oil resulted in a more rapid decay of the film thickness. Additionally, the film thickness measurements revealed that in the absence of track replenishment, the oil thickness at the centre of the contact was found to be less than that at the side. This indicates that the centre of the EHL contact is severely starved, while the side is well flooded.

In 2022, Gao et al. [57] conducted an experimental study combined with a numerical analysis. They investigated track replenishment on a stationary bearing (i.e., at rest) solely considering gravitational and surface tension forces. To accomplish the numerical analysis, they solved the thin layer equation. Their findings indicated that track replenishment in these conditions is considerable, exceeding ten minutes. They observed that decreasing the viscosity results in a more rapid replenishment of the track.

In conclusion, track replenishment is defined as the phenomenon whereby oil re-enters the track downstream of the contact. Oil ridges are formed downstream of the contact and are expected to re-enter the track due to surface tension, gravity, capillarity, and other forces. Experimental studies have demonstrated the occurrence of this phenomenon; however, the majority of these studies are based on the use of grease, which presents a complex behaviour. Nevertheless, the phenomenon of oil track replenishment has been beneficial to experimental and numerical studies conducted under a variety of operating conditions. Numerical studies that have employed the thin layer equation have demonstrated that replenishment occurs with minimal occurrence between two successive overrollings. However, experimental studies have indicated that following a transient period during which the film thickness decreases, a steady period ensues during which it reaches a stabilised value. This behaviour has been attributed to the supposed presence of the track replenishment phenomenon, although this has not been explicitly proven.

1.4 Conclusion

This chapter presented the composition of a REB and highlighted the complexity of this mechanical component due to the numerous parts composing

it. It was then concluded that it is difficult to study the whole assembly. Consequently, only one contact between a rolling element and the raceway is being investigated with the aim of extrapolating its behaviour to the whole assembly in the future.

A review of the literature on lubrication has been conducted. The principal factors that play a crucial role within an EHL contact have been outlined. Subsequently, the focus has been placed on numerical works, although experimental works have been referenced.

The core focus of this study is the phenomenon of starvation. Therefore, the phenomenon of starvation and related works have been enumerated. Two distinct behaviours have been observed throughout this section for the same application, designated as Loss of Lubricant (LoL). A LoL process necessitates that the EHL contact operate with an minimal quantity of oil, devoid of an additional lubricant supply. In certain instances, the frictional coefficient (or film thickness) exhibits stabilisation, whereas in other instances, an augmentation of the friction coefficient is evident.

The stabilisation of the frictional coefficient has been attributed to the supposed presence of the track replenishment phenomenon. Accordingly, a dedicated subsection has been included for the purpose of providing an explanation of the track replenishment process. This phenomenon has been observed in experimental settings, particularly in cases where grease lubrication was employed. The research conducted with oil indicated that this phenomenon is associated with the viscosity of the oil and the entrainment velocity. In contrast with the experimental findings, the numerical investigation demonstrated that the characteristic time of the track replenishment is considerably longer than the time between two overrollings, suggesting that it is a relatively insignificant concern in their respective applications. Consequently, the study of track replenishment is essential to ascertain whether it needs to be considered or not.

Lastly, the film thickness decay obtained during the LoL application has been compared to two analytical laws: one from Chevalier et al. [30] and the other from van Zoelen [127]. As evidenced in the literature cited above, both models demonstrated qualitative alignment with experimental outcomes in the absence of stabilisation. However, none of the aforementioned analytical laws is capable of predicting the occurrence of stabilisation a priori. The formula proposed by Chevalier [29] is able to suggest the possibility of stabilisation a posteriori, but this requires knowledge of the specific value of the film thickness at which stabilisation occurs. Consequently, a strategy involving hypotheses is developed in this work in order to gain insight into

the essential ingredient encountered in a Loss of Lubricant (LoL) process.

Chapter 2

Classical EHL equations

An ElastoHydrodynamic Lubrication (EHL) problem encompasses a range of physical phenomena, including solid mechanics, fluid mechanics, rheology, and others. The aforementioned physics are governed by equations that are defined based on the specific working conditions. In this manuscript, a sphere-on-plane contact is considered. Both solids are moving in the same direction, namely the rolling direction. The contact operates in the full film regime, and the surfaces are assumed to be smooth. Furthermore, a constant load is applied to the system.

Consequently, an EHL contact is governed by an equation that permits the calculation of elastic deformations, another equation that determines the pressure field, in addition to the laws governing density as a function of pressure and temperature, as well as viscosity as a function of pressure and temperature. Finally, a load balance equation is employed to ensure load-carrying capacity. In the case of a Thermal ElastoHydrodynamic Lubrication (TEHL) contact, an additional equation related to thermal dependency can be incorporated into the aforementioned set of equations.

2.1 The Reynolds equation

In order to calculate the fluid velocities and pressure into the gap of the contact, it is possible to simplify the Navier-Stokes equations into the Reynolds equation [115]. The initial hypotheses are that the fluid behaves as Newtonian, that the flow is laminar and that inertia forces are negligible in comparison to viscous forces (which results in a very small Reynolds number). Hamrock et al. [71] investigated all the terms within the Navier-Stokes equations in order to validate the aforementioned hypotheses. Secondly, the film thickness is much smaller than the other dimensions of the gap, implying that the pressure is considered constant in the thickness direction. Bruyère [23] studied EHL contact in 2012, solving Navier-Stokes equations and demonstrating that the aforementioned hypotheses hold true in lubricated contacts.

2.1.1 Derivation of the transient Reynolds equation

The derivation commences with the establishment of a state of equilibrium in the flow of an elementary column with a thickness of h and a base of $\mathrm{d}x\mathrm{d}y$, as demonstrated in figure 2.1.

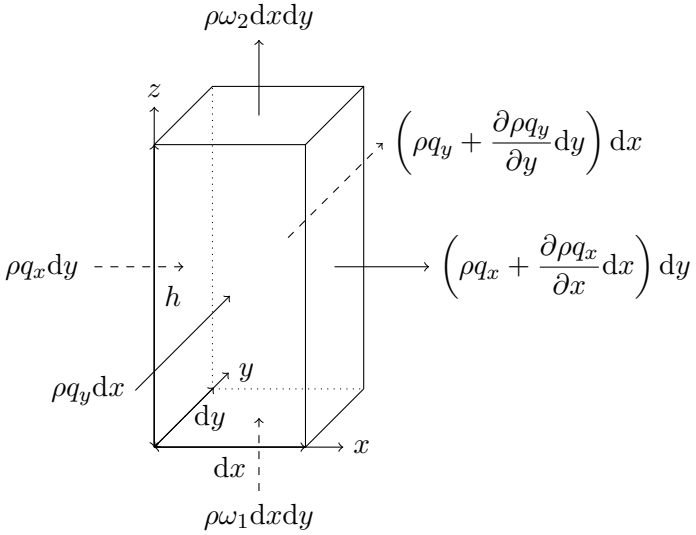

Figure 2.1: Mass flow rate equilibrium of an elementary column

The total mass flow rate entering the volume element must be equal to the total mass flow rate leaving the volume element such as

$$\begin{aligned}\rho q_x \mathrm{d}y + \rho q_y \mathrm{d}x + \rho\omega_1 \mathrm{d}x\mathrm{d}y = \\ \rho q_x \mathrm{d}y + \rho q_y \mathrm{d}x + \rho\omega_2 \mathrm{d}x\mathrm{d}y + \frac{\partial \rho q_x}{\partial x}\mathrm{d}x\mathrm{d}y + \frac{\partial \rho q_y}{\partial y}\mathrm{d}x\mathrm{d}y.\end{aligned} \tag{2.1}$$

The difference in velocity between the bottom and top surfaces of the column implies a rate of change in thickness h such as $\omega_2 - \omega_1 = \partial h/\partial t$. Moreover, this equilibrium must be equal to the rate of mass decrease within the element

$$-h\frac{\partial \rho}{\partial t}\mathrm{d}x\mathrm{d}y. \tag{2.2}$$

Finally, the equality between equations (2.1) and (2.2) gives rise to the continuity equation

$$\frac{\partial \rho q_x}{\partial x} + \frac{\partial \rho q_y}{\partial y} + \frac{\partial \rho h}{\partial t} = 0. \tag{2.3}$$

The second step is to determine the flow rates q_x and q_y. This is achieved through the application of an equilibrium, as illustrated in figure 2.2.

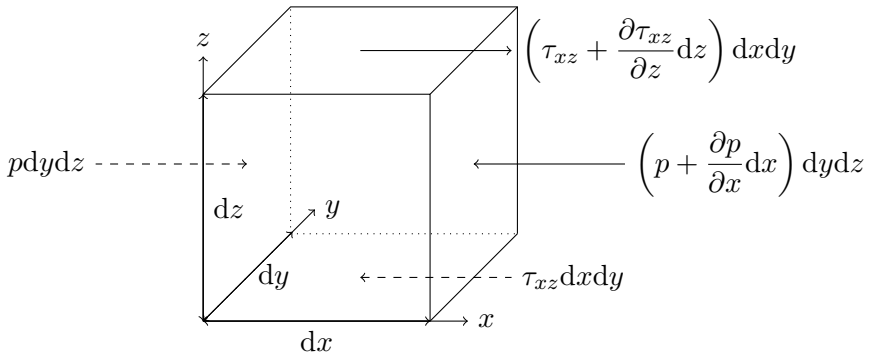

Figure 2.2: Equilibrium of an elementary volume of fluid in the x-direction

The force balance in the x-direction leads to

$$p\mathrm{d}y\mathrm{d}z + \left(\tau_{xz} + \frac{\partial \tau_{xz}}{\partial z}\mathrm{d}z\right)\mathrm{d}x\mathrm{d}y = \left(p + \frac{\partial p}{\partial x}\,\mathrm{d}\,x\right)\mathrm{d}y\mathrm{d}z + \tau_{xz}\mathrm{d}x\mathrm{d}y,$$

once simplifications had been made and the identical procedure had been

followed for the y-direction, the following set equations was obtained

$$\frac{\partial \tau_{xz}}{\partial z} = \frac{\partial p}{\partial x}, \tag{2.4a}$$

$$\frac{\partial \tau_{yz}}{\partial z} = \frac{\partial p}{\partial y}, \tag{2.4b}$$

$$\frac{\partial p}{\partial z} = 0. \tag{2.4c}$$

Equation (2.4c) ensures that pressure remains constant throughout the thickness. The introduction of the Newton law for viscous fluid $\tau_{xz} = \eta \frac{\partial u_f}{\partial z}$ and $\tau_{yz} = \eta \frac{\partial v_f}{\partial z}$ enables the substitution of the shear stress and leads to

$$\eta \frac{\partial^2 u_f}{\partial z^2} = \frac{\partial p}{\partial x}, \tag{2.5a}$$

$$\eta \frac{\partial^2 v_f}{\partial z^2} = \frac{\partial p}{\partial y}. \tag{2.5b}$$

Integrating twice equations (2.5a) and (2.5b) in the z-direction yields the fluid velocities. Under the assumption that the fluid adheres to the solid walls, the velocity at $z = 0$ is equal to u_1, the velocity of surface 1, and the velocity at $z = h$ is equal to u_2, the velocity of surface 2. Additionally, there is no velocity along y (i.e. $v_1 = v_2 = 0$). Therefore, the fluid velocities are

$$u_f = \frac{1}{2\eta} \frac{\partial p}{\partial x} z \left(z - h\right) + \frac{u_1 - u_2}{h} z + u_1, \tag{2.6a}$$

$$v_f = \frac{1}{2\eta} \frac{\partial p}{\partial y} z \left(z - h\right). \tag{2.6b}$$

Finally, the flowrate q_x is obtained integrating equation (2.6a) from $z = 0$ to $z = h$ leading to

$$q_x = -\frac{h^3}{12\eta} \frac{\partial p}{\partial x} + h u_m, \tag{2.7}$$

with $u_m = \frac{u_1 + u_2}{2}$ the arithmetical mean velocity. The flowrate q_y is obtained similarly by integrating equation (2.6b) from $z = 0$ to $z = h$ leading to

$$q_y = -\frac{h^3}{12\eta} \frac{\partial p}{\partial y}. \tag{2.8}$$

The application of equations (2.7) and (2.8) within the continuity equation (2.3) results in the derivation of the Reynolds equation [115].

$$\frac{\partial}{\partial x}\left(\frac{\rho h^3}{12\eta} \frac{\partial p}{\partial x}\right) + \frac{\partial}{\partial y}\left(\frac{\rho h^3}{12\eta} \frac{\partial p}{\partial y}\right) - \frac{\partial u_m \rho h}{\partial x} - \frac{\partial \rho h}{\partial t} = 0. \tag{2.9}$$

The two first terms represent the Poiseuille fluxes, the third term is the Couette flux and the last one is the transient also known as squeeze term.

2.1.2 Boundary conditions

The Reynolds equation (2.9) is solved on the contact domain, designated as Ω_L ("L" refers to lubricant) which represents a two-dimensional xy plan. The pressure is set to the ambient pressure at the boundary $\partial\Omega_L$ of the contact domain Ω_L. In practice, the ambient pressure is defined as the reference pressure, such that $p = 0$ on $\partial\Omega_L$. Furthermore, the solution of the Reynolds equation (2.9) with the aforementioned boundary condition may yield negative pressure. Given that the vapour pressure is assumed to be of a similar magnitude to the ambient pressure, it is not possible to obtain negative pressure; instead, the fluid undergoes cavitation. In order to complete the problem, it is necessary to ensure that the pressure is either positive or equal to zero ($p \geqslant 0$) and that a zero pressure gradient ($\partial p/\partial n$) is imposed on the cavitation boundary.

2.1.3 The lubricant properties

As outlined in chapter 1, the density (ρ) and viscosity (η) are not constant in an EHL contact due to the high pressure present. A review of the literature reveals numerous laws relating to either the density-pressure-temperature relationship or the viscosity-pressure-temperature relationship.

Density

The Dowson and Higginson [45] model is the most accessible and widespread representation of the variation of density with pressure and temperature. Its formulation is as follows:

$$\rho\left(p, \mathbb{T}\right) = \rho_R \left\{ \frac{5.9 \times 10^8 + 1.34p}{5.9 \times 10^8 + p} - \beta_{DH}\left(\mathbb{T} - \mathbb{T}_R\right) \right\}, \tag{2.10}$$

with ρ_R the reference density, $\mathbb{T}_R$ the reference temperature and β_{DH} the density-temperature coefficient. The model in question requires only two inputs: ρ_R (defined at $\mathbb{T}_R$) and β_{DH} to be used.

The Tait equation of state [49] is more accurate than the model proposed by Dowson and Higginson [45] (see chapter 1), which can be expressed as follows:

$$\rho\left(p, \mathbb{T}\right) = \frac{\rho_R}{\left\{1 + a_v\left(\mathbb{T} - \mathbb{T}_R\right)\right\}\left\{1 - \frac{1}{1+K_0'}\ln\left[1 + \frac{\left(1+K_0'\right)p}{K_\infty e^{-\beta_K \mathbb{T}}}\right]\right\}}. \tag{2.11}$$

For a given fluid, equation (2.11) requires the determination of five parameters: ρ_R, a_v the volume-temperature coefficient, K_0' the rate of change of isothermal bulk modulus at zero absolute temperature , K_∞ the isothermal bulk modulus at zero absolute temperature and β_K the isothermal bulk modulus temperature coefficient.

The Murnaghan [102] model is analogous to the Tait [49] model. The former is formulated as follows:

$$\rho\left(p,\mathbb{T}\right)=\frac{\rho_R}{1+a_v\left(\mathbb{T}-\mathbb{T}_R\right)}\left\{1+\frac{K_0'p}{K_\infty e^{-\beta_K\mathbb{T}}}\right\}^{1/K_0'}. \tag{2.12}$$

As is the case with the Tait model, equation (2.12) requires the input of the same five parameters.

Viscosity

The Barus [10] model, initially employed by Ertel [53], represents the most straightforward viscosity-pressure relationship such as:

$$\eta\left(p\right)=\eta_R e^{\alpha p}, \tag{2.13}$$

with η_R is the reference viscosity. This model only requires α, the viscosity pressure index and η_R.

The Roelands [118] model, similarly to the Barus [10]model, is straightforward to employ and necessitates the same input variables. It is the most widespread model for representing the variation of viscosity with pressure and temperature such that:

$$\eta\left(p,\mathbb{T}\right)=\eta_R e^{\left\{\ln\left(\eta_R\right)+9.67\right\}\left\{\left(1+\frac{p}{p_0}\right)^{z_R}\left(\frac{\mathbb{T}_R-138}{\mathbb{T}-138}\right)^{s_0}-1\right\}}, \tag{2.14}$$

with $p_0=1.98\times10^8\,\mathrm{Pa}$ a constant, $z_R=\alpha p_0/\left\{\ln\left(\eta_R\right)+9.67\right\}$ the Roelands parameter and s_0 the viscosity–temperature index.

The Williams, Landel, and Ferry [137] (WLF)/Yasutomi et al. [141] model is more accurate than previous models and can be expressed as follows:

$$\eta\left(p,\mathbb{T}\right)=\eta_g e^{\frac{-2.303C_1\left[\mathbb{T}-\mathbb{T}_g(p)\right]F(p)}{C_2+\left[\mathbb{T}-\mathbb{T}_g(p)\right]F(p)}}, \tag{2.15}$$

with $\mathbb{T}_g\left(p\right)=\mathbb{T}_{g0}+A_1\ln\left(1+A_2p\right)$ and $F\left(p\right)=1-B_1\ln\left(1+B_2p\right)$. The improvement povided by Bair et al. [9] reduces to $F\left(p\right)=\left(1+B_1p\right)^{B_2}$. Williams, Landel, and Ferry [137] or Yasutomi et al. [141] model requires eight parameters, η_g the viscosity at the glass temperature $\mathbb{T}_{g0}$, A_1, A_2, B_1, B_2, C_1 and C_2.

The Doolittle [40] model is founded upon the concept of free volume, which can be defined as follows:

$$\eta\left(p,\mathbb{T}\right)=\eta_R e^{BR_0\left(\frac{\frac{V_\infty}{V_{\infty R}}}{\frac{V}{V_R}-R_0\frac{V_\infty}{V_{\infty R}}}\right)-\frac{1}{1-R_0}}, \tag{2.16}$$

with $V_\infty/V_{\infty R}=1+\varepsilon_c\left(\mathbb{T}-\mathbb{T}_R\right)$ and $V/V_R=\rho_R/\rho$. Equation 2.16 needs four parameters η_R, B, R_0 and ε_c plus the addition of the density equation.

2.2 The film thickness

The film thickness h represents the gap between the two solids, as illustrated in figures 2.3(a) and 2.3(b).

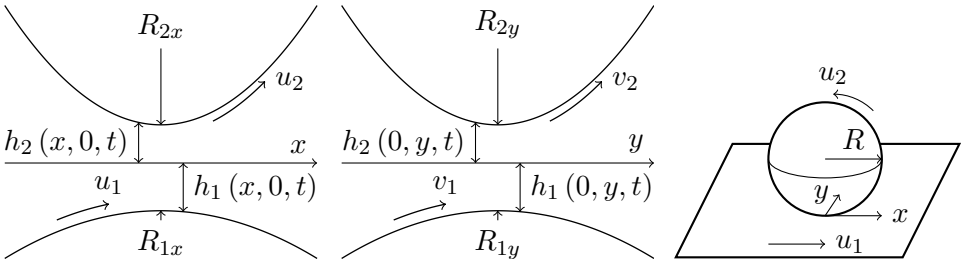

(a) x-direction (b) y-direction (c) 3D simplification

Figure 2.3: Film thickness

Due to the small film thickness and contact width, the undeformed surface geometry can be approximated by paraboloids, such as:

$$h\left(x,y,t\right)=h_1\left(x,y,t\right)+h_2\left(x,y,t\right)= \\ h_{10}\left(t\right)+\frac{x^2}{2R_{1x}}+\frac{y^2}{2R_{1y}}+h_{20}\left(t\right)+\frac{x^2}{2R_{2x}}+\frac{y^2}{2R_{2y}},$$

with h_{i0} the gap between the solid i and the line $z=0$ for $x=y=0$. In order to reduce the geometry to a sphere-on-a plane contact (see figure 2.3(c)), it is necessary to consider only spherical contacts, that is to say, $R_{ix}=R_{iy}=R_i$. This allows for the calculation of an equivalent/reduced radius of curvature

$$R=\left(\frac{1}{R_1}+\frac{1}{R_2}\right)^{-1}, \tag{2.17}$$

with R_1 the radius of curvature of solid 1 and R_2 the radius of curvature of solid 2. The equivalent film thickness, which considers the total displacement at the aforementioned two surfaces resulting from elastic deformation (hereafter denoted as w), is given by

$$h\left(x,y,t\right) = h_{00}\left(t\right) + \frac{1}{2R}\left(x^2+y^2\right) - w\left(x,y,t\right), \tag{2.18}$$

with $h_{00}\left(t\right) = h_{10}\left(t\right) + h_{20}\left(t\right)$ the total gap at $x = y = w = 0$.

2.3 Elastic deformations

The elastic deformations of the solid surfaces play a crucial role in the EHL contact. Indeed, the displacement are bigger than the film thickness itself. Equation (2.18) introduced the total displacement of the two surfaces w. To obtain the displacement w, the pressure given by the Reynolds equation (2.9) is then applied on the edge Ω_L of an equivalent solid Ω as presented figure 2.4. The displacement of the equivalent solid is fixed to zero on the edge called $\partial\Omega_F$ and free everywhere else. This equivalent solid combines the properties of both contacting bodies, which are detailed in the following of this section.

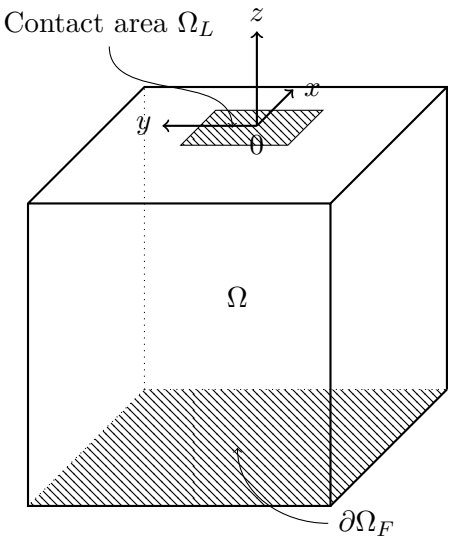

Figure 2.4: Equivalent solid Ω

By taking an elementary cube within the domain Ω and applying Newton's second law in each direction, as illustrated in figure 2.5, the result in the x-

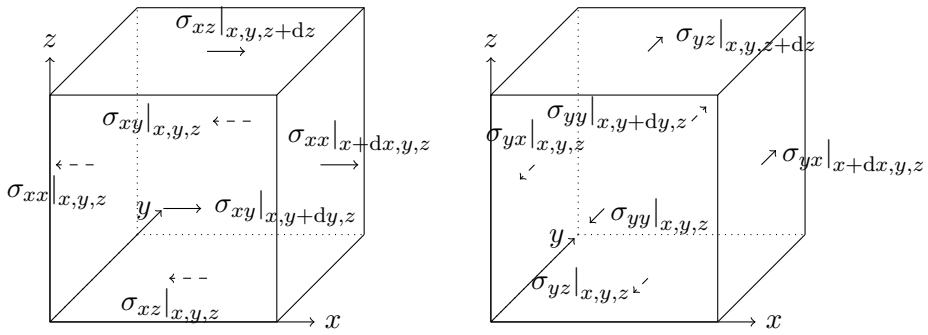

(a) In the x-direction (b) In the y-direction

Figure 2.5: Equilibrium of a cube (same procedure in the z-direction)

direction is

$$\begin{aligned}
&\sigma_{xx}|_{x+\mathrm{d}x,y,z}\,\mathrm{d}y\mathrm{d}z - \sigma_{xx}|_{x,y,z}\,\mathrm{d}y\mathrm{d}z + \\
&\sigma_{xy}|_{x,y+\mathrm{d}y,z}\,\mathrm{d}x\mathrm{d}z - \sigma_{xy}|_{x,y,z}\,\mathrm{d}x\mathrm{d}z + \\
&\sigma_{xz}|_{x,y,z+\mathrm{d}z}\,\mathrm{d}x\mathrm{d}y - \sigma_{xy}|_{x,y,z}\,\mathrm{d}x\mathrm{d}y + f_x\mathrm{d}V = \rho_s\mathrm{d}V\ddot{u},
\end{aligned} \tag{2.19}$$

where f_x is a body force in the x-direction. By neglecting the body forces and identifying the instantaneous rate of change, as well as simplifying all $\mathrm{d}V$, equation (2.19) can be rewritten as follows:

$$\frac{\partial\sigma_{xx}}{\partial x} + \frac{\partial\sigma_{xy}}{\partial y} + \frac{\partial\sigma_{xz}}{\partial z} = \rho_s\ddot{u}. \tag{2.20}$$

By repeating the identical procedure in both the y-direction and the z-direction, the equilibrium in rectilinear translation of an elementary cube leads to

$$\underline{\mathrm{div}}\left(\underline{\underline{\sigma}}\right) = \rho_s\underline{\ddot{\mathfrak{U}}}, \tag{2.21}$$

with $\underline{\mathfrak{U}} = [u,\ v,\ w]$.

Furthermore, equation (2.21) may be expressed in terms of displacement as a function of material properties for isotropic and homogeneous media*. The displacement constitutes the requisite output for EHL calculations. This may be achieved through the application of Hooke's law (see Timoshenko et al. [124]), whereby

$$\sigma_{ij} = \Lambda\delta_{ij}\varepsilon_{kk} + 2\mu\varepsilon_{ij}, \tag{2.22}$$

*For anisotropic and inhomogeneous media the derivation changes and is not presented here

where δ_{ij} is the Kronecker delta, Λ and μ the Lamé parameters such as $\Lambda = \frac{\nu E}{(1+\nu)(1-2\nu)}$ and $\mu = \frac{E}{2(1+\nu)}$. It is necessary to include the equivalents of the Young modulus and Poisson ratio within the Lamé parameters. Subsequently, from Habchi [62], it can be inferred that $E = E_{eq}$ and $\nu = \nu_{eq}$, which may be expressed as follows:

$$E_{eq} = \frac{E_1^2 E_2 \left(1+\nu_2\right)^2 + E_2^2 E_1 \left(1+\nu_1\right)^2}{\left\{E_1\left(1+\nu_2\right) + E_2\left(1+\nu_1\right)\right\}^2}, \tag{2.23a}$$

$$\nu_{eq} = \frac{E_1\nu_2\left(1+\nu_2\right) + E_2\nu_1\left(1+\nu_1\right)}{E_1\left(1+\nu_2\right) + E_2\left(1+\nu_1\right)}. \tag{2.23b}$$

Given that the deformations and displacements are deemed to be sufficiently minor, the relationship between these two phenomena can be described as follows:

$$\varepsilon_{ij} = \frac{1}{2}\left(\frac{\partial u_i}{\partial x_j} + \frac{\partial u_j}{\partial x_i}\right). \tag{2.24}$$

The derivation is only detailed for equation (2.20), but the procedure is the same for σ_{yj} and σ_{zj}. By employing equations (2.22) and (2.24) it is possible to compute σ_{xj}

$$\begin{cases} \sigma_{xx} = \Lambda\left(\varepsilon_{xx}+\varepsilon_{yy}+\varepsilon_{zz}\right) + 2\mu\varepsilon_{xx} = \Lambda\left(\dfrac{\partial u}{\partial x} + \dfrac{\partial v}{\partial y} + \dfrac{\partial w}{\partial z}\right) + 2\mu\dfrac{\partial u}{\partial x}, \\ \sigma_{xy} = 2\mu\varepsilon_{xy} = \mu\left(\dfrac{\partial u}{\partial x} + \dfrac{\partial v}{\partial y}\right), \\ \sigma_{xz} = 2\mu\varepsilon_{xz} = \mu\left(\dfrac{\partial u}{\partial x} + \dfrac{\partial w}{\partial z}\right). \end{cases}$$

Upon substituting into equation (2.20), the result is

$$\left(\Lambda+\mu\right)\frac{\partial}{\partial x}\left(\frac{\partial u}{\partial x} + \frac{\partial v}{\partial y} + \frac{\partial w}{\partial z}\right) + \mu\left(\frac{\partial^2 u}{\partial x^2} + \frac{\partial^2 u}{\partial y^2} + \frac{\partial^2 u}{\partial z^2}\right) = \rho_s \ddot{u}. \tag{2.25}$$

The application of the aforementioned procedure in all the directions results in the derivation of the Navier-Cauchy equation

$$\left(\Lambda+\mu\right)\underline{\nabla}\left(\nabla\left(\underline{\mathfrak{U}}\right)\right) + \mu\underline{\Delta}\left(\underline{\mathfrak{U}}\right) = \rho_s\underline{\ddot{\mathfrak{U}}}, \tag{2.26}$$

When the study is stationary, the inertia term (i.e. the right-hand side of equation (2.26)) vanishes. However, the presence of the inertia term in the context of transient lubricated applications requires further discussion. According to Achenbach [1]: "The importance of dynamic effects depends

on the relative magnitudes of two characteristic times: the time characterizing the external application of the disturbance and the characteristic time of transmission of disturbances across the body.". The Navier-Cauchy equation (2.26) can be rearranged to yield an elastic wave equation form such that

$$\underbrace{\frac{\Lambda + 2\mu}{\rho_s}}_{v_p^2} \underline{\text{grad}} \left\{ \text{div} \left(\underline{\mathfrak{U}} \right) \right\} - \underbrace{\frac{\mu}{\rho_s}}_{v_t^2} \underline{\text{rot}} \left\{ \underline{\text{rot}} \left(\underline{\mathfrak{U}} \right) \right\} = \underline{\ddot{\mathfrak{U}}}. \tag{2.27}$$

It is notable that equations (2.26) and (2.27) are analogous but have been rearranged in a different manner, with the Lamé parameters Λ and μ being identical. This equation illustrates two velocities that are well-established in the field of seismology: the velocity of the longitudinal wave (v_p), which is also known as the P-wave, and the velocity of the shear wave (v_t), which is also known as the S-wave. For further details, please refer to Timoshenko et al. [124]. By employing the expression of the Lamé parameters, it becomes evident that v_t represents the smallest velocity. Subsequently, v_t is utilised to compute the characteristic time of transmission of disturbance across the solid. The characteristic time is defined as the time taken by a disturbance to travel the contact half-width a, as detailed in section §2.6. This methodology is analogous to that proposed by Raisin et al. [113]

$$\tau_{wave} = \frac{a}{v_t} = \frac{a}{\sqrt{E/2\rho_s \left(1 + \nu\right)}}. \tag{2.28}$$

The characteristic time of the disturbance is defined as the time taken for the fluid to travel the contact half-width, a, in a manner analogous to that described by Raisin et al. [113]

$$\tau_{dist} = \frac{a}{u_m}. \tag{2.29}$$

Figure 2.6 shows τ_{wave} using steel properties and τ_{dist} for varying u_m and a. It can be observed that τ_{wave} is significantly smaller than τ_{dist}, which suggests that v_t may be considerably larger than u_m. In terms of physical processes, this result indicates that the solid reaches a steady state at a considerably faster rate than the fluid. This implies that the solid deforms instantaneously. Therefore, the problem is quasi-static rather than dynamic, and the inertia term is disregarded in equation (2.26). A review of the literature revealed that various EHL transient studies have employed a quasi-static approach, solving the Navier-Cauchy equation (2.26) to obtain transient solutions. For instance, Hultqvist [75] employed this strategy in 2020. Additionally, other

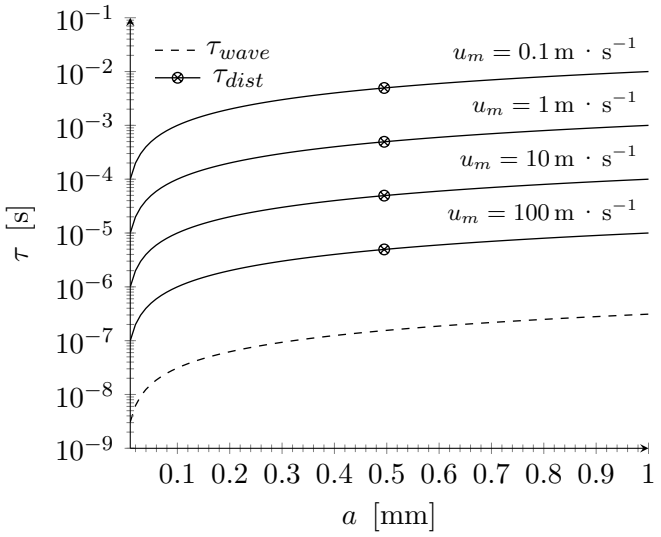

Figure 2.6: Comparison of the characteristic time (for steel solid)

researchers have adopted alternative methodologies for computing elastic deformations, such as Biboulet [15], Popovici [110] and Wijnant [136]. These studies also disregarded inertia terms in their transient applications.

2.4 Force balance

In order to obtain a complete EHL problem, it is necessary to ensure that the lift generated by the pressure is equal to the mass multiplied by the acceleration, plus the applied load F (Newton's second law)

$$m\frac{\partial^2 h_{00}}{\partial t^2} + F = \iint p \, \mathrm{d}x\mathrm{d}y, \tag{2.30}$$

with Ω_L the lubricant domain where the Reynolds equation is solved as illustrated figure 2.4. The first term on the left-hand side represents the inertia term, which vanishes if the study is stationary or quasi-static. This mass, designated as m, represents the equivalent mass, such as the equivalent radius (see equation (2.17)). In the case of bearing, the mass of the raceway (i.e. the ring) is much larger than the rolling element. Consequently, the equivalent mass reduces to the rolling element mass, and this result is analogous to that observed in a ball-on-disc test rig.

Similarly, as has been done with the linear elasticity equation, the role of the inertia term within the load balance equation (2.30) is examined.

In order to facilitate this analysis, equation (2.30) is made dimensionless, thereby reducing the number of independent variables. The dry contact parameters introduced in section §2.6 are employed. Subsequently, using the substitutions $X = x/a$, $Y = y/a$, $P = p/p_H$ with $p_H = 3F/2\pi a^2$, $H_{00} = h_{00}R/a^2$ and $T = tu_m/a$, equation (2.30) becomes

$$\frac{mu_m^2}{RF}\frac{\partial^2 H_{00}}{\partial T^2} = \frac{3}{2\pi}\iint P \,\mathrm{d}X\mathrm{d}Y - 1. \tag{2.31}$$

The aforementioned equation permits the introduction of the natural dimensionless frequency of the system. In the case where the equivalent mass is reduced to the mass of the ball i.e. $m = 4\rho_s\pi R^3/3$ with R denoting the radius of the ball), the dimensionless natural frequency is given by

$$\Omega_n^2 = \frac{RF}{mu_m^2} = \frac{F}{\frac{4}{3}\rho_s\pi R^2 u_m^2}. \tag{2.32}$$

Figure 2.7 illustrates the evolution of the dimensionless natural frequency as a function of F and u_m for $R = 1\,\mathrm{cm}$ and $\rho_s = 7800\,\mathrm{kg}\cdot\mathrm{m}^{-3}$. It can be observed that for these coefficients, the square of natural frequency reaches high values, indicating that inertia effects are negligible in comparison to the right-hand side of equation (2.31), which is equal to unity. Nevertheless, an increase in R results in a reduction in Ω_n. Furthermore, as velocity increases, the value of Ω_n approaches the order of magnitude of the right-hand side of equation (2.31). Nevertheless, given that the presented case assumes a constant load, rigid displacements (i.e. $H_{00}\,(T)$) are negligible.

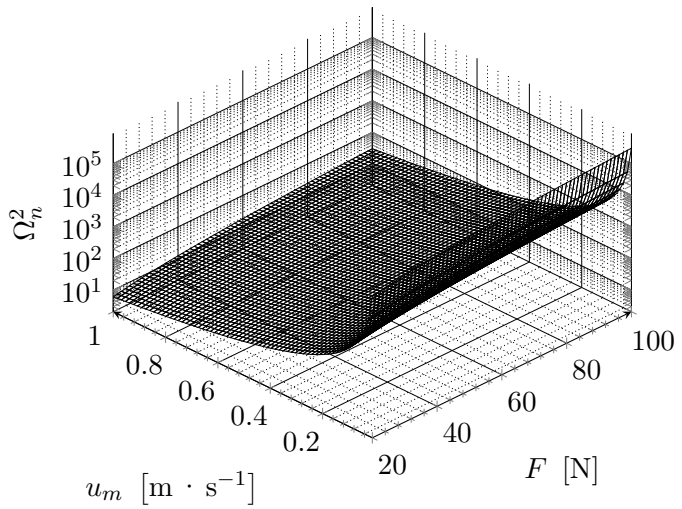

Figure 2.7: Dimensionless natural frequency function of speed and load

Consequently, the combination of the natural frequency and the negligible rigid displacements indicates that the inertia term can be disregarded in this study, in a similar manner to the approaches proposed by Venner et al. [132], Biboulet [15] and Messé [99]. Therefore, the force balance equation can be simplified as follows:

$$\int_{\Omega_L} p \, \mathrm{d}\Omega_L - F = 0. \tag{2.33}$$

2.5 Thermal contribution

Chapter 1 emphasised the significance of thermal effects within an EHL contact. These effects are predominantly observed in the context of sliding motion, as evidenced by the Slide to Roll Ratio (SRR), which is defined as $\mathrm{SRR} = (u_2 - u_1)/u_m$. However, the introduction of thermal effects presents a challenge.

2.5.1 Reynolds equation including thermal effects

It is not possible to employ the classical isothermal Reynolds equation in this instance; instead, the Generalized Reynolds equation must be utilised. In 1962, Dowson [42] introduced a form of Generalized Reynolds equation. However, one of the most general forms, which includes non-Newtonian behaviour and allows for density variation, was presented by Yang et al. [140] in 1990. The derivation of the Generalized Reynolds equation diverges from the classical derivation of the Reynolds equation (section §2.1) with the introduction of the Newton law for viscous fluids $\tau_{xz} = \eta \frac{\partial u_f}{\partial z}$ and $\tau_{yz} = \eta \frac{\partial v_f}{\partial z}$ (see equations (2.5a) and (2.5b)). At this stage, the integrations of equations (2.5a) and (2.5b) must take into account the variation in viscosity across the thickness direction, yielding at

$$u_f = u_1 + \frac{\partial p}{\partial x}\left(\int_0^z \frac{z\mathrm{d}z}{\eta} - \frac{\eta_e}{\eta'_e}\int_0^z \frac{\mathrm{d}z}{\eta}\right) + \eta_e u_s \int_0^z \frac{\mathrm{d}z}{\eta}, \tag{2.34a}$$

$$v_f = \frac{\partial p}{\partial y}\left(\int_0^z \frac{z\mathrm{d}z}{\eta} - \frac{\eta_e}{\eta'_e}\int_0^z \frac{\mathrm{d}z}{\eta}\right), \tag{2.34b}$$

with $u_s = u_2 - u_1$, the sliding velocity. For a comprehensive derivation, the reader is encouraged to refer to either the work of Yang et al. [140] or that of Habchi [62]. The Generalized Reynolds equation can be expressed as follows:

$$\frac{\partial}{\partial x}\left\{\left(\frac{\rho}{\eta}\right)_e \frac{\partial p}{\partial x}\right\} + \frac{\partial}{\partial y}\left\{\left(\frac{\rho}{\eta}\right)_e \frac{\partial p}{\partial y}\right\} - \frac{\partial \rho_x^\star}{\partial x} - \frac{\partial \rho_e}{\partial t} = 0 \tag{2.35}$$

with

$$\begin{cases} \left(\dfrac{\rho}{\eta}\right)_e = \dfrac{\eta_e}{\eta'_e}\rho'_e - \rho''_e, \\ \rho^\star_x = \rho'_e \eta_e \left(u_1 - u_2\right) + \rho_e u_2, \\ \dfrac{1}{\eta_e} = \displaystyle\int_0^h \frac{\mathrm{d}z}{\eta}, \\ \dfrac{1}{\eta'_e} = \displaystyle\int_0^h \frac{z\mathrm{d}z}{\eta}, \\ \rho_e = \displaystyle\int_0^h \rho \mathrm{d}z, \\ \rho'_e = \displaystyle\int_0^h \rho \int_0^z \frac{\mathrm{d}z}{\eta}\mathrm{d}z, \\ \rho''_e = \displaystyle\int_0^h \rho \int_0^z \frac{z\mathrm{d}z}{\eta}\mathrm{d}z. \end{cases} \tag{2.36}$$

In this context, the subscript "e" is used to denote equivalent quantities, taking into account the variations in the lubricant's density (ρ) and viscosity (η) across the film thickness.

2.5.2 Thermal model

The derivation of the energy equation is analogous to that of the Reynolds equation. An equilibrium of the heat fluxes, represented by the equation $\varphi_\varnothing = -k\partial\mathbb{T}/\partial\varnothing$, is established when heat enters and leaves an elementary cube in the $\varnothing$-direction. Furthermore, the presence of a heat source, designated as Q, must be considered. This results in the following equation:

$$\begin{aligned} \frac{\partial}{\partial x}\left(k\frac{\partial \mathbb{T}}{\partial x}\right) + \frac{\partial}{\partial y}\left(k\frac{\partial \mathbb{T}}{\partial y}\right) + \frac{\partial}{\partial z}\left(k\frac{\partial \mathbb{T}}{\partial z}\right) \\ - \rho C_p\left(\mathrm{u}_x\frac{\partial \mathbb{T}}{\partial x} + \mathrm{u}_y\frac{\partial \mathbb{T}}{\partial y} + \mathrm{u}_z\frac{\partial \mathbb{T}}{\partial z}\right) + Q = \rho C_p\frac{\partial \mathbb{T}}{\partial t}, \end{aligned} \tag{2.37}$$

which is known as the energy equation and bears resemblance to the Reynolds equation (2.9). For a full account of the derivation, the reader is directed to consult, for instance, the work of Bejan [14]. According to Raisin et al. [113], determining the thermal characteristic time is a non-trivial task. Therefore, the transient term is assumed to be negligible during the initial stages of this research project.

Equation (2.37) must be applied to both the solids and the lubricant film thickness, as illustrated in figure 2.8. As stated by Habchi [61], "heat

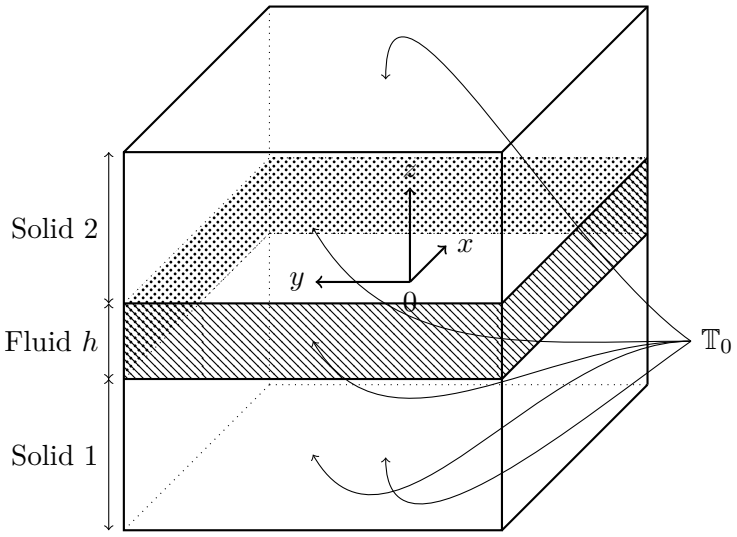

Figure 2.8: Thermal domains

convection in the film thickness and conduction in the film plane can be neglected compared to the convection in the film plane and conduction in the film thickness, respectively". This allows for the simplification of the equation, resulting in

$$\begin{cases} \dfrac{\partial}{\partial x}\left(k_i \dfrac{\partial \mathbb{T}}{\partial x}\right) + \dfrac{\partial}{\partial y}\left(k_i \dfrac{\partial \mathbb{T}}{\partial y}\right) + \dfrac{\partial}{\partial z}\left(k_i \dfrac{\partial \mathbb{T}}{\partial z}\right) - \rho_i C_{p_i} u_i \dfrac{\partial \mathbb{T}}{\partial x} = 0 \quad i = \text{solid 1}, \\ \dfrac{\partial}{\partial x}\left(k_i \dfrac{\partial \mathbb{T}}{\partial x}\right) + \dfrac{\partial}{\partial y}\left(k_i \dfrac{\partial \mathbb{T}}{\partial y}\right) + \dfrac{\partial}{\partial z}\left(k_i \dfrac{\partial \mathbb{T}}{\partial z}\right) - \rho_i C_{p_i} u_i \dfrac{\partial \mathbb{T}}{\partial x} = 0 \quad i = \text{solid 2}, \\ \dfrac{\partial}{\partial z}\left(k_{oil} \dfrac{\partial \mathbb{T}}{\partial z}\right) - \rho C_{p_{oil}} \left(u_f \dfrac{\partial \mathbb{T}}{\partial x} + v_f \dfrac{\partial \mathbb{T}}{\partial y}\right) = Q \quad \text{oil}. \end{cases}$$

The heat source Q represents the addition of two heat sources, one resulting from compression and the other from shear such as

$$\begin{cases} Q_{comp} = -\dfrac{\mathbb{T}}{\rho}\dfrac{\partial \rho}{\partial \mathbb{T}}\left(u_f \dfrac{\partial p}{\partial x} + v_f \dfrac{\partial p}{\partial y}\right), \\ Q_{shear} = \eta \left\{ \left(\dfrac{\partial u_f}{\partial z}\right)^2 + \left(\dfrac{\partial v_f}{\partial z}\right)^2 \right\}, \end{cases} \tag{2.38}$$

with u_f and v_f the generalized fluid velocities in the x- and y-directions respectively (see equations (2.34a) and (2.34b)) and

$$\frac{\partial u_f}{\partial z} = \frac{1}{\eta}\frac{\partial p}{\partial x}\left(z - \frac{\eta_e}{\eta'_e}\right) + \frac{\eta_e u_s}{\eta}, \tag{2.39a}$$

$$\frac{\partial v_f}{\partial z} = \frac{1}{\eta}\frac{\partial p}{\partial y}\left(z - \frac{\eta_e}{\eta'_e}\right). \tag{2.39b}$$

Finally, to ensure an energetic equilibrium, heat flux continuity is imposed at the two interfaces lubricant-solid such as

$$\begin{cases} k_{oil}\left.\dfrac{\partial \mathbb{T}}{\partial z}\right|_{0^+} = k_{\text{solid 1}}\left.\dfrac{\partial \mathbb{T}}{\partial z}\right|_{0^-}, \\ k_{oil}\left.\dfrac{\partial \mathbb{T}}{\partial z}\right|_{h^-} = k_{\text{solid 2}}\left.\dfrac{\partial \mathbb{T}}{\partial z}\right|_{h^+}. \end{cases}$$

The temperature is imposed on the bottom surface of solid 1 and on the top surface of solid 2 (see figure 2.8). It is necessary to fix the temperature of the entering parts (fluid and solids) at the inlet of the subdomains, while ensuring that all other surfaces benefit from thermal insulation, thus guaranteeing a zero gradient flux.

2.6 Dimensionless equations

In the course of reading the preceding sections, a multitude of parameters had to be taken into account in order to successfully resolve an EHL contact problem. As a result, the utilisation of dimensionless groups would serve to reduce the number of parameters. Furthermore, an EHL contact problem gives rise to considerable pressure values and exceedingly small values for the film thickness. These factors can result in a severely ill-conditioned matrix, which in turn causes numerical issues. The EHL contact is typically normalised in accordance with the dry contact theory proposed by Hertz [73]. Hertz formulated the radius of the contact area, a, as a function of the geometry of the two contacting solids, the applied load, and the properties of the solids such as:

$$a = \sqrt[3]{\frac{3FR}{2E'}}, \tag{2.40}$$

with F the applied load. The reduced elasticity modulus of the two solids in contact is represented by the symbol E' such as:

$$E' = \left\{\frac{1}{2}\left(\frac{1-\nu_1^2}{E_1} + \frac{1-\nu_2^2}{E_2}\right)\right\}^{-1}, \tag{2.41}$$

with E_1 the Young modulus and ν_1 the Poisson coefficient of the first solid and index 2 refers to the second solid. Finally the maximum Hertzian pressure is

$$p_H = \frac{3F}{2\pi a^2} \tag{2.42}$$

and the Hertzian pressure field is

$$p\left(x,y\right) = p_H\sqrt{1-\left(\frac{x}{a}\right)^2-\left(\frac{y}{a}\right)^2} \qquad \text{for} \qquad \begin{cases} -a \leqslant x \leqslant a, \\ -a \leqslant y \leqslant a. \end{cases} \tag{2.43}$$

All physical quantities are normalised using the following dimensionless parameters. Variables with $\varnothing_0$ refer to ambient conditions, i.e. $p = 0\,\text{Pa}$ and $\mathbb{T} = \mathbb{T}_0$.

$$\begin{cases} X = \dfrac{x}{a}, \quad Y = \dfrac{y}{a}, \quad Z = \begin{cases} \dfrac{z}{a} & \text{solids} \\ \dfrac{z}{h} & \text{lubricant film} \end{cases}, \\ U = \dfrac{u}{a}, \quad V = \dfrac{v}{a}, \quad W = \dfrac{w}{a}, \quad \bar{E}_{eq} = \dfrac{E_{eq}}{p_H} \\ P = \dfrac{p}{p_H}, \quad H = \dfrac{hR}{a^2}, \quad T = \dfrac{tu_m}{a}, \\ \bar{\rho} = \dfrac{\rho}{\rho_0}, \quad \bar{\eta} = \dfrac{\eta}{\eta_0}, \quad \overline{\mathbb{T}} = \dfrac{\mathbb{T}}{\mathbb{T}_0}. \end{cases}$$

2.6.1 Isothermal Newtonian Reynolds equation

The dimensionless isothermal Newtonian Reynolds equation reduces to

$$\frac{\partial}{\partial X}\left(\bar{\xi}_{\mathrm{P}}\frac{\partial P}{\partial X}\right) + \frac{\partial}{\partial Y}\left(\bar{\xi}_{\mathrm{P}}\frac{\partial P}{\partial Y}\right) - \frac{\partial \bar{\rho}H}{\partial X} - \frac{\partial \bar{\rho}H}{\partial T} = 0, \tag{2.44}$$

where $\bar{\xi}_{\mathrm{P}} = \frac{\bar{\rho}H^3}{\bar{\eta}\bar{\lambda}}$ is the Poiseuille dimensionless coefficient with $\bar{\lambda} = \frac{12\eta_0 u_m R^2}{a^3 p_H}$. The dimensionless film thickness reads as

$$H\left(X,Y,T\right) = H_{00}\left(T\right) + \frac{1}{2}\left(X^2+Y^2\right) - \frac{R}{a}W\left(X,Y,T\right) \tag{2.45}$$

with $W\left(X,Y,T\right)$ the dimensionless displacement resulting from the dimensionless elastic deformation equation. Finally, the dimensionless load balance equation develops into

$$\frac{3}{2\pi}\iint P\ \mathrm{d}X\mathrm{d}Y - 1 = 0. \tag{2.46}$$

2.6.2 Generalized Reynolds equation

According to Habchi [62], the dimensionless Generalized Reynolds equation becomes

$$\frac{\partial}{\partial X}\left(\bar{\xi}'_{\mathrm{P}}\frac{\partial P}{\partial X}\right)+\frac{\partial}{\partial Y}\left(\bar{\xi}'_{\mathrm{P}}\frac{\partial P}{\partial Y}\right)-\frac{\partial\bar{\rho}^{\star}_{x}H}{\partial X}-\frac{\partial\bar{\rho}_{e}H}{\partial T}=0, \tag{2.47}$$

with

$$\begin{cases}\bar{\xi}'_{\mathrm{P}}=\dfrac{H^{3}p_{H}a^{3}}{u_{m}\eta_{0}R^{2}}\left(\dfrac{\bar{\eta}_{e}}{\bar{\eta}'_{e}}\bar{\rho}'_{e}-\bar{\rho}''_{e}\right),\\ \bar{\rho}^{\star}_{x}=\dfrac{\bar{\rho}'_{e}\bar{\eta}_{e}\left(u_{1}-u_{2}\right)+\bar{\rho}_{e}u_{2}}{u_{m}},\\ \dfrac{1}{\bar{\eta}_{e}}=\displaystyle\int_{0}^{1}\frac{\mathrm{d}Z}{\bar{\eta}},\\ \dfrac{1}{\bar{\eta}'_{e}}=\displaystyle\int_{0}^{1}\frac{Z\mathrm{d}Z}{\bar{\eta}},\\ \bar{\rho}_{e}=\displaystyle\int_{0}^{1}\bar{\rho}\mathrm{d}Z,\\ \bar{\rho}'_{e}=\displaystyle\int_{0}^{1}\bar{\rho}\int_{0}^{1}\frac{\mathrm{d}Z}{\bar{\eta}}\mathrm{d}Z,\\ \bar{\rho}''_{e}=\displaystyle\int_{0}^{1}\bar{\rho}\int_{0}^{1}\frac{Z\mathrm{d}Z}{\bar{\eta}}\mathrm{d}Z.\end{cases} \tag{2.48}$$

2.6.3 Elastic deformation

The dimensionless Navier-Cauchy equation develops into

$$\left(\bar{\Lambda}+\bar{\mu}\right)\underline{\nabla}\left(\nabla\left(\underline{\mathcal{U}}\right)\right)+\bar{\mu}\underline{\Delta}\left(\underline{\mathcal{U}}\right)=\underline{0} \tag{2.49}$$

with $\underline{\mathcal{U}}=[U,\ V,\ W]$ and $\bar{\Lambda}=\frac{\nu_{eq}\bar{E}_{eq}}{(1+\nu_{eq})(1-2\nu_{eq})}$ and $\bar{\mu}=\frac{\bar{E}_{eq}}{2(1+\nu_{eq})}$, see for instance Hultqvist [75].

2.6.4 Energy equation

The dimensionless energy equation in each domain, derived using the aforementioned dimensionless groups, is as follows:

$$\begin{cases} \dfrac{\partial}{\partial X}\left(\dfrac{k_i}{a}\dfrac{\partial \overline{\mathbb{T}}}{\partial X}\right)+\dfrac{\partial}{\partial Y}\left(\dfrac{k_i}{a}\dfrac{\partial \overline{\mathbb{T}}}{\partial Y}\right)+\dfrac{\partial}{\partial Z}\left(\dfrac{k_i}{a}\dfrac{\partial \overline{\mathbb{T}}}{\partial Z}\right) \\ \qquad\qquad -\rho_i C_{p_i} u_i \dfrac{\partial \overline{\mathbb{T}}}{\partial X}=0 \quad \text{solid 1}, \\ \dfrac{\partial}{\partial X}\left(\dfrac{k_i}{a}\dfrac{\partial \overline{\mathbb{T}}}{\partial X}\right)+\dfrac{\partial}{\partial Y}\left(\dfrac{k_i}{a}\dfrac{\partial \overline{\mathbb{T}}}{\partial Y}\right)+\dfrac{\partial}{\partial Z}\left(\dfrac{k_i}{a}\dfrac{\partial \overline{\mathbb{T}}}{\partial Z}\right) \\ \qquad\qquad -\rho_i C_{p_i} u_i \dfrac{\partial \overline{\mathbb{T}}}{\partial X}=0 \quad \text{solid 2}, \\ \dfrac{\partial}{\partial Z}\left(\dfrac{k_{oil}R^2}{H^2a^3}\dfrac{\partial \overline{\mathbb{T}}}{\partial Z}\right)-\rho_0\bar{\rho}C_{p_{oil}}\left(u_f\dfrac{\partial \overline{\mathbb{T}}}{\partial X}+v_f\dfrac{\partial \overline{\mathbb{T}}}{\partial Y}\right)=\bar{Q} \quad \text{oil}, \end{cases} \tag{2.50}$$

with

$$\begin{cases} \bar{Q}_{comp}=-\dfrac{\overline{\mathbb{T}}}{\bar{\rho}}\dfrac{\partial \bar{\rho}}{\partial \overline{\mathbb{T}}}\dfrac{p_H}{\mathbb{T}_0}\left(u_f\dfrac{\partial P}{\partial X}+v_f\dfrac{\partial P}{\partial Y}\right), \\ \bar{Q}_{shear}=\dfrac{\eta_0\bar{\eta}R^2}{H^2a^3\mathbb{T}_0}\left\{\left(\dfrac{\partial u_f}{\partial Z}\right)^2+\left(\dfrac{\partial v_f}{\partial Z}\right)^2\right\}. \end{cases}$$

Finally, the velocities written with the dimensionless parameters are

$$\begin{cases} u_f=u_1+\dfrac{p_H H^2a^3}{\eta_0 R^2}\dfrac{\partial P}{\partial X}\left(\displaystyle\int_0^Z\dfrac{Z\mathrm{d}Z}{\bar{\eta}}-\dfrac{\bar{\eta}_e}{\bar{\eta}'_e}\int_0^Z\dfrac{\mathrm{d}Z}{\bar{\eta}}\right)+\bar{\eta}_e u_s\displaystyle\int_0^Z\dfrac{\mathrm{d}Z}{\bar{\eta}}, \\ v_f=\dfrac{p_H H^2a^3}{\eta_0 R^2}\dfrac{\partial P}{\partial Y}\left(\displaystyle\int_0^Z\dfrac{Z\mathrm{d}Z}{\bar{\eta}}-\dfrac{\bar{\eta}_e}{\bar{\eta}'_e}\int_0^Z\dfrac{\mathrm{d}Z}{\bar{\eta}}\right), \end{cases}$$

Lastly, the heat flux continuity at the two interfaces lubricant-solid becomes

$$\begin{cases} \dfrac{k_{oil}R}{Ha}\dfrac{\partial \overline{\mathbb{T}}}{\partial Z}\Big|_{0^+}=k_{\text{solid 1}}\dfrac{\partial \overline{\mathbb{T}}}{\partial Z}\Big|_{0^-}, \\ \dfrac{k_{oil}R}{Ha}\dfrac{\partial \overline{\mathbb{T}}}{\partial Z}\Big|_{1^-}=k_{\text{solid 2}}\dfrac{\partial \overline{\mathbb{T}}}{\partial Z}\Big|_{1^+}. \end{cases}$$

2.7 Numerical procedure

In order to solve the EHL or TEHL problem numerically, the finite element (FE) method is employed. The dimensionless Reynolds equation (2.44) and

Navier-Cauchy equation (2.49) are discretised using the Galerkin method, respectively with quintic and quadratic Lagrangian elements in accordance with Habchi [62]. To complete the solution, the ordinary integral equation (2.46) is incorporated into the system of equations. In consideration of the aforementioned symmetry, a factor of two must be employed in either the multiplication of the lift generated by pressure or the division of the applied load in the force balance equation (2.46). The dimensionless Reynolds equation (2.44) is discretised on a rectangular plan XY with coordinates $X_{in} = -4.5$, $X_{out} = 1.5$ and $Y_{out} = -3$, as illustrated in figure 2.9(a). The dimensionless Navier-Cauchy equation (2.49) is discretised on a rectangular cuboid Ω with dimensions as indicated in figure 2.9(b).

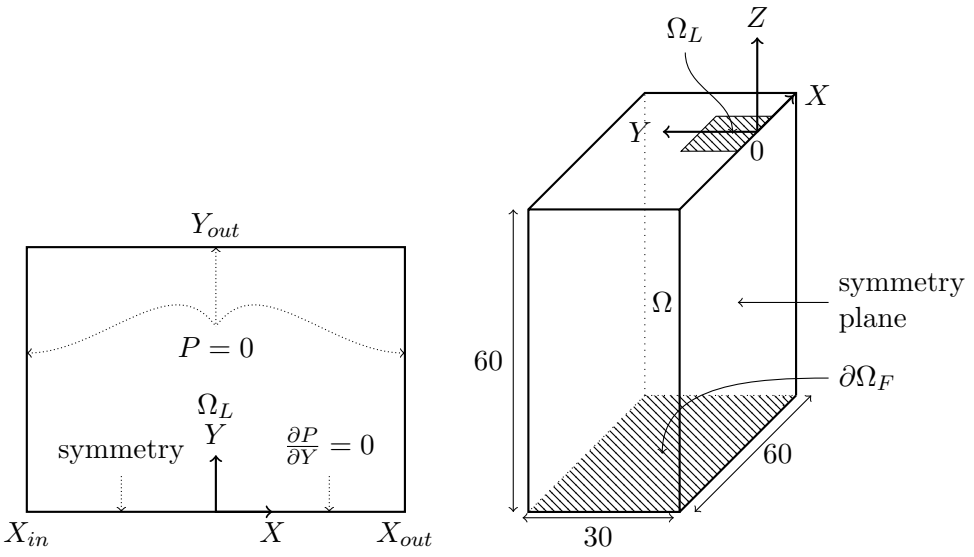

(a) Reynolds equation domain Ω_L (b) Elastic deformation domain Ω

Figure 2.9: Domains computation to solve the EHL problem

In the event that a TEHL problem must be considered, it is necessary to discretise the Generalized Reynolds equation (2.47) rather than the classical Reynolds equation (2.44). Quintic Lagrangian elements are employed for this purpose. The Navier-Cauchy equation (2.49) and its computational domain highlighted in figure 2.9 remain unchanged. However, the thermal model must be incorporated into the system of equations to be solved with the dimensionless energy equations (2.50) using quadratic Lagrangian elements. The energy equations (2.50) are discretised in their respective domains (solids and fluid) as illustrated in figure 2.10, with $d_X = X_{out} - X_{in}$ and $d_Y = Y_{out}$.

All domains are meshed using triangle elements for the plan domain and tetrahedral elements for the volume domain.

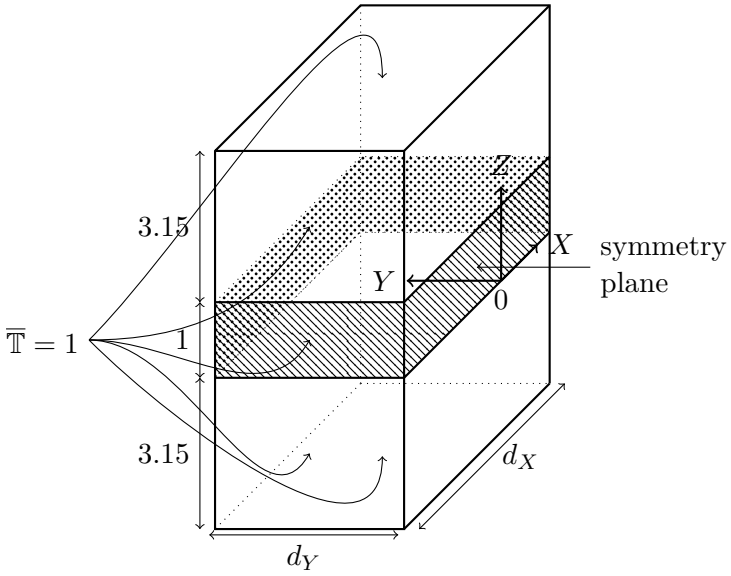

Figure 2.10: Domains computation to solve the energy equations

As posited by Habchi [62], the free boundary problem resulting from the phenomenon of cavitation can be resolved by incorporating a penalty coefficient into the Reynolds or Generalized Reynolds equation. The role of the penalty coefficient in the Reynolds or Generalized Reynolds equation is limited to instances where negative pressures are present. In this instance, the penalty term introduces a significant positive pressure value to counterbalance the negative values resulting from the diverging geometry of the film thickness. Consequently, within the cavitated zone with the penalty term, the sole root that satisfies the penalised Reynolds or Generalized Reynolds equation is a zero pressure. Furthermore, as postulated by Habchi [62], the utilisation of the penalty term within the cavitation area ensures the conservation of the mass flow rate.

The Reynolds or Generalized Reynolds equation is a diffusive-convective equation that becomes convective in the high-pressure zone due to the significant increase in the viscosity term. This implies that the Poiseuille term $\bar{\xi}_{\mathrm{P}}$ (or $\bar{\xi}'_{\mathrm{P}}$ for the Generalized case) vanishes. This situation gives rise to instabilities when using FE discretisation. To address this challenge, Habchi [61] pro-

posed the introduction of residual-based stabilisation terms, namely Streamline Upwind Petrov–Galerkin (SUPG) and Galerkin Least Squares (GLS). These terms do not alter the equation, as they are multiplied by the residual. For further details, the reader is invited to consult Habchi [61]. Nevertheless, the use of residual-based methods is not sufficient, and Habchi [61] introduced an artificial diffusion term, $\bar{\xi}_{id}$, which fully resolved the stability issue. Artificial diffusion plays a crucial role in the following chapter, and is discussed in further detail subsequently. In order to explain this new term, it is necessary to rewrite the dimensionless Reynolds equation (2.44) in the diffusive-convective-source form $\mathcal{R}(P) = 0$ such as:

$$\underbrace{\underbrace{-\frac{\partial}{\partial X}\left(\bar{\xi}\frac{\partial P}{\partial X}\right) - \frac{\partial}{\partial Y}\left(\bar{\xi}\frac{\partial P}{\partial Y}\right)}_{\text{“Diffusion”: } -\nabla\left(\bar{\xi}\nabla P\right)} + \underbrace{H\frac{\partial \bar{\rho}}{\partial P}\frac{\partial P}{\partial X}}_{\text{“Convection”: } \beta\nabla P} + \underbrace{\bar{\rho}\frac{\partial H}{\partial X} + \frac{\partial \bar{\rho} H}{\partial T}}_{\text{“Source”: } -Q} = 0,}_{\mathcal{R}(P)=0}$$

introducing $\bar{\xi} = \bar{\xi}_{\mathrm{P}} + \bar{\xi}_{id}$ with

$$\bar{\xi}_{id} = \delta_{id}\frac{\hbar\,||\beta||}{2\mathcal{O}_{\mathcal{R}}}, \tag{2.51}$$

where $\hbar$ represents the element size, $\mathcal{O}_{\mathcal{R}}$ denotes the order of discretisation of the dimensionless Reynolds equation (2.44), and δ_{id} is a coefficient employed to monitor artificial diffusion. The aforementioned procedure must be replicated for the case of the Generalized Reynolds equation, where the introduction of $\bar{\xi}' = \bar{\xi}'_{\mathrm{P}} + \bar{\xi}_{id}$ necessitates

$$\beta = H\frac{\partial \bar{\rho}^{\star}_{x}}{\partial P}.$$

The solution to the isothermal Newtonian EHL contact employs a fully coupled Newton-Raphson algorithm; in contrast, the TEHL application utilises a segregated solver. In the segregated solver, steps can be created, whereby first, the Generalized Reynolds equation, Navier-Cauchy equation and load balance equation are solved; second, the integral terms are computed; and finally, the energy equation is solved. These steps are repeated until the residual reaches the selected threshold criteria.

The application of the Newton-Raphson algorithm necessitates the identification of initial values for the unknowns that are already in proximity to the final solution, thereby enhancing the probability of convergence. Given the close proximity of the EHL problem to the dry one, the dry contact

solution is employed as the initial point of reference. This entails initiating the dimensionless pressure field with the dimensionless Hertzian pressure field (equation (2.43) which is subsequently divided by p_H). Consequently, the initial displacements W are derived from the aforementioned pressure loading. The initial mutual approach is sourced from Damiens [37] such as:

$$H_{00} = 1.67M^{-1/9} - 1.897 + \frac{0.2}{50}L, \tag{2.52}$$

with M and L the Moes [101] dimensionless parameters defined such as:

$$M = \frac{F}{E'R^2}\left(\frac{2\eta_0 u_m}{E'R}\right)^{-3/4} \qquad \text{and} \qquad L = \alpha E'\left(\frac{2\eta_0 u_m}{E'R}\right)^{1/4}. \tag{2.53}$$

At this juncture, the stationary EHL problem is prepared for resolution.

It should be noted that the aforementioned information remains valid in the event that the study is made time-dependent. Transient computations are performed using the backward differentiation formula. The time step size is selected adaptively based on local error estimates in relation to the tolerances; typically, this value falls within the range of 1×10^{-4} to 1×10^{-3}. Furthermore, the transient solver selects either a first- or a second-order time step.

2.8 Conclusion

This chapter presents the fundamental equations that govern an EHL problem. The pressure field can be obtained by means of the Reynolds equation (2.9) or, alternatively, the Generalized Reynolds equation (2.35), with thermal dependency taken into account. The isothermal Newtonian Reynolds equation (2.9) has been derived in a rigorous manner. In section §2.1.3, the fluid properties, including density and viscosity, have been presented as a function of pressure and temperature. Subsequently, the geometry of the contact has been presented, thereby enabling the mathematical formulation of the film thickness equation (2.18). The Navier-Cauchy equation (2.26) has been rigorously derived, returning an elastic deformations field resulting from high pressure loading. The role of the inertia term within this equation has been subjected to scrutiny, and it has been demonstrated that in the context of lubrication, the influence of inertia terms within the Navier-Cauchy equation can be effectively disregarded. To conclude the EHL problem, the load balance equation (2.30) has been presented. Once more, the role of the inertia term has been examined, and the outcome aligns with that of the Navier-Cauchy equation: it can be disregarded. Finally, the energy equation (2.37)

has been introduced, which enables the calculation of temperature within the TEHL contact. The transient term has been briefly addressed, leading to the conclusion that it can be omitted in the initial phase.

The equations have been written in dimensionless form in order to minimise the number of parameters and to prevent numerical issues arising from a poorly conditioned matrix system. Subsequently, section §2.7 presented the treatment of the free boundary problem and the stabilisation of the Reynolds equation. Thereafter, the solving method was discussed.

Chapter

3

New approaches introducing starvation

.

In the latest chapter, the classical equations that are relevant to fully flooded lubricated contact are presented. This chapter presents the methodology for introducing starvation. As previously stated, starvation has been widely introduced using the Jakobsson-Floberg-Olsson (JFO) theory, whereas Porras Vazquez [111] employed a biphasic approach.

Two distinct strategies have been developed and are elucidated herein. Both are founded upon the JFO theory. The initial strategy is based on a Penalty Method (PM), while the subsequent one is based on a Moving Mesh (MM). Both models are confronted with the results of existing literature. The models and results presented in this chapter are derived from Decote et al. [38].

3.1 Penalty Method (PM)

3.1.1 The modified Reynolds equation

As Chevalier [29] noted, Bayada et al. [11] presented the so-called modified Reynolds equation, which includes the JFO theory, in 1990. The modified Reynolds equation is as follows:

$$\frac{\partial}{\partial x}\left(\frac{\rho h^3}{12\eta}\frac{\partial p}{\partial x}\right)+\frac{\partial}{\partial y}\left(\frac{\rho h^3}{12\eta}\frac{\partial p}{\partial y}\right)-\frac{\partial u_m \rho\theta h}{\partial x}-\frac{\partial \rho\theta h}{\partial t}=0. \tag{3.1}$$

The equation presents two variables, namely the pressure, p, and the oil ratio, θ, which is defined as follows:

$$\theta=\frac{h_{oil}}{h}. \tag{3.2}$$

The term "oil thickness" (h_{oil}) represents the total oil thickness. The introduction of the second variable, θ, necessitates the introduction of a second equation. This equation is a complementarity equation, which yields an equation of the form:

$$p\ \cdot\ (1-\theta)=0. \tag{3.3}$$

This equation can be translated as follows: if $\theta=1$, then $h_{oil}=h$, and thus $p\neq 0$. On the other hand, when $\theta<1$ then $p=0$. Consequently, if $\theta=1$, the modified Reynolds equation (3.1) reduces to the classical Reynolds equation (2.9). Conversely, when $\theta<1$, the pressure p is equal to zero, resulting in the modified Reynolds equation (3.1) becoming a transport equation of the form:

$$\frac{\partial u_m\theta h}{\partial x}+\frac{\partial \theta h}{\partial t}=0. \tag{3.4}$$

In accordance with the JFO theory, which posits a zero pressure when $\theta<1$, the density is rendered null within the context of equation (3.4). With the dimensionless parameters defined in section §2.6 and $H_{oil}=h_{oil}R/a^2$, the dimensionless starved lubricated problem may be expressed as follows:

$$\frac{\partial}{\partial X}\left(\bar{\xi}_{\mathrm{P}}\frac{\partial P}{\partial X}\right)+\frac{\partial}{\partial Y}\left(\bar{\xi}_{\mathrm{P}}\frac{\partial P}{\partial Y}\right)-\frac{\partial \bar{\rho}\theta H}{\partial X}-\frac{\partial \bar{\rho}\theta H}{\partial T}=0, \tag{3.5a}$$

$$P\ \cdot\ (1-\theta)=0. \tag{3.5b}$$

As elucidated by Wijnant [136], the couple of equations {(3.5a) & (3.5b)} manifests a discontinuity in the variable θ, characterised by a jump. This discontinuity occurs at the point of film formation, namely the inlet meniscus.

Accordingly, a bijection between P and θ is proposed as a means of solving the coupled problem numerically. Some authors who solved this set of equations while developing an in-house solver managed to overcome this discontinuity without recourse to a bijection (see, for example, Wijnant [136]). The parameter $P^\star$, which represents the pressure threshold between the cavited or starved zone and the pressurised zone, is introduced and presented in figure 3.1. Figure 3.1(a) illustrates the sharp formulation of the JFO theory, which does not include a bijection between P and θ. Figure 3.1(b) displays the penalised formulation of the JFO theory, which incorporates the concept of $P^\star$. From figure 3.1(b), it can be seen that when the pressure is greater than $P^\star$, then $\theta \approx 1$; otherwise, $\theta < 1$. In order to permit this behaviour, the following relationship between$P$ and θ is proposed:

$$\theta = 1 - e^{-\frac{P}{P^\star/5}}. \tag{3.6}$$

A reduction of $P^\star$ thus brings the penalised method closer to the original JFO theory, as illustrated in figure 3.1(a).

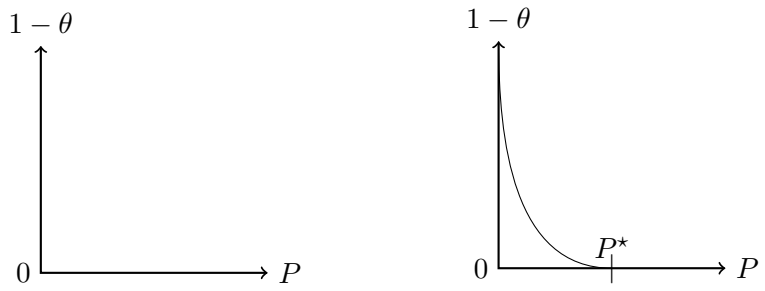

(a) JFO sharp formulation (b) Penalised JFO

Figure 3.1: Graphical representation of the JFO theory

The function represented by equation (3.6) can be described as an exponential decay, exhibiting a dual-regime behaviour. The first regime, referred to as the transient regime below $P^\star$, is characterised by a significant variation in the variable θ. In contrast, the second regime, the permanent regime, exhibits an infinitely small variation in θ for any change in the value of P. The value of $P^\star$ can be defined as five times the value where the tangent line evaluated at the origin crosses the axis $y = 0$. Figure 3.2 illustrates an example of an exponential decay of P with a tuning parameter κ. Figure 3.2 indicates that as P approaches 5κ, the limit of $e^{-P/\psi}$ approaches zero. This implies that as P increases, θ tends towards one, and consequently, the gap

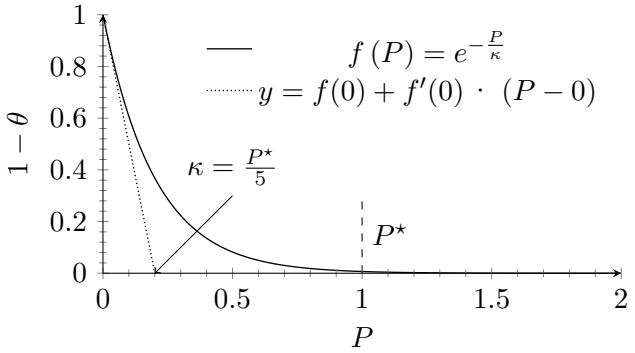

Figure 3.2: Exponential decay

is filled with lubricant when P is greater than or equal to 5κ. Therefore, the tuning parameter κ can be replaced by $P^\star/5$, which is more accessible to the user as $P^\star$ represents the threshold between complete film formation and starvation/cavitation. This choice of penalisation method permits the equation (3.5a) to be considered solely, thus replacing θ with the function defined in equation (3.6), which is a function of P.

In their work, Yin et al. [142] presented a thermal starved point contact simulation, which considered the modified Generalized Reynolds equation. They proposed that the dimensionless modified Generalized Reynolds equation could be expressed as follows:

$$\frac{\partial}{\partial X}\left(\bar{\xi}'_{\mathrm{P}}\frac{\partial P}{\partial X}\right) + \frac{\partial}{\partial Y}\left(\bar{\xi}'_{\mathrm{P}}\frac{\partial P}{\partial Y}\right) - \frac{\partial \bar{\rho}^\star_x \theta H}{\partial X} - \frac{\partial \bar{\rho}_e \theta H}{\partial T} = 0. \tag{3.7}$$

3.1.2 Numerical procedure

The introduction of the dimensionless modified Reynolds equation (3.5a) results in modifications of the classical numerical procedure presented in section §2.7. However, it should be noted that only those physical phenomena which are included in the domain Ω_L are affected. All other physics discussed in section §2.7 remain unchanged. Consequently, only the modifications induced by the use of the modified Reynolds equation are discussed in order to avoid unnecessary repetition.

The modified Reynolds equation (3.5a) introduces a modification to the boundary conditions that are applied at the frontier of Ω_L. The classical approach, as outlined in chapter 2, employed a zero pressure value at the frontier. An analysis of equation (3.6) reveals that a zero dimensionless pressure results in the imposition of $\theta = 0$ at the frontier, indicating the

absence of oil due to the fact that $\theta = H_{oil}/H$. In order to mimic the classical approach, it is necessary to set the pressure imposed at the frontier to $P^\star$. When this boundary condition is applied, it results in a fully flooded application, as indicated by the value of θ, which is equal to 1, as calculated using equation (3.6). In order to impose a total oil layer thickness at the inlet of the domain Ω_L, which is referred to as H_{oil}^{inlet}, it is necessary to impose the corresponding inlet pressure, P_{inlet}, below $P^\star$, as calculated using equation (3.6). Thus, P_{inlet} is expressed as follow:

$$P_{inlet} = -\frac{P^\star}{5} \log\left(1 - \frac{H_{oil}^{inlet}}{H}\right), \tag{3.8}$$

with $\theta_{inlet} = H_{oil}^{inlet}/H$. Consequently, the value of P_{inlet} is defined on the entire boundary of the domain, with the exception of the symmetry boundary, as illustrated in figure 3.3.

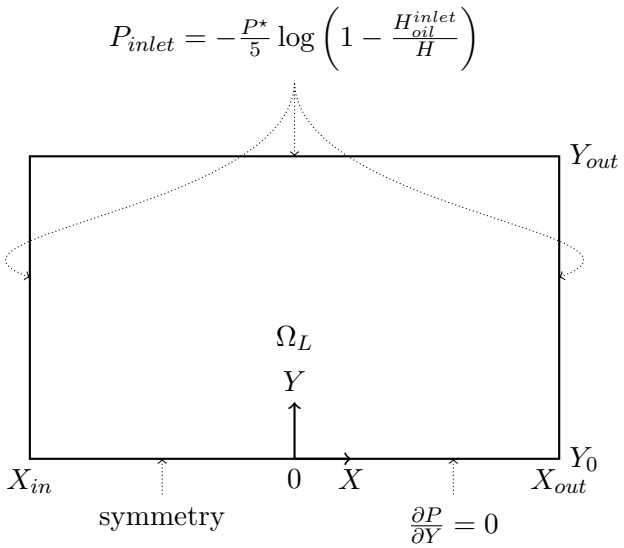

Figure 3.3: Domain Ω_L for the PM

Furthermore, the utilisation of the dimensionless modified Reynolds equation (3.5a) results in a modification to the stabilisation method outlined in section §2.7. Indeed, due to the introduction of the variable θ, the term β in the diffusive-convective-source form becomes

$$\beta = \theta H \frac{\partial \bar{\rho}}{\partial P} + \bar{\rho} H \frac{\partial \theta}{\partial P}. \tag{3.9}$$

The proposed modification has an impact on the value $\bar{\xi}_{id}$ as defined in equation (2.51).

The resolution of the starved EHL problem using the PM is found to be almost identical to the one developed in section §2.7. The differences can be attributed to two primary factors. Firstly, the pressure is initialised in a manner that differs from the standard approach. In the PM framework, the pressure is initialised using the Hertzian dimensionless dry contact pressure field, where the value of $P^\star$ is appended. This ensures that the computation commences in a fully flooded state. Secondly, the PM incorporates both starvation and cavitation, thereby rendering the penalty term referenced in section §2.7 (page 54) superfluous in this context.

3.2 Moving Mesh (MM)

3.2.1 Isothermal Newtonian approach

The phenomenon of starvation represents a free boundary problem between a transport zone Ω_T and a pressurised zone Ω_P, which are separated by a frontier Σ into the lubricant domain $\Omega_L = \Omega_T \cup \Omega_P$ (see figure 3.4). In this context, the normal of Σ points towards Ω_T, and is represented by the vector n.

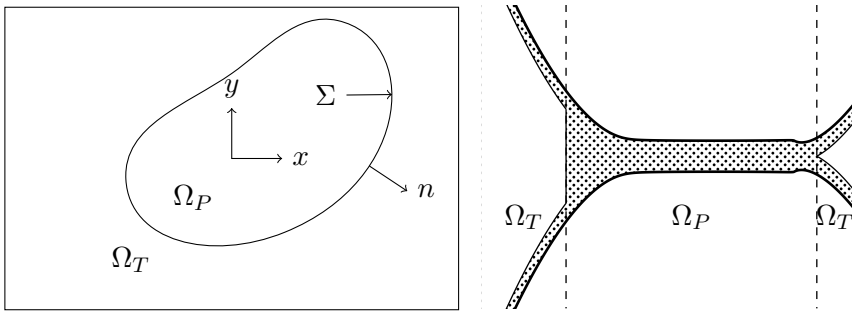

(a) Lubricant domain $\Omega_L = \Omega_T \cup \Omega_P$ (b) Side view

Figure 3.4: Lubricant domain Ω_L and subdomains Ω_T and Ω_P

In the pressurised domain Ω_P, the pressure p satisfies the Reynolds equation, as previously presented in section §2.1 and recalled here

$$\frac{\partial}{\partial x}\left(\frac{\rho h^3}{12\eta}\frac{\partial p}{\partial x}\right) + \frac{\partial}{\partial y}\left(\frac{\rho h^3}{12\eta}\frac{\partial p}{\partial y}\right) - \frac{\partial u_m \rho h}{\partial x} - \frac{\partial \rho h}{\partial t} = 0 \qquad \in \Omega_P. \tag{2.9}$$

In regions external to the aforementioned domain, the fluid flows at ambient pressure within the domain Ω_T. In this region, it is postulated that some

oil layers (of total thickness h_{oil}) adhere to the two solid walls/surfaces, and the gap h between the two surfaces is partially filled with air (or ambient gas). Consequently, the Poiseuille flux is absent, and only the Couette and transient terms are present in the velocity fields. This configuration represents the transport (convection) of h_{oil}, which is governed by the following equation:

$$\frac{\partial u_m h_{oil}}{\partial x} + \frac{\partial h_{oil}}{\partial t} = 0 \qquad \in \Omega_T. \tag{3.10}$$

The position of the frontier Σ between Ω_P and Ω_T is currently unknown. To determine its position, it is necessary to establish an equilibrium of the mass flow rate at the frontier, as demonstrated in figure 3.5.

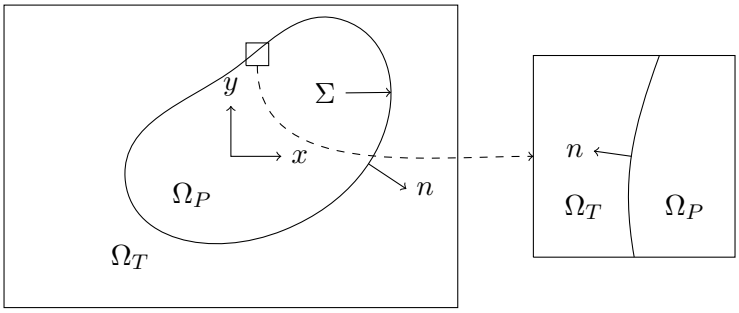

Figure 3.5: Zoom over Ω_L

This equilibrium can only be achieved by ensuring that the difference in flow rate entering and leaving the frontier is equal to the induced mass flow rate resulting from the motion of the frontier itself, which can be expressed in the following equation:

$$\left(\rho q^{\Omega_P} - \rho_0 q^{\Omega_T}\right) \cdot n = (\rho h - \rho_0 h_{oil}) \cdot \dot{\Sigma}_n. \tag{3.11}$$

In this context, the symbol $\dot{\Sigma}_n$ represents the normal velocity of the frontier Σ. The notation q^{Ω_P} represents the flow rate within the domain Ω_P, while the notation q^{Ω_T} denotes the flow rate within Ω_T. The aforementioned flow rates have been derived in equations (2.7) and (2.8). Given that the Poiseuille flux is absent within the domain Ω_T, equation (3.11) leads to

$$-\frac{\rho h^3}{12\eta}\frac{\partial p}{\partial n} + \rho u_m h \cdot n_x - \rho_0 u_m h_{oil} \cdot n_x - \rho h \cdot \dot{\Sigma}_n + \rho_0 h_{oil} \cdot \dot{\Sigma}_n = 0,$$

with n_x the projection of n the normal vector of Σ over the x-axis. In accordance with the boundary conditions pertaining to the Reynolds equation (2.9), as discussed section§2.1.2 (i.e. a zero pressure on the frontier of

$\Omega_P \equiv \Sigma$), this equation becomes

$$-\frac{h^3}{12\eta_0}\frac{\partial p}{\partial n} + (h - h_{oil}) \cdot \left(u_m n_x - \dot{\Sigma}_n\right) = 0. \tag{3.12}$$

It thus follows that equation (3.12) governs the position of the frontier. This equation is satisfied only if the frontier is positioned in a way that ensures mass flow rate conservation. In the literature, Wijnant [136] obtained a somewhat similar equation using the Green theorem in the (x, y, z, t) domain, which resulted in the appearance of the n_t vector. Additionally, El Alaoui Talibi et al. [51] presented the same equation as equation (3.12), although they did not provide a detailed derivation.

3.2.2 Starved Generalized Reynolds equation

Chapter 1, together with the concluding section on PM (section §3.1), has demonstrated the modified Generalized Reynolds equation (3.7). However, to the best of the author's knowledge, the starved thermal non-Newtonian application has not benefited from the theoretical analysis presented in section §3.2.1. Therefore, precisely the same procedure is followed. In the pressurized domain Ω_P, the pressure p satisfies the Generalized Reynolds equation recalled herein

$$\frac{\partial}{\partial x}\left\{\left(\frac{\rho}{\eta}\right)_e \frac{\partial p}{\partial x}\right\} + \frac{\partial}{\partial y}\left\{\left(\frac{\rho}{\eta}\right)_e \frac{\partial p}{\partial y}\right\} - \frac{\partial \rho_x^\star}{\partial x} - \frac{\partial \rho_e}{\partial t} = 0 \qquad \in \Omega_P. \tag{2.35}$$

In this context, it is preferable to refrain from postulating that layers of oil are adhering to solid walls or surfaces, as this can potentially introduce errors into the analysis. Indeed, in the domain Ω_T, the computation of the general viscosity and density through the integrals lying between 0 and h does not allow for the term h_{oil} to be employed. It is proposed that the gap is filled by an oil-air mixture. Consequently, starvation and cavitation must be conceptualised as a fog of oil and air, rather than as layers of oil (see Martin [98]). Accordingly, the filling rate of oil, denoted by the variable θ, is introduced in accordance with the equation (3.2). Consequently, within the domain Ω_T, a generalized mixture of oil and air is transported by the following equation:

$$\frac{\partial \rho_x^\star \theta}{\partial x} + \frac{\partial \rho_e \theta}{\partial t} = 0 \qquad \in \Omega_T. \tag{3.13}$$

Subsequently, the frontier equation can be formulated in a manner analogous to the isothermal case, commencing with equation (3.11), which ultimately

yields

$$-\left(\frac{\rho}{\eta}\right)_e \frac{\partial p}{\partial n} + \rho_x^\star (1-\theta) \cdot \left(n_x - \dot{\Sigma}_n\right) = 0. \tag{3.14}$$

Equation (3.14) bears resemblance to equation (3.12), as anticipated. However, the Poiseuille flux differs, and the presence of $\rho_x^\star$ in front of the Couette flux is notable.

3.2.3 Boundary conditions

The boundary conditions to be applied to the Reynolds equation (2.9) have been previously discussed. Consequently, a zero pressure is imposed on the boundary of $\Omega_P \equiv \partial\Omega_P \equiv \Sigma$, as detailed in section §2.1.2. In the specific context of this study, equation (3.10) is aimed at modelling the transport of the oil in the x-direction. Consequently, the total thickness of oil present at the inlet of the domain Ω_T, designated as h_{oil}^{inlet}, must be specified. This Dirichlet boundary condition is a function of both space and time, and is represented by the notation $h_{oil}^{inlet}(y,t)$. Furthermore, as equation (3.10) is a first-order partial differential equation, only one Dirichlet boundary condition is required. This is represented by h_{oil}^{inlet}, and a zero h_{oil} gradient is imposed on the remaining boundaries of Ω_T.

The frontier equation (3.12) returns the spatial coordinate of the frontier position, designated herein as xy_Σ. In the context of starved lubrication, the frontier Σ is faced with two distinct scenarios. The inlet meniscus Σ^{inlet} represents the film formation frontier, whereas the outlet meniscus Σ^{outlet} delineates the cavitation frontier or the film rupture zone. Accordingly, a simplified version of equation (3.12) can be derived for both "sub-frontiers", which is discussed in the following paragraphs. Such simplifications are obtained depending on the roots of equation (3.12). However, as it is non-linear, it possesses multiple roots. Some of these roots lack physical meaning and can be excluded, which is presented herein.

Equation (3.12) has been the subject of significant research in its stationary form (i.e. $\dot{\Sigma}_n = 0$), as evidenced by the work of Wijnant [136] and Chevalier [29]. Building upon this, the discussion now turns to a consideration of the transient form.

Stationary analysis

In this case, equation (3.12) reduces to

$$-\frac{h^3}{12\eta}\frac{\partial p}{\partial n} + (h - h_{oil})\, u_m \cdot n_x = 0. \tag{3.15}$$

Outlet zone Σ^{outlet} Given that the thickness of the gap (h) cannot be exceeded, it follows that the difference between h and the thickness of the oil h_{oil} is always positive. Given that the normal vector n is directed towards Ω_T, it follows that n_x is either positive or null at the outlet. Therefore, the product $(h - h_{oil})\, u_m \cdot n_x$ is positive. As the outlet is approached, the pressure decreases. Consequently, the pressure gradient is negative, and since the normal n is directed towards Ω_T, the normal pressure gradient is also negative. This analysis leads to the conclusion that positive Poiseuille and Couette fluxes must be added. Therefore, in order to satisfy the mass flow rate conservation, it is necessary for the normal pressure gradient to be zero, and thus $h_{oil} = h$. As a result, equation (3.15) is reduced to

$$\frac{\partial p}{\partial n} = 0 \qquad \in \Sigma^{outlet}. \tag{3.16}$$

Inlet zone Σ^{inlet} As evidenced in the literature (see, for example, Wijnant [136] or Chevalier [29]), a non-zero pressure gradient is observed at the inlet Σ^{inlet}, which implies a discontinuity in h_{oil}. Therefore, it can be stated that a positive pressure gradient exists at the inlet meniscus of a stationary starved lubricated contact. Furthermore, the existence of a zero pressure gradient would indicate that $h_{oil} = h$, suggesting that there is no accumulation of oil upstream of the contact. This conclusion is not supported by experimental observations, which have demonstrated the presence of an accumulation of oil upstream of the contact (see, for example, Wedeven [135] or Kostal et al. [84]). Consequently, the frontier equation in the inlet zone remains equation (3.15).

Transient analysis

In this case, equation (3.12) is recalled herewith

$$-\frac{h^3}{12\eta_0}\frac{\partial p}{\partial n} + (h - h_{oil}) \cdot \left(u_m n_x - \dot{\Sigma}_n\right) = 0. \tag{3.12}$$

Outlet zone Σ^{outlet} Equation (3.12) demonstrates the presence of at least two discernible roots. The first solution was obtained under stationary conditions, with $h_{oil} = h$ and a zero normal pressure gradient at the outlet. Furthermore, in transient applications, equation (3.12) allows for the possibility of balancing a non-zero pressure gradient, provided that $\dot{\Sigma}_n > u_m n_x$. In this scenario, a discontinuity in h_{oil} would be observed at the outlet, accompanied by the introduction of a non-zero pressure gradient. To the best

of the author's knowledge, the presence of a non-zero pressure gradient has never been observed in the literature. Furthermore, this is consistent with the assertion made by Dowson et al. [47] that the steady-state condition is also suitable for dynamic situations. Consequently, equation (3.12) in transient condition reduces to equation (3.16).

Inlet zone Σ^{inlet} As a function of the sign produced by $\left(u_m n_x - \dot{\Sigma}_n\right)$, equation (3.12) generates either a positive or a negative pressure gradient, which serves to balance the product $(h - h_{oil}) \cdot \left(u_m n_x - \dot{\Sigma}_n\right)$. However, since the pressure at the inlet meniscus is set to zero, a negative pressure gradient implies negative pressure build-up (i.e. negative pressure values). This is not permitted by the JFO theory, which only admits pressure values positive or equal to zero. Furthermore, it is not a physically realistic scenario, as it would imply pressure below the saturation pressure. Consequently, the frontier equation at the inlet zone in transient condition remains equation (3.12).

3.2.4 Normalisation

By employing the dimensionless parameters established in section §2.6, in which H_{oil} is defined as $h_{oil}R/a^2$, the dimensionless Reynolds equation remains unaltered and is recalled herewith:

$$\frac{\partial}{\partial X}\left(\bar{\xi}_{\mathrm{P}}\frac{\partial P}{\partial X}\right) + \frac{\partial}{\partial Y}\left(\bar{\xi}_{\mathrm{P}}\frac{\partial P}{\partial Y}\right) - \frac{\partial \bar{\rho} H}{\partial X} - \frac{\partial \bar{\rho} H}{\partial T} = 0. \tag{2.44}$$

Then dimensionless transport equation reads as

$$\frac{\partial H_{oil}}{\partial X} + \frac{\partial H_{oil}}{\partial T} = 0. \tag{3.17}$$

Exactly the same procedure is followed regarding the dimensionless Generalized Reynolds equation which is called back

$$\frac{\partial}{\partial X}\left(\bar{\xi}'_{\mathrm{P}}\frac{\partial P}{\partial X}\right) + \frac{\partial}{\partial Y}\left(\bar{\xi}'_{\mathrm{P}}\frac{\partial P}{\partial Y}\right) - \frac{\partial \bar{\rho}^{\star}_{x} H}{\partial X} - \frac{\partial \bar{\rho}_{e} H}{\partial T} = 0. \tag{2.47}$$

As a consequence of the aforementioned normalisation, the term H was introduced into equation (2.47). Consequently, H also appears within the dimensionless generalized transport equation, thus enabling the replacement of θH by H_{oil}, as follows:

$$\frac{\partial \bar{\rho}^{\star}_{x} H_{oil}}{\partial X} + \frac{\partial \bar{\rho}_{e} H_{oil}}{\partial T} = 0. \tag{3.18}$$

3.2.5 Numerical method

Treatment of the sub domains

Similarly to the numerical method related to PM discussed in section §3.1.2, only the modifications of the classical numerical method established in section §2.7 are discussed in this subsection. Consequently, the modifications only occur within the lubricant domain Ω_L which is divided into two subdomains Ω_T and Ω_P.

The stabilised Reynolds equation (2.44) is discretised exactly within Ω_P as was previously presented in section §2.7. The MM offers the advantage of not modifying the dimensionless Reynolds equation presented in chapter 2.

Within Ω_T, the dimensionless transport equation (3.17) is discretised by the use of quadratic Lagrangian elements. However, equation (3.17) is of purely convective nature, thereby engendering a stability issue. Consequently, the stabilisation of equation (3.17) is presented next. The utilisation of artificial diffusion is precluded, thus ensuring the conservation of the mass flow rate. Subsequently, residual-based stabilisation is employed. The GLS method is inapplicable in a purely convective case, as it necessitates the diffusive term of equation (3.17). In this instance, the GLS method reduces to the SUPG method, which yields the following weak form:

$$\text{SUPG} = \int_{\Omega_T} \tau_{\mathcal{T}} \mathcal{R}\left(H_{oil}\right) \beta \cdot \frac{\partial \widetilde{H}_{oil}}{\partial x} \, \mathrm{d}\Omega_T, \tag{3.19}$$

with $\beta = 1$ the convective term of equation (3.17). $\mathcal{R}\left(H_{oil}\right)$ represents the residual of equation (3.17), while $\widetilde{H}_{oil}$ the weighting function of H_{oil}. The term $\tau_{\mathcal{T}}$ is used to denote a tuning parameter such as

$$\tau_{\mathcal{T}} = \frac{\hbar}{2\left|\left|\beta\right|\right| \mathcal{O}_{\mathcal{T}}}, \tag{3.20}$$

with $\mathcal{O}_{\mathcal{T}}$ the order of discretisation of the dimensionless transport equation (3.17). The initial definition of $\tau_{\mathcal{T}}$ is multiplied by $\left\{\coth\left(Pe\right) - \frac{1}{Pe}\right\}$ with Pe representing the Péclet number. The mathematical expression of the Péclet number demonstrates a division by the diffusive term. In a purely convective equation, the Péclet number tends to infinity, and the relationship between the two terms can be expressed as $\left\{\coth\left(Pe\right) - \frac{1}{Pe}\right\} = 1$.

Treatment of the frontiers

The numerical procedure to solve the stabilised dimensionless Reynolds equation (2.44) inside Ω_P and the stabilised dimensionless transport equa-

tion (3.17) inside Ω_T has been discussed in detail. The numerical procedure to solve the frontier equation is therefore presented herewith. To begin, the artificial diffusion incorporated into the stabilised dimensionless Reynolds equation (2.44) must be considered in the frontier equation. Consequently, the new dimensionless frontier equation incorporating the artificial diffusion is obtained using equation (3.11) and is given by

$$-\bar{\xi}\frac{\partial P}{\partial n} + (H - H_{oil}) \cdot \left(n_X - \dot{\Sigma}_n\right) = 0, \tag{3.21}$$

remembering that $\bar{\xi} = \bar{\xi}_{\mathrm{P}} + \bar{\xi}_{id}$.

As indicated in section §3.2.3, the frontier Σ is subdivided into two sub-frontiers, namely Σ^{inlet} and Σ^{outlet}. In section §3.2.3, it was demonstrated that the equation (3.21) is solved on the sub-frontier Σ^{inlet}, while a normal zero pressure gradient is solved on the sub-frontier Σ^{outlet}. The unknowns within the aforementioned equations are the spatial coordinates at which the frontier should be positioned in order to ensure the conservation of mass flow rate, specifically XY_{inlet} and XY_{oultet}, respectively, for Σ^{inlet} and Σ^{outlet}. The solution of equation (3.21), in conjunction with the stabilised dimensionless Reynolds equation (2.44) within Ω_P and the stabilised dimensionless transport equation (3.17) within Ω_T, provides the position of the inlet meniscus and similarly for the position of Σ^{outlet} where a zero normal pressure gradient is solved. It should first be acknowledged that the sub-frontiers in question are not compatible at the junctions where they are required to meet. In other words, equation (3.21) also exhibits a discontinuity at the transition between the inlet and outlet meniscus. Subsequently, a very small "free" segment, designated as Σ^{free}, is introduced between the two, as illustrated in figure 3.6. This segment is designated as "free" due to the absence of a governing phys-

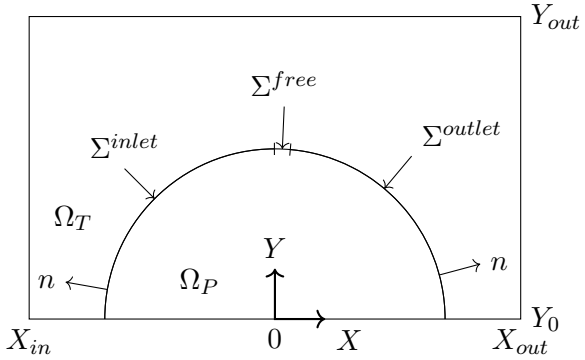

Figure 3.6: MM domains with all sub-frontiers

ical equation for its position, in contrast to the governing equations for Σ^{inlet} and Σ^{outlet}. It is solely driven by the motion of Σ^{inlet} and Σ^{outlet}, as it is linked to them. Consequently, the three sub-frontiers must undergo displacement in accordance with the prescribed values obtained through the solution of their respective equations. To enable the motion of the frontiers, a Moving Mesh (MM) strategy is employed.

Treatment of the motion of the mesh

The application of a MM technique necessitates the introduction of a set of equations that govern the motion of the mesh. To this end, the Winslow [138] smoothing method is proposed, and the set of equations is as follows:

$$\begin{cases} \dfrac{\partial^2 \mathcal{X}}{\partial X^2} + \dfrac{\partial^2 \mathcal{X}}{\partial Y^2} = 0, \\ \dfrac{\partial^2 \mathcal{Y}}{\partial X^2} + \dfrac{\partial^2 \mathcal{Y}}{\partial Y^2} = 0. \end{cases} \tag{3.22}$$

The set of equations enables the construction of a map that establishes a link between the two frames. The initial classical frame is the spatial frame (X and Y), which is fixed in space. This frame is the Eulerian one. The newly introduced frame, the Lagrangian ($\mathcal{X}$ and $\mathcal{Y}$), is linked to the mesh, which is permitted to deform. Subsequently, an Arbitrary Eulerian Lagragian (ALE) approach is introduced. The frontier equations and the Winslow smoothing equations are discretised using linear Lagrangian elements. The Dirichlet boundary conditions, designated as δ_X, δ_Y and δ_n represent the displacement of the mesh and must be imposed on the edges and sub-frontiers of the domain Ω_L. This enables the solution of the set of equations (3.22). Firstly, the mesh is fixed on the boundary of Ω_L, with the exception of the symmetry, where only displacements perpendicular to the symmetry line are prohibited ($\delta_Y\left(\forall X, 0\right) = 0$). Secondly, the motion of the sub-frontiers is obtained by imposing the spatial coordinates returned by the frontiers equations as means of Dirichlet boundary condition for the set of equations (3.22), as illustrated in figure 3.7.

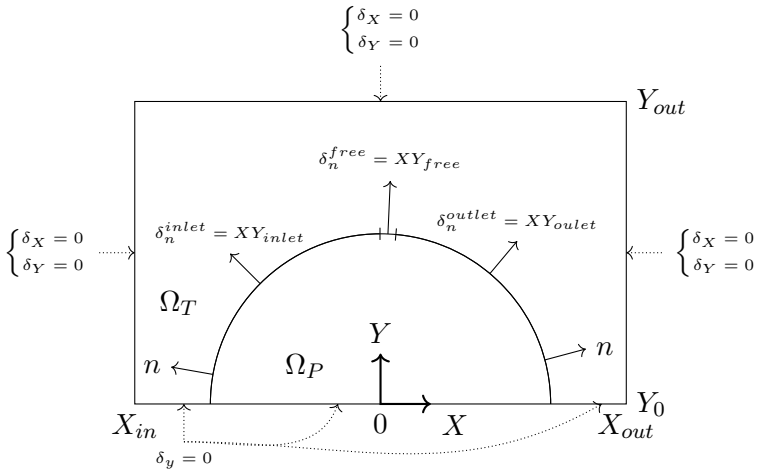

Figure 3.7: Boundary conditions for the Winslow [138] smoothing method

At last, a Laplacian is solved on Σ^{free}, such as

$$\frac{\partial^2 XY_{free}}{\partial X^2} + \frac{\partial^2 XY_{free}}{\partial Y^2} = 0, \tag{3.23}$$

which permits the equitable displacement of the limited number of elements present within Σ^{free} in order to prevent the formation of elongated elements. The displacement of Σ^{inlet} and Σ^{outlet} are prescribed as Dirichlet boundary conditions to equation (3.23) at the respective extremities.

Figure 3.8 provides an illustrative example of the motion of the mesh, wherein oblique bars are employed to delineate the extremities of Σ^{free}. Figure 3.8(a) displays the initial mesh prior to the execution of the computational process. Figure 3.8(b) demonstrates the mesh at the convergence of the computation with the presence of elongated elements in the free frontier, Σ^{free}. In the event of excessive deformation of the elements (with an element size that is twice the maximum permitted size), a re-meshing operation is necessary. Subsequently, a re-meshing operation is conducted based on the converged result, as illustrated in figure 3.8(b). This ensures that the subfrontiers are already at the optimal position. This is followed by the launch of a new computation, which is initiated using the latest result and therefore has a negligible computation time. Figure 3.8(c) presents the converged computation using the new mesh, which demonstrates the absence of elongated elements.

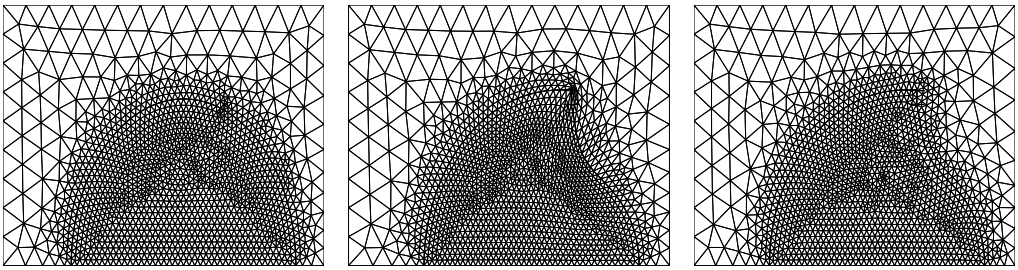

(a) Initial mesh (b) Intermediate mesh (c) Final mesh

Figure 3.8: Motion of the mesh

To sum up, a starved lubricated* problem where sub-frontiers Σ^{inlet} and Σ^{outlet} are linked each other can be solved using MM by computing the following set of equations

$$\begin{cases} \dfrac{\partial}{\partial X}\left(\bar{\xi}\dfrac{\partial P}{\partial X}\right) + \dfrac{\partial}{\partial Y}\left(\bar{\xi}\dfrac{\partial P}{\partial Y}\right) - \dfrac{\partial \bar{\rho} H}{\partial X} - \dfrac{\partial \bar{\rho} H}{\partial T} = 0 & \Omega_P, \\ \dfrac{\partial H_{oil}}{\partial X} + \dfrac{\partial H_{oil}}{\partial T} = 0 & \Omega_T, \\ \dfrac{\partial^2 \mathcal{X}}{\partial X^2} + \dfrac{\partial^2 \mathcal{X}}{\partial Y^2} = 0 & \Omega_L, \\ \dfrac{\partial^2 \mathcal{Y}}{\partial X^2} + \dfrac{\partial^2 \mathcal{Y}}{\partial Y^2} = 0 & \Omega_L, \\ -\bar{\xi}\dfrac{\partial P}{\partial n} + (H - H_{oil}) \cdot \left(n_X - \dot{\Sigma}_n\right) = 0 & \Sigma^{inlet}, \\ \dfrac{\partial P}{\partial n} = 0 & \Sigma^{outlet}, \\ \dfrac{\partial^2 XY_{free}}{\partial X^2} + \dfrac{\partial^2 XY_{free}}{\partial Y^2} = 0 & \Sigma^{free}. \end{cases} \tag{3.24}$$

Coupling

The section §2.7 outlines the utilisation of a fully coupled Newton-Raphson algorithm in the resolution of an isothermal Newtonian EHL problem. This identical methodology is employed in the solution of a starved isothermal Newtonian EHL contact using the MM. The Newton-Raphson method is as follows:

$$\mathbb{X}^{k+1} = \mathbb{X}^k + \Upsilon \delta \mathbb{X}^k,$$

*i.e. Hydrodynamic Lubrication (HL) as well as EHL contact problems

with $\mathbb{X}$ the vector containing all the unknowns $P, \mathcal{U}, \ldots$ and k representing the iteration index. The parameter Υ represents the under or over relaxation coefficient, whereas $\delta\mathbb{X}$ denotes the correction appended to the vector $\mathbb{X}$ at each iteration such as

$$\mathbb{J}\delta\mathbb{X} = -\mathbb{F}.$$

The residual, designated as $\mathbb{F}$, comprises all the discretised equations. The Newton-Raphson algorithm is deemed to have reached convergence when the residual norm, represented by $\mathbb{F}$, is less than or equal to the imposed threshold, denoted by Γ. Finally, $\mathbb{J}$ represents the Jacobian matrix, which "quantifies" the dependence of the equations on all the unknowns.

The principal advantage of the Newton-Raphson method is that it establishes a strong coupling between all variables. However, the Newton-Raphson method requires the inversion of the Jacobian matrix. Habchi [62] demonstrated that the Jacobian matrix resulting from his method is sparse. Despite the addition of other equations to the original model due to starvation introduction, the Jacobian matrix retains a significant number of zeros, maintaining its sparse nature as illustrated in figure 3.9. In this figure, the Jacobian matrix is used to solve approximately 400000 degrees of freedom, with non-zero terms representing only 0.02 % of the matrix.

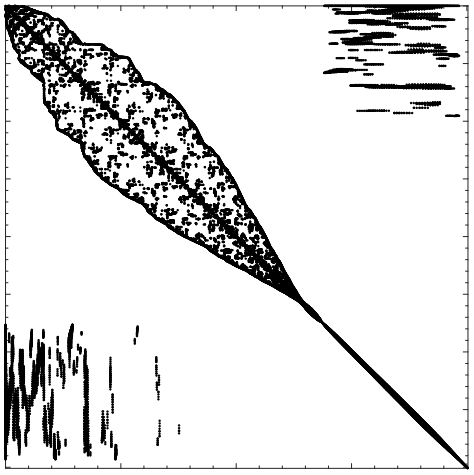

Figure 3.9: Spyplot of the Jacobian matrix $\mathbb{J}$

In the framework of the MM, the initialisation of the pressure and displacement fields, as presented in section §2.7, remains unchanged. The initial value of H_{oil} are calculated according to $H_{oil}^{inlet}(Y)$. The mutual approach H_{00} employs equation (2.52), which is here multiplied by a coefficient Ψ such

as:

$$H_{00} = \Psi \left(1.67 M^{-1/9} - 1.897 + \frac{0.2}{50} L \right).$$

This coefficient, Ψ, is used to monitor the degree of starvation, with a value of unity indicating that the application is moderately starved.

It is now necessary to determine the initial position of the frontier Σ and Σ^{free}. The positions of these sub-frontiers are contingent upon the degree of starvation. In the case of a moderately starved application, the initialisation of Σ is performed using a half circle of radius 1.25, centred at $X = -0.1$ and $Y = 0$. The positioning of the free frontier Σ^{free} is at 70° on the aforementioned half circle, as illustrated in figure 3.8(a). As starvation increases, the initialisation of Σ is performed using a half circle of radius 1.075, centred at $X = Y = 0$. The positioning of the free frontier Σ^{free} is at the midpoint of the half circle, at 90° degrees, as illustrated in figure 3.6. Lastly, the MM ensures both starvation and cavitation. In this configuration, the penalty term mentioned in section §2.7 (page 54) is superfluous. Consequently, it is removed from the formulation.

About the Generalized starved application

The aforementioned numerical method is applicable to isothermal cases, whereby the classical dimensionless Reynolds equation (2.44) must be resolved. The procedure to compute a starved TEHL contact remains largely unchanged. The stabilisation of the transport equation is achieved through the introduction of the term $\beta = \bar{\rho}_x^\star$. Furthermore, the frontier equation also undergoes modification and becomes

$$-\bar{\xi}' \frac{\partial P}{\partial n} + \bar{\rho}_x^\star \left(H - H_{oil} \right) \cdot \left(n_X - \dot{\Sigma}_n \right) = 0, \tag{3.25}$$

with $\bar{\xi}' = \bar{\xi}'_{\mathrm{P}} + \bar{\xi}_{id}$. The MM strategy remains identical with regard to the frontier partition. Ultimately, the set of equations (3.24) must take into

account the modification to the generalized case, resulting in the following:

$$\begin{cases} \dfrac{\partial}{\partial X}\left(\bar{\xi}'\dfrac{\partial P}{\partial X}\right)+\dfrac{\partial}{\partial Y}\left(\bar{\xi}'\dfrac{\partial P}{\partial Y}\right)-\dfrac{\partial \bar{\rho}_x^{\star}H}{\partial X}-\dfrac{\partial \bar{\rho}_e H}{\partial T}=0 & \Omega_P, \\ \dfrac{\partial \bar{\rho}_x^{\star}H_{oil}}{\partial X}+\dfrac{\partial \bar{\rho}_e H_{oil}}{\partial T}=0 & \Omega_T, \\ \dfrac{\partial^2 \mathcal{X}}{\partial X^2}+\dfrac{\partial^2 \mathcal{X}}{\partial Y^2}=0 & \Omega_L, \\ \dfrac{\partial^2 \mathcal{Y}}{\partial X^2}+\dfrac{\partial^2 \mathcal{Y}}{\partial Y^2}=0 & \Omega_L, \\ -\bar{\xi}'\dfrac{\partial P}{\partial n}+\bar{\rho}_x^{\star}\left(H-H_{oil}\right)\cdot\left(n_X-\dot{\Sigma}_n\right)=0 & \Sigma^{inlet}, \\ \dfrac{\partial P}{\partial n}=0 & \Sigma^{outlet}, \\ \dfrac{\partial^2 XY_{free}}{\partial X^2}+\dfrac{\partial^2 XY_{free}}{\partial Y^2}=0 & \Sigma^{free}. \end{cases} \tag{3.26}$$

Lastly, the coupling strategy differs somewhat from that described in section §2.7. As previously stated, a segregated solver is the preferred method for solving the Generalized problem. Consequently, the starved TEHL problem is also solved using a segregated solver. The procedure involves first solving the entire set of equations (3.26), including the Navier-Cauchy equation and load balance equation. This is followed by the computation of the integrals terms, and finally, the dimensionless energy equation is solved.

3.3 Isothermal model validation

3.3.1 Stationary case

Chapter 3 presents two distinct methodologies for facilitating starvation computation. It is therefore necessary to validate these methods using a literature reference with the aim of using one of them in subsequent works. Venner et al. [131] presented multiple point contact starved computations using different degrees of starvation. In these applications, the degree of starvation is controlled by the total oil thickness entering the contact, denoted H_{oil}^{inlet}, which is constant across Y and which depends on H_c^{ff}, the dimensionless central film thickness in fully flooded conditions. This leads to

$$H_{oil}^{inlet}=\psi H_c^{ff} \tag{3.27}$$

where ψ is a coefficient that aims for the severity of the starvation.

In their study, Venner et al. [131] employed a value of $M = 20$, $L = 10$ (see equation (2.53)), with $\eta_0 = \eta_R = 8.9 \times 10^{-3}\,\mathrm{Pa}\cdot\mathrm{s}$ and $\alpha = 1.7 \times 10^{-8}\,\mathrm{Pa}^{-1}$. Additionally, Venner [130] stated that

$$\bar{\lambda} = \left(\frac{128\pi^3}{3M^4}\right)^{1/3} \qquad \text{and} \qquad \bar{\alpha} = \frac{L}{\pi}\left(\frac{3M}{2}\right)^{1/3}, \tag{3.28}$$

with $\bar{\alpha} = \alpha p_H$. The aforementioned information allows for the determination of all the requisite parameters for the reproduction of the application. Furthermore, the applications employ the Dowson and Higginson [45] density-pressure law (2.10) and Roelands [118] viscosity-pressure law (2.14). In order to provide the most accurate replication of the simulations presented by Venner et al. [131], these laws are then utilised within both models.

Penalty Method (PM) validation

The performance of the Penalty Method (PM) is conditioned by the value of the penalty term, denoted as $P^\star$. Subsequently, computations were performed with varying values of $P^\star$. The results are presented in table 3.1. The first column shows the degree of starvation, the second column shows the value applied to $P^\star$, the third and fourth columns are related to the dimensionless central and minimum film thicknesses. Both columns possess

Table 3.1: Comparison of the PM with a reference coming from the literature (ϵ represents the relative gap between the result from [131] and the current method)

H_{oil}^{inlet}	$P^\star$	H_c			H_m		
		Ref.[131]	PM	ϵ [%]	Ref.[131]	PM	ϵ [%]
H_c^{ff}	0.01	0.3037	0.2875	5.3206	0.2217	0.2134	3.7353
	0.008		0.2907	4.2692		0.2151	2.9551
	0.005		0.2956	2.6647		0.2177	1.7866
	0.003		0.2989	1.5788		0.2195	1.0148
$0.5H_c^{ff}$	0.01	0.1756	0.1634	6.9531	0.1453	0.1360	6.3838
	0.008		0.1657	5.6503		0.1378	5.1546
	0.005		0.1693	3.6090		0.1406	3.2537
	0.003		0.1717	2.1939		0.1425	1.9484
$0.25H_c^{ff}$	0.01	0.0901	0.0821	8.9719	0.0837	0.0736	12.1125
	0.008		0.0827	8.2846		0.0739	11.8124

three sub-columns. The first sub-column indicates the value printed in reference [131], the second sub-column shows the obtained value using the PM model, and the last sub-column indicates the relative gap between the two, as follows:

$$\epsilon = \frac{\left| \underline{H}^{\text{Ref.}[131]} - \underline{H} \right|}{\underline{H}^{\text{Ref.}[131]}} \cdot 100.$$

As illustrated in table 3.1, a reduction in $P^\star$ results in an enhancement in the relative accuracy of the PM, manifested as a decline in ϵ. Nevertheless, at a certain point, it becomes unfeasible to utilise a smaller value of $P^\star$ due to the excessive penalisation, which then results in a discontinuity. However, as the degree of starvation increases, the relative gap also increases, indicating that the PM is negatively affected in terms of accuracy. In a final computation presented by Venner et al. [131], the H_{oil}^{inlet} value was set to $0.125 H_c^{ff}$. However, the PM was unable to produce a satisfactory result for this case. Indeed, the degree of starvation was so extreme that even with the least restrictive penalty value for $P^\star$, the Newton-Raphson algorithm never reached the threshold.

The decline in accuracy with increasing degrees of starvation can be elucidated. The PM does not provide absolute assurance regarding the conservation of mass flow rate. The incorporation of a penalty term suggests that the Poiseuille flux is not equal to zero within the region where $P < P^\star$, whereas the JFO theory dictates a zero Poiseuille flux. Therefore, the loss of mass flow rate results from the small residual pressure gradient in the cavited or starved zones. Consequently, the total oil thickness H_{oil} decreases through the transport area, as illustrated in figure 3.10.

Consequently, the meniscus formation is modified, situated in closer proximity to the Hertzian area. The aforementioned figure displays the reference curve, which represents the curve obtained through the MM method. As the degree of starvation increases, the meniscus position approaches the Hertzian area. In this case, the distance between the point of origin of the computational domain and the meniscus position increases, which results in a greater loss of mass flow rate. This is the reason why the accuracy of the PM method is affected when the degree of starvation increases. To reduce this loss, the distance between the inlet zone and the meniscus must be reduced by modifying the computational domain size (i.e. X_{in}).

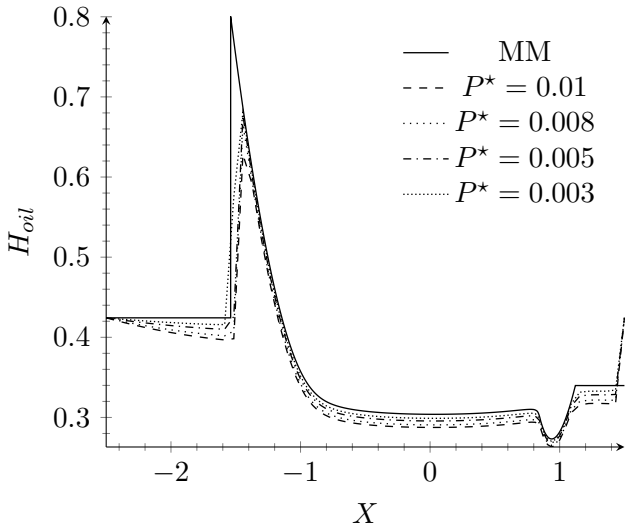

Figure 3.10: Analysis of the consequence of the oil losses along the rolling direction for the case $H_{oil}^{inlet} = H_c^{ff}$

Moving Mesh (MM) validation

The same procedure has been established in order to ascertain the accuracy of the MM method. In contrast to the previous scenario, there is no penalty coefficient to be monitored in this case. For that reason, a table with a similar structure to that of table 3.1 is presented in table 3.2. The relative gap for H_c and H_m is consistently below 1 %, indicating a close alignment between the MM and the reference [131], which employs an alternative approach involving a Multi-Level Multi-Integral (MLMI) method and finite difference (FD). The MM method has demonstrated its capacity to accu-

Table 3.2: Comparison of the MM method with a reference coming from the literature (ϵ represents the relative gap between the result from [131] and the MM)

H_{oil}^{inlet}	ψ	H_c			H_m		
		Ref.[131]	MM	ϵ [%]	Ref.[131]	MM	ϵ [%]
H_c^{ff}	1	0.3037	0.3039	0.0737	0.2217	0.2219	0.1009
$0.5H_c^{ff}$	0.5	0.1756	0.1756	0.0360	0.1453	0.1453	0.0238
$0.25H_c^{ff}$	0.25	0.0901	0.0908	0.8240	0.0837	0.0845	0.9098
$0.125H_c^{ff}$	0.125	0.0453	0.0456	0.6772	0.0453	0.0456	0.6741

rately reproduce the full range of starvation scenarios presented by Venner et al. [131].

Figure 3.11 presents the results for all the applications outlined in table 3.2. The legend is only referenced within figure 3.11(a), where H_{oil}^{inlet} is equal to a range of values for ψH_c^{ff}. The remaining figures adhere to the same legend. Figure 3.11(e) clearly demonstrates the position of the inlet meniscus, which implies the jump discontinuity inside H_{oil}. Figure 3.12 illustrates a two-dimensional representation[†] of the $H_{oil}^{inlet} = H_c^{ff}$ application. Figure 3.12(b) highlights the presence of oil ridges in the downstream region, which were previously discussed in chapter 1. Figure 3.13 displays the location of the frontier Σ, with the free frontier Σ^{free} delimited by oblique bars on both extremities for all degrees of starvation. The same legend is used as in figure 3.11(a).

[†]2D plots within this manuscript are obtained using a projection of the solution on a regular grid which is generally composed of 151×151 grid points. The reason is that the author desired to realise only vector black and white graphics and spend a lot of time to find the best way to plot 2D graphics. Then this choice seemed to be the best compromise between graphics memory size and visual quality instead of plotting full wireframe solution resulting in unreadable somewhat black potato. The author took his inspiration from the style of the manuscript of Wijnant [136] in 1998. Well, there's no accounting for taste « des goûts et des couleurs, on ne discute pas ».

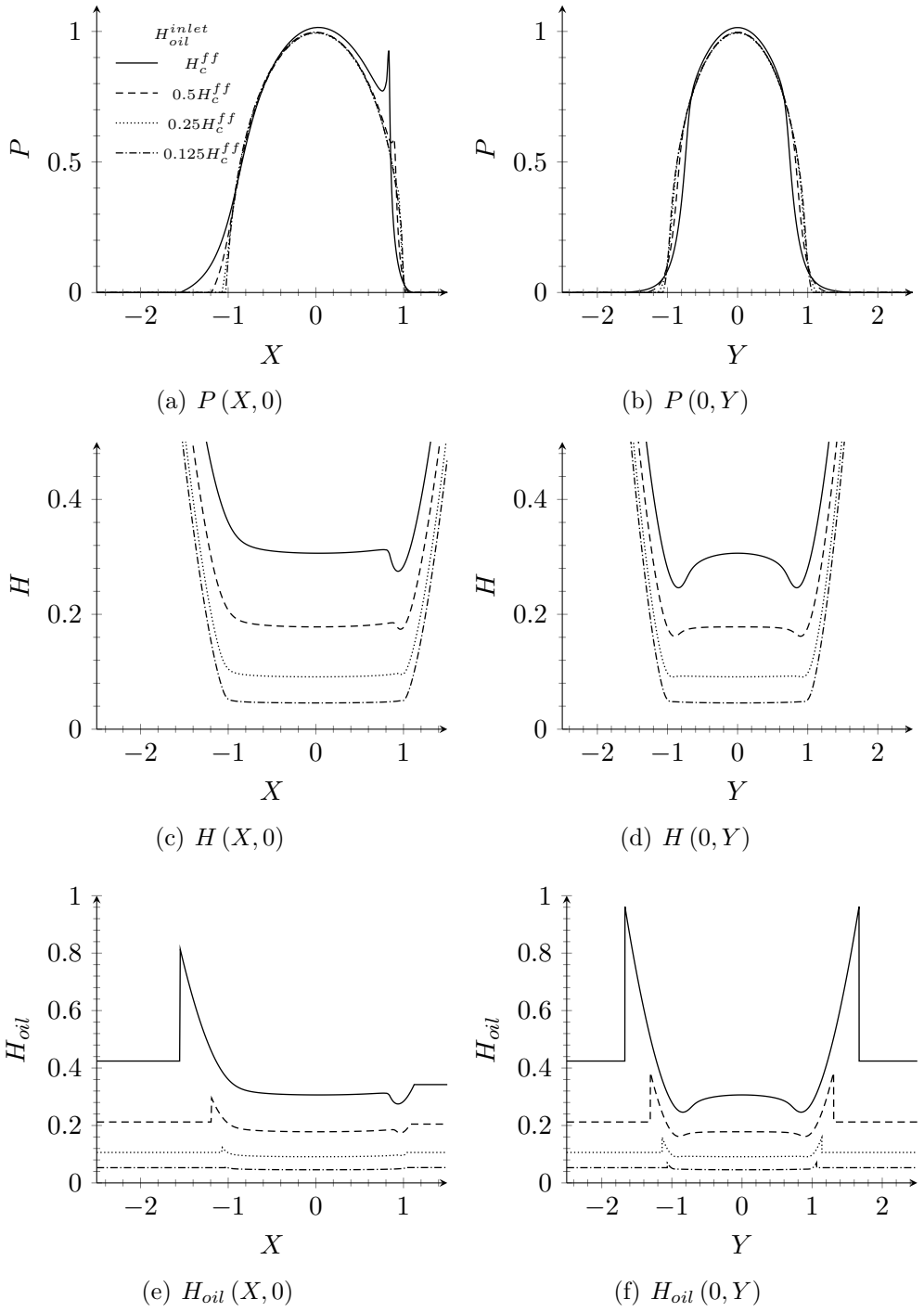

(a) $P\,(X,0)$ (b) $P\,(0,Y)$

(c) $H\,(X,0)$ (d) $H\,(0,Y)$

(e) $H_{oil}\,(X,0)$ (f) $H_{oil}\,(0,Y)$

Figure 3.11: Results for all degrees of starvation

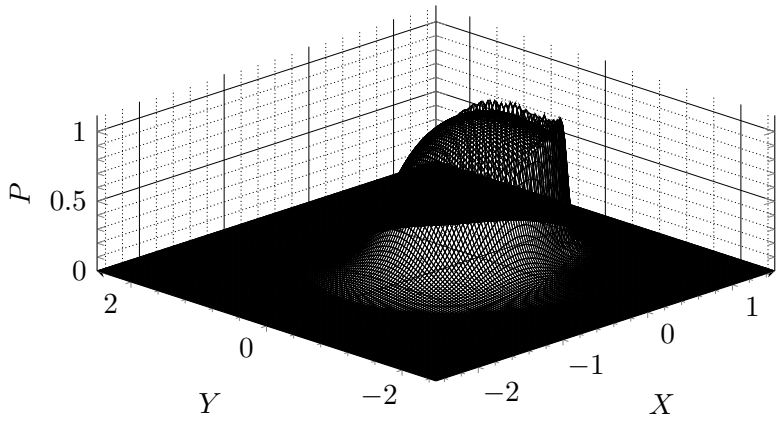

(a) P

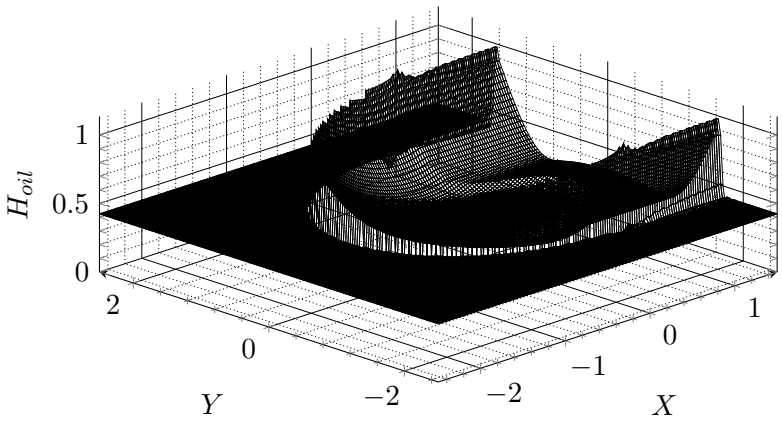

(b) H_{oil}

Figure 3.12: Two dimensional result for the case $H_{oil}^{inlet} = H_c^{ff}$

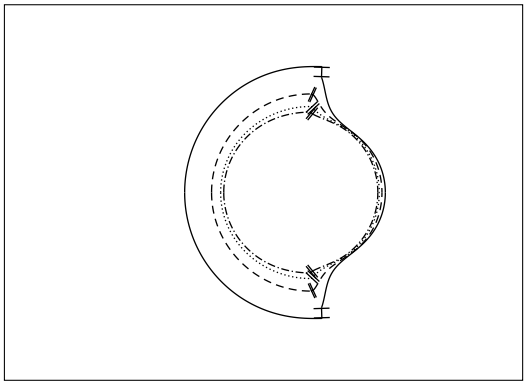

Figure 3.13: Frontiers position for all degrees of starvation

Conclusion

The stationary validation demonstrated that the MM method exhibited superior accuracy, with results that were more closely aligned with the literature reference. Furthermore, the MM method was able to compute an extremely starved application where the PM method did not produce a result. It is also noteworthy that the computation time has not yet been discussed. On average, the PM method required approximately one hour to reach the threshold, while the MM method required just a couple of minutes.

3.3.2 Transient case

This research examines transient applications, with a view to validating both the models in question in relation to transient phenomena. In order to achieve this validation, both models were run through the same simulation. This simulation employed the identical parameters as those used in section §3.3.1, in addition to the same laws governing density and viscosity as pressure. In this instance, the PM model employed a value of $P^\star = 3 \times 10^{-3}$. The EHL contact was initiated with a stationary application such as $H_{oil}^{inlet} = H_c^{ff}$. Subsequently, H_{oil}^{inlet} decreased to $H_{oil}^{inlet} = 0.5 H_c^{ff}$, as illustrated in figure 3.14. The transition between the two total oil thicknesses at the inlet is achieved through the application of a smoothed step function, as represented in figure 3.14. The reduction in oil thickness begins at the outset of the computation and exhibits a transition zone of $T = 2$.

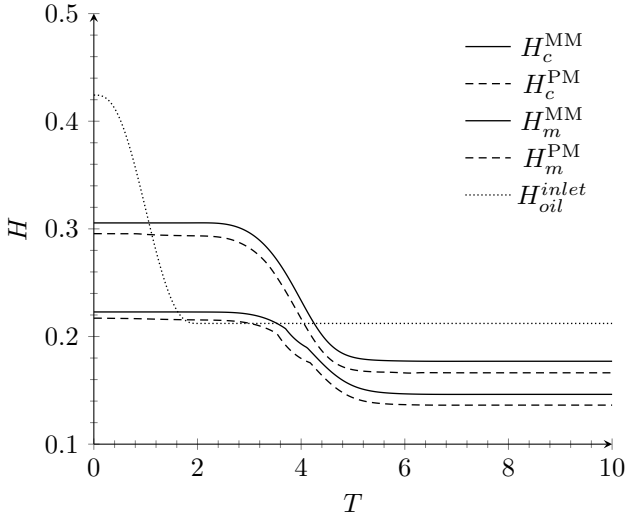

Figure 3.14: Transient comparison between MM and PM

Figure 3.14 illustrates that both models demonstrate comparable behaviour. There is a slight discrepancy between the two for both H_c and H_m. This discrepancy has been attributed to the weakness of the PM, which is caused by the small loss of mass flow rate induced by the use of a penalty term.

In conclusion, the same transient application was run for both methods, namely PM and MM. The results returned by both methods for the entire simulation period were found to be highly similar. An explanation has been provided regarding the discrepancy observed in the values of H_c and H_m between the two methods. Finally, in terms of computation time, the MM method required approximately half a day to compute the entire range of time steps, whereas the PM method required approximately two days.

3.4 Investigation of an oil-off

The development of the transient-starved EHL numerical model permitted the computation of a transient numerical application. This transient application simulates a sudden cessation of lubrication, which is referred to as "oil-off". The EHL contact operates at steady state, and the oil supply H_{oil}^{inlet} is abruptly cut off, resulting in a complete cessation of lubricant transport into the contact area. This application represents the most unfavourable scenario. The results presented in this section were published in Decote et al. [38].

3.4.1 Preamble

The objective of this analysis is to quantify the critical dimensionless time preceding a dry contact event denoted as T_{end}. A dry contact is defined as a situation where the minimum film thickness H_m reaches a value of zero. Given that there is no further oil entering the pressurised domain, it can be anticipated that the dry contact is occurring with considerable rapidity.

The following computations employ the same strategy as that presented in the previous section §3.3.1. The oil inlet layer, H_{oil}^{inlet}, is flat and based on the central film thickness in a fully flooded condition (see equation (3.27)). However, the central film thickness in a fully flooded condition is determined directly from the analytical formula provided by Evans et al. [56]

$$H_c^{ff} = 1.7 M^{-0.026} L^{0.4} \left(\frac{6\pi}{\bar{\lambda}} \right)^{-1/2} \tag{3.29}$$

with $\bar{\lambda}$ already defined in equation (3.28).

Given the significance of domain size in the transportation of oil, all computations are performed using the same inlet distance, $X_{in} = -3.5$. Consequently, for a larger domain, the transport time can be extrapolated on the basis that one dimensionless time is required to travel one dimensionless length. Conversely, the initial position of the domain X_{in} should not be situated in close proximity to the inlet meniscus. The fluid properties remain consistent with those of the previous study, with $\alpha = 1.7 \times 10^{-8}\,\mathrm{Pa}^{-1}$ and $\eta_0 = \eta_R = 8.9 \times 10^{-3}\,\mathrm{Pa} \cdot \mathrm{s}$. However, the values of M and L are subject to variation. From a numerical standpoint, it is important to note that waiting for dry contact and then setting $H = 0$ may potentially lead to numerical issues. Subsequently, a dry contact is posited as soon as the film thickness is below the nanometre (i.e. $H < 1 \times 10^{-9} \cdot R/a^2$). A similar observation can be made with regard to oil convection. A zero value for H_{oil} can result in numerical issues. H_{oil}^{inlet} varies from ψH_c^{ff} f to $0.1 \times 10^{-9} \cdot R/a^2$, as illustrated in figure 3.15.

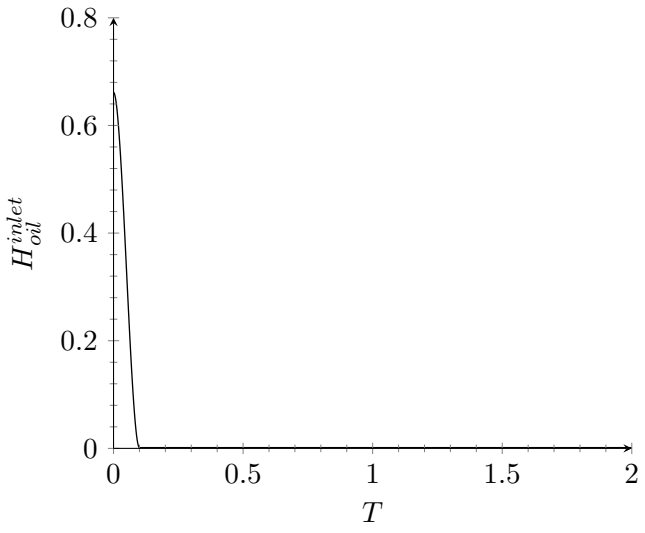

Figure 3.15: Evolution of the variable H_{oil}^{inlet} for $\psi = 1$ and $M = 10$ and $L = 10$

3.4.2 Results

This section presents the results for the oil-off applications. A parametric study is performed, in which ψ is varied from 1 to 0.125, as described in section §3.3.1. Additionally, M is set to 10 and 100, while L is set to 5 and 10. One application is subjected to thorough observation, after which the overall results are discussed.

Discussion of one case

The application utilising $\psi = 1$, $M = 10$ and $L = 10$ is to be subjected to comprehensive examination in due course. Figure 3.16(a) illustrates the temporal evolution of the dimensionless pressure along the X-direction. The difference between each curve is represents 0.1 dimensionless time. Figure 3.16(b) illustrates the temporal evolution of the dimensionless film thickness, H, and the oil film thickness, H_{oil}, along the X-direction. The figure clearly demonstrates the instant at which dry contact occurs. Figure 3.16(c) presents the evolution of H_c and H_m. From this figure, it can be observed that although the perturbation on H_{oil}^{inlet} is transported, the film thickness

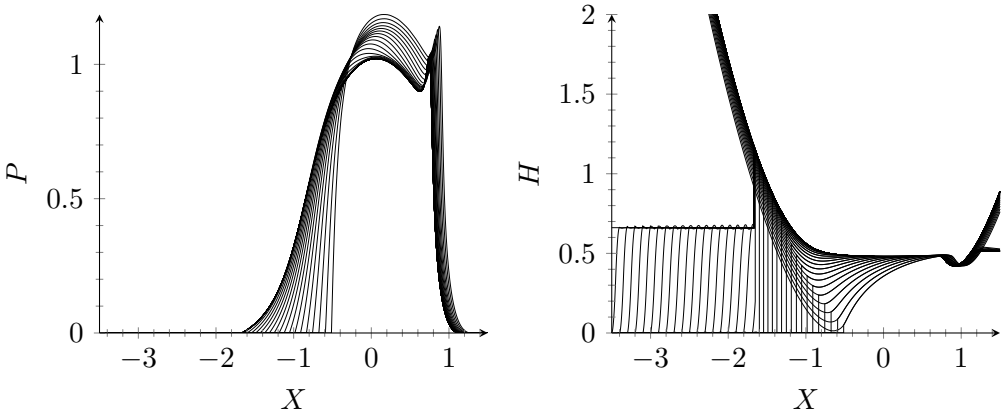

(a) Pressure

(b) Film and oil thicknesses

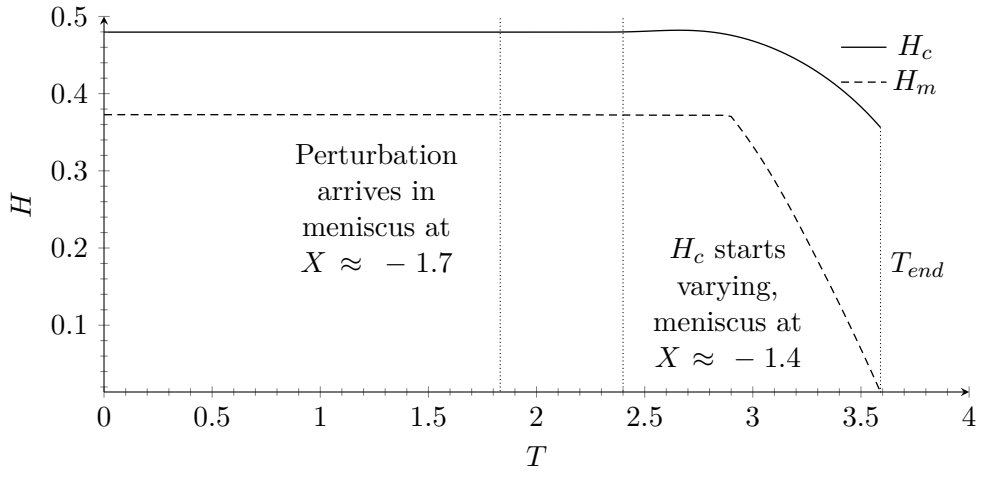

(c) Evolution of H_c and H_m

Figure 3.16: Transient result for the investigated application

remains unaltered since the perturbation does not reach the inlet meniscus. Furthermore, upon arrival of the perturbation at the inlet meniscus, both H_c and H_m remain unaltered. This phenomenon can be attributed to the accumulation of oil within the inlet meniscus. As the accumulation is not replenished and due to the convection process, the volume of oil inside the meniscus is reduced as it passes through the contact. H_c begins to increase slightly before declining, whereas H_m shows a decrease. The evolution of the film thickness within the Hertzian region is illustrated through contour plots at four distinct dimensionless times in figure 3.17. From this figure, the marker $\otimes$ indicates the position of H_m, while the marker $\oplus$ denotes the location of the maximum film thickness within the Hertzian area. For the sake of clarity, the latter has not been included in the two initial plots, as it is situated at the first level. These contour plots demonstrate that when the film thickness begins to decline to $H = 0$, the maximum film thickness is situated in close proximity to the outlet, where the restriction of the film thickness occurs.

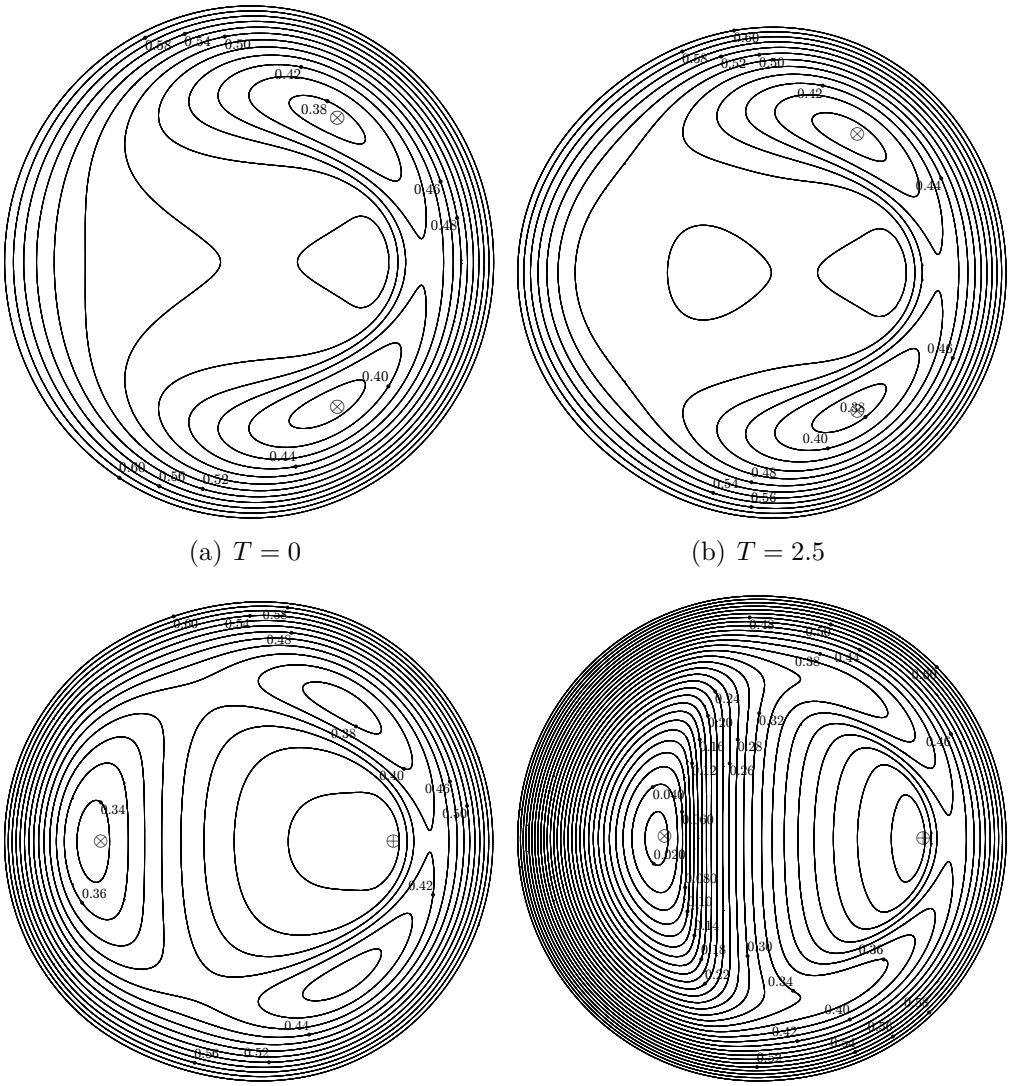

(a) $T = 0$ (b) $T = 2.5$

(c) $T = 3$ (d) $T = T_{end}$

Figure 3.17: Evolution of the film thickness for at four different dimensionless times ($\Delta H = 0.02$)

General results

The computation observed in the previous subsection has been reproduced for various values of M, L and ψ, with the aim of determining T_{end}. Figure 3.18 shows the critical time T_{end} as a function of ψ and depending on M and L. The square markers relate to $M = 10$, while the diamond markers relate to $M = 100$. When the marker is black filled, then $L = 10$; otherwise, $L = 5$.

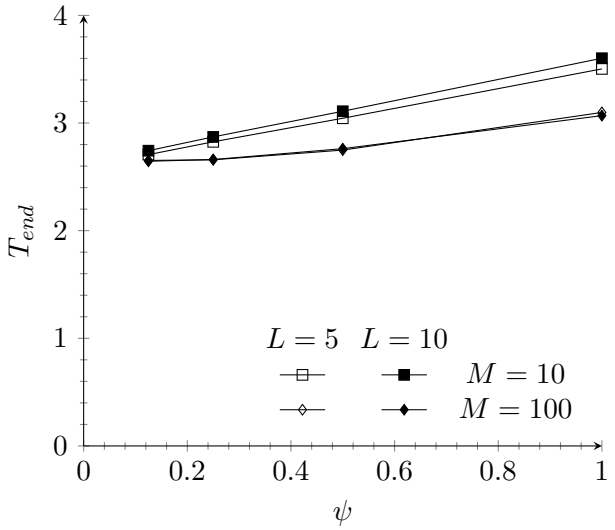

Figure 3.18: Critical time T_{end} as a function of the degree of starvation

Figure 3.18 illustrates that an increase in oil quantity is associated with an increase in T_{end}. This result appears to be logical; it can be reasonably deduced that the film thickness is greater, and therefore the time taken to reach the threshold is longer. Secondly, the reservoir of oil in the inlet meniscus is also larger, which permits a longer duration of contact. Additionally, this figure demonstrates that L does not contribute significantly to the overall outcome. The discrepancy between the two values of L can be considered insignificant. Nevertheless, M has a more pronounced effect. A reduction in the value of M corresponds with an increase in the value of T_{end}. In the work of Moes [101], M is defined as the "load parameter". Therefore, an increase in M indicates a greater load applied to the EHL contact. A high load is indicative of a reduced film thickness, which in turn corresponds to a diminished oil reservoir. Consequently, the critical time T_{end} is reduced. As anticipated, a reduction in ψ is accompanied by a reduction in the critical time. This is due to the same reason as previously stated: a reduction in oil

quantity results in a smaller film thickness. When the starvation is extreme (i.e. $\psi = 0.125$), it appears that both M converge to the same behaviour. Indeed, in this case the meniscus is in close proximity to the Hertzian area, indicating that the reservoir is of a minimal size. It can be observed that T_{end} tends to 2.5, which represents the dimensionless time required for the perturbation to travel from $X_{in} = -3.5$ to -1 (given that the dimensionless convection velocity is 1).

3.4.3 Conclusion

A transient application undergoing an oil-off situation has been conducted. It has been observed that the critical time, T_{end}, defined as the time before a dry contact occurs, occurred with remarkable rapidity. Furthermore, the impact of M and L, as well as the quantity of oil (governed by ψ), has been examined. It has been demonstrated that L does not exert a notable influence on T_{end}. However, M and ψ have been observed to produce discernible effects on T_{end}. A greater value of ψ is associated with a larger T_{end}, while a smaller value of M is linked to a larger T_{end}. Nevertheless, this application appears challenging to reproduce in an experimental setting and lacks a clear physical meaning. In other words, the probability of encountering such a critical scenario within a Rolling Element Bearing (REB) is exceedingly low or non-existent. Consequently, the oil-off application primarily serves as a means of evaluating the efficacy of the recently developed numerical solver.

3.5 Conclusion

Two distinct methodologies have been developed for the computation of a starved EHL contact, applicable to both stationary and transient conditions. These methodologies are based on the JFO theory and employ the finite element (FE) method for their numerical solution.

The initial method, designated Penalty Method (PM), is notably analogous to the approach proposed by Marian et al. [95] in 2019. The PM employs the use of a penalty term, as outlined in equation (3.6), which serves to mitigate the discontinuity between the two variables within the modified Reynolds equation (3.1). This is achieved through the utilisation of an exponential decay function that facilitates a bijection between the pressure and oil ratio. Additionally, the modifications that have been made to the numerical procedure, as presented in section §2.7, have been elucidated in great detail.

The second method is an entirely original approach, designated as the

Moving Mesh (MM) method. In this instance, the exact JFO theory is employed. In order to achieve this, the JFO theory has been derived, which has led to the emergence of two distinct zones: a pressurised one and a transport one. Subsequently, the conservation of the mass flow rate at the frontier between the two has been established, which has enabled the development of a numerical strategy that allows the frontier to move. The introduction of the ALE approach has enabled the motion of the mesh and has allowed the frontier to move to the correct position, thereby ensuring the mass flow rate conservation.

Subsequently, both numerical methods were confronted with a literature reference in a stationary application. It was observed that both methods demonstrated a highly accurate approximation of the results obtained from the literature reference. However, the MM method exhibited superior accuracy, a more efficient computation time, and enhanced flexibility, enabling the calculation of extreme cases. Additionally, the MM method does not necessitate the utilisation of a penalty coefficient.

In order to test the reliability of the two models, they were subjected to the same transient application, which involved a varying total inlet oil thickness H_{oil}^{inlet} over time. The results demonstrated that both models behaved similarly, thereby providing confidence in their use when dealing with transient applications.

Ultimately, the MM demonstrated a multitude of advantages based on the comparative analysis conducted in this chapter. Consequently, an initial transient application was conducted to ascertain the duration of an EHL contact during an oil-off event. The findings indicated that the remaining operational time is minimal, implying that a dry contact occurs rapidly. However, the application lacks physical relevance, hence a more realistic process (termed Loss of Lubricant (LoL)) must be employed.

Chapter 4

Application: Loss of Lubricant (LoL)

This chapter is dedicated to the analysis and modelling of experimental research on ElastoHydrodynamic Lubrication (EHL) contacts that have experienced a Loss of Lubricant (LoL). Initially, a comprehensive review of the literature, based on the findings presented in chapter 1, is presented, with a particular attention to a specific application and the underlying hypothesis that must be considered when modelling it. Furthermore, the chapter discusses the numerical adaptations that have been made to reproduce the experimental studies. Finally, the isothermal and thermal simulations that have been developed to reproduce the experimental results are analysed.

4.1 Review of LoL applications

4.1.1 Experimental works

Chapter 1 provided an overview of the experimental works related to a LoL applications, which are summarised in table 4.1. These studies are focused

on investigating the reduction in film thickness due to a LoL. The majority of these works were conducted on a ball-on-disc test rig, with the exception of the study by Eichler et al. [50], which was performed on a thrust bearing test rig. The experiments were initiated with a specified mass of oil deposited on the surfaces of the specimens.

The experimental works entail measuring either the film thickness, the friction coefficient, or even the torque. The final column of table 4.1 illustrates how this measurement progresses over time/overrollings. The outcome may be a stable state (i.e. a constant value), or it can be characterised as unstable with a potential for either an increase (if it is the friction coefficient) or a decrease (if it is the film thickness). According to Querlioz [112], an overrolling of the longer specimen may be considered to represent an overrolling of the system as a whole.

The second column of table 4.1 presents a comprehensive overview of the working conditions of the experimental works referenced in the first column. The initial rows preceding a horizontal line pertain to the overarching parameters that are applicable to the entirety of the experimental work. However, dedicated rows are provided for the parameters that are subject to variation and are delineated by horizontal lines. To illustrate, all of the experimental works conducted by Popovici [110] were performed at $\mathbb{T} = 25\,^{\circ}\mathrm{C}$ with $F = 20\,\mathrm{N}$. Nevertheless, he employed two distinct oils and a range of entrainment velocities.

Table 4.1 illustrates that when the working conditions are severe, namely when Hertzian pressure exceeds one gigapascal or velocity exceeds one metre per second, the EHL contact fails to reach a steady state. In such instances, scuffing occurs. The objective of the aforementioned studies was to ascertain the impact of different oils and coatings on the time before scuffing occurs.

Conversely, when the working conditions are less severe, the EHL contact reaches a steady state, with the exception of the elliptical contact cases of van Zoelen [127] and one case from Querlioz [112]. The stabilisation occurred at approximately 100 overrollings, which precludes any definitive conclusion regarding the work of Popovici [110]. The experimental procedures were conducted to permit a comparison with analytical formulae that predict film thickness decay. Indeed, the existing literature indicates the existence of two formulas that enable the analytical determination of film thickness decay during an overrolling process. The two formulas are presented below.

Table 4.1: LoL applications presented within literature

Ref.	Working conditions	Result
Cann et al. [26]	Oil droplets on the disc (0.5 mL) $p_H = 0.48\,\text{GPa}$, $\mathbb{T} = 25\,°\text{C}$ Steel ball and glass disc $u_m = 0.1\,\text{m} \cdot \text{s}^{-1}$, $\text{SRR} = 0\,\%$ $\eta_0 = 0.1\,\text{Pa} \cdot \text{s}$ and $0.4\,\text{Pa} \cdot \text{s}$	Stab.
Popovici [110]	$\mathbb{T} = 25\,°\text{C}$, $F = 20\,\text{N}$	
	Oil: PAO8 $u_m = 0.577\,\text{m} \cdot \text{s}^{-1}$	Stab.
	$u_m = 1.13\,\text{m} \cdot \text{s}^{-1}$	Unstab.[a]
	Oil: PAO100 $u_m = 0.05\,\text{m} \cdot \text{s}^{-1}$ and $0.1\,\text{m} \cdot \text{s}^{-1}$	Unstab.[a]
Querlioz [112]	Oil droplets on the disc (PAO100) $R_{ball} = 19.05\,\text{mm}$, specimens: steel 100Cr6 $\eta_0 = 1.08\,\text{Pa} \cdot \text{s}$, $\mathbb{T} = 40\,°\text{C}$, $\text{SRR} = 1.9\,\%$	
	Mass of oil: 10 mg, $F = 25\,\text{N}$ $u_m \in [60;\ 75]\ \text{mm} \cdot \text{s}^{-1}$, $p_H = 0.89\,\text{GPa}$	Stab.
	Mass of oil: 10 mg, $F = 12\,\text{N}$ $u_m \in [85;\ 110]\ \text{mm} \cdot \text{s}^{-1}$, $p_H = 0.69\,\text{GPa}$	Stab.
	Mass of oil: 10 mg, $F = 25\,\text{N}$ $u_m = 100\,\text{mm} \cdot \text{s}^{-1}$, $p_H = 0.89\,\text{GPa}$	Unstab.
	Mass of oil: 15 mg, $F = 25\,\text{N}$ $u_m \in [85;\ 100]\ \text{mm} \cdot \text{s}^{-1}$, $p_H = 0.89\,\text{GPa}$	Stab.
Van Zoelen [127]	$p_H = 0.51\,\text{GPa}$, $\eta_0 = 0.84\,\text{Pa} \cdot \text{s}$ $\eta_0 = 0.84\,\text{Pa} \cdot \text{s}$, $F = 20\,\text{N}$ Steel rolling element and glass disc	
	Point contact, $a = 136\,\mu\text{m}$ $u_m \in [60;\ 800]\ \text{mm} \cdot \text{s}^{-1}$	Stab.
	Elliptical contact $a_x = 108\,\mu\text{m}$, $a_y = 398\,\mu\text{m}$ $u_m \in [60;\ 800]\ \text{mm} \cdot \text{s}^{-1}$	Unstab.

Continuation of table 4.1

Ref.	Working conditions	Result
Eichler et al. [50]	$p_H = 1\,\text{GPa}$, $u_m = 14\,\text{m} \cdot \text{s}^{-1}$ Thrust bearing model: 51306 balls are coated (1 µm)	Unstab.
Riggs et al. [117]	$p_H = 2.38\,\text{GPa}$, $u_m = 16\,\text{m} \cdot \text{s}^{-1}$ SRR = 200 %, $R_{ball} = 20.64\,\text{mm}$ AISI 9310 gear steel for the ball and disc Various couple of coatings	Unstab.

[a]The test may be too short (only 100 overrollings) to conclude.

4.1.2 Film thickness decay formulas

Film thickness decay from Chevalier

According to Chevalier et al. [30] the film thickness decay is established as follow:

$$\mathcal{R}_c(n) = \frac{1}{\sqrt[\gamma]{\frac{1}{r_0^\gamma} + n}}, \tag{4.1}$$

with

$$\mathcal{R}_c = \frac{H_c}{H_c^{ff}} \tag{4.2}$$

the central film thickness decay and

$$r_0 = \frac{H_{oil}^{inlet}(n=1)}{\bar{\rho}(p_H) H_c^{ff}} \tag{4.3}$$

the initial oil quantity parameter, n the number of overrolling and γ the resistance to side flow parameter which depends on the operating conditions M and L (see equation (2.53)). If the initial quantity of oil is significantly greater than the H_c^{ff}, then r_0 tends to large values and equation (4.1) reduces to a simpler form

$$\mathcal{R}_c(n) = n^{-\frac{1}{\gamma}}. \tag{4.4}$$

Chevalier [29] further developed the film thickness decay equation (4.1) to incorporate replenishment. However, this extension is unable to predict whether stabilisation will occur. Instead, it provides a visual representation of the film thickness decay curve between the inaugural contact ($n = 1$) and the asymptotic value (which is a pre-determined constant and is discussed subsequently). In accordance with Chevalier [29], the film thickness

decay that occurs during the process of stabilisation is evaluated as follows:

$$\mathcal{R}_c(n) = \frac{\mathcal{R}_c(n-1)}{\sqrt[\gamma]{1+\mathcal{R}_c(n-1)^{\gamma}}} + dr \tag{4.5}$$

where for a stabilised value of $\mathcal{R}_c$, dr (the replenishment flowrate) yields to

$$dr = \frac{\mathcal{R}_c(\infty)}{\sqrt[\gamma]{1-\mathcal{R}_c(\infty)^{\gamma}}} - \mathcal{R}_c(\infty). \tag{4.6}$$

Equation (4.1) predicts the film thickness decay through the overrollings, n. Equation (4.4) is a simplified version of equation (4.1) when the first contact, $n = 1$, is fully flooded. Therefore, equation (4.5) demonstrates the film thickness decay between the initial contact ($n = 1$) and the established equilibrium value (which is a known quantity) when the process of stabilisation occurs (it should be noted that equation (4.5) does not provide an a priori indication as to whether stabilisation will occur).

Film thickness decay from van Zoelen

According to Lugt et al. [94] the van Zoelen [127] film thickness decay can be expressed as follows:

$$h_c(t) = \frac{1}{\sqrt{\frac{1}{6}\bar{\rho}(p_H)\,\mathfrak{F}_k(0)\,t + h_c(t=0)^{-2}}}, \tag{4.7}$$

with

$$\mathfrak{F}_k(0) = \frac{2p_H\pi}{l_t a \eta_0}\left(\frac{\pi\alpha p_H}{2}\right)^{-1} \tag{4.8}$$

where for a single ball-on-disc setup

$$l_t = 2\pi\left(R_{ball}^{\mathrm{MTM}} + R_{mid}^{disc}\right). \tag{4.9}$$

R_{mid}^{disc} represents the radial position on the disc where the contact occurs (defined equation (4.15) and on figure 4.1) Lastly, van Zoelen et al. [128] provided a formula for converting time t into corresponding overrolling n or vice versa such as

$$t = \frac{4\pi}{u_m}\frac{R_{mid}^{disc}R_{ball}^{\mathrm{MTM}}}{R_{mid}^{disc}+R_{ball}^{\mathrm{MTM}}}n. \tag{4.10}$$

4.1.3 Conclusion

In summary, the various experimental works associated with a LoL application have been collated. A LoL application can be observed to generate two different behaviours. Either the film thickness (or friction coefficient) reaches a steady state, or it decreases (respectively, increases) when the number of overrollings increases. Additionally, two analytical formulas have been presented that enable the prediction of film thickness decay: one from Chevalier et al. [30] and one from van Zoelen [127]. Despite Chevalier [29] having established a formulation that enables the prediction of film thickness decay when stabilisation occurs, the formula does not predict stabilisation a priori. Consequently, it is necessary to understand why stabilisation occurs and how it works.

4.2 Case study

4.2.1 Introduction

In light of the experiments presented in table 4.1, it is proposed that the work of Querlioz [112] be simulated, in which the author relates both stabilisation and unstabilisation.

4.2.2 Description

All experimental applications performed by Querlioz [112] were conducted using the MTM test rig. The characteristics of the MTM are presented in table 4.2 and illustrated in figure 4.1.

Table 4.2: MTM properties

Variable	Value
R_{int}^{MTM}	19 mm
R_{ext}^{MTM}	23 mm
R_{ball}^{MTM}	3/8 in
$E_{disc} = E_{ball}$	210 GPa
$\nu_{disc} = \nu_{ball}$	0.3

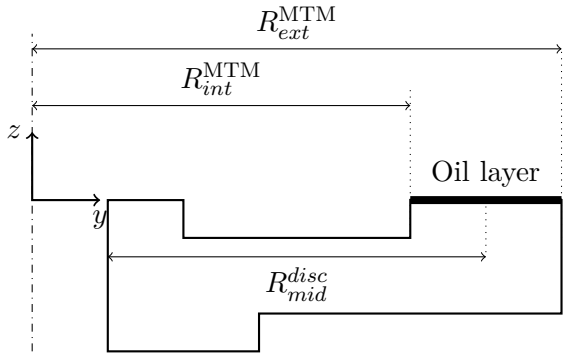

Figure 4.1: Dimensions of the disc

A defined quantity of oil is applied to the raceway of the MTM disc in

the form of droplets using a micro-syringe. The test rig is heated until a temperature of $\mathbb{T}_0 = 40\,°\mathrm{C}$ is reached. The experiment is conducted for a period of two hours or until there is a notable increase in the friction coefficient. Table 4.3 provides the parameters set out by Querlioz [112]. The oil employed is PAO100.

Table 4.3: Input data from Querlioz [112]

Variable	Value	Note
ρ_0	$850\,\mathrm{kg}\cdot\mathrm{m}^{-3}$	At 15.6 °C
η_0	$1.08\,\mathrm{Pa}\cdot\mathrm{s}$	At 40 °C
	$85\,\mathrm{mPa}\cdot\mathrm{s}$	At 100 °C
α	$19.8\,\mathrm{GPa}^{-1}$	
m_{oil}	10 mg	
	15 mg	
	20 mg	
u_m	$60\,\mathrm{mm}\cdot\mathrm{s}^{-1}$	
	$65\,\mathrm{mm}\cdot\mathrm{s}^{-1}$	
	$70\,\mathrm{mm}\cdot\mathrm{s}^{-1}$	
	$100\,\mathrm{mm}\cdot\mathrm{s}^{-1}$	
F	25 N	
SRR	1.9 %	
a	115.67 µm	equation (2.40)
p_H	0.89 GPa	equation (2.42)

The MTM used by Querlioz [112] only measured the friction coefficient. Figure 4.2, which has already been presented in chapter 1 as figure 1.11, illustrates the friction coefficient of a stabilised and an unstabilised case. Both applications were conducted using an oil mass of $m_{oil} = 10\,\mathrm{mg}$. The aforementioned experiments form the reference for the following.

In order to enable comparison with the film thickness decay of Chevalier [29], Querlioz [112] converted the friction coefficient into central film thickness h_c using the Johnson, Tevaarwerk, and Tabor [82] viscoelastic rheological model which is expressed as follows:

$$h_c = \frac{\eta\left(p_H\right)\Delta u}{\tau_0 \sinh\left(\frac{c_f 2 p_H}{3\tau_0}\right)}, \tag{4.11}$$

with $\Delta u = u_m \mathrm{SRR}/100$ and τ_0 the Eyring shear stress value. The viscosity at Hertzian pressure, designated as $\eta\left(p_H\right)$, is calculated using the Roelands [118]

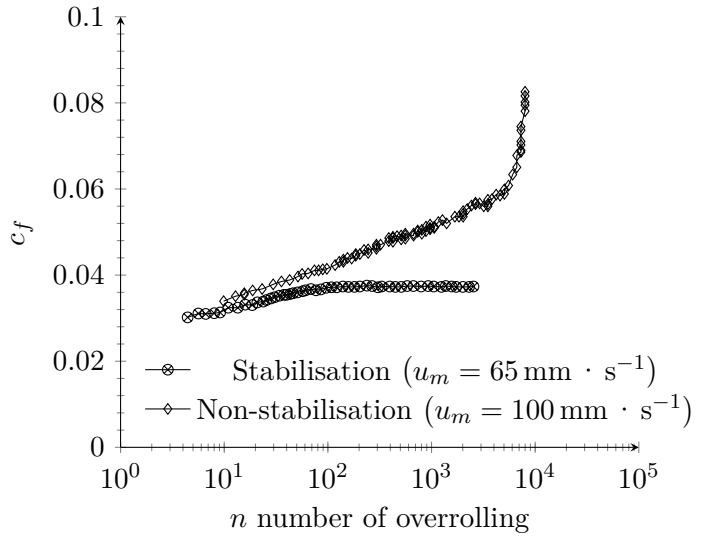

Figure 4.2: Two LoL applications made on MTM with different entrainment velocities leading to two different behaviours (data has been extracted from Querlioz [112] figure using OriginLab® software)

viscosity-pressure law, as outlined in equation (2.14). Querlioz [112] did not specify the value utilised for τ_0; however, Johnson [79] or Jacod [78] postulated that this value may be approximated at $\tau_0 = 5\,\text{MPa}$.

4.2.3 Conclusion

This section presents the data and findings of the experimental work performed by Querlioz [112]. The case study is thus modelled in accordance with the presented information.

4.3 Numerical modelling strategy

4.3.1 Focus on the initial condition

In order to enable the application of starvation computation using the Moving Mesh (MM) model, it is necessary to convert the mass of oil into total oil thickness upstream of the contact.

Hypothesis 1. It is postulated that the initial mass of oil deposited during the experiment was distributed in a uniform manner across the entire surface area of the disc, forming an annulus with a surface area designated as A_a

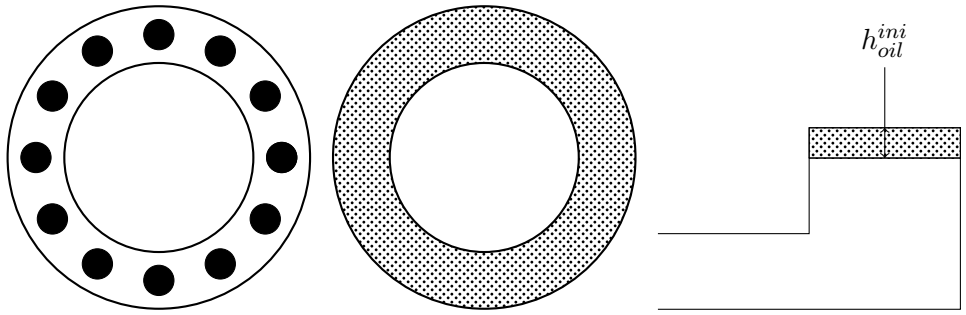

(a) Oil droplets on the disc (b) Annulus of oil (c) Side view of the disc

Figure 4.3: Initial repartition of the oil droplets on the disc raceway

and a thickness equal to the initial oil film thickness $h_{oil}^{ini} = h_{oil}^{inlet}$ $(n = 1)$, as illustrated in figure 4.3. Then, the area of the annulus is

$$A_a = \pi \left(R_{ext}^{\mathrm{MTM}^2} - R_{int}^{\mathrm{MTM}^2} \right).$$

Consequently the thickness of the annulus is

$$h_{oil}^{ini} = \frac{m_{oil}}{\rho A_a} = 22.3\,\mu\mathrm{m}. \tag{4.12}$$

As noted by Venner et al. [131], when the total oil thickness upstream of the contact is greater than five times the predicted central film thickness (in fully flooded conditions), the contact is considered fully flooded. This is because, in such cases, the significant quantity of oil results in the inlet meniscus being situated at a considerable distance from the centre of the contact (see figure 1.9). Table 4.4 illustrates the ratio between the quantity of oil and the central film thickness.

Table 4.4: Comparison between the quantity of oil and the fully flooded central film thickness

u_m [mm · s^{-1}]	Hamrock et al. [67]		Querlioz [112] from (4.11)	
	h_c^{ff} [µm]	$\frac{h_{oil}^{ini}}{h_c^{ff}}$	h_c^{ff} [µm]	$\frac{h_{oil}^{ini}}{h_c^{ff}}$
65	0.368	>60	0.334	>60
100	0.491	>45	0.493	>45

Table 4.4 demonstrates that the ratio h_{oil}^{ini}/h_c^{ff} is significantly larger than 5. The final column represents the experimental value, which has been con-

verted by Querlioz [112] using equation (4.11). This hypothesis enables the computation of the first contact, $n = 1$, from a fully flooded condition. ¶

4.3.2 Fully flooded computation

In order to achieve a fully flooded computation using the MM method as outlined in chapter 3, both sub-frontiers Σ^{inlet} and Σ^{free} must disappear. Indeed, in a fully flooded application, the position of the inlet meniscus, which is situated far from the contact, has no impact on the film thickness. Thus, the inlet position was chosen as $X_{in} = -4.5$ and the outlets were selected as $X_{out} = 1.5$ and $Y_{out} = 3$, based on the recommendations provided by Habchi [61].

The outlet frontier of Ω_P, designated as Σ^{outlet}, is illustrated in figure 4.4(a). It can be seen that the inlet of the transport domain, Ω_T, coincides with Σ^{outlet}. Consequently, in accordance with the study conducted in the frontier equation section §3.2.3, the Dirichlet boundary condition of Ω_T, on the frontier Σ^{outlet} is $H_{oil} = H$. It is important to note that this boundary condition for Ω_T should not be confused with the equation solved on Σ^{outlet} governing its position, which remains the zero normal pressure gradient. The corresponding boundary conditions for mesh motion are outlined in figure 4.4(b). As a consequence, the system (3.24) must be solved without the equations related to Σ^{inlet} and Σ^{free}.

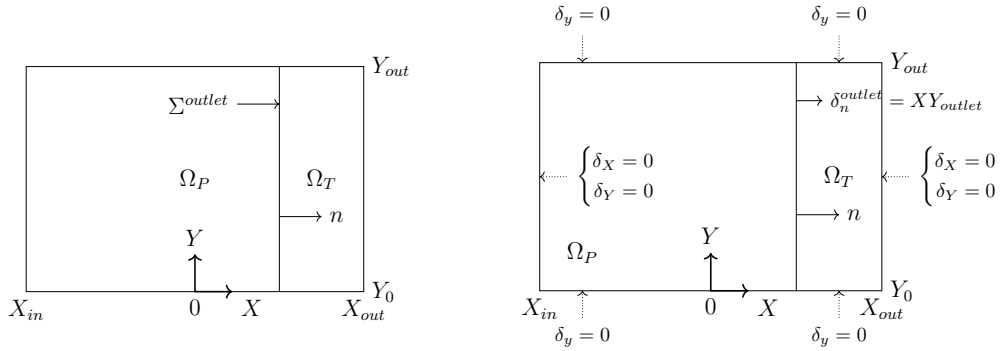

(a) Domains decomposition (b) MM boundary condition

Figure 4.4: MM domains in fully flooded configuration

In this configuration, the MM model provides an oil thickness profile downstream of the contact. This profile can be employed to determine whether track replenishment occurs in this application.

4.3.3 Track replenishment

The formation of oil ridges downstream of the contact point, and the potential for these ridges to flow back onto the racetrack, was demonstrated in chapters 1 and 3. Consequently, it is necessary to establish the behaviour of the oil profile as it leaves the contact, whether this is by disc or ball transportation, until it re-enters the contact point, as illustrated in figures 4.5(a) and 4.5(b).

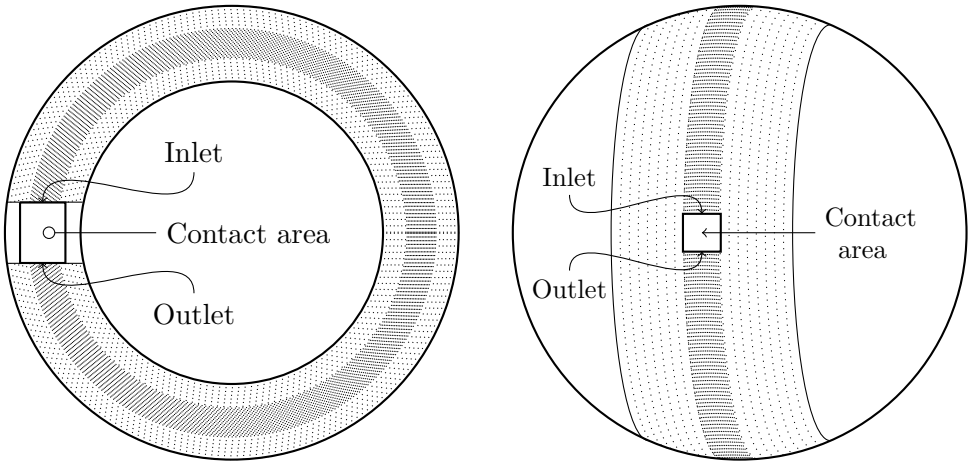

(a) Disc of the MTM (b) Ball of the MTM

Figure 4.5: Components of the MTM

The oil outside the contact area is subjected to external forces, such as centrifugal force, which have the potential to modify the profile of the layer of oil. Figure 4.6(a) represents a qualitative cross-section of the layer of oil (dotted pattern) adhering to an element (ball or disc; for illustrative purposes only) situated downstream of the contact. Similarly, figure 4.6(b) illustrates a qualitative cross-section of the layer of oil subjected to a tangential external force, resulting in a change in its profile over time.

The MM method, which employs the Jakobsson-Floberg-Olsson (JFO) theory, provides the total thickness of oil present within the gap between the two solids. As demonstrated by Bruyere et al. [22] who conducted Computational Fluid Dynamics simulations using the Navier-Stokes equations, when the SRR is zero, the total oil mass (thickness) is divided equally between the two surfaces at the outlet of the contact. One half adheres to the ball, while the other adheres to the disc.

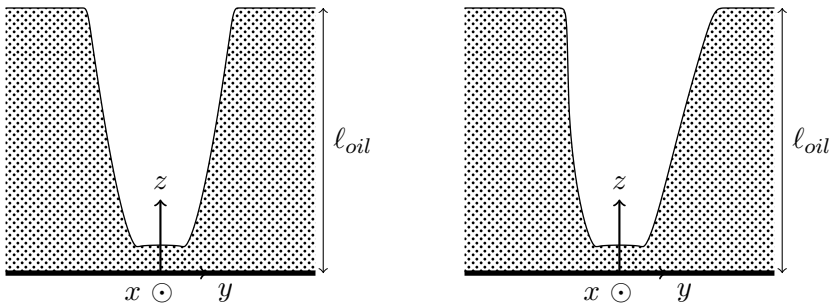

(a) Oil layer sticking to a surface

(b) Oil layer deformed by a tangential external force (such as centrifugal force)

Figure 4.6: Thin layer explanation

Hypothesis 2. Given that the applications under investigation in this chapter exhibit a markedly low value of SRR (1.9 %), it is postulated that the total oil thickness is partitioned into two equal layers downstream of the contact. ¶

Thin layer equation

The behaviour of the layer of oil downstream of the EHL contact and during the complete revolution of either the disc or the ball can be calculated using the thin layer equation proposed by van Zoelen [127] such as:

$$\frac{\partial \ell_{oil}}{\partial t} + \frac{1}{3\eta_0}\frac{\partial}{\partial y}\left(\ell_{oil}^3\left\{f_z\frac{\partial \ell_{oil}}{\partial y} + \sigma_f\frac{\partial^3 \ell_{oil}}{\partial y^3} + f_y\right\}\right) = 0. \tag{4.13}$$

The external forces, f_z and f_y, are defined as the forces acting in the z-direction, which is the thickness direction, and in the y-direction, which is the tangential direction. Finally, σ_f represents the air-oil surface tension. In this study, it is assumed that $\sigma_f = 0.3\,\mathrm{J}\cdot\mathrm{m}^{-2}$, which is situated midway within the interval proposed by Lugt et al. [94] (ranging from $0.2\,\mathrm{J}\cdot\mathrm{m}^{-2}$ to $0.4\,\mathrm{J}\cdot\mathrm{m}^{-2}$). This equation determines the behaviour of the oil layer in the yz-plane, which is the transverse plane with respect to the rolling direction (i.e. the x-direction). The aforementioned equation employs the dimensionless parameters mentioned in section §2.6 and normalises ℓ_{oil} in a manner analogous to that employed for h_{oil} and h and also

$$\begin{cases} \bar{f}_{Z,Y} = \dfrac{f_{z,y}a^2}{\eta_0 u_m}, \\ \bar{\sigma}_f = \dfrac{\sigma_f}{\eta_0 u_m}. \end{cases}$$

Therefore, the dimensionless thin layer equation is as follow:

$$\frac{\partial \bar{\ell}_{oil}}{\partial T} + \frac{a^2}{3R^2}\frac{\partial}{\partial Y}\left(\bar{\ell}_{oil}^3\left\{\bar{f}_Z\frac{a}{R}\frac{\partial \bar{\ell}_{oil}}{\partial Y} + \bar{\sigma}_f\frac{a}{R}\frac{\partial^3 \bar{\ell}_{oil}}{\partial Y^3} + \bar{f}_Y\right\}\right) = 0. \tag{4.14}$$

According to Gershuni et al. [58], this equation is solved with the following boundary condition

$$\frac{\partial \bar{\ell}_{oil}}{\partial Y} = 0.$$

Thus far, the behaviour of the oil layer on the disc and the ball can be observed and analysed in a manner that is independent of one another.

On the disc

The text begins by setting out the methodology used to calculate the oil layer on the disc. This is followed by a detailed account of the numerical procedure employed and a presentation of the resulting data.

Numerical procedure The objective of this application is to obtain the oil layer profile $\bar{\ell}_{oil}$ immediately prior to re-entry into the contact zone. In this context, one complete revolution of the disc has been completed. The time required for the disc to complete one revolution is expressed as a dimensionless quantity, denoted T_{end}^{disc}.

Hypothesis 3. The contact occurs at the centre of the raceway (see figure 4.1) i.e.

$$R_{mid}^{disc} = \frac{R_{ext}^{\mathrm{MTM}} + R_{int}^{\mathrm{MTM}}}{2}. \tag{4.15}$$

¶

Subsequently, it is possible to calculate T_{end}^{disc}, for example, as follows:

$$T_{end}^{disc} = \frac{2\pi R_{mid}^{disc}}{u_{disc}} \cdot \frac{u_m}{a}$$

with

$$u_{disc} = u_m\left(1 + \frac{\mathrm{SRR}}{2}\right).$$

In accordance with the specifications set forth in figure 1.10, the axis of revolution of the disc is oriented vertically on the MTM. Consequently, the gravitational acceleration exerts a force in the thickness direction as follow:

$$f_z = -g\rho_0,$$

with g the gravitational acceleration and ρ_0 the fluid density at ambient pressure. Subsequently, the centrifugal force generates a tangential force.

$$f_y = \rho_0 R_{mid}^{disc} \omega_{disc}^2$$

with $\omega_{disc} = u_{disc}/R_{mid}^{disc}$ which denotes the angular velocity of the disc.

Having defined the input parameters, the initial oil profile at $T = 0$ must be established. Equation (4.14) is solved on a line domain, denoted by $\Omega_{t\ell}$, wherein the parameter $t\ell$ corresponds to the thin layer. Since this application involves a tangential force, the full raceway width is considered. The raceway half width is designated as L_{rw} and expressed as follow:

$$L_{rw} = \frac{R_{ext}^{\mathrm{MTM}} - R_{int}^{\mathrm{MTM}}}{2} = 2\,\mathrm{mm}.$$

The layer of oil resulting from the MM EHL computation, $\bar{\ell}_{oil}$, is situated between $Y_0 = 0$ and $Y_{out} = 3$. By employing the principle of symmetry, the range may be extended to encompass both negative and positive values of Y_{out}, -3 and 3, respectively. In regions beyond this zone, $\bar{\ell}_{oil}$ is extrapolated using a second-order polynomial until reaching the value of $H_{oil}^{ini}/2$ (see equation (4.12)), as illustrated in figure 4.7 which delineates three distinct zones:

- zone (a): The value of $\bar{\ell}_{oil}$ is obtained from the resolution of the EHL contact through the use of the MM solver and takes the value of $H_{oil}^{outlet}/2$;
- zone (b): The value of $\bar{\ell}_{oil}$ is extrapolated using a second-order polynomial until it reaches the value of $H_{oil}^{ini}/2$;
- Zone (c): The value of $\bar{\ell}_{oil}$ is set to $H_{oil}^{ini}/2$.

A configuration of this kind has been employed by Jacod et al. [77] in the resolution of the thin layer equation.

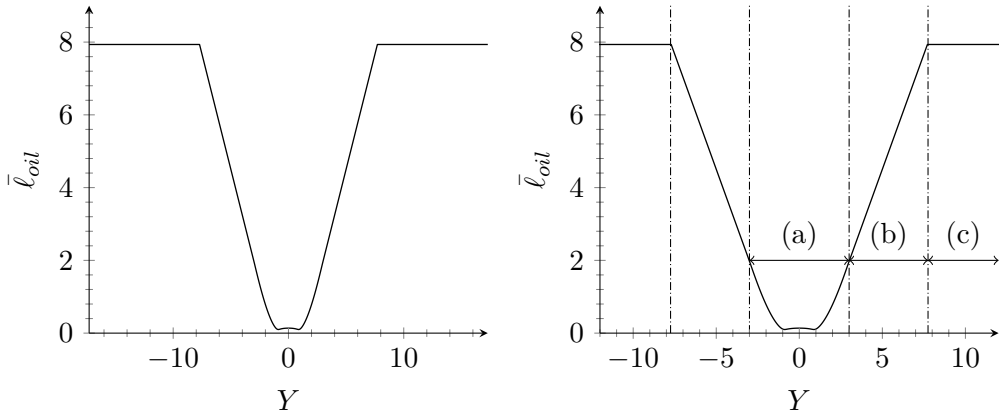

(a) Initial thin layer on the disc (b) Different zones enabling to build $\bar{\ell}_{oil}$

Figure 4.7: Details of the initial thin layer on the disc for the case where $u_m = 65\,\text{mm} \cdot \text{s}^{-1}$ and $m_{oil} = 10\,\text{mg}$

Results In order to obtain $\bar{\ell}_{oil}\,(T = 0)$ on the disc, the fully flooded results for both cases, namely $u_m = 65\,\text{mm} \cdot \text{s}^{-1}$ and $u_m = 100\,\text{mm} \cdot \text{s}^{-1}$, are employed. Figure 4.8 illustrates the behaviour of the dimensionless oil layer adhering to the disc, $\bar{\ell}_{oil}$, for both entrainment velocities. Figure 4.8(a) presents the initial layer profile, as well as those observed after one and 10^4 revolutions, respectively. It can be observed that following one revolution,

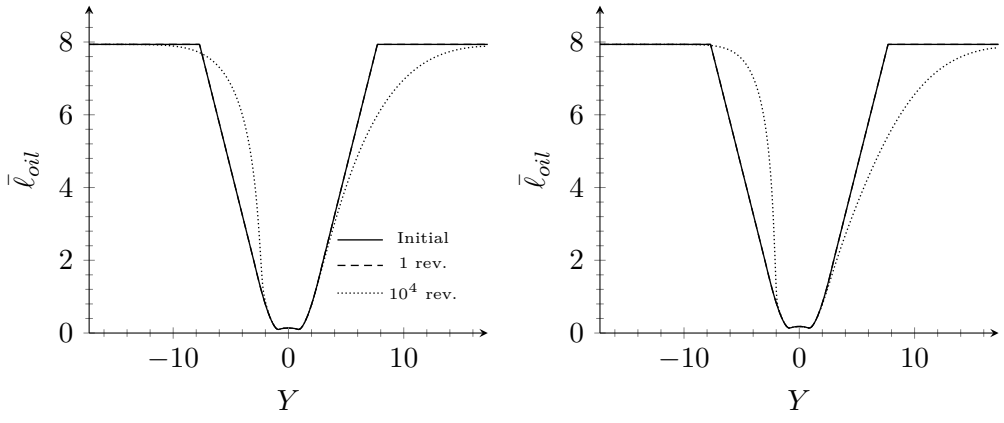

(a) $u_m = 65\,\text{mm} \cdot \text{s}^{-1}$ (b) $u_m = 100\,\text{mm} \cdot \text{s}^{-1}$

Figure 4.8: Thin layer evolution on the disc at the initiation of the computation, after one revolution and after 10^4 revolutions

the layer profile exhibited minimal change, with a relative difference of 0.42 % in comparison to the slope at $T = 0$. This suggests that centrifugal force, gravity and surface tension can be considered negligible after one revolution. The profile after 10^4 revolutions has been included as an example to illustrate how the layer evolves. However, this profile is only applicable in the absence of any obstacles on the track, which is not the case here since the layer profile meets the ball at each revolution. Exactly the same behaviour is reproduced at $u_m = 100\,\mathrm{mm} \cdot \mathrm{s}^{-1}$ (figure 4.8(b)).

On the ball

Subsequently, the evolution of the oil layer on the ball is examined. The numerical procedure that enables the computation is then described in detail, and the resulting data are presented.

Numerical procedure The procedure is analogous on the ball; the dimensionless end time is

$$T_{end}^{ball} = \frac{2\pi R_{ball}^{\mathrm{MTM}}}{u_{ball}} \cdot \frac{u_m}{a}$$

with

$$u_{ball} = u_m \left(1 - \frac{\mathrm{SRR}}{2}\right).$$

In assuming that the axis of rotation of the ball is parallel to the ground, it can be seen that both gravity and centrifugal force act in the same direction such as

$$f_z = g\rho_0 \cos\left(\omega_{ball}\frac{a}{u_m}T\right) + \rho_0 R_{ball}^{\mathrm{MTM}}\omega_{ball}^2$$

with $\omega_{ball} = u_{ball}/R_{ball}^{\mathrm{MTM}}$ the angular velocity of the ball. This application is comparable to that presented by Gershuni et al. [58], wherein both the centrifugal force and gravity are in the same direction. In the absence of action in the tangential direction, with the exception of surface tension, which only acts when the oil layer is not constant, a domain length of $\omega_{t\ell} \in [-10; 10]$ is imposed. The initial values of $\bar{\ell}_{oil}$ are then set in the same manner as for the disc, but on a smaller domain.

Results Similarly, the progression of the oil layer $\bar{\ell}_{oil}$ emanating from the fully flooded result and adhering to the ball is illustrated in figure 4.9. Figure 4.9(a) depicts the initial layer profile with a velocity of $u_m = 65\,\mathrm{mm} \cdot \mathrm{s}^{-1}$, as well as the layer profile after one revolution. The discrepancy between

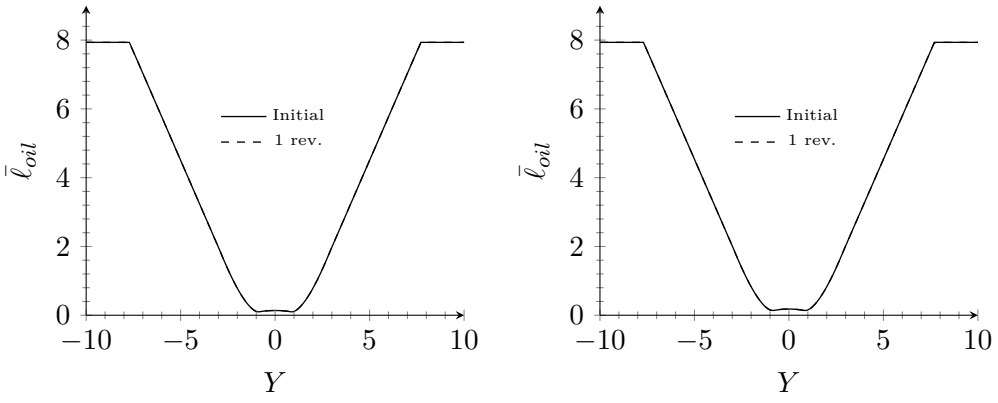

(a) $u_m = 65\,\mathrm{mm} \cdot \mathrm{s}^{-1}$ (b) $u_m = 100\,\mathrm{mm} \cdot \mathrm{s}^{-1}$

Figure 4.9: Thin layer evolution on the ball at the initiation of the computation and after one revolution

the two curves after one revolution is 0.2 %. This suggests that the effects of centrifugal force, gravity and surface tension are negligible after one revolution. The identical behaviour is replicated for the case of $u_m = 100\,\mathrm{mm} \cdot \mathrm{s}^{-1}$. In this approach, the curvature of the ball has been neglected $\left(10a/R_{ball}^{\mathrm{MTM}} \approx 0.1\right)$. Appendix A employs a thin layer equation in curvilinear coordinates to account for the curvature of the ball, following the methodology established by van Zoelen [127] in 2009. Both methods yield comparable outcomes, suggesting that the curvature of the ball can be reasonably neglected in this context.

Conclusion

The dimensionless thin layer equation (4.14) has been solved for two applications. The primary case study concerns the layer of oil that adheres to the disc. The disc is subjected to a combination of forces, including centrifugal force in the tangential direction and gravity in the thickness plus surface tension. It has been demonstrated that minimal observable phenomena occur during a single revolution. This can be explained by the high viscosity of the oil, which results in significant resistance to deformation. Additionally, as stated by van Zoelen et al. [129], the term including the surface tension coefficient σ_f is of an order of magnitude smaller than other terms, including the density. Consequently, van Zoelen et al. [129] neglected this term. The conclusion regarding the absence of track replenishment is in accordance with the findings of Jacod et al. [77] and Gershuni et al. [58], who also solved the thin layer equation for different operating conditions. The same observation

is applicable to the study on the ball.

Hypothesis 4. The layer of oil emanating from the fully flooded computation has been the sole focus of analysis. In reality, this represents the maximum thickness of oil that can be expected during the LoL process. It stands to reason that the greater the oil thickness, the more pronounced the deformations. Conversely, the thinner the oil, the less significant the deformations. Consequently, the assumption can be made that in the absence of track replenishment during this phase, the subsequent cases involving overrollings will remain unaffected. ¶

4.3.4 Multiple overrollings on ball and disc

The preceding section demonstrated that between two overrollings, the oil profile in the region outside the contact area remains unaltered. Therefore, the oil profile exiting the contact area at overrolling n re-enters at overrolling $n+1$ with the same shape. In accordance with Querlioz [112], an overrolling of the system can be considered to be equivalent to an overrolling of the longest specimen on the test rig. In line with Damiens [37] explanations, the ratio between the number of overrolling of the disc n_1 and the number of overrolling of the ball n_2 in the same time lap can be defined as follows:

$$\frac{n_2}{n_1} = \frac{R_{mid}^{disc}\left(1+\frac{\mathrm{SRR}}{2}\right)}{R_{ball}^{\mathrm{MTM}}\left(1-\frac{\mathrm{SRR}}{2}\right)} = 2.16, \tag{4.16}$$

for this case study.

In the case of Damiens [37], the scenario in which $n_2/n_1 = 2$ with $\gamma = 3$ results in a relative gap of 9 % in the film thickness decay in comparison to the reference scenario of $n_2/n_1 = 1$. This analysis is purely numerical and was conducted with the application of equation (4.4). According to Querlioz [112], the corresponding values of M, L, and γ are presented in the printed table 4.5.

Table 4.5: Dimensionless values given by Querlioz [112] for the selected applications

Speed [mm · s^{-1}]	M	L	γ
65	52.74	12.93	2.81
100	38.18	14.40	2.76

Therefore, when combining the successful operations of Querlioz [112] and Damiens [37], the relative discrepancy in the current case study, with the reference $n_2/n_1 = 1$, should be in the range of approximately 9 %.

Hypothesis 5. As the objective is to represent the qualitative decay in film thickness, it is assumed that both oil layers re-enter the contact area simultaneously. ¶

Then, hypothesis 5 enables the use of the recursive relation established by Damiens [37]

$$H_{oil}^{inlet}\left(\text{of overrolling } n\right) = H_{oil}^{outlet}\left(\text{of overrolling } n-1\right). \tag{4.17}$$

4.3.5 Numerical adaptation

The initial contact, designated as $n = 1$, has been calculated using the EHL MM solver in a fully flooded configuration, as previously outlined. Subsequently, the following overrolling can be computed using relation (4.17) recursively. However, starting from the second overrolling, all subsequent overrollings are starved. Furthermore, given that the initial contact was conducted in fully flooded conditions, it becomes evident that modifications are necessary for the starved MM method developed in chapter 3. In this scenario, both the inlet frontier Σ^{inlet} and the outlet frontier Σ^{outlet} are not connected to each other. This is due to the fact that the value of $H_{oil}^{inlet}(Y)$ is always greater than the minimum value of a slice of H in the transverse direction (i.e. the Y-direction). Subsequently, the free frontier, denoted by Σ^{free}, is no longer present, and the inlet and outlet frontiers, are linked to Ω_L. The domain decomposition is illustrated in figure 4.10(a). The associated frontier boundary conditions with regard to mesh motion are illustrated in figure 4.10(b). In this context, two Ω_T zones can be identified. At the inlet of the first Ω_T zone, $H_{oil}^{inlet}(n)$ is equal to $H_{oil}^{outlet}(n-1)$. In the outlet zone Ω_T next to the pressurised zone Ω_P at Σ^{outlet}, H_{oil} is equal to H. Consequently, the system (3.24) must be solved without the equation related to Σ^{free}. The computational domain Ω_P has been selected such that $X_{in} = -2.5$, $X_{out} = 1.5$ and $Y_{out} = 3$. As a result of this adaptation of the original starved MM method, which was presented in chapter 3, a strategy can be established to compute multiple overrollings with the aim of mimicking the experimental works.

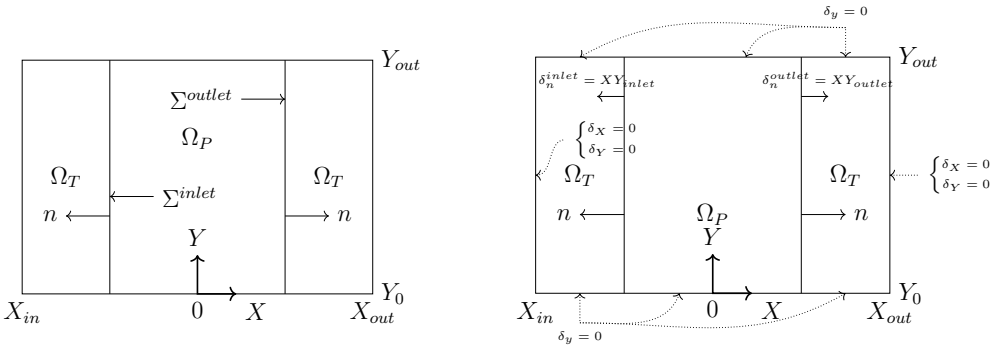

(a) Domains decomposition (b) MM boundary condition

Figure 4.10: MM domains in condition of overrolling starting from fully flooded

4.3.6 Computation of multiple overrollings

Now that all preliminary steps have been discussed, it is necessary to develop a strategy that enables the computation of hundreds of overrollings. In their respective works, Chevalier et al. [30] and Damiens [37] both assumed a succession of stationary computations. The MM model was initially constructed for the purpose of performing transient computations. For this reason, an illustrative example (utilising disparate values from the case study) of an EHL contact undergoing multiple overrollings has been conducted and is presented in appendix B. In conclusion, a transient computation is performed using a periodic boundary condition regarding H_{oil}, such that $H_{oil}(X_{in}, Y, T) = H_{oil}(X_{out}, Y, T)$. The film thickness decay in such a scenario exhibits a decrementing stair-steps profile where the horizontal segments align with a stationary computation of the corresponding overrolling. Consequently, an overrolling process can be classified as a quasi-stationary rather than a transient issue. This signifies that to compute n overrollings, it is necessary to perform n stationary computations utilising the relation defined by (4.17). Hence, the computational time is reduced through the implementation of numerous stationary computations in lieu of costly transient computations, thereby facilitating the consideration of multiple models.

4.3.7 Isothermal and thermal models

The requisite equations for solving either a starved EHL or a starved Thermal ElastoHydrodynamic Lubrication (TEHL) application were elucidated

in detail in chapters 2 and 3. The following section details the methodology employed in both applications. Two models have therefore been proposed:

- model #1, which solves the problem of the starved MM EHL application by means of the Dowson and Higginson [45] density-pressure law (2.10) and the Roelands [118] viscosity-pressure law (2.14);
- model #2, which solves the problem of the starved MM TEHL application by means of the Williams, Landel, and Ferry [137]/Yasutomi et al. [141] density-pressure law (2.15) and Tait equation of state (2.11);

The following paragraphs describe these models in detail.

Model #1: isothermal + simplified rheology

Model #1 addresses the issue of starved MM EHL by employing the Dowson and Higginson [45] density-pressure law (2.10) and the Roelands [118] visocsity-pressure law (2.14). The oil properties are outlined in table 4.3. The strategy presented previously has been used to compute hundreds of overrollings.

Model #2: thermal + advanced rheology

Model #2 addresses the issue of starved MM TEHL using the viscosity-pressure-temperature law proposed by Williams, Landel, and Ferry [137] and Yasutomi et al. [141] (2.15) and the Tait equation of state (2.11). As outlined in chapter 1, these laws facilitate a more accurate assessment of both viscosity and density in relation to pressure and temperature. Furthermore, as Querlioz [112] conducted experimental work at a temperature of $\mathbb{T}_0 = 40\,^{\circ}\mathrm{C}$, this temperature is employed for the normalisation of the dimensionless energy equation (2.50).

Viscosity The required parameters for utilisation of the WLF viscosity-pressure-temperature law are presented in table 4.6, as outlined by Bair et al. [8]. Furthermore, figure 4.11 illustrates the viscosity as a function of pressure (equation (2.15)) using the enhanced version from Bair et al. [9], based on the data presented in table 4.6. Figure 4.11 also presents the Roelands [118] viscosity-pressure law (2.14) for comparison purposes. The relative error between the two at the Hertzian pressure ($p_H = 0.89\,\mathrm{GPa}$) and $\mathbb{T} = 40\,^{\circ}\mathrm{C}$ with respect to the WLF law is $-85.11\,\%$.

Table 4.6: Values of the parameters of the Williams, Landel, and Ferry [137]/Yasutomi et al. [141] viscosity-pressure-temperature law from Bair et al. [8]

Variable	Value
η_g	$10^{12}\,\mathrm{Pa}\cdot\mathrm{s}$
$\mathbb{T}_{g0}$	$-74.42\,^\circ\mathrm{C}$
A_1	$281.4\,\mathrm{K}$
A_2	$0.2280\,\mathrm{GPa}^{-1}$
B_1	$8.75\,\mathrm{GPa}^{-1}$
B_2	-0.3490
C_1	15.86
C_2	$37.25\,\mathrm{K}$

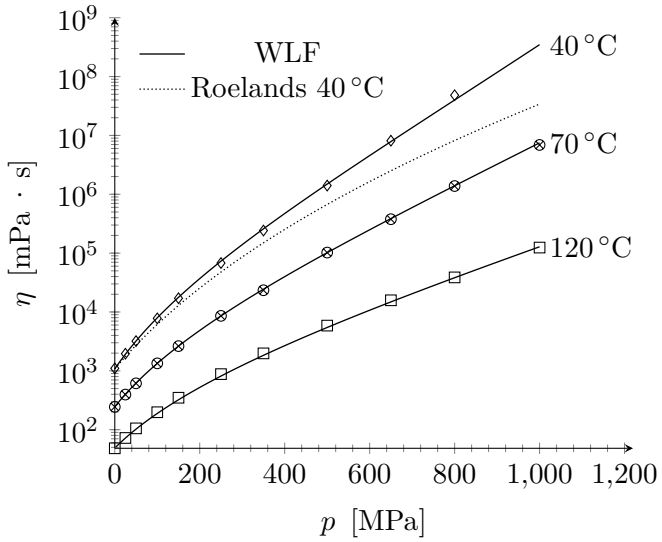

Figure 4.11: Viscosity as a function of the pressure and temperature

Density Table 4.7 presents the values of the parameters required to utilise the Tait equation of state (2.11). These values have been sourced from Bair [7] and are provided at the reference temperature $\mathbb{T}_R = 70\,^\circ\mathrm{C}$.

Table 4.7: Coefficient to use Tait equation of state from Bair [7] at $\mathbb{T}_R = 70\,^{\circ}\mathrm{C}$

Variable	Value
K_0'	11.74
K_∞	$-1.051\,\mathrm{GPa}$
$\dot{K}_0$	$568.5\,\mathrm{GPa}\cdot\mathrm{K}$
a_v	$8\times10^{-4}\,^{\circ}\mathrm{C}^{-1}$

Moreover, according to Bair [7]

$$K_\infty e^{-\beta_K \mathbb{T}} = K_\infty + \frac{\dot{K}_0}{\mathbb{T}}. \tag{4.18}$$

The reference density ρ_R is not mentioned in the source text [7]. Esmaeili et al. [54] in 2020 presented the behaviour of the density as a function of the temperature of the PAO100 at ambient pressure. A linear interpolation between the measured data by Esmaeili et al. [54] allows the calculation of $\rho_R = 821.95\,\mathrm{kg}\cdot\mathrm{m}^{-3}$ at $\mathbb{T}_R = 70\,^{\circ}\mathrm{C}$ and ambient pressure.

Thermal properties In order to employ the dimensionless energy equation (2.50), the thermal properties of the material are still a requisite factor. The thermal properties of PAO100, which have been obtained from Larsson et al. [87], are referenced in table 4.8. For the purposes of this investigation, the thermal properties of classical steel have been assumed for both solids.

Table 4.8: Thermal properties of both the oil and the solids

Variable	Value	Note
k_{oil}	$0.154\,\mathrm{W}\cdot\mathrm{K}^{-1}\cdot\mathrm{m}^{-1}$	
$\rho C_{p_{oil}}$	$1.77\times10^{6}\,\mathrm{J}\cdot\mathrm{K}^{-1}\cdot\mathrm{m}^{-3}$	At $21.85\,^{\circ}\mathrm{C}$
k_s	$45\,\mathrm{W}\cdot\mathrm{K}^{-1}\cdot\mathrm{m}^{-1}$	
C_{p_s}	$466\,\mathrm{J}\cdot\mathrm{K}^{-1}\cdot\mathrm{kg}^{-1}$	
ρ_s	$7800\,\mathrm{kg}\cdot\mathrm{m}^{-3}$	

Discussion on the boundary conditions The fluid and the solid initially enter the contact area at the temperature of the experiment, designated as $\mathbb{T}_0 = \mathbb{T} = 40\,^{\circ}\mathrm{C}$, which is equivalent to $\overline{\mathbb{T}} = 1$. Nevertheless, at the outlet of

this initial contact, both the solids and the fluid have undergone a heating process, resulting in temperatures that exceed $\mathbb{T}_0$. The precise determination of the temperature of the bodies re-entering the contact necessitates an investigation into the cooling of all bodies undergoing forced convection due to the motion of the solids and diffusion. Achieving this outcome is not a straightforward process. For that reason, two scenarios/cases are identified within the scope of this work. The objective of this approach is to constrain the problem by identifying the most favourable and least favourable scenarios:

- case #A, the most favourable: the bodies are fully cooled and re-enter the contact at $\mathbb{T}_0 = \mathbb{T} = 40\,^{\circ}\mathrm{C}$ which is equivalent to $\overline{\mathbb{T}} = 1$;
- case #B, the least favourable: the bodies are not cooled down at all and re-enter the contact at exactly the same temperature, which can be described as a periodic boundary condition.

The two cases are detailed in the following paragraphs..

Case #A In this configuration, the Dirichlet boundary conditions are precisely those presented in section §2.7 on figure 2.10. In conclusion, all the faces entering the contact area, that is to say those moving in the X-direction, are fixed at $\overline{\mathbb{T}} = 1$. Furthermore, the top and bottom surfaces are also fixed at $\overline{\mathbb{T}} = 1$, as illustrated in figure 2.10. A Neumann boundary condition, corresponding to a null flux, is imposed on the remaining surfaces.

Case #B In this configuration, a periodic Dirichlet boundary condition is imposed on the faces that enter and exit the contact area. This boundary condition is analogous to the one governing the oil layer, as described in relation (4.17), and leads to

$$\overline{\mathbb{T}}\left(X_{in}, Y, Z, \text{of overrolling } n\right) = \overline{\mathbb{T}}\left(X_{out}, Y, Z, \text{of overrolling } n-1\right). \quad (4.19)$$

This relationship can be expressed as the temperature field entering the contact area at overrolling n equalling the temperature field leaving the contact area at overrolling $n-1$ (referred to as $\overline{\mathbb{T}}^{out}$). Figure 4.12 presents a graphical representation of relation (4.19), which also demonstrates that a Neumann boundary condition is imposed on the top and bottom surfaces, in contrast to the conditions observed in case #A.

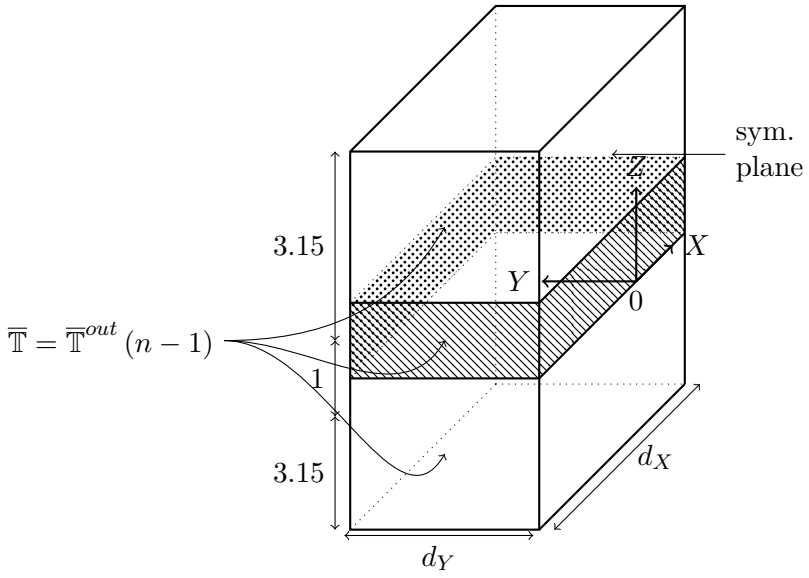

Figure 4.12: Boundary condition of the model #2 case #B related to dimensionless energy equation

4.3.8 Conclusion

This section presented the numerical strategy that enables the reproduction of the case study. Firstly, the initial condition of the experimental work has been discussed, resulting in the formulation of a preliminary hypothesis (H1) regarding the initial oil quantity h_{oil}^{ini} upstream of the EHL contact. This hypothesis permitted the initial contact, designated as $n = 1$, to be considered as fully flooded. Subsequently, the EHL MM solver was modified to enable the execution of a fully flooded computation. As a result of this adaptation, the oil layer profile downstream of the contact was obtained, and an investigation into track replenishment was made possible. In order to achieve this, the thin layer equation was introduced with the corresponding boundary condition and was made dimensionless based on the normalisation of an EHL contact, as outlined in section §2.6. A second hypothesis has been put forth regarding the distribution of oil outside the contact area (see H2). This hypothesis permitted the examination of the behaviour of the thin layer outside the contact area on both the disc and the ball. The computation of the thin layer equation on both solids demonstrated that track replenishment does not occur for the selected applications of this work after the fully flooded contact (i.e. the first contact $n = 1$). Furthermore, hypothesis 4 posits that if nothing occurred after the first overrolling, then nothing will occur on subsequent overrollings. Consequently, a strategy for numerically

computing multiple overrollings can be developed.

Subsequently, a debate was held concerning the definition of an overrolling. This led to the formulation of the hypothesis (see H5) that both oil layers re-enter the contact at the same time. This hypothesis has been proposed on the basis of a theoretical study of the literature. As a result of this initial phase, the starved MM EHL solver has been modified to account for the fact that the initial contact is fully flooded. Subsequently, it has been demonstrated that an overrolling problem is quasi-stationary in nature, rather than transient. In conclusion, two models have been presented. The first model addresses the isothermal starved EHL contact, while the second model addresses the starved TEHL problem. During the presentation of model #2, two distinct cases were identified with regard to the temperature of the bodies entering the contact area. In case #A, it is assumed that the bodies are completely cooled between two overrollings and then re-enter the contact area at the ambient temperature $\mathbb{T}_0$. In contrast, case #B assumes that there is no cooling and that the bodies re-enter the contact area with the same temperature field as when they initially left the contact area. The following two sections present the numerical reproduction of the experimental applications performed by Querlioz [112], which have led to a deeper understanding of the phenomena occurring in a LoL process.

4.4 Unstable friction coefficient

The objective of this section is to investigate the case study, which revealed an unstable friction coefficient during a LoL application (see figure 4.2). The experimental application was conducted at a velocity of $u_m = 100\,\mathrm{mm} \cdot \mathrm{s}^{-1}$.

4.4.1 Exploitation of model #1

Results

The model presented earlier, designated as model #1, has been utilised to undertake 600 overrollings. At each overrolling, the dimensionless central film thickness H_c has been assessed. Figure 4.13 illustrates the variation in the dimensionless central film thickness as a function of the number of overrollings, employing a range of methodologies, which are enumerated and described subsequently.

The primary outcome, illustrated by the solid line, depicts the numerical dimensionless central film thickness utilising model #1 across the range

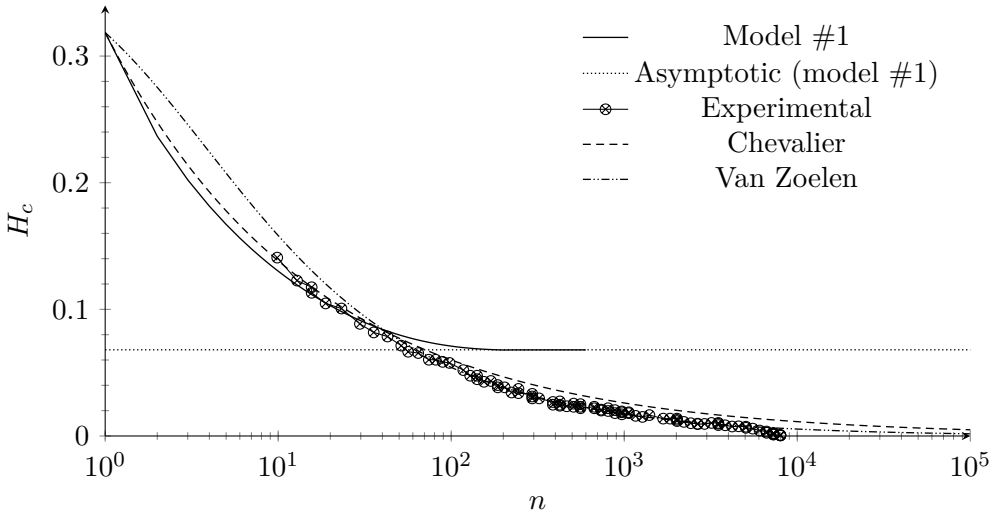

Figure 4.13: Dimensionless central film thickness as a function of the number of overrollings for model #1 with $u_m = 100\,\mathrm{mm} \cdot \mathrm{s}^{-1}$

of overrollings. The second result, represented by a densely dotted line, corresponds to a specific value of the dimensionless central film thickness obtained through the application of model #1. Given that the preceding result indicated that model #1 had reached a stable state, a single stationary computation utilising a periodic boundary condition, such as

$$H_{oil}\left(X_{in}, Y\right) = H_{oil}\left(X_{out}, Y\right), \tag{4.20}$$

has been performed in this instance. The third result, indicated by the marker $\otimes$, represents the experimental dimensionless central film thickness converted from the friction coefficient in accordance with the strategy proposed by Querlioz [112], as outlined in section §4.2.2. The fourth and fifth results represent the dimensionless central film thickness using the two analytical film thickness decay formulas introduced in section §4.1.2. The first result, represented by a densely dashed line, has been obtained using equation (4.4), which describes the film thickness decay from Chevalier, with the parameter γ as defined in table 4.5. The second result, represented by a densely dash-dotdotted line, has been obtained using equation (4.7), which describes the film thickness decay from van Zoelen.

Discussion

As illustrated in figure 4.13, model #1 exhibits two distinct phases. The initial phase is characterised by a reduction in film thickness, which then

reaches a plateau, signifying a state of equilibrium and the stabilisation of the film thickness decay. This behaviour demonstrates the existence of an equilibrium state where the inlet total oil thickness layer profile is identical to the profile at the outlet. Based on the results obtained from model #1, it can be concluded that the EHL contact in a multiple overrolling condition should be capable of functioning for extended periods. Furthermore, the asymptotic value reached by model #1, which was obtained through a single computation utilising periodic boundary conditions, correlates with the value obtained from a computation involving 600 overrollings. However, it is notable that the experimental work did not reach a steady state, as indicated by the third curve presented in figure 4.13.

Figure 4.13 illustrates that the declining phase of model #1 is analogous to that observed in the experimental data. However, after approximately 50 overrollings, a discrepancy emerges between the experimental and numerical curves. Furthermore, the decreasing phase of model #1 aligns qualitatively with both film thickness analytical formulas. After approximately 50 overrollings, a divergence is observed between the numerical film thickness decay and the analytical formulas. Finally, as illustrated in figure 4.13, both film thickness decays demonstrate a superior qualitative prediction in comparison to the experimental curve.

Conclusion

The utilisation of model #1 for the case study, which demonstrated an unstable film thickness decay (or friction coefficient), did not permit the qualitative reproduction of the experimental result. Indeed, as per the predictions of model #1, the film thickness decay reached a steady state. Furthermore, the steady-state value can be obtained via a single computation utilising model #1 with periodic boundary conditions regarding the mass flow rate. Subsequently, the experimental and analytical film thickness decays have been plotted alongside the numerical results. The analytical formulas exhibited a superior qualitative alignment with the experimental curve, particularly the van Zoelen equation (4.7). The analytical formulas presented are founded upon the principles of resistance to side flow or side flow fluxes, as observed in the models proposed by Chevalier and van Zoelen, respectively. Therefore, the attainment of a vanishing film thickness decay signifies the absence of side flows. Consequently, the occurrence of a phenomenon capable of generating side flows is postulated to take place during this overrolling process. In particular, a thermal contribution is anticipated due to the sliding condition SRR = 1.9 %.

4.4.2 Exploitation of model #2

The model presented earlier, designated as model #2, was employed to perform 600 overrollings for case #A (complete cooling) and 800 overrollings for case #B (no cooling). The ensuing paragraphs will present, analyse, and discuss the results obtained from cases #A and #B.

Results

Figure 4.14 illustrates the dimensionless central film thickness decay as a function of the number of overrollings, taking into account the thermal dependency. The initial result, represented by the solid line, pertains to case #A, which has undergone 600 overrollings. The subsequent result, illustrated by the densely dotted line, concerns case #B, which has undergone 800 overrollings. As with the preceding figure, the curve marked with ⊗ is associated with the experimental film thickness, which has been converted from the friction coefficient.

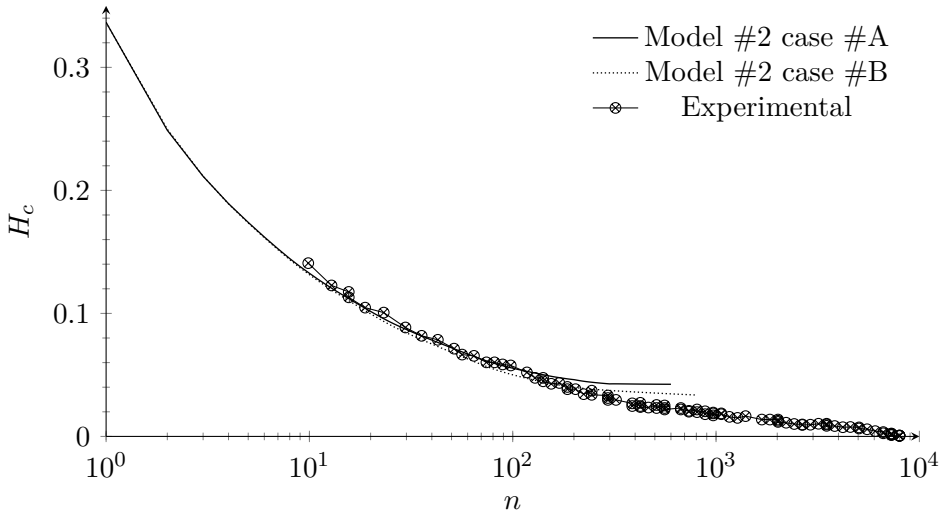

Figure 4.14: Dimensionless central film thickness as a function of the number of overrollings for model #2 with $u_m = 100\,\mathrm{mm} \cdot \mathrm{s}^{-1}$

Discussion

Given that case #A and case #B represent the most favourable and unfavourable scenarios, respectively, it is anticipated that the experimental film thickness decay will fall between the two numerical film thickness decays. However, the results do not align with the anticipated outcomes. Similarly to model #1, case #A reaches a state of stabilisation with regard to the decay

of the film thickness. Case #B demonstrates that the decay rate diminishes significantly with each overrolling. At the commencement of the overrolling process, the two curves exhibit a high degree of proximity. A gap begins to emerge after 10 overrollings and increases with time. Qualitative observation indicates that both curves align closely with the experimental data until approximately 100 overrollings, offering a superior fit to model #1. Subsequently, from this point the rate of decay of the dimensionless film thickness from model #2, case #A and case #B begins to diminish, resulting in a gap with the experimental data.

The attainment of a steady state in case #A can be attributed, in part, to the stabilisation of the maximum temperature within the contact area. Figure 4.15 illustrates the maximum temperature attained during the overrollings for both cases. Figure 4.15 indicates that case #A reached an asymptotic value after 400 overrollings, with a maximum temperature of $\mathbb{T} = 42.51\,^{\circ}\mathrm{C}$. Conversely, the figure demonstrates that the maximum temperature of case #B increases rapidly after approximately 300 overrollings. This behaviour may be a potential explanation for the ongoing decrease in film thickness observed in case #B.

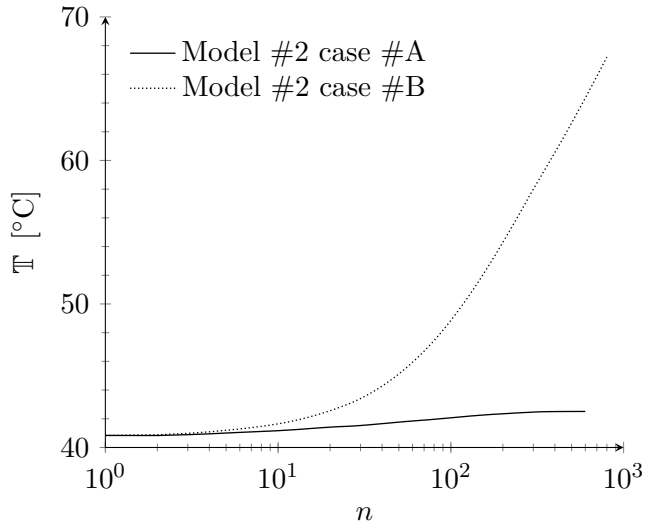

Figure 4.15: Maximum temperature growth through overrollings

In order to gain a deeper insight into the thermal behaviour, the temperature profile along the X-direction is evaluated at $Z = 0.5$, which represents the midpoint of the film thickness. Figure 4.16 illustrates that the temperature in case #A exhibited a gradual increase from the fixed temperature $\mathbb{T}_0$

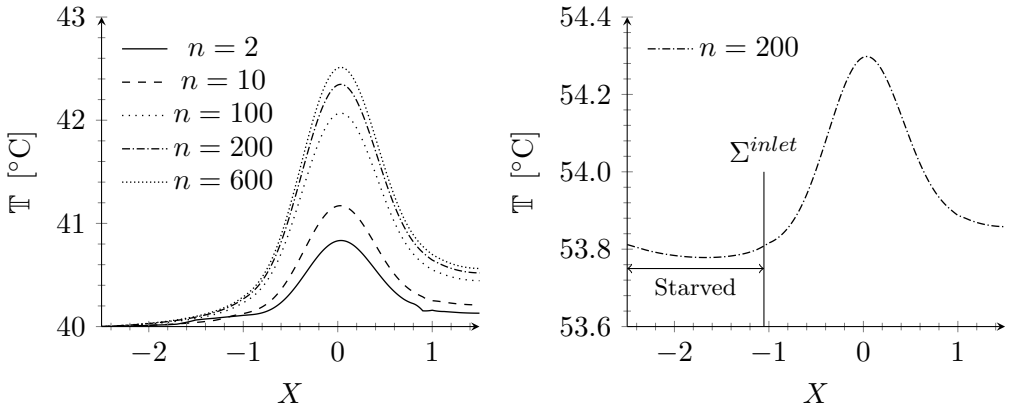

(a) Case #A

(b) Case #B

Figure 4.16: Evolution of the temperature at $Z = 0.5$ i.e. $H/2$ in the X-direction

until reaching the Hertzian area $X = -1$. Subsequently, the rate of increase in temperature becomes more pronounced until it reaches its maximum value, after which it declines. The same profile is obtained through overrollings with higher values of temperature. Figure 4.16(b) displays the temperature profile associated with case #B at $n = 200$. The profile demonstrates a decline in temperature within the starved zone from X_{in} until the vertical line inscribed within figure 4.16(b), which delineates the position of Σ^{inlet}. This indicates that the application modelled in case #B is influenced by the size of the computational domain. Specifically, the longer the domain upstream of the inlet meniscus, the larger the cooling effect, and vice versa. In accordance with the JFO theory, within the starved zone, the pressure is equal to zero, indicating the absence of a heat source (see equation (2.38)). Consequently, only the diffusive and convective terms remain in the dimensionless energy equation. In the absence of a Poiseuille flux within the starved zone, the heater zone is confined to the vicinity of the Hertzian area. Consequently, there is a state of equilibrium between the temperature in the immediate vicinity of the fluid and the temperature at a distance from the fluid, in both solid materials. Figure 4.16(b) illustrates that in the given situation, this equilibrium generates a cooling effect in the starved zone. As a result, since a cooling effect occurred in a zone in close proximity to the contact, it follows that a cooling effect must occur in a zone distant from the contact on both the layer adhering to the disc and the layer adhering to the ball. This phenomenon may be attributed to forced convection. Thus, there is no thermal runaway in this particular case study.

Conclusion

Model #2, which run both case #A and case #B, was unable to reproduce the experimental observation from Querlioz [112] in a qualitative manner. Model #2 case #A, reached a steady state and exhibited a film thickness decay that was less pronounced than that observed in the experiment (i.e. H_c from model #2 case #A was greater than H_c from Querlioz [112]). Model #2 case #B yielded a film thickness decay wherein the rate of decay continue diminished at elevated instances of overrolling. Nevertheless, the decay persists. Similarly to case #A, case #B also demonstrated a tendency to underestimate the film thickness decay in comparison with the experimental data, although it exhibited a more favourable performance than that of model #1. The reduction in film thickness observed in case #A can be attributed to the stabilisation of the temperature within the contact. With regard to case #B, the maximum temperature increased with each additional overrolling. Therefore, an analysis of the temperature field distribution was conducted. This analysis revealed the presence of cooling upstream of the inlet meniscus, i.e. in the starved zone, in front of the inlet meniscus, where the temperature decreased. This outcome indicates that the numerical application is contingent upon the domain size. Consequently, the results obtained from case #B should not be included in the analysis, with the exception of one particular instance. This finding indicates that a thermal runaway does not occur due to the presence of cooling, suggesting that cooling should have a significant impact. Therefore, cooling must be accounted for and modelled in the starved zone, as well as on the disc and ball far from the contact, where forced convection plays a role. Consequently, model #2 case #B is not used in the latter part of this study.

4.4.3 Conclusion

The objective of this section was to reproduce the experimental application, resulting in a sharp increase in the friction coefficient (or conversely, a sharp decrease in the film thickness). In order to achieve this objective, models #1 (isothermal) and #2 (thermal) were employed. Neither model #1 nor model #2 yielded the desired result, as they did not reproduce the experimental outcome in a qualitative manner. This may indicate the need for an additional ingredient in the numerical model in order to achieve qualitative reproduction of the results observed by Querlioz [112]. It is also possible that an unforeseen event occurred during the experimental procedure, such that the use of H1 was not viable. For instance, the oil distribution may not have been perfectly uniform, resulting in localised starvation at the initial

contact ($n = 1$). This could manifest as a localised defect in the oil supply, as discussed by Damiens [37] or Chevalier et al. [32].

4.5 Stable friction coefficient

The objective of this section is to investigate the case study, which revealed a stable friction coefficient during a LoL application (see figure 4.2). The experimental application was conducted at a velocity of $u_m = 65\,\text{mm} \cdot \text{s}^{-1}$.

4.5.1 Exploitation of model #1

Results

Similarly to the results presented in section §4.4.1, the model #1 has been subjected to 600 overrollings. Figure 4.17 illustrates the dimensionless central film thickness as a function of the number of overrollings, employing a variety of methodologies, which are elucidated subsequently. As previously, the solid line represents the result obtained by model #1. The densely dotted line indicates the value returned by model #1 with the periodic boundary condition (only one computation). The curve with markers ⊗ refers to the experimental dimensionless central film thickness converted from the friction coefficient in accordance with the strategy presented by Querlioz [112] in sec-

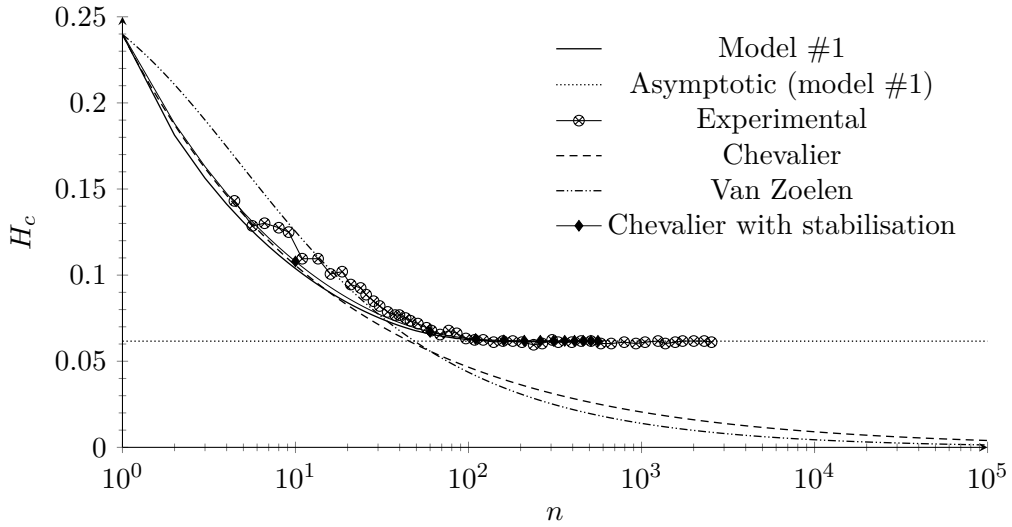

Figure 4.17: Dimensionless central film thickness as a function of the number of overrollings for model #1 with $u_m = 65\,\text{mm} \cdot \text{s}^{-1}$

tion §4.2.2. The dimensionless central film thickness using the two analytical film thickness decay formulas is presented with the fourth and fifth curves. Lastly, the formula from Chevalier [29] enabling the decay to stabilise has been printed with black filled diamond markers.

Discussion

Model #1 reached a steady state regarding the dimensionless film thickness decay, which stabilised in a manner analogous to that observed in model #1 during the previous application. This stabilisation has been superimposed upon the experimental result presented in figure 4.17, which demonstrates a satisfactory qualitative agreement.

Remark. The experimental dimensionless film thickness decay presented in figure 4.17 has been obtained using equation (4.11) and a specific value for τ_0. This allows for the discussion of the accuracy of the converted film thickness values. For this reason, a quantitative comparison with the numerical model is not provided. The objective was to reproduce the trend qualitatively and to gain an understanding of it.

In regard to the declining phase, the outcomes of model #1 and those of the experimental procedure demonstrate a notable correlation. However, the experimental curve exhibits a sawtooth profile during the initial ten overrollings. Damiens [37] also observed a similar sawtooth profile when investigating the impact of a different re-entering time regarding the oil layers through numerical analysis. As Damiens [37] noted, a sawtooth profile arises when both oil layers do not re-enter the contact area simultaneously. However, as the number of overrollings increases, as illustrated in the experimental curve in figure 4.17, this sawtooth profile is flattened, in accordance with the observations made by Damiens [37].

Analysis The following paragraphs present a comprehensive analysis of the data, integrating both qualitative and quantitative approaches.

Meniscus position In accordance with an analytical analysis conducted by Damiens [37], it was observed that as the inlet meniscus approaches the Hertzian area, the lateral side fluxes undergo a decline until they reach a null value. Figure 4.18 presents a series of graphs illustrating the position of the sub-frontiers, namely Σ^{inlet} and Σ^{outlet}. The initial row, from figure 4.18(a) to 4.18(d), illustrates the qualitative positioning of both sub-frontiers at varying overrollings. The introduction of two new variables, namely Σ_X^{inlet} and Σ_X^{outlet},

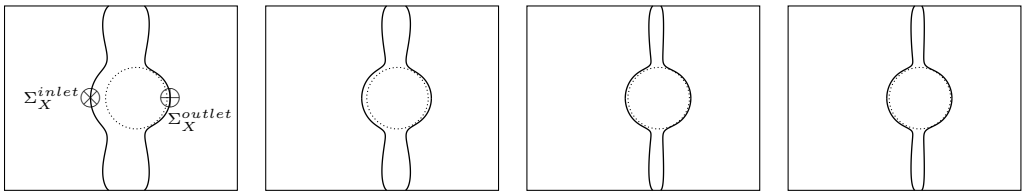

(a) $\Sigma\,(n=2)$ (b) $\Sigma\,(n=10)$ (c) $\Sigma\,(n=50)$ (d) $\Sigma\,(n=\infty)$

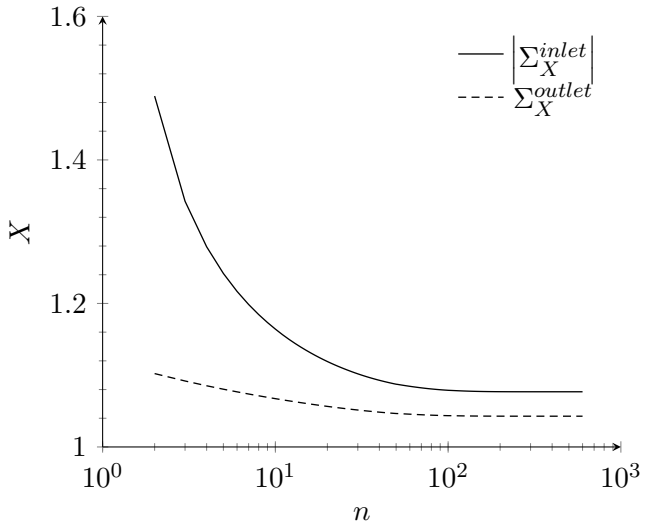

(e) X position at $Y=0$ of the frontiers Σ^{inlet} and Σ^{outlet}

Figure 4.18: Frontiers position (first raw) and Σ_X^{inlet} and Σ_X^{outlet} values at $Y=0$ through overrollings (second raw)

respectively representing the X-position at $Y=0$ for the inlet and outlet sub-frontiers, is presented in figure 4.18(a). Figure 4.18(e) presents the absolute X-position of both the inlet and outlet meniscus throughout the overrollings. It is evident that both X-positions reached a constant value. However, as illustrated in figure 4.18(e), the two values do not align with the dimensionless Hertzian half width. In this application, the absolute X-position of Σ_X^{inlet} is observed to approach 1.0769, while the X-position of Σ_X^{outlet} is seen to reach 1.0429. Consequently, the inlet meniscus is not aligned with the Hertzian area. According to Damiens [37], this indicates the presence of side flows.

Side flows The attainment of a zero film thickness decay indicates that the side flow fluxes in the Y-direction are insignificant in comparison to the flow in the X-direction. Figure 4.19(a) depicts the computed side flow at $Y=2.75$. The side flow is observed to be negligible, though not precisely

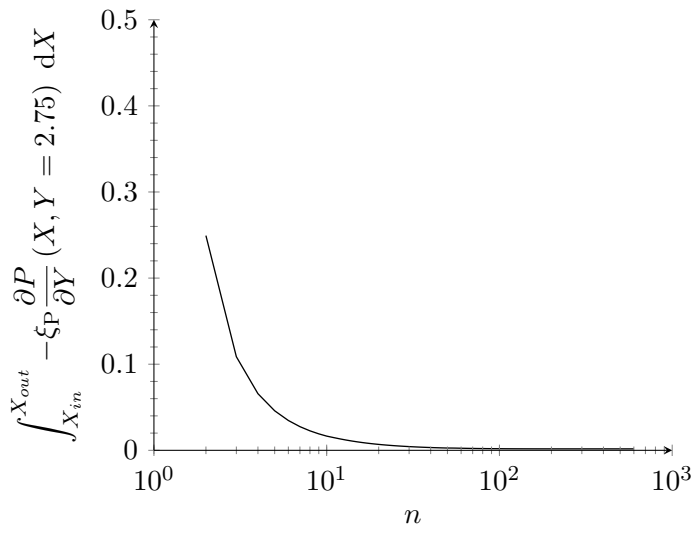

(a) Side flow fluxes at $Y = 2.75$

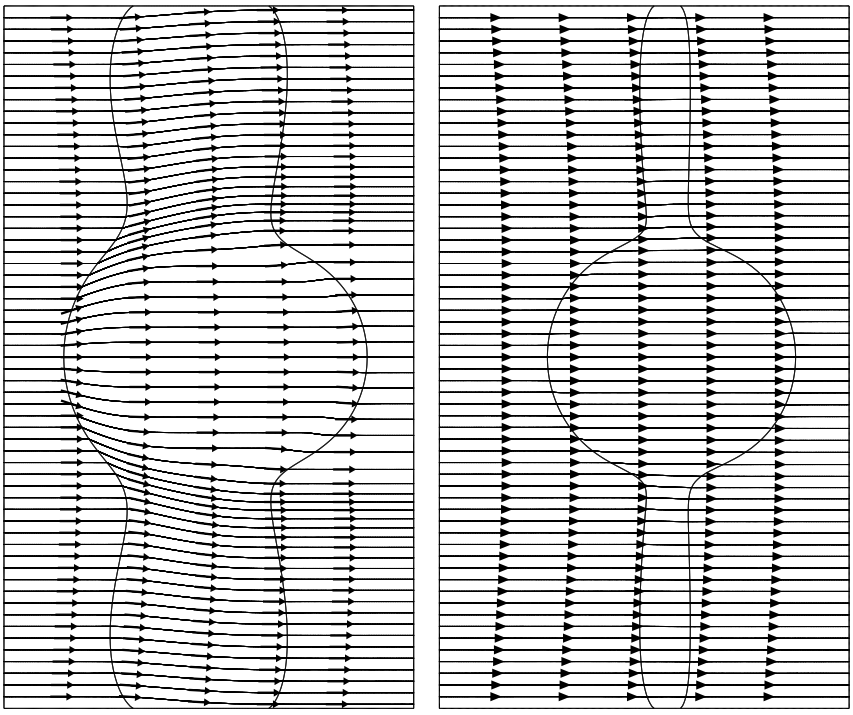

(b) Stream line at $n = 2$

(c) Stream line at $n = \infty$

Figure 4.19: Numerical evaluation of the transverse mass flow rate at $Y = 2.75$ and stream line of mass flow rate

zero, with a value of approximately 0.0017. It is evident that a residual pressure gradient in the Y-direction persists, thereby giving rise to a Poiseuille flux. This is the reason why there is still a very small film thickness decay through the overrolling. The difference in H_c between overrolling 599 and 600 is approximately 1.4×10^{-11}, which is negligible. Furthermore, both figures 4.19(b) and 4.19(c) illustrate the streamlines of the mass flow rate

$$\begin{cases} Q_{fx} = -\xi_{\mathrm{P}} \dfrac{\partial P}{\partial X} + \bar{\rho} H_{oil}, \\ Q_{fy} = -\xi_{\mathrm{P}} \dfrac{\partial P}{\partial Y}. \end{cases}$$

The utilisation of the stream line allows for the qualitative demonstration that the mass flow rate in the Y-direction is insignificant in comparison to that in the X-direction. Figure 4.19(c) demonstrates that the streamlines are qualitatively parallel, indicating that the mass flow rate in the X-direction is constant. Indeed, figure 4.19(b) illustrates a case where the streamlines are not parallel, indicating the presence of side flow fluxes, for example, around the inlet meniscus (both sub-frontiers are also printed). Subsequently, the majority of the oil flows in the X-direction. The relative difference between the mass flow rate at X_{in} and at X_{out} with respect with the mass flow rate at X_{in} is approximately $1.6 \times 10^{-9}\,\%$ for $n = \infty$ ($n = \infty$ represents the value obtained using one computation with the periodic boundary condition). Therefore, it can be concluded that the mass flow rate is nearly constant in the X-direction.

Figure 4.20 presents the mass flow rate along the X-direction evaluated at three points: at the inlet of the computational domain $(X_{in}, 0) = \bar{\rho}\,(0)\, H_{oil}^{inlet}$, at the centre of the contact $(0, 0) = \bar{\rho}\,(p_H)\, H_c$, and at the outlet of the computational domain $(X_{out}, 0) = \bar{\rho}\,(0)\, H_{oil}^{outlet}$. These coordinates represent the points where there is no Poiseuille flux for all values of n. Consequently, due to the disappearance of side flow fluxes, the three curves converge towards a single value, as illustrated in figure 4.20.

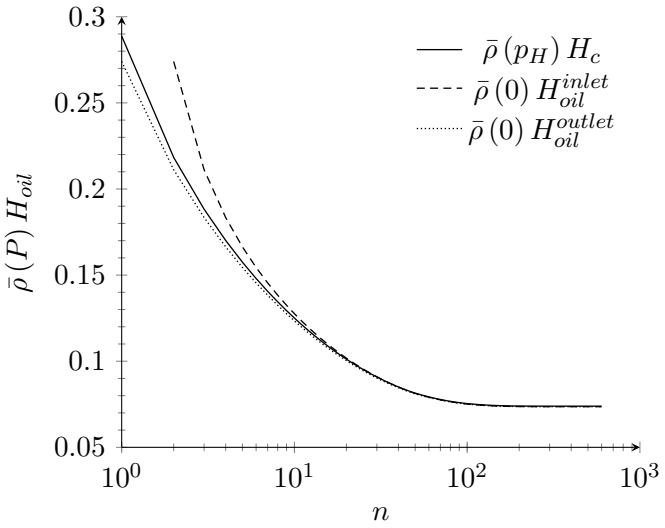

Figure 4.20: Evolution of the dimensionless mass flow rate at $(X_{in}, 0)$, $(0, 0)$ and $(X_{out}, 0)$ for all overrollings

Analytical formulas As illustrated in figure 4.17, the analytical models failed to predict the stabilisation of the film thickness, which occurred in both the experimental and numerical results. However, the extension enabling stabilisation proposed by Chevalier [29] (equation (4.5)) shows a good agreement in the decreasing phase with both the experimental and numerical results. In order to obtain analytically the stabilised film thickness decay using equation (4.5), it is necessary to know at which value the film thickness stabilises in order to determine dr (see equation (4.6)). Indeed, equation (4.5) does not predict a priori whether the decay stabilises or not.

Conclusion

Model #1 was found to be capable of reproducing the qualitative experimental results for the case in which a stabilisation was reached. It can be seen that the film thickness decay has reached a steady state, in which the value of H_c remains constant. This behaviour is in qualitative agreement with the experimental result. Therefore, the possibility of achieving a zero film thickness decay has been considered in light of the existing literature. Consequently, an analysis was conducted on the position of the inlet meniscus. The investigation demonstrated that the inlet meniscus attained a stable equilibrium position and did not overlap with the Hertzian region. This conclusion prompted an investigation into the side flow fluxes. It has been demonstrated that the side flow fluxes decreased until they reached a value that was neg-

ligible in comparison to the mass flux in the X-direction (rolling direction). The aforementioned analysis has been combined with the use of stream line plots, which enable the direction of flow to be observed. Furthermore, it has been demonstrated that the mass flow rate in the X-direction approached a nearly constant value. Finally, the film thickness decay obtained through numerical analysis was compared to the analytical formulas. It was evident that the analytical formula did not accurately replicate the numerical result, as they only predicted a decreasing film thickness decay. However, the extension of the film thickness decay proposed by Chevalier [29] was shown to effectively reproduce the transient phase, as evidenced by its alignment with both the numerical and experimental curves.

4.5.2 Exploitation of model #2

In the following sections, only the results obtained from the analysis of case #A of model #2 will be presented.

Results

Figure 4.21 displays the dimensionless central film thickness as a function of the number of overrolling. The solid line represents the dimensionless central film thickness decay from model #1, which has been conserved on this plot for the purpose of facilitating comparison with model #2 case #A. The

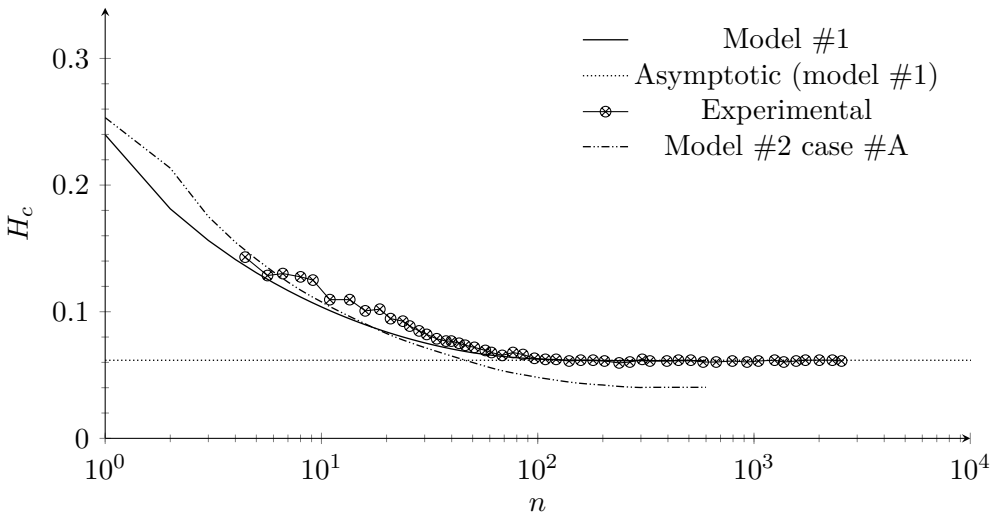

Figure 4.21: Dimensionless central film thickness as a function of the number of overrollings for model #2 with $u_m = 65\,\mathrm{mm} \cdot \mathrm{s}^{-1}$

densely dotted line represents the asymptotic value for model #1, computed using the periodic boundary condition. The curve with the marker ⊗ depicts the experimentally converted central film thickness, utilising the friction coefficient. Finally, the densely dashdotdotted line illustrates the dimensionless central film thickness decay, employing model #2 case #A.

Discussion

Similarly to model #1, model #2 case #A proposes a stabilisation of the dimensionless film thickness decay. The discrepancy between the two models in terms of the attained stabilised value can be attributed to the thermal contribution and the distinct rheological approach employed in model #2 case #A. The attainment of a stabilised value for the dimensionless central film thickness decay is in accordance with the experimental observations. Despite the introduction of a thermal contribution, the TEHL contact has reached a steady state. The difference in H_c between overrolling 599 and 600 is approximately 5.2×10^{-9}, which is negligible. This behaviour can be attributed to the stabilisation of the temperature through the overrollings, as illustrated in figure 4.22.

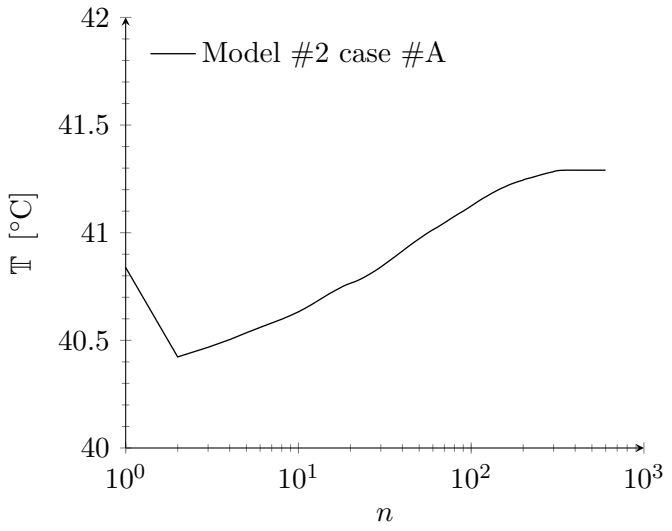

Figure 4.22: Maximum of the temperature through the overrollings from model #2 case #A for the case study at $u_m = 65\,\mathrm{mm} \cdot \mathrm{s}^{-1}$

Remark. Figure 4.22 illustrates a decline in the maximum temperature after $n = 1$, followed by an increase. This decline is attributed to the reduction of the Poiseuille flux at the inlet of the contact due to the presence of

starvation. Consequently, the shear heating with a minimal degree of starvation is less than that observed in a fully flooded application under the given circumstances (with a low SRR of 1.9 %).

Similarly, as with model #1, the attainment of a steady state by model #2 case #A indicates the cessation of side flow fluxes through the overrollings. In quantitative terms, the relative difference at $n = 600$ between the integration of $\bar{\rho}_x^\star H_{oil}$ at X_{in} and X_{out} along the transverse direction with respect to the value at X_{in} is approximately 8.5×10^{-3} %, thereby demonstrating that the fluid flows predominantly in the rolling direction.

As in section §4.3.7, a comparison may be made between the film thickness decay obtained numerically and that obtained analytically by Chevalier [29] using the stabilised extension equation (4.5). In order to accomplish this, it is necessary to specify the value at which the dimensionless film thickness tends to a high number of overrollings. Figure 4.23 presents a comparison of the dimensionless central film thickness decay obtained through numerical and analytical methods. The solid line represents model #1, while the densely dashdotdotted line corresponds to model #2 case #A which respects the standard employed in figure 4.21. The same line style but with black filled diamonds and black filled circles, in turn, are related to the computation of equation (4.5) using the asymptotic value from model #1 and model #2

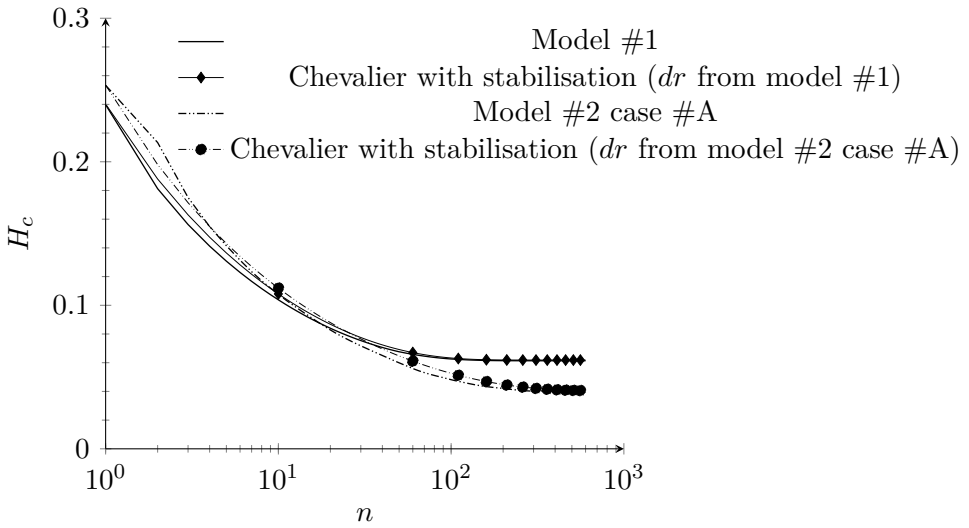

Figure 4.23: Dimensionless central film thickness through overrollings computed with model #1 and model #2 case #A for the case study at $u_m = 65\,\text{mm} \cdot \text{s}^{-1}$ against the analytical model from Chevalier [29]

case #A, respectively. For further details, please refer to section §4.3.7. Therefore, the use of equation (4.5) allows for a qualitative reproduction of the film thickness decay obtained numerically.

Conclusion

A total of 600 overrollings have been conducted for model #2 case #A. A steady state was reached, whereby the decay in film thickness became null through the overrolling process. This behaviour is in accordance with the experimental result obtained by Querlioz [112]. A number of physical analyses have been presented as a means of enhancing comprehension of this behaviour. The evolution of temperature was analysed with reference to the maximum temperature reached, which demonstrated that this also reached a steady state. The direction of fluid mass flow was then investigated and, as in model #1, the side flow fluxes vanished during the process. Finally, the numerical film thickness decay was compared with the analytical result enabling stabilisation, which showed qualitative proximity between the two within the transient phase.

4.5.3 Conclusion

The isothermal and thermal models yielded comparable results, namely, a stabilisation of the film thickness during the overrolling process. This outcome aligns with the experimental findings reported by Querlioz [112]. To gain insight into this behaviour, a comprehensive qualitative and quantitative analysis was conducted. It was established that the contact must operate for several hours under these conditions.

4.6 Conclusion

The objective of this chapter thus was to gain insight into the experimental observations made in the context of a Loss of Lubricant (LoL) process through the application of numerical techniques.

A comprehensive overview of the various LoL processes has been conducted. Despite the existence of analogous protocols, discrepancies have been observed with regard to loading, entrainment velocity and sliding. Two distinct behavioural categories have been identified: those applications that result in the stabilisation of either the friction coefficient or the film thickness, and those that give rise to an unstable friction coefficient (or film thickness). The stabilisation phenomenon occurs when the load, velocity and sliding are

relatively low, whereas the unstable cases manifest when the values of these parameters are high.

As posited by the experimenters, the stabilisation of the film thickness (or the friction coefficient or the torque) is presumed to be due to the occurrence of track replenishment. The process of replenishment has been quantified as oil re-entering the raceway due to a number of factors (see chapter 1), including surface tension, capillarity forces, external forces, shear degradation, oil bleeding and so forth. With respect to the second observed phenomenon, the authors hypothesised that it was attributable to thermal effects.

The work by Querlioz [112] has been selected as a case study due to its detailed presentation of two distinct behaviours. The experimental conditions and the established protocol utilising the Mini Traction Machine (MTM) test rig have been thoroughly outlined. The two behaviours, characterised by stable and unstable friction coefficients, emerged under two distinct entrainment velocities.

Based on the working conditions of the experimental study conducted by Querlioz [112] and a finding from Venner et al. [131], it has been postulated that the initial contact occurred in a fully flooded state. This was predicated on the assumption that the distribution of oil would be uniform prior to initiating the experiment. Consequently, the starved Moving Mesh (MM) solver has been extended to accommodate fully flooded computations.

The phenomenon of track replenishment has been the subject of investigation using the thin layer equation. In order to facilitate such a computation, it has been assumed that the oil which is leaving the contact area is divided into two equal oil layers, with one layer adhering to the ball and the other adhering to the disc. Therefore, the ball and disc oil layers have been examined separately, taking into account the effects of centrifugal force, air-oil surface tension, and gravity. Based on the oil layer leaving the fully flooded contact, the thin layer equation indicated that replenishment did not occur on either the ball or the disc. Consequently, it was postulated that if replenishment did not occur after the fully flooded contact, it would not occur at a later stage.

This conclusion, derived from the observation of the absence of track replenishment, facilitated the formulation of a numerical strategy to perform multiple overrollings. The assumption that the re-entry of both oil layers occurs simultaneously has been made in accordance with the findings presented in the theoretical analysis conducted by Damiens [37]. Subsequently, adaptations of the starved MM solver have been presented, enabling the com-

putation of multiple overrollings. It has been assumed that an overrolling process is a succession of quasi-stationary computations rather than a transient process based on a test case presented in appendix B. Two models have been presented: model #1, which is isothermal, and model #2, which is thermal. Within model #2, two cases have been proposed: case #A, in which the oil and solids are totally cooled down between two overrollings, and case #B, in which no cooling occurs.

Subsequently, the aforementioned hypotheses and adaptations to the staved MM EHL (and TEHL) solver permitted the investigation of both behaviours (unstable and stable friction coefficients) as distinct entities.

The numerical computations of the experimental work, which yielded an unstable friction coefficient (film thickness) through overrollings, were performed using models #1 and #2. Model #1 yielded a film thickness reduction during the initial one hundred overrollings, after which the film thickness attained a stabilised value, wherein the reduction ceased. Therefore, model #1 has been unable to reproduce the film thickness decay observed experimentally by Querlioz [112] across the entire range of overrolling. Indeed, qualitative agreement between model #1 and experimental observations is observed only during the first hundred overrollings. Model #2 case #A also proposed a film thickness decay that vanished at high numbers of overrollings. In qualitative terms, Model #2 case #A demonstrated superior performance to model #1. However, the model underestimated the film thickness decay in comparison to the experimental observation. Model #2 case #B yielded a result whereby the film thickness decay continued to decrease at elevated numbers of overrolling. Similarly, case #B also demonstrated an underestimation of the film thickness decay in comparison to the experimental observation. The analysis of the temperature field returned by both thermal models demonstrated that cooling occurred within model #2 case #B in the starved area, located upstream of the inlet meniscus. As a result, any evaluation of the results obtained from model #2 case #B must, except in the case of one comment, proceed with caution. Indeed, case #B permitted the conclusion that there is no possibility of thermal runaway within the specified application, and that the cooling process must be accounted for in the starved zone and on the disc, as well as on the ball located at a distance from the contact, where forced convection plays a role. Consequently, two potential scenarios have been proposed: either an element is absent within the numerical model, or an unforeseen event occurred during the experimental work, resulting in the formulation of an hypothesis that is no longer applicable.

The numerical reproduction of the experimental work, which resulted in

the attainment of a stable friction coefficient (film thickness) after multiple overrollings, was successfully accomplished using both model #1 and model #2. Model #1 yielded a stabilisation of the film thickness decay throughout the overrollings. The result was then compared qualitatively with the experimental data, which demonstrated a high level of concordance. The position of the inlet meniscus and the side flow fluxes have been analysed in accordance with the statement of Damiens [37], who presented a simplified analytical evaluation of the side flow fluxes based on the meniscus position. In the event that the inlet meniscus is situated within the Hertzian region, the aforementioned side flow fluxes are expected to become undetectable. In this particular application, the inlet meniscus has reached a state of equilibrium in the vicinity of the Hertzian area. It was subsequently demonstrated that the side flow fluxes remained present. The difference in mass flow rate between the inlet and outlet demonstrates a relative difference of 1.6×10^{-9} % at $n = 600$. Therefore, it can be asserted that these quantities are negligibly small in comparison to the flow in the rolling direction. Finally, the numerical results were compared with the analytical formulas proposed by Chevalier et al. [30] and van Zoelen [127]. Neither of the formulas was able to predict the stabilisation. However, Chevalier [29] extended his own formula to enable a zero film thickness decay only if the stabilised value is known. Since the numerical model #1 has reached a state of equilibrium, the stabilized value is now known. This can be employed in the analytical formula developed by Chevalier [29]. The superposition of both models demonstrated qualitative agreement. Lastly, as model #1 reached a steady state, a single computation was performed using periodic boundary conditions regarding the mass flow rate entering and leaving the contact. The asymptotic value was found to correspond to the stabilised phase of the film thickness decay from model #1. Model #2 case #A has been calculated in a manner analogous to model #1, which also exhibited a stabilisation of the film thickness decay. This stabilisation is attributable to a concomitant stabilisation of the temperature. Furthermore, the discrepancy in mass flow rate between the inlet and outlet has been quantified, resulting in a relative difference of approximately 8.5×10^{-3} % at $n = 600$. Consequently, both model #1 and model #2 reached a steady state in a manner consistent with the experimental observation. This indicates that under these conditions, the contact must operate for extended periods at a constant film thickness, eliminating the necessity for track replenishment.

General conclusion

This study investigates the film thickness decay of an ElastoHydrodynamic Lubrication (EHL) contact due to a transient starvation phenomenon.

Chapter 1 presented an overview of the mechanical parts encountered within Rolling Element Bearing (REB). It has therefore been determined that the devices are overly complex, and that instead of studying the entire assembly, only one contact is analysed. In such a situation, the contact is reduced to a sphere in contact with a plane. Therefore, the theoretical and experimental works related to sphere-on-plane contact have been presented. The experimental works from the literature based on ball-on-disc contact, which present a transient starvation phenomenon, have been detailed. The aforementioned works are either concerned with measuring the friction coefficient or the film thickness. Such works are referred to as Loss of Lubricant (LoL) applications. The LoL process can be initiated either by shutting off the oil supply or by restricting the initial oil quantity on the test rig. In such circumstances, the EHL contact results in the production of multiple overrollings in a starved condition. The experimental works yielded two distinct outcomes. The first scenario demonstrates a stabilisation of either the friction coefficient or the film thickness, whereas the second scenario exhibits a notable increase in the friction coefficient (or a corresponding decrease in the film thickness). The prevailing hypothesis, as postulated in the extant literature, attributes the observed stabilisation to the presumed existence of track replenishment. Conversely, the unstable phenomenon is hypothesised to arise from the combined influence of thermal effects and the absence of track replenishment. Nevertheless, the question of whether stabilisation will occur remains unanswered, despite the completion of numerical works dedicated to film thickness decay. Two analytical laws have been proposed which allow the prediction of film thickness decay in the absence of stabilisation, based on the results of numerical simulations. One of the aforementioned laws can

only produce a stabilisation effect if the stabilised value is known a priori; thus, the law does not predict stabilisation. In parallel, both experimental and numerical works have been performed to gain a deeper understanding of the track replenishment phenomenon. This phenomenon depends on the time between two overrollings, the viscosity of the fluid and other parameters. The objective was then set on understanding the stabilisation phenomena and determining the ingredient involved within the experimental work in order to reproduce it.

Chapter 2 presents a comprehensive overview of the classical theory for computing either ElastoHydrodynamic Lubrication (EHL) or Thermal ElastoHydrodynamic Lubrication (TEHL) contact. It includes detailed discussions on the theoretical underpinnings of the Reynolds and Generalized Reynolds equations, along with an in-depth analysis of fundamental equations governing the behaviour of elastic deformations and energy transfers within the contact zone. Furthermore, it delineates the numerical strategy employed to compute these complex contact scenarios.

Given that no model is capable of accurately explaining and predicting stable or unstable contact, a numerical model is proposed with the objective of reproducing the experiments. In order to achieve this objective, a model of EHL or TEHL contact that incorporates starvation has been developed using the Jakobsson-Floberg-Olsson (JFO) theory. The introduction of starvation, as presented in chapter 3, resulted in the development of two distinct strategies for conducting starvation simulations. The initial approach resolves the so-called modified Reynolds equation through the utilisation of the Penalty Method (PM), thereby mitigating the discontinuity introduced by the application of the JFO theory. The second model employs a Moving Mesh (MM) approach to facilitate the computation of the JFO theory without the necessity of a penalty term. Both developed models have been validated through a comparison with literature reference. Furthermore, the incorporation of starvation within the Generalized Reynolds equation has enabled starved thermal studies. The MM model has been selected for subsequent use due to its enhanced accuracy and reduced computation time. Finally, a simulation of a brutal oil-off phenomenon has been conducted.

Subsequently, chapter 4 presents a numerical investigation into the phenomenon of Loss of Lubricant (LoL), inspired by experimental literature. One experimental study, which demonstrated both stabilisation and unstabilisation, has been selected for reference. A number of hypotheses have been formulated with a view to adapting the numerical model based on the MM solver in order to emulate the experimental results. The absence of track

replenishment has been demonstrated numerically through the resolution of the thin layer equation. In consequence, two models have been proposed: an isothermal EHL contact model (referred to as model #1) and a TEHL contact model (referred to as model #2). Two different cases in terms of boundary conditions were investigated using the TEHL model. In case #A, it was assumed that both the oil and the surfaces were completely cooled between each overrolling, whereas in case #B, no cooling was assumed. The two models were unable to reproduce the qualitative unstabilisation of the film thickness observed experimentally by Querlioz [112]. Indeed, the isothermal model (model #1) and the thermal-#A (model #2 case #A) both proposed a stabilisation of the film thickness through the overrollings. A variety of explanations have been proposed to account for the discrepancy between the experimental and numerical results. The TEHL-#B (Model #2 case #B) returned a result indicating a decrease in film thickness. However, the thermal result demonstrated the occurrence of cooling within the starved zone. This behaviour permitted the conclusion to be drawn that there was no thermal runaway. Therefore, Model #2 case #B has not been considered further in this work. Subsequently, both the isothermal (model #1) and the thermal-#A (model #2 case #A) models yielded favourable outcomes when reproducing the experimental application, resulting in the stabilisation of the film thickness. Indeed, both models demonstrated a stabilisation of the film thickness through the overrollings. Model #1 exhibited stabilisation at approximately 100 overrollings, while model #2 demonstrated stabilisation at around 400 overrollings. These outcomes were subjected to analysis, which led to the conclusion that the side flow fluxes diminished until they became insignificant in comparison to the mass flow in the rolling direction. Consequently, in such circumstances, both the EHL and TEHL contact models reproduce a scenario in which a lubricated contact can function effectively for extended periods without the necessity for additional lubricant supply.

In conclusion, this research demonstrated that an EHL or TEHL contact operating in conjunction with a low Slide to Roll Ratio (SRR) can operate effectively for extended periods with a limited quantity of lubricant. The contact that occurs between a rolling element and a raceway within a REB is of the form of a rolling contact. Consequently, such a situation is very similar to an isothermal application in which there is no sliding. Therefore, it can be deduced that the contact should be capable of working for extended periods with a minimum quantity of lubricant. This ultimately suggests the potential for lubricant optimisation within REB.

Perspectives

To corroborate the principal findings of this thesis, a dual methodology integrating experimental (with film thickness measurements) and numerical techniques is recommended. The primary findings indicate that isothermal and thermal numerical models of Loss of Lubricant (LoL) application have demonstrated the capacity to reproduce a stable lubricated contact, despite the absence of track replenishment. Consequently, the utilisation of a less viscous oil may be necessary to ascertain the influence of oil replenishment. Similarly, the examination of a higher Slide to Roll Ratio (SRR) and thermal parameters may be beneficial in determining the role of thermal effects in the stabilisation process.

The thermal dependency within a starved Thermal ElastoHydrodynamic Lubrication (TEHL) contact may be investigated with a view to optimising it. It is important to note that in non-pressurised zones, the presence of air is not taken into account when considering the gap between the two solids. Therefore, the thermal properties must be a combination of both the air and the oil, which may have an effect, for example, on the conductivity. Furthermore, an investigation should be conducted to ascertain whether the transient term within the energy equation needs to be considered in a LoL process. Indeed, as Raisin et al. [113] have observed, determining the thermal transient characteristic time is not straightforward. In some cases, it can be of the same order of magnitude as the fluid disturbance transient characteristic time. Finally, the cooling of both layers of oil adhering to the ball and the disc, which occurs far outside the contact area and undergoes forced convection, must be determined. This would allow the temperature of the bodies entering the contact area after completing one complete revolution to be known.

The final improvement to be discussed is that of the Moving Mesh (MM) method. For instance, the free frontier may be enhanced through the sub-

stitution of a more realistic equation, which can facilitate an even transition between the inlet and outlet frontiers.

Appendix

A

Thin layer in curvilinear coordinates

The objective of this appendix is to examine the thin layer equation on a curved surface. To this end, the thin layer equation is presented and solved in curvilinear coordinates. To facilitate the study, the equation is solved with dimensions.

A.1 Preamble

The ball of the Mini Traction Machine (MTM) is not flat and presents a curvature as illustrated in figure A.1. The curvilinear axis is indicated with its normal n. In figure A.1, the ball is viewed in the transverse plane, then it rotates around the y-direction. Furthermore, the parameter $r\,(s)$ is introduced, representing the radius of curvature of the substrate at each point. For a centred ball, it is written

$$r\,(s) = R_{ball}^{\mathrm{MTM}} \sin\left(\pi \frac{s - R_{ball}^{\mathrm{MTM}}}{2R_{ball}^{\mathrm{MTM}}}\right). \tag{A.1}$$

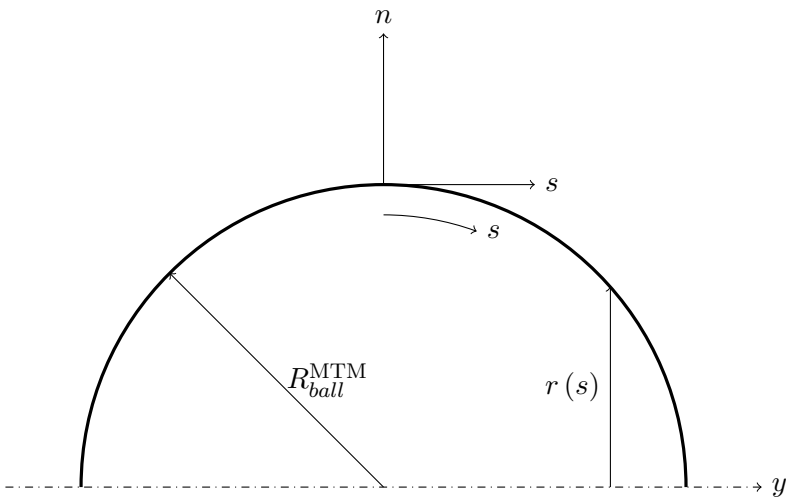

Figure A.1: Curvilinear parametrisation of the ball of the MTM

A.2 Thin layer equation

In accordance with van Zoelen [127], the thin layer equation in curvilinear coordinates is given by:

$$\frac{1}{3\eta r\left(s\right)}\frac{\partial}{\partial s}\left(r\left(s\right)\ell_{oil}^{3}\left\{f_s+f_n\frac{\partial \ell_{oil}}{\partial s}\right\}\right)+\frac{\partial \ell_{oil}}{\partial t}=0. \tag{A.2}$$

Following the statement of van Zoelen [127], the surface tension term is ignored in equation (A.2). In this equation, f_s and f_n represent the force components in the s-direction and n-direction with respect to figure A.1, respectively. The force components are given by the following expressions, as presented by van Zoelen [127] and Gao et al. [57]:

$$\begin{cases} f_s=\rho_0\dfrac{\partial r}{\partial s}\left(R_{ball}^{\mathrm{MTM}}\omega_{ball}^{2}-g\cos\left(\omega_{ball}t\right)\right), \\ f_n=\rho_0\dfrac{\partial y}{\partial s}\left(R_{ball}^{\mathrm{MTM}}\omega_{ball}^{2}-g\cos\left(\omega_{ball}t\right)\right). \end{cases} \tag{A.3}$$

According to van Zoelen [127]

$$\frac{\partial y}{\partial s}=\sqrt{1-\frac{\partial r}{\partial s}^{2}}, \tag{A.4}$$

which is not defined on the whole half-circle $s\in\left[-R_{ball}^{\mathrm{MTM}};\ R_{ball}^{\mathrm{MTM}}\right]$. Hence, for that reason, the thin layer equation in curvilinear coordinates is studied

for $s \in \left[-\frac{R_{ball}^{\mathrm{MTM}}}{2.3};\ \frac{R_{ball}^{\mathrm{MTM}}}{2.3}\right]$. Equation (A.2) is solved by imposing

$$\frac{\partial \ell_{oil}}{\partial s} = 0$$

on both boundaries.

A.3 Results

Figure A.2 presents the results for both entrainment velocities. As with the primary cases, the consideration of ball curvature does not result in a distinct outcome. In essence, the curve following one revolution is superposed onto the initial position at the commencement of the same revolution.

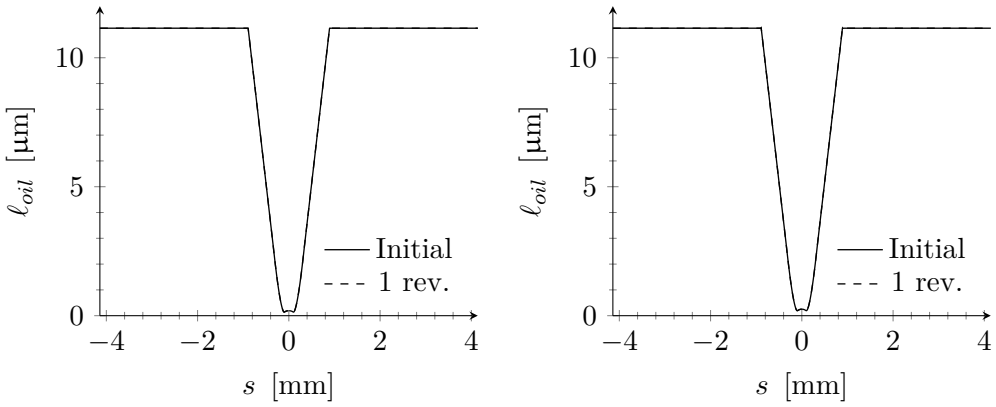

(a) $u_m = 65\,\mathrm{mm} \cdot \mathrm{s}^{-1}$ (b) $u_m = 100\,\mathrm{mm} \cdot \mathrm{s}^{-1}$

Figure A.2: Thin layer evolution on the ball at the initiation of the computation and after one revolution

A.4 Conclusion

The thin layer equation in curvilinear coordinates has been presented and solved to consider the curvature of the ball of the MTM. As in the case presented in chapter 4, track replenishment does not occur. Therefore, the assumption that neglected the curvature is well suited for this case.

Appendix B

Transient overrolling process

This appendix presents a transient overrolling process and compares it with a succession of quasi-stationary results. The objective is to demonstrate that an overrolling process is quasi-stationary rather than transient.

B.1 Numerical strategy

This example application is based on the parameters used during the section §3.3.1 which are $M = 20$, $L = 10$, $\alpha = 1.7 \times 10^{-8}\,\mathrm{Pa}^{-1}$ and $\eta_0 = \eta_R = 8.9 \times 10^{-3}\,\mathrm{Pa} \cdot \mathrm{s}$, without sliding. The length of the domain in the X-direction is fixed, with $X_{in} = -2.5$ and $X_{out} = 1.5$. This configuration implies that the problem is periodic with a period of 4, driven by the length of the transport direction.

Chapter 4 presented the methodology for computing a fully flooded contact and the subsequent starved contacts undergoing an overrolling process. It has been demonstrated that the frontier inlet does not exist in the context of a fully flooded case. However, in the context of a starved case, it is a necessary component. It is not possible to perform a transient computation starting from a fully flooded state, as the inlet cannot be added during the computation. Consequently, the transient application begins at the overrolling $n = 2$, which is starved. The initial condition for $H_{oil}^{inlet}(T = 0)$ is

the value of $H_{oil}^{outlet}\,(n=1)$. A periodic boundary condition is then imposed, such as

$$H_{oil}\left(X_{in}, Y, T\right) = H_{oil}\left(X_{out}, Y, T\right).$$

In the initial time steps (up to $T = 0.5$), the boundary condition is smoothed to prevent a discontinuity by utilising a step function.

B.2 Results

Figure B.1 illustrates the temporal decay of the film thickness. From this figure, it can be observed that H_c through time presents a descending stair-step profile. As time increases, the height of these stair-steps decreases, indicating that the film thickness reduction through time becomes smaller. The short stationary value on each step represents the stationary behaviour between two successive overrollings. From a mathematical perspective, this implies that the transient term inside Reynolds equation (2.44) vanishes. Consequently, these constant portions must coincide with a stationary computation of each overrolling.

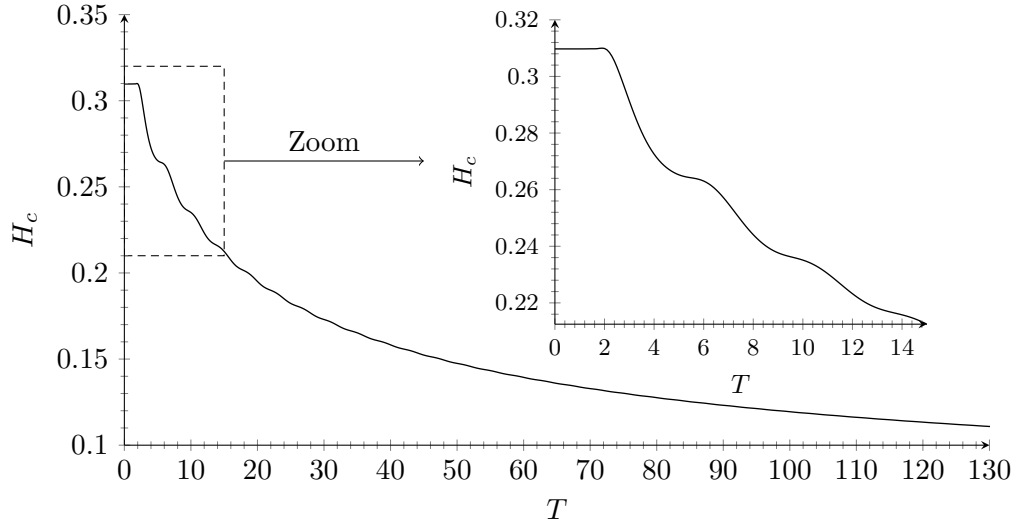

Figure B.1: Transient evolution of the central film thickness H_c

Remark. As a consequence of the manner in which the boundary condition has been smoothed, it is no longer a simple matter to attribute an overrolling to a specific dimensionless time.

Figure B.2 illustrates the superposition of the transient evolution of H_c, with horizontal lines representing the value of H_c derived from a series of stationary computations conducted in accordance with the methodology outlined in section §4.3.4. The constant portions/plateaus are in alignment with the stationary computations. The stationary and transient computations were performed using the same mesh size, threshold, and other relevant parameters. The overrolling $n = 2$ and the transient curve coincide because the transient computation was initiated from the stationary result $n = 2$. A minor discrepancy emerges after $n = 2$, which is attributed to the numerical damping of the transient scheme. The absolute discrepancy between the transient curve and a stationary value is evaluated on a plateau where there is an inflection point; each time the absolute discrepancy is approximately 0.15 %.

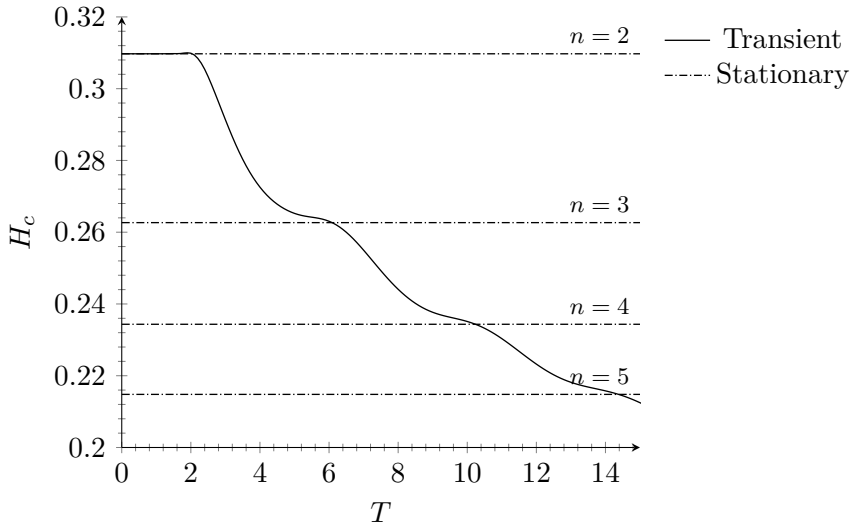

Figure B.2: Transient evolution of the central film thickness H_c superposed with stationary computations

Figure B.3(a) illustrates the position of the outlet in a fully flooded application, while figure B.3(b) displays the position of the frontiers of multiple overrrollings. The dotted circle represents the Hertzian contact area. It can be observed that as the value of n increases, the inlet frontier approaches the Hertzian circle, while the cavitation boundary exhibits minimal movement during the overrollings.

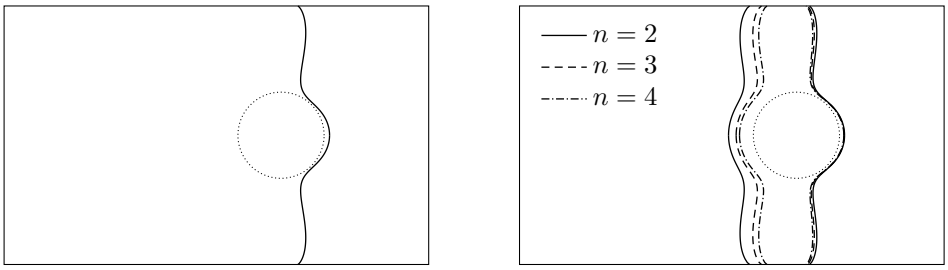

(a) $n = 1$ (b) $n = 2,\ 3,\ 4$

Figure B.3: Frontiers position after convergence

B.3 Conclusion

This appendix provided a transient computation of an illustrative example in which a periodic boundary condition was applied between the outlet and the inlet with respect to the variable H_{oil}. The resulting film thickness decay exhibited a descending stair-step profile, which aligned with the stationary computations conducted using the strategy outlined in section §4.3.4. Consequently, a series of quasi-stationary computations were able to reproduce the observed behaviour of the transient computation.

Bibliography

[1] J.D. Achenbach. “Introduction”. In: *Wave Propagation in Elastic Solids*. Elsevier, 1975 ..... ⇑ 42

[2] F. Ali, I. Krupka, and M. Hartl. “Mechanism for Controlling Oil Replenishment in Starved Elliptical EHL Contacts”. In: *Tribology Letters* (2015) ..... ⇑ 28

[3] G. Amine et al. “Dual experimental-numerical study of oil film thickness and friction in a wide elliptical TEHL contact: From pure rolling to opposite sliding”. In: *Tribology International* (2023) ..... ⇑ 13

[4] A. Anifa Mohamed Faruck et al. “How lubricant formulations and properties influence the performance of rotorcraft transmissions under loss of lubrication conditions”. In: *Tribology International* (2020) ⇑ 24

[5] D.G. Astridge. “Helicopter Transmissions—design for Safety and Reliability”. In: *Proceedings of the Institution of Mechanical Engineers, Part G: Journal of Aerospace Engineering* (1989) ..... ⇑ 1, 167

[6] R. Aubert et al. “Tribological devices in cycling: A review”. In: *Proceedings of the Institution of Mechanical Engineers, Part P: Journal of Sports Engineering and Technology* (0) ..... ⇑ 7

[7] S. Bair. *High pressure rheology for quantitative elastohydrodynamics*. Elsevier, 2019 ..... ⇑ 11, 114, 115

[8] S. Bair and S. Flores-Torres. “The Viscosity of Polyalphaolefins Mixtures at High Pressure and Stress”. In: *Journal of Tribology* (2018) ⇑ 113, 114

[9] S. Bair et al. “An improved Yasutomi correlation for viscosity at high pressure”. In: *Proceedings of the Institution of Mechanical Engineers, Part J: Journal of Engineering Tribology* (2013) ..... ⇑ 11, 38, 113

[10] C. Barus. “Isothermals, isopiestics and isometrics relative to viscosity”. In: *American Journal of Science* (1893) ..... ⇑ 9, 11, 38

[11] G. Bayada, M. Chambat, and M. El Alaoui. “Variational Formulations and Finite Element Algorithms for Cavitation Problems”. In: *Journal of Tribology* (1990) ..... ⇑ 17, 18, 60, 172

[12] G. Bayada, M. Chambat, and M. El Alaoui Talibi. “Stationary and moving free boundary problems related to the cavitation problem”. In: *Boundary Control and Boundary Variations*. Ed. by J. P. Zolésio. Berlin, Heidelberg: Springer Berlin Heidelberg, 1988 ..... ⇑ 17, 19

[13] G. Bayada and L. Chupin. “Compressible Fluid Model for Hydrodynamic Lubrication Cavitation”. In: *Journal of Tribology* (2013) ⇑ 20, 21

[14] A. Bejan. “Fundamental Principles”. In: *Convection Heat Transfer*. John Wiley & Sons, Ltd, 2013. Chap. 1 ..... ⇑ 47

[15] N. Biboulet. “Influence of indentations on rolling bearing life”. PhD thesis. INSA de Lyon, 2008 ..... ⇑ 14, 15, 44, 46

[16] N. Biboulet and A.A. Lubrecht. “Efficient solver implementation for Reynolds equation with mass-conserving cavitation”. In: *Tribology International* (2018) ..... ⇑ 17

[17] J. Boussinesq. *Application des potentiels à l’étude de l’équilibre et du mouvement des solides élastiques: principalement au calcul des déformations et des pressions que produisent, dans ces solides, des efforts quelconques exercés sur une petite partie de leur surface ou de leur intérieur : mémoire suivi de notes étendues sur divers points de physique, mathematique et d’analyse*. Gauthier-Villars, 1885 ⇑ 11, 14

[18] A. Brandt and O.E. Livne. *Multigrid Techniques*. Society for Industrial and Applied Mathematics, 2011 ..... ⇑ 14, 171

[19] A. Brandt and A.A Lubrecht. “Multilevel matrix multiplication and fast solution of integral equations”. In: *Journal of Computational Physics* (1990) ..... ⇑ 14

[20] M.J. Braun and W.M. Hannon. “Cavitation formation and modelling for fluid film bearings: A review”. In: *Proceedings of the Institution of Mechanical Engineers, Part J: Journal of Engineering Tribology* (2010) ..... ⇑ 17

[21] J. Brunetti et al. “System dynamic instabilities induced by sliding contact: A numerical analysis with experimental validation”. In: *Mechanical Systems and Signal Processing* (2015) ..... ⇑ 8

[22] V. Bruyere et al. “A Two-Phase Flow Approach for the Outlet of Lubricated Line Contacts”. In: *Journal of Tribology* (2012) ... ⇑ 103

[23] V Bruyère. “Une modélisation multi-physique et multi-phasique du contact lubrifié”. Theses. INSA de Lyon, 2012 ..... ⇑ 34

[24] P.M.E. Cann. “Starvation and Reflow in a Grease-Lubricated Elastohydrodynamic Contact”. In: *Tribology Transactions* (1996) .... ⇑ 26, 174

[25] P.M.E. Cann. “Thin-film grease lubrication”. In: *Proceedings of the Institution of Mechanical Engineers, Part J: Journal of Engineering Tribology* (1999) ..... ⇑ 26, 174

[26] P.M.E. Cann, F. Chevalier, and A.A. Lubrecht. “Track Depletion and Replenishment in a Grease Lubricated Point Contact: A Quantitative Analysis”. In: *Elastohydrodynamics - ’96 Fundamentals and Applications in Lubrication and Traction*. Ed. by D. Dowson et al. Elsevier, 1997 ..... ⇑ 26, 95, 174

[27] A. Chapkov. “Etude des contacts élastohydrodynamiques lubrifiés avec un fluide non newtonien”. PhD thesis. INSA de Lyon, 2006 ⇑ 15

[28] H.S. Cheng and B. Sternlicht. “A Numerical Solution for the Pressure, Temperature, and Film Thickness Between Two Infinitely Long, Lubricated Rolling and Sliding Cylinders, Under Heavy Loads”. In: *Journal of Basic Engineering* (1965) ..... ⇑ 11

[29] F. Chevalier. “Modélisation des conditions d’alimentation dans les contacts élastohydrodynamiques ponctuels”. PhD thesis. INSA de Lyon, 1996 . ⇑ 18, 19, 26, 30, 60, 67, 68, 96, 98, 99, 119, 120, 126, 130, 131, 133, 137, 172

[30] F. Chevalier et al. “Film Thickness in Starved EHL Point Contacts”. In: *Journal of Tribology* (1998) ⇑ 18, 22, 23, 30, 96, 98, 112, 137, 172

[31] F. Chevalier et al. “Starvation Phenomena in E.H.L. Point Contacts: Influence of Inlet Flow Distribution.” In: *The Third Body Concept Interpretation of Tribological Phenomena*. Ed. by D. Dowson et al. Elsevier, 1996 ..... ⇑ 18, 172

[32] F. Chevalier et al. “The Evolution of Lubricant Film Defects in the Starved Regime”. In: *Tribology for Energy Conservation*. Ed. by D. Dowson et al. Elsevier, 1998 ..... ⇑ 18, 125, 172

[33] R.J. Chittenden et al. “A theoretical analysis of the isothermal elastohydrodynamic lubrication of concentrated contacts. I. Direction of lubricant entrainment coincident with the major axis of the Hertzian contact ellipse”. In: *Proceedings of the Royal Society of London. A. Mathematical and Physical Sciences* (1985) ..... ⇑ 13

[34] R.J. Chittenden et al. “A theoretical analysis of the isothermal elastohydrodynamic lubrication of concentrated contacts. II. General case, with lubricant entrainment along either principal axis of the Hertzian contact ellipse or at some intermediate angle”. In: *Proceedings of the Royal Society of London. A. Mathematical and Physical Sciences* (1985) ..... ⇑ 13

[35] P. Guay. “Principes de base de la lubrification”. In: *Techniques de l’ingénieur Frottement, usure et lubrification* (2014) ..... ⇑ 7, 169

[36] J.J. Coy and E.V. Zaretsky. “Some Limitations in Applying Classical EHD Film Thickness Formulas to a High-Speed Bearing”. In: *Journal of Lubrication Technology* (1981) ..... ⇑ 17

[37] B. Damiens. “Modélisation de la lubrification sous-alimentée dans les contacts élastohydrodynamiques elliptiques”. PhD thesis. INSA de Lyon, 2003 . ⇑ 19, 22, 56, 110, 111, 112, 125, 126, 127, 135, 137, 173

[38] M. Decote et al. “An original methodology to model stationary and transient starvation in EHL contact”. In: *Journal of Tribology* (2024) ⇑ 59, 85

[39] T. Doki-Thonon. “Thermal effects in elastohydrodynamic spinning circular contacts”. Theses. INSA de Lyon, 2012 ..... ⇑ 15

[40] A.K. Doolittle. “Studies in Newtonian Flow. II. The Dependence of the Viscosity of Liquids on Free-Space”. In: *Journal of Applied Physics* (1951) ..... ⇑ 12, 39

[41] H. Dormois et al. “First Traction Results of High Spinning Large-Size Circular EHD Contacts from a New Test Rig: Tribogyr”. In: *Tribology Transactions* (2009) ..... ⇑ 10

[42] D. Dowson. “A generalized Reynolds equation for fluid-film lubrication”. In: *International Journal of Mechanical Sciences* (1962) . ⇑ 46

[43] D. Dowson. “The inlet boundary condition”. In: *Cavitation and Related Phenomena in Lubrication*. Ed. by D. Dowson, M. Godet, and C.M. Taylor. Mechanical Engineering Publications, 1975 ..... ⇑ 18

[44] D. Dowson and G.R. Higginson. “A Numerical Solution to the Elasto-Hydrodynamic Problem”. In: *Journal of Mechanical Engineering Science* (1959) ..... ⇑ 13

[45] D. Dowson and G.R. Higginson. *Elasto-hydrodynamic Lubrication: The Fundamentals of Roller and Gear Lubrication*. Pergamon Press, 1966 ..... ⇑ 12, 37, 78, 113

[46] D. Dowson, A.A.S. Miranda, and C.M. Taylor. “Paper III(ii) - Implementation of an algorithm enabling the determination of film rupture and reformation boundaries in a liquid film bearing”. In: *Developments in Numerical and Experimental Methods Applied to Tribology*. Ed. by D. Dowson et al. Butterworth-Heinemann, 1984 ..... ⇑ 17

[47] D. Dowson and C.M. Taylor. “Fundamental aspects of cavitation in bearings”. In: *Cavitation and Related Phenomena in Lubrication*. Ed. by D. Dowson, M. Godet, and C.M. Taylor. Mechanical Engineering Publications, 1975 ..... ⇑ 69

[48] D. Dowson and V. Wright. “The Lubrication of Human Joints”. In: *Perspectives in Biomedical Engineering: Proceedings of a Symposium organised in association with the Biological Engineering Society and held in the University of Strathclyde, Glasgow, June 1972*. Ed. by R. M. Kenedi. London: Palgrave Macmillan UK, 1973 ..... ⇑ 7

[49] J.H. Dymond and R. Malhotra. “The Tait equation: 100 years on”. In: *International journal of thermophysics* (1988) ..... ⇑ 12, 37, 38

[50] J.W. Eichler et al. “The influence of coatings on the oil-out performance of rolling bearings”. In: *Surface and Coatings Technology* (2007). ICMCTF 2007 ..... ⇑ 24, 94, 96

[51] M. El Alaoui Talibi and G. Bayada. “Une méthode du type caractéristique pour la résolution d’un problème de lubrification hydrodynamique en régime transitoire”. fr. In: *ESAIM: Mathematical Modelling and Numerical Analysis - Modélisation Mathématique et Analyse Numérique* (1991) ..... ⇑ 66

[52] H.G. Elrod and M.L. Adams. “A computer program for cavitation and starvation problems”. In: *Cavitation and related phenomena in lubrication*. Proceeding of the 1st Leeds-Lyon Symposium on Tribology, 1975 ..... ⇑ 17

[53] A.M. Ertel. “Hydrodynamic lubrication based on new principles”. In: *Akad. Nauk SSSR Prikadnaya Mathematica i Mekhanika* (1939) ⇑ 9, 10, 11, 19, 38

[54] S. Esmaeili et al. “Effect of temperature on relative permeability – Role of viscosity ratio”. In: *Fuel* (2020) ..... ⇑ 115

[55] European Aviation Safety Agency. *Certification Specifications and Acceptable Means of Compliance for Large Rotorcraft CS-29*. CS.29.927 (c) Lubrication system failure. 2018 ..... ⇑ 1, 167

[56] H.P. Evans and R.W. Snidle. “The Isothermal Elastohydrodynamic Lubrication of Spheres”. In: *Journal of Lubrication Technology* (1981) ⇑ 85

[57] M. Gao et al. “Oil redistribution and replenishment on stationary bearing inner raceway”. In: *Tribology International* (2022) ⇑ 29, 146

[58] L. Gershuni, M.G. Larson, and P.M. Lugt. “Lubricant Replenishment in Rolling Bearing Contacts”. In: *Tribology Transactions* (2008) ⇑ 25, 27, 28, 105, 108, 109, 174

[59] A.N. Grubin. “Fundamentals of the hydrodynamic theory of lubrication of heavily loaded cylindrical surfaces”. In: *Investigation of the Contact Machine Componets* (1949) ..... ⇑ 9, 10

[60] G. Guangteng and H.A. Spikes. “The Role of Surface Tension and Disjoining Pressure in Starved and Parched Lubrication”. In: *Proceedings of the Institution of Mechanical Engineers, Part J: Journal of Engineering Tribology* (1996) ..... ⇑ 17, 27, 172

[61] W. Habchi. “A full-system finite element approach to elastohydrodynamic lubrication problems : application to ultra-low-viscosity fluids”. PhD thesis. INSA de Lyon, 2008 .⇑ 15, 21, 47, 54, 55, 102, 171, 177, 178

[62] W. Habchi. *Finite Element Modelling of Elastohydrodynamic Lubrication Problems*. John Wiley & Sons, Ltd, 2018 ⇑ 11, 12, 15, 42, 46, 51, 53, 54, 75

[63] W. Habchi and S. Bair. “Quantitative Compressibility Effects in Thermal Elastohydrodynamic Circular Contacts”. In: *Journal of Tribology* (2012) ..... ⇑ 12

[64] W. Habchi et al. “A Full-System Approach of the Elastohydrodynamic Line/Point Contact Problem”. In: *Journal of Tribology* (2008) . ⇑ 15

[65] B. Hamrock and D. Dowson. “Isothermal Elastohydrodynamic Lubrication of Point Contacts: Part 1—Theoretical Formulation”. In: *Journal of Lubrication Technology* (1975) ..... ⇑ 13

[66] B. Hamrock and D. Dowson. “Isothermal Elastohydrodynamic Lubrication of Point Contacts: Part II—Ellipticity Parameter Results”. In: *J Lubr Technol Trans ASME* (1976) ..... ⇑ 13

[67] B. Hamrock and D. Dowson. “Isothermal Elastohydrodynamic Lubrication of Point Contacts: Part III-Fully Flooded Result”. In: *Journal of Lubrication Technology* (1976) ..... ⇑ 13, 17, 101

[68] B.J. Hamrock and W.J. Anderson. *Rolling-Element Bearing*. 1983 ⇑ 4, 22

[69] B.J. Hamrock, S.R. Schmid, and B.O. Jacobson. “Elastohydrodynamic Lubrication of Elliptical Conjunctions”. In: *Fundamentals of Fluid Film Lubrication*. CRC Press, 2004. Chap. 19 ..... ⇑ 13

[70] B.J. Hamrock, S.R. Schmid, and B.O. Jacobson. *Fundamentals of Fluid Film Lubrication*. CRC Press, 2004 ..... ⇑ 8

[71] B.J. Hamrock, S.R. Schmid, and B.O. Jacobson. “Reynolds Equation”. In: *Fundamentals of Fluid Film Lubrication*. CRC Press, 2004. Chap. 7 ..... ⇑ 34

[72] M. Hartl et al. “Thin Film Colorimetric Interferometry”. In: *Tribology Transactions* (2001) ..... ⇑ 10

[73] H. Hertz. *Miscellaneous Papers*. Macmillan, 1896 ..... ⇑ 9, 11, 49

[74] K. Holmberg, P. Andersson, and A. Erdemir. “Global energy consumption due to friction in passenger cars”. In: *Tribology International* (2012) ..... ⇑ 7

[75] T. Hultqvist. “Transient elastohydrodynamic lubrication : Effects of geometry, surface roughness, temperature, and plastic deformation”. PhD thesis. Luleå University of Technology, Machine Elements, 2020 ⇑ 43, 51

[76] S. Hurley, P.M.E. Cann, and H.A. Spikes. “Lubrication and Reflow Properties of Thermally Aged Greases”. In: *Tribology Transactions* (2000) ..... ⇑ 26, 174

[77] B. Jacod et al. “An Analysis of Track Replenishment Mechanisms in the Starved Regime”. In: *Lubrication at the Frontier*. Ed. by D. Dowson et al. Elsevier, 1999 ..... ⇑ 26, 27, 106, 109, 174

[78] B.C. Jacod. “Friction in elasto-hydrodynamic lubrication”. PhD Thesis. 2002 ..... ⇑ 100

[79] K.L. Johnson. “Non-Newtonian Effects in Elastohydrodynamic Lubrication”. In: *Thin Films in Tribology*. Ed. by D. Dowson et al. Elsevier, 1993 ..... ⇑ 100

[80] K.L. Johnson. “Point loading of an elastic half-space”. In: *Contact Mechanics*. Cambridge University Press, 1985 ..... ⇑ 11

[81] K.L. Johnson and R. Cameron. “Fourth Paper: Shear Behaviour of Elastohydrodynamic Oil Films at High Rolling Contact Pressures”. In: *Proceedings of the Institution of Mechanical Engineers* (1967) ⇑ 9, 170

[82] K.L. Johnson, J.L. Tevaarwerk, and D. Tabor. “Shear behaviour of elastohydrodynamic oil films”. In: *Proceedings of the Royal Society of London. A. Mathematical and Physical Sciences* (1977) ..... ⇑ 99

[83] I. Jubault et al. “In Situ Pressure and Film Thickness Measurements in Rolling/Sliding Lubricated Point Contacts”. In: *Tribology Letters* (2003) ..... ⇑ 10

[84] D. Kostal et al. “Artificial Surface Roughness Deformation in the Starved EHL Contacts”. In: *Tribology Online* (2018) ..... ⇑ 68

[85] D. Kostal et al. “Experimental observation of elastohydrodynamically lubricated contacts replenishment”. In: *MM Science Journal* (2015) ⇑ 28

[86] D. Kostal et al. “Influence of Lubricant Inlet Film Thickness on Elastohydrodynamically Lubricated Contact Starvation”. In: *Journal of Tribology* (2017). 051503 ..... ⇑ 19

[87] R. Larsson and O. Andersson. “Lubricant thermal conductivity and heat capacity under high pressure”. In: *Proceedings of the Institution of Mechanical Engineers, Part J: Journal of Engineering Tribology* (2000) ..... ⇑ 115

[88] C. Liu et al. “Laser pattern-induced unidirectional lubricant flow for lubrication track replenishment”. In: *Friction* (2021) . . . . . ⇑ 26

[89] H.C. Liu et al. “Influences of solid and lubricant thermal conductivity on traction in an EHL circular contact”. In: *Tribology International* (2020) . . . . . ⇑ 15

[90] A.A. Lubrecht. *An Introduction To ElastoHydrodynamic Lubrication*. Laboratoire de Mécanique des Contacts et des Structures UMR CNRS 5259, INSA de Lyon, France. 2014 . . . . . ⇑ 9, 12, 170

[91] A.A. Lubrecht. “The numerical solution of the elastohydrodynamically lubricated line- and point contact problem, using multigrid techniques”. PhD thesis. Netherlands: University of Twente, 1987 . ⇑ 14, 171

[92] P.M. Lugt. “Lubrication Mechanisms”. In: *Grease Lubrication in Rolling Bearings*. John Wiley & Sons, Ltd, 2012. Chap. 2 . . . . . ⇑ 26

[93] P.M. Lugt, M.T. van Zoelen, and C.H. Venner. “Film Thickness in Grease Lubricated Rolling Bearings”. In: *Grease Lubrication in Rolling Bearings*. John Wiley & Sons, Ltd, 2012. Chap. 10 . . . . . ⇑ 20

[94] P.M. Lugt, M.T. van Zoelen, and C.H. Venner. “Film Thickness Theory for Single Contacts”. In: *Grease Lubrication in Rolling Bearings*. John Wiley & Sons, Ltd, 2012. Chap. 9 . . . . . ⇑ 8, 20, 97, 104, 170

[95] M. Marian et al. “Designing surface textures for EHL point-contacts - Transient 3D simulations, meta-modeling and experimental validation”. In: *Tribology International* (2019) . . . . . ⇑ 21, 91

[96] H.M. Martin. “Lubrication of Gear Teeth”. In: *Engineering London* (1916) . . . . . ⇑ 8, 170

[97] J.C. Martin et al. “Validation of a Mathematical Model for Road Cycling Power”. In: *Journal of Applied Biomechanics* (1998) . . . . ⇑ 7

[98] S. Martin. “Contribution à la modélisation de phénomènes de frontière libre en mécanique des films minces”. PhD thesis. INSA de Lyon, 2005 ⇑ 66

[99] S. Messé. “Analyse transitoire de la lubrification et du frottement dans un système de distribution automobile”. PhD thesis. INSA de Lyon, 2001 . . . . . ⇑ 14, 46

[100] A.G.M. Michell. “Progress of Fluid-Film Lubrication”. In: *Transactions of the American Society of Mechanical Engineers* (1929) . . ⇑ 8, 170

[101] H. Moes. “Optimum similarity analysis with applications to elastohydrodynamic lubrication”. In: *Wear* (1992) . . . . . ⇑ 56, 90

[102] F.D. Murnaghan. “The Compressibility of Media under Extreme Pressures”. In: *Proceedings of the National Academy of Sciences of the United States of America* (1944) . . . . . ⇑ 12, 38

[103] K.C. Mutyala et al. “Effect of Diamond-Like Carbon Coatings on Ball Bearing Performance in Normal, Oil-Starved, and Debris-Damaged Conditions”. In: *Tribology Transactions* (2016) . . . . . ⇑ 24

[104] C.L.M.H. Navier. *Mémoire sur les lois du mouvement des fluides*. 1827 ⇑ 8

[105] G. Nijenbanning, C.H. Venner, and H. Moes. “Film thickness in elastohydrodynamically lubricated elliptic contacts”. In: *Wear* (1994) ⇑ 14

[106] R.J. Parker. *Lubrication of Rolling Element Bearings*. 1980 . . . . ⇑ 22

[107] T. Patrigeon et al. “Truncation effects on circular EHL contact film thickness”. In: *Proceedings of the Institution of Mechanical Engineers, Part J: Journal of Engineering Tribology* (0) . . . . . ⇑ 10

[108] J. Pemberton and A. Cameron. “A mechanism of fluid replenishment in elastohydrodynamic contacts”. In: *Wear* (1976) . . . . . ⇑ 25, 27, 174

[109] A.I. Petrusevich. “Fundamental conclusions from the contact-hydrodynamic theory of lubrication”. In: *Izv. Akad. Nauk. SSSR (OTN)* (1951) ⇑ 13

[110] G. Popovici. “Effects of lubricant starvation on performance of elastohydrodynamically lubricated contacts”. English. PhD thesis. Netherlands: University of Twente, 2005 . . . . . ⇑ 20, 23, 24, 27, 44, 94, 95

[111] A. Porras Vazquez. “Lubricant starvation in elastohydrodynamic large-size spinning contacts”. PhD thesis. INSA de Lyon, 2020 . . ⇑ 20, 21, 59

[112] E. Querlioz. “Etude de la durée de vie des contacts sous-alimentés en lubrifiant”. PhD thesis. INSA de Lyon, 2007 ⇑ 22, 23, 24, 26, 94, 95, 98, 99, 100, 101, 102, 110, 111, 113, 118, 119, 124, 125, 134, 135, 136, 141, 173, 178, 179

[113] J. Raisin et al. “Characteristic times in transient thermal elastohydrodynamic line contacts”. In: *Tribology International* (2015) . ⇑ 43, 47, 143

[114] H.S.J. Rashid et al. “Reliability model for helicopter main gearbox lubrication system using influence diagrams”. In: *Reliability Engineering & System Safety* (2015) ..... ⇑ 1, 167

[115] O. Reynolds. “IV. On the theory of lubrication and its application to Mr. Beauchamp Tower’s experiments, including an experimental determination of the viscosity of olive oil”. In: *Philosophical Transactions of the Royal Society of London* (1886) ..... ⇑ 8, 34, 36, 170, 176

[116] M.R. Riggs, N.K. Murthy, and S.P. Berkebile. “Scuffing Resistance and Starved Lubrication Behavior in Helicopter Gear Contacts: Dependence on Material, Surface Finish, and Novel Lubricants”. In: *Tribology Transactions* (2017) ..... ⇑ 24

[117] M.R. Riggs et al. “Scuffing Resistance and Starved Lubrication Behavior in Helicopter Gear Steels Coated with Nanocomposite Surface Coatings with and without a Hard Sublayer”. In: *Tribology Transactions* (2020) ..... ⇑ 24, 96, 173

[118] C.J.A. Roelands. “Correlational Aspects of the Viscosity-temperature-pressure Relationship of Lubricating Oils”. PhD thesis. The Netherlands: Technical University Delft, 1966 ..... ⇑ 11, 38, 78, 99, 113

[119] F. Sahlin et al. “A cavitation algorithm for arbitrary lubricant compressibility”. In: *Tribology International* (2007) ..... ⇑ 17

[120] T. Seoudi et al. “CdSe-Based Quantum Dots as In Situ Pressure and Temperature Non-intrusive Sensors in Elastohydrodynamic Contacts”. In: *Tribology Letters* (2020) ..... ⇑ 10

[121] H.A. Spikes. “Sixty years of EHL”. In: *Lubrication Science* (2006) ⇑ 9, 170

[122] G.G. Stokes. *On the Theories of the Internal Friction of Fluids in Motion, and of the Equilibrium and Motion of Elastic Solids*. 1845 ⇑ 8

[123] P. Svoboda et al. “Experimental study of starved EHL contacts based on thickness of oil layer in the contact inlet”. In: *Tribology International* (2013) ..... ⇑ 18, 19, 21

[124] S. Timoshenko and J.N. Goodier. *Theory of elasticity*. McGraw-Hill, 1951 ..... ⇑ 11, 41, 43, 176

[125] B. Tower. “First Report on Friction Experiments”. In: *Proceedings of the Institution of Mechanical Engineers* (1883) ..... ⇑ 8, 170

[126] B. Tower. “Research Committee on Friction: Second Report on Friction Experiments”. In: *Proceedings of the Institution of Mechanical Engineers* (1885) ..... ⇑ 8, 170

[127] M.T. van Zoelen. “Thin layer flow in rolling element bearings”. PhD thesis. University of Twente, 2009 . ⇑ 20, 30, 94, 95, 97, 98, 104, 109, 119, 120, 137, 146, 173

[128] M.T. van Zoelen, C.H. Venner, and P.M Lugt. “Prediction of film thickness decay in starved elasto-hydrodynamically lubricated contacts using a thin layer flow model”. In: *Proceedings of the Institution of Mechanical Engineers, Part J: Journal of Engineering Tribology* (2009) ..... ⇑ 20, 23, 24, 97

[129] M.T. van Zoelen, C.H. Venner, and P.M. Lugt. “Free Surface Thin Layer Flow on Bearing Raceways”. In: *Journal of Tribology* (2008) ⇑ 20, 109

[130] C.H. Venner. “Multilevel solution of the EHL line and point contact problems”. PhD thesis. Netherlands: University of Twente, 1991 ⇑ 7, 14, 78, 171

[131] C.H. Venner, G. Berger, and P.M. Lugt. “Waviness Deformation in Starved EHL Circular Contacts ”. In: *Journal of Tribology* (2004) ⇑ 77, 78, 79, 80, 81, 101, 135, 178

[132] C.H. Venner and A.A. Lubrecht. “Amplitude Reduction of Non-Isotropic Harmonic Patterns in Circular EHL Contacts, under Pure Rolling”. In: *Lubrication at the Frontier*. Ed. by D. Dowson et al. Elsevier, 1999 ⇑ 46

[133] C.H. Venner and A.A. Lubrecht. “Numerical Simulation of a Transverse Ridge in a Circular EHL Contact Under Rolling/Sliding”. In: *Journal of Tribology* (1994) ..... ⇑ 14

[134] J. Wang and M. Kaneta. “A study on starved micro-thermal elastohydrodynamic lubrication in simple sliding circular contacts”. In: *Proceedings of the Institution of Mechanical Engineers, Part J: Journal of Engineering Tribology* (2007) ..... ⇑ 21

[135] L.D. Wedeven. “Optical measurements in elastohydrodynamic rolling-contact bearings”. PhD thesis. Imperial College London, 1970 . ⇑ 17, 68, 172

[136] Y.H. Wijnant. “Contact dynamics in the field of elastohydrodynamic Lubrication”. PhD thesis. University of Twente, 1998 .. ⇑ 19, 44, 60, 61, 66, 67, 68, 81

[137] M.L. Williams, R.F. Landel, and J.D. Ferry. “The Temperature Dependence of Relaxation Mechanisms in Amorphous Polymers and Other Glass-forming Liquids”. In: *Journal of the American Chemical Society* (1955) ..... ⇑ 11, 38, 113, 114

[138] A.M. Winslow. “Numerical solution of the quasilinear poisson equation in a nonuniform triangle mesh”. In: *Journal of Computational Physics* (1966) ..... ⇑ 72, 73

[139] P. Yang, J. Wang, and M. Kaneta. “Thermal and Non-Newtonian Numerical Analyses for Starved EHL Line Contacts”. In: *Journal of Tribology* (2005) ..... ⇑ 21

[140] P. Yang and S. Wen. “A Generalized Reynolds Equation for Non-Newtonian Thermal Elastohydrodynamic Lubrication”. In: *Journal of Tribology* (1990) ..... ⇑ 46

[141] S. Yasutomi, S. Bair, and W.O. Winer. “An Application of a Free Volume Model to Lubricant Rheology I—Dependence of Viscosity on Temperature and Pressure”. In: *Journal of Tribology* (1984) ... ⇑ 11, 38, 113, 114

[142] C. Yin et al. “Thermal elastohydrodynamic lubrication of starved elliptical contacts”. In: *Tribology International* (2009) ..... ⇑ 21, 62

[143] F. Zhang et al. “Thermal-Elastohydrodynamic Contacts Lubricated With Oil/Refrigerant Solutions: A New Cavitation Modeling Approach Based on Refrigerant Solubility”. In: *Journal of Tribology* (2022) ⇑ 7

[144] M. Zhang et al. “A thermal EHL investigation for finite line contact under starved condition on bush-pin hinge pairs in industrial chains”. In: *Proceedings of the Institution of Mechanical Engineers, Part J: Journal of Engineering Tribology* (2023) ..... ⇑ 21

Résumé étendue Français

Introduction générale

La lubrification est un élément clef de nombreux assemblages mécaniques. Elle permet en effet de réduire le frottement et l'usure. Dans certaines applications, c'est même un élément crucial, car une défaillance du système de lubrification peut entraîner des conséquences dramatiques.

L'hélicoptère en est un parfait exemple. La boîte de vitesse reliant le moteur aux pales permet à l'hélicoptère de voler. Cette boîte de vitesse comporte de nombreux composants, tels que des engrenages et des roulements. Ce travail étudie uniquement les roulements. En conséquence, si une avarie de lubrification apparaît, combien de temps les roulements présents dans la boîte de vitesse peuvent-ils assurer leur fonction principale de réalisation d'une liaison pivot ? Ce type de défaillance est problématique lors d'interventions en mer, où l'hélicoptère ne possède pas de lieu où se poser d'urgence. Selon Rashid et al. [114] en 2015, 1232 rapports d'accident impliquant une défaillance de lubrification sur la boîte de vitesse ont été recensés. Astridge [5] en 1989 mentionne que ce type de problème représente 22 % des accidents, ce qui en fait la troisième cause d'accident. L'agence de l'union européenne pour la sécurité aérienne (European Aviation Safety Agency [55]) requiert que certains types d'hélicoptères doivent pouvoir voler pendant 30 minutes afin de réaliser une autorotation (les hélices tournent grâce au déplacement de l'hélicoptère) lorsqu'une avarie de lubrification se présente. L'objectif à long terme est d'augmenter ce temps minimum. Pour ce faire, ce travail représente une première étape dans cette direction.

La section intitulée « Etat de l'art » présente le fonctionnement d'un roulement ainsi que l'état de l'art en matière de lubrification.

La section intitulée « Modélisation numérique » mentionne les équations nécessaires au calcul d'un contact EHD. Par la suite, l'introduction de la

sous-alimentation est expliquée et validée grâce à une comparaison avec un cas existant dans la littérature.

La section intitulée « Etude de la perte de lubrification » présente un cas d'étude et adapte le modèle numérique afin de pouvoir reproduire un travail expérimental. Enfin, les résultats sont comparés et commentés.

Etat de l'art

Combien de temps un roulement peut-il fonctionner en cas de panne du système de lubrification ? Afin de répondre à cette question, le fonctionnement d'un roulement est présenté. Cette présentation met en évidence différentes physiques et les explique.

Roulement

Le roulement présenté sur la figure 1 comprend deux bagues : une bague extérieure (1) généralement montée dans un carter et une bague intérieure (2) montée sur un arbre. Entre ces deux bagues se trouvent les éléments roulants (5). Ils peuvent être des billes, des rouleaux, etc.. Ces éléments roulants

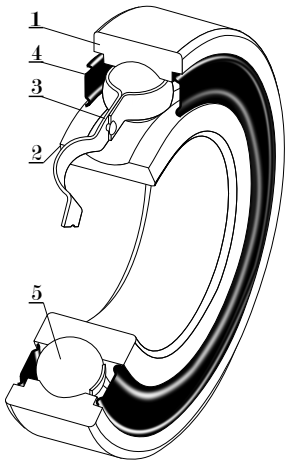

FIGURE 1 : Coupe d'un roulement

Crédit: Image provenant de Wikimedia Commons créée par Silberwolf & Malyszkz – intitulée « Radial-deep-groove-ball-bearing din625-t1 2rs 120 » – distribuée sous la licence CC BY-SA 3.0 – modifications: convertie en noir & blanc, la fonte a été changée en Modern 20 et certaines dimensions caractéristiques ont été retirées

sont en contact avec les deux bagues. En conséquence, à la place d'un contact glissant comme c'est le cas pour un palier, il y a un contact roulant. Afin de minimiser le frottement et l'usure, un lubrifiant (huile ou graisse) est présent sur la bande de roulement afin de séparer les surfaces en contact. En fonction du type de roulement, une cage (3) maintenant les éléments roulants peut être présente. De même, la présence de joints (4) aux extrémités du roulement n'est pas toujours nécessaire. En effet, ils permettent de maintenir le lubrifiant déposé à l'intérieur du roulement pendant le processus de fabrication, tout en protégeant l'intérieur du roulement des contaminants externes.

Un roulement est un assemblage mécanique qui comporte de nombreux composants, ce qui rend son étude difficile. Il est nécessaire de simplifier le système en considérant, en première approche, uniquement un contact entre un élément roulant et une bande de roulement, comme présenté en figure 2. Dans cette configuration, la surface de contact est extrêmement petite, induisant alors de très fortes pressions. Dans cette situation, le contact est qualifié de contact ElastoHydroDynamique (EHD).

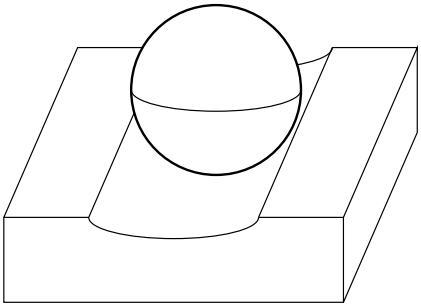

FIGURE 2 : Contact entre un élément roulant et une bande de roulement

Lubrification

La lubrification est une discipline qui fait partie du vaste domaine de la Tribologie. Elle est omniprésente lorsque deux solides sont en mouvement relatif. Aujourd'hui, la lubrification peut être trouvée par exemple dans les voitures, les appareils électroménagers, les articulations du corps humain, etc.. Selon GUAY [35] : « L'usage des lubrifiants remonte à l'Antiquité. Les essieux des chars et des charrettes étaient lubrifiés avec du suif (lard ou graisse animale) ou avec de l'huile d'olive mélangée avec de la poudre de calcaire, pour l'épaissir et obtenir la consistance d'une graisse ».

Le phénomène de lubrification a été étudié dans les années 1880 par Tower [125, 126] durant des travaux expérimentaux. Ensuite, Reynolds [115] a réussi à retrouver les résultats présentés par Tower grâce à une étude théorique en 1886. Le travail de Reynolds a donné naissance à la théorie de la lubrification et a abouti à l'équation de Reynolds, qui permet de déterminer le champ de pression dans un contact. Grâce à l'équation de Reynolds, de nombreuses études ont été réalisées dans le domaine des paliers hydrodynamiques (cf. Michell [100] en 1929) ou sur les dents d'engrenages (cf. Martin [96]). Cependant, dans ce dernier cas, les résultats théoriques ne corrélaient pas avec ceux issus des travaux expérimentaux.

Selon Lugt et al. [94], l'épaisseur du film d'huile de Martin [96] obtenue grâce à l'application de l'équation de Reynolds était bien plus faible que l'épaisseur des rugosités, un résultat qui n'est pas admissible. Comme la surface de contact est très faible, les pressions sont élevées au point que les surfaces en contact présentent des déformations. Il est ainsi nécessaire de parler de lubrification EHD. La lubrification EHD est un régime de lubrification où la pression est de l'ordre du GigaPascal. Sous une telle pression, les surfaces se déforment. Le fluide est comprimé, donc les molécules sont plus proches les unes des autres, ce qui augmente sa masse volumique. Comme les molécules sont rapprochées, le nombre d'interactions entre elles augmente, engendrant ainsi une augmentation de la viscosité (cf. Lubrecht [90]). Ce régime de lubrification apparaît majoritairement lorsqu'il y a un contact non conforme (par exemple une sphère sur un plan) dans un roulement ou entre des dents d'engrenage. Malgré la très faible épaisseur du film d'huile (quelques centaines de nanomètres), le coefficient de frottement est très faible, de l'ordre de $1 \cdot 10^{-2}$ (c.f. Johnson et al. [81] ou Spikes [121]).

Il est possible d'observer ce type de contact expérimentalement sur un banc d'essai, comme présenté sur la figure 3. Ce type de banc d'essai permet d'observer et de mesurer le contact et le frottement. Ici, il s'agit d'une machine bille-disque.

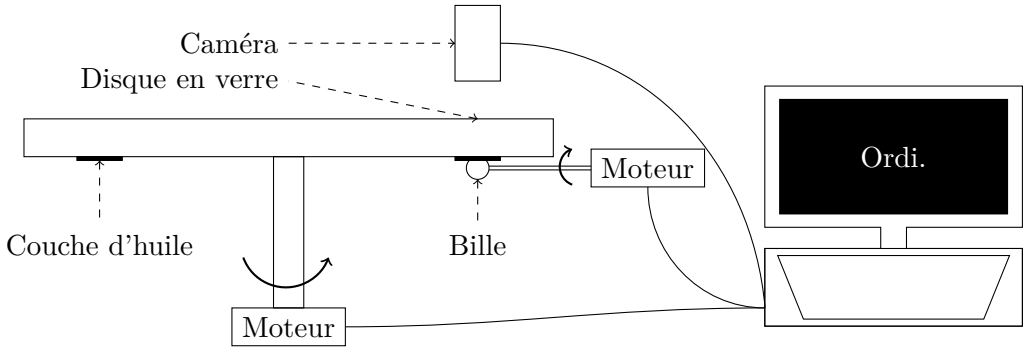

FIGURE 3 : Exemple d'un banc d'essai permettant d'observer un film d'huile dans un contact bille disque

Aujourd'hui, il existe principalement deux méthodes pour calculer un contact EHD :

— LUBRECHT [91] a introduit en 1987 la méthode multi-grille (cf. BRANDT et al. [18]) basée sur une discrétisation aux différences finies, qui a été par la suite améliorée et optimisée par VENNER [130] en 1991 ;

— HABCHI [61] en 2008 propose une approche différente basée sur une discrétisation éléments finis entièrement couplée, sans utiliser la méthode multi-grille Elle permet de calculer le contact EHD couplé à des phénomènes thermiques non-Newtoniens présentant des indentations*, et aussi de prendre en compte la présence de revêtement.

En conclusion, la lubrification EHD a fait l'objet de nombreuses études. Cependant, un domaine restait à explorer : la prise en compte de la sous-alimentation.

Lubrification sous-alimentée

En lubrification, il existe deux régimes d'alimentation :

— sur-alimenté (cf. figure 4(a)) ;

— sous-alimenté (cf. figure 4(b)).

*Calculs aussi été réalisés avec la méthode multi-grille

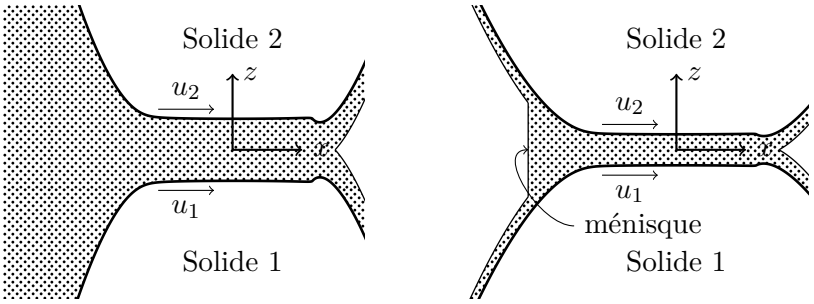

(a) Sur-alimenté (b) Sous-alimenté

FIGURE 4 : Difference entre un contact sur-alimenté et sous-alimenté

Le motif en pointillé représente l'huile. La figure 4(b) présente un ménisque au niveau de l'endroit où les deux couches de lubrifiant adhérant aux surfaces se rencontrent. Techniquement, la même chose se produit dans un cas de suralimentation, mais le ménisque se situe extrêmement loin du contact. La position du ménisque est régie par la conservation du débit massique et par la quantité de lubrifiant présente en amont du contact. Ainsi, pour des conditions de fonctionnement identiques, l'épaisseur du film peut être impactée par la position du ménisque relative à la quantité de lubrifiant présente en amont du contact. En effet, si la position du ménisque/la quantité de lubrifiant change entre deux applications et que le film d'huile ne présente pas de différence, alors c'est un contact suralimenté. Inversement, si l'épaisseur du contact diffère pour deux positions du ménisque/quantité d'huile différentes, alors c'est un contact sous-alimenté.

Selon GUANGTENG et al. [60], la plupart des roulements fonctionnent dans des conditions de sous-alimentation. WEDEVEN [135] a mené en 1970 des travaux expérimentaux dédiés à l'observation d'un contact sous-alimenté et a prouvé expérimentalement l'existence d'un ménisque d'huile en amont du contact. Il a également observé que la position du ménisque dépend de la quantité de lubrifiant entrant dans le roulement.

CHEVALIER [29] en 1996 (ainsi que [30, 31, 32]) a réalisé une importante contribution numérique à l'introduction de la sous-alimentation dans un contact EHD. Pour ce faire, il a introduit la résolution de l'équation de REYNOLDS modifiée (présentée par BAYADA et al. [11]) dans l'algorithme multi-grille. Il a notamment présenté une formule permettant de prédire l'épaisseur du film d'un contact en fonction de la quantité de lubrifiant présente en amont. Il a également établi une formule analytique permettant de déterminer la réduction de l'épaisseur du film du contact lorsqu'un passage

cyclique se produit, comme dans le cas d'un roulement.

Perte de lubrifiant

De nombreux travaux expérimentaux sont réalisés sur des machines type bille-disque telles que présentées sur la figure 3, comme par exemple ceux de Querlioz [112] en 2007, van Zoelen [127] en 2009, Damiens [37] en 2003 ou encore Riggs et al. [117] en 2020. Dans ces travaux, une certaine quantité de lubrifiant est déposée sur le disque sous la forme de gouttelettes à l'aide d'une micro-seringue. Le disque et la bille sont mis en mouvement, ce qui permet la formation d'un contact EHD et l'établissement d'un passage cyclique. Ces travaux mesurent généralement le coefficient de frottement ou l'épaisseur de film. D'après les mesures, deux comportements ont été identifiés (cf. figure 5). Le premier présente une stabilisation soit du coefficient de frottement, soit de l'épaisseur du film. Ainsi, dans ce cas, le contact peut fonctionner durant de nombreux passages successifs (cycles). Ce résultat est attribué à la présence supposée du phénomène de réalimentation de la piste de roulement. Le second, quant à lui, ne présente pas de stabilisation. Le coefficient de frottement augmente au cours des cycles (ou l'épaisseur d'huile diminue), jusqu'à un moment où une augmentation brutale se produit, conduisant ainsi à l'apparition d'un contact sec.

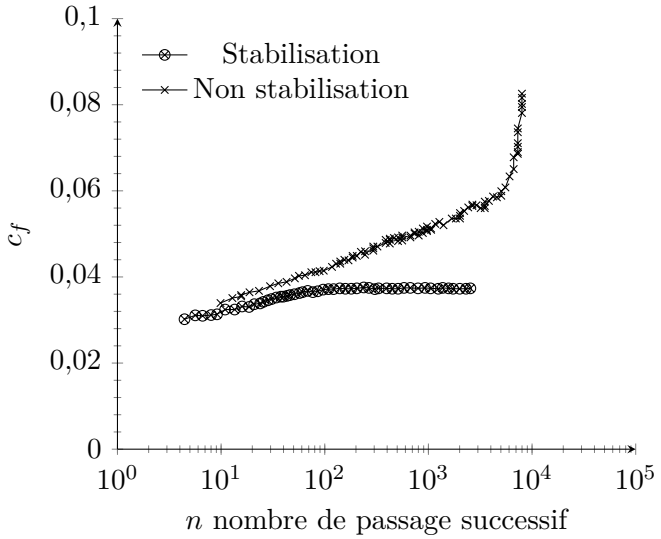

Figure 5 : Résultats obtenus par Querlioz [112] (données extraites d'une figure de Querlioz [112])

Phénomène de réalimentation

Ce phénomène a été étudié expérimentalement par Pemberton et al. [108] en 1976. Ils ont observé la formation de crêtes en aval du contact/de la bille, générant une forme de papillon, comme présentée sur la figure 6. Selon Pemberton et al. [108], les crêtes doivent couler dans la bande de roulement et ainsi réalimenter le contact. De nombreuses études, utilisant principalement des graisses, ont été menées afin d'affirmer ce phénomène, notamment par Hurley et al. [76] en 2000 et Cann [24] en 1996. Selon Cann [25], la graisse est poussée sur les flancs de la bande de roulement et libère ainsi l'huile de base qui la forme, de manière à jouer le rôle de réservoir. Ce présent travail ne traite pas des graisses, qui représentent une solution de lubrification difficile à modéliser, et se focalise uniquement sur les huiles lubrifiantes.

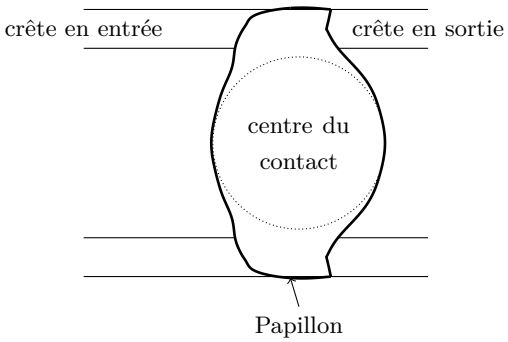

Figure 6 : Dessin schématique de la forme de papillon autour du contact EHD

Cann et al. [26] en 1997 ont réalisé des essais de type perte de lubrifiant avec les huiles de base des graisses. Ils ont obtenu à chaque fois une phase transitoire où l'épaisseur de contact diminuait, puis une phase stationnaire où elle se stabilisait (comme sur la figure 5). Ils attribuent ce résultat au phénomène de réalimentation.

Jacod et al. [77] en 1999 et Gershuni et al. [58] en 2008 ont étudié ce phénomène numériquement grâce à la résolution de l'équation d'une couche mince. Leurs études montrent que le phénomène de réalimentation de la bande de roulement ne se produit pas dans leurs applications.

Conclusion

Dans un premier temps, ce résumé a présenté le contexte de ce travail. Par la suite, l'objet d'étude, à savoir un roulement, a été détaillé. Il ressort de ces explications qu'un roulement présente de nombreux composants et qu'il est soumis à de nombreuses charges de différents types. Son étude complète est donc très difficile. C'est pour cette raison qu'il a été décidé de focaliser ce travail uniquement sur un seul contact entre une bande de roulement et un élément roulant, où une huile sépare les solides.

En conséquence, les principes de base de la lubrification ont été abordés en détail, plus particulièrement la lubrification EHD qui intervient dans le type de contact considéré. Il a été montré que ces contacts pouvaient être observés expérimentalement, permettant de mesurer l'espacement entre les deux solides, mais aussi de les calculer numériquement. Le phénomène de lubrification sous-alimentée a également été introduit, car il a été mentionné que la quasi-totalité des roulements fonctionnent en condition de sous-alimentation. A travers les études citées, il a été observé que celles réalisées en condition de perte de lubrifiant généraient deux comportements différents : un état stable ou un état instable.

La question émergente est alors la suivante : pourquoi certaines applications rejoignent un état stable et d'autres non ? Le phénomène de réalimentation est-il réellement présent ou se passe-t-il quelque chose d'autre ? Un modèle numérique est proposé pour répondre à ces questions.

Modélisation numérique

Un contact EHD fait intervenir plusieurs phénomènes physiques. Celles-ci sont expliquées dans ce chapitre. L'introduction de la sous-alimentation y est aussi présentée. Cette section résume les chapitres 2 et 3 du manuscrit anglais.

Les équations du contact EHD

Un contact EHD est gouverné par trois équations

— une pour la détermination du champ de pression dans le fluide, c'est l'équation de Reynolds ;

— une pour calculer les déformations élastiques induites par les fortes pressions, c'est l'équation de Navier-Cauchy ;

— une d'équilibre afin d'assurer que la portance générée par la pression équilibre la charge, c'est la deuxième loi de Newton.

L'équation de Reynolds

Reynolds [115] a simplifié les équations de Navier et Stokes en 1886, qui régissent le comportement d'un fluide. Cette simplification a abouti à l'équation de Reynolds, qui est utilisée dans le domaine de la lubrification. Pour parvenir à cette simplification, il a supposé que l'épaisseur du film d'huile était très faible et que les contraintes visqueuses étaient nettement plus importantes que les contraintes inertielles.

La pression dans le contact étant très élevée, il est nécessaire de caractériser le comportement du fluide en fonction de la pression. Pour ce faire, l'équation de Reynolds est couplée à une relation liant la viscosité à la pression et à une relation liant la masse volumique à la pression.

Finalement, cette équation est résolue dans un plan 2D.

Déformations élastiques

Le champ de pression calculé précédemment est appliqué sur la face supérieure d'un parallélépipède rectangle représentant un solide équivalent. Ce solide équivalent combine les propriétés matériaux des deux solides réels. Il est encastré sur la face qui est opposée au chargement de la pression.

Ainsi, l'équation d'élasticité linéaire, ou équation de Navier-Cauchy, qui a par exemple été présentée par Timoshenko et al. [124] en 1951, est résolue sur ce solide équivalent. Cette équation permet de déterminer les déformations élastiques induites par l'application du champ de pression.

Equilibre de la charge

L'équilibre de la charge s'obtient grâce à l'application de la seconde loi de Newton, qui aboutit à une équation d'équilibre. Cette dernière stipule que la force appliquée sur le contact doit être compensée par la portance du fluide, générée par le champ de pression.

Introduction de la sous-alimentation

La sous-alimentation a un impact direct sur l'équation de Reynolds et indirect sur les autres équations citées précédemment. En effet, l'équation de

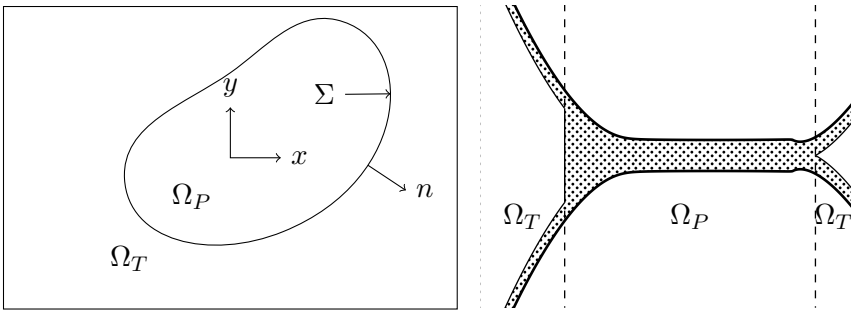

(a) Plan 2D $\Omega_L = \Omega_T \cup \Omega_P$ (b) Vue de côté

FIGURE 7 : Domaine 2D Ω_L et ses sous-domaines Ω_T et Ω_P

REYNOLDS n'est plus résolue dans l'ensemble du plan 2D mentionné précédemment, mais dans une partie de ce plan. Le transport de fluide est quant à lui résolu dans la portion restante. Ces portions sont appelées des sous-domaines (cf. figure 7). Ainsi, le premier sous-domaine Ω_P permet d'obtenir le champ de pression via la résolution de l'équation de REYNOLDS, tandis que le second Ω_T permet d'obtenir la répartition du lubrifiant grâce à la résolution d'une équation de transport de fluide. Ces deux sous-domaines sont séparés par une frontière appelée Σ. Un équilibre des débits entrants et sortants réalisé sur cette frontière permet d'obtenir une équation qui détermine sa position afin d'assurer la conservation du débit.

Effets thermiques

En raison de la compression du fluide et du cisaillement, un échauffement peut se produire au niveau du contact. Ainsi, pour le calculer, il est nécessaire de modifier l'équation de REYNOLDS en introduisant l'équation de REYNOLDS généralisée. Il faut également ajouter l'équation de l'énergie, qui permet de calculer la température en tout point du fluide et des solides.

Procédure numérique

Toutes les équations sont discrétisées à l'aide d'un logiciel commercial utilisant la méthode des éléments finis. En 2008, HABCHI [61] a présenté une méthode permettant de résoudre toutes les équations simultanément grâce à l'algorithme de NEWTON-RAPHSON. La sous-alimentation est ajoutée à cette méthode.

La théorie présentée dans le paragraphe « Introduction de la sous-alimentation »

comporte des difficultés numériques qui rendent non triviale l'ajout de la sous-alimentation dans le modèle de Habchi [61]. Pour ce faire, une méthode de maillage mobile est utilisée afin de permettre le déplacement de la frontière Σ de manière à assurer la conservation du débit.

Validation

L'ajout de la sous-alimentation utilisant une méthode de maillage mobile dans le modèle développé par Habchi [61] nécessite une étape de validation. Pour ce faire, des cas présentés dans la littérature sont reproduits. En 2004, Venner et al. [131] ont présenté des résultats numériques de calculs de contacts EHD soumis à différents degrés de sous-alimentation. Ces calculs ont été reproduits avec le modèle développé. L'écart relatif entre les résultats de Venner et al. [131] et ceux du modèle est à chaque fois inférieur à 1 %.

Conclusion

Les équations nécessaires à la résolution d'un problème EHD ont été abordées. L'introduction de la sous-alimentation a été démontrée. La stratégie de résolution du problème sous-alimenté a été introduite dans le modèle développé par Habchi [61] en 2008. Enfin, une confrontation avec une référence de la littérature a été réalisée afin de valider le modèle numérique pour une utilisation plus sûre par la suite.

Etude de la perte de lubrification

Cette section a pour but de présenter une comparaison entre des résultats issus du modèle numérique et des résultats issus de la littérature qui sont basés sur des travaux expérimentaux. Deux comportements aboutissant à des résultats différents sont étudiés. Pour ce faire, le modèle numérique, qui a été présenté dans la section précédente, est adapté aux conditions expérimentales.

Contexte

Différentes études expérimentales présentes dans la littérature ont été citées dans la section « Etat de l'art ». Parmi elles, l'étude de Querlioz [112] en 2007 a été sélectionnée afin d'être étudiée numériquement et pour mieux comprendre les phénomènes impliqués dans le processus.

Querlioz [112] a présenté des travaux expérimentaux en lien avec des conditions de perte de lubrifiant ou de fonctionnement avec une quantité de lubrifiant fixe. Sur une machine bille-disque, elle a notamment déposé une certaine quantité de lubrifiant sous la forme de gouttelettes. Ensuite, le disque et la bille ont été entraînés en rotation et le contact EHD a opéré durant plusieurs milliers de cycles. Le contact EHD a donc vu passer un grand nombre de fois un point arbitraire et a donc réalisé des milliers de passages successifs.

Durant ces travaux, Querlioz [112] a mesuré le coefficient de frottement dans le contact. Ainsi, pour des conditions de fonctionnement identiques à l'exception de la vitesse d'entraînement moyenne, elle a obtenu deux tendances de coefficient de frottement très différentes. Dans le premier cas, le coefficient de frottement a rejoint un régime stabilisé dans lequel il n'évoluait plus, alors que le nombre de passage successifs augmentait. Dans le second, il a continué d'augmenter jusqu'à un moment où l'augmentation a été très forte en réponse à un contact sec.

Résultats

Préambule

Le modèle numérique a été adapté de manière à reproduire le phénomène de passage successifs. La réalimentation de la zone de passage mentionnée dans le chapitre 1 a été étudiée a l'aide d'une équation dédiée. Cette équation prend en compte les effets centrifuges, la tension de surface entre l'air et l'huile ainsi que la gravité. Elle a été appliquée à la couche d'huile adhérant au disque ainsi qu'à celle adhérant à la bille. L'étude de l'évolution de la couche d'huile entre deux passages successifs a montré que le phénomène de réalimentation n'apparaissait pas pour les applications sélectionnées. Ainsi, la géométrie de l'épaisseur d'huile à la sortie d'un contact EHD rentre de manière identique dans le contact suivant après une révolution des composants. D'ailleurs, une discussion a été menée démontrant que faire l'hypothèse que les surfaces rentrent en même temps dans le contact surestime théoriquement l'épaisseur d'huile de 9 %.

Du fait de l'efficience de la méthode de calcul, différentes résolutions ont été réalisées. Dans un premier temps, la température n'a pas été prise en compte et le modèle isotherme a donc été utilisé. Dans un second temps, le modèle thermique a été employé. Deux cas d'étude ont été établis lors de l'utilisation du modèle thermique. Le premier cas part du principe que le fluide et les solides sont totalement refroidis entre deux passages successifs.

Le second cas suppose qu'aucun refroidissement n'est présent entre deux passages successifs.

Coefficient de frottement instable

L'utilisation du modèle isotherme et du modèle thermique n'a pas permis de reproduire de manière qualitative les résultats expérimentaux, comme l'illustre la figure 88.

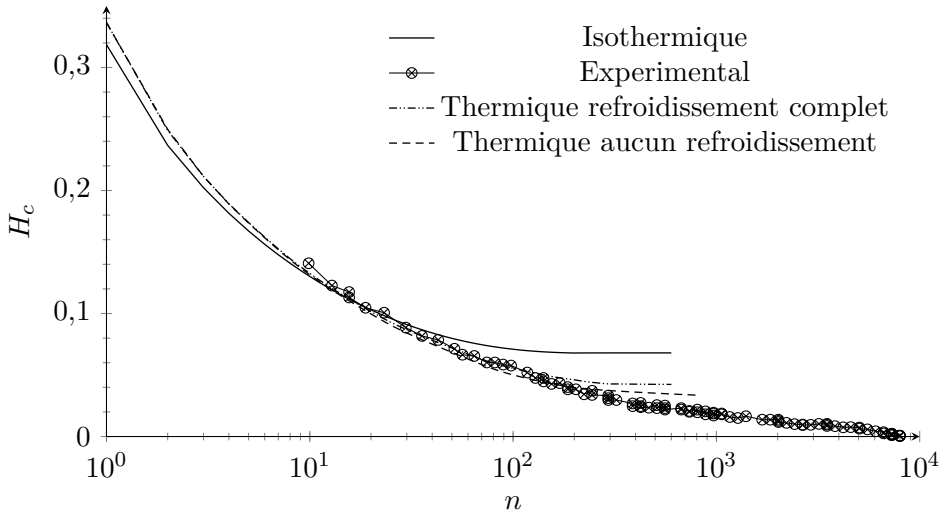

FIGURE 8 : Epaisseur de film sans dimensions en fonction du nombre de passage successif

En effet, le modèle isotherme a retourné une stabilisation de la décroissance de l'épaisseur d'huile. Cela implique que le contact fonctionnera durant des heures. Le premier cas du modèle thermique a également rejoint un régime stabilisé. Le second cas a présenté une diminution de l'épaisseur du film d'huile, qui devenait de plus en plus petite. Cependant, aucun des deux cas n'a été capable de proposer un résultat qualitativement proche des résultats expérimentaux. De plus, lors de l'analyse de la répartition de la température dans le contact, il a été observé que le second cas présentait un résultat non physique, car un refroidissement se produisait dans la partie sous-alimentée. Cela confirme qu'aucun emballement thermique ne se produit. Il doit forcément y avoir un refroidissement, par conduction d'une part et par convection forcée loin du contact d'autre part, étant donné qu'il y a effectivement du refroidissement sur une toute petite zone proche du contact.

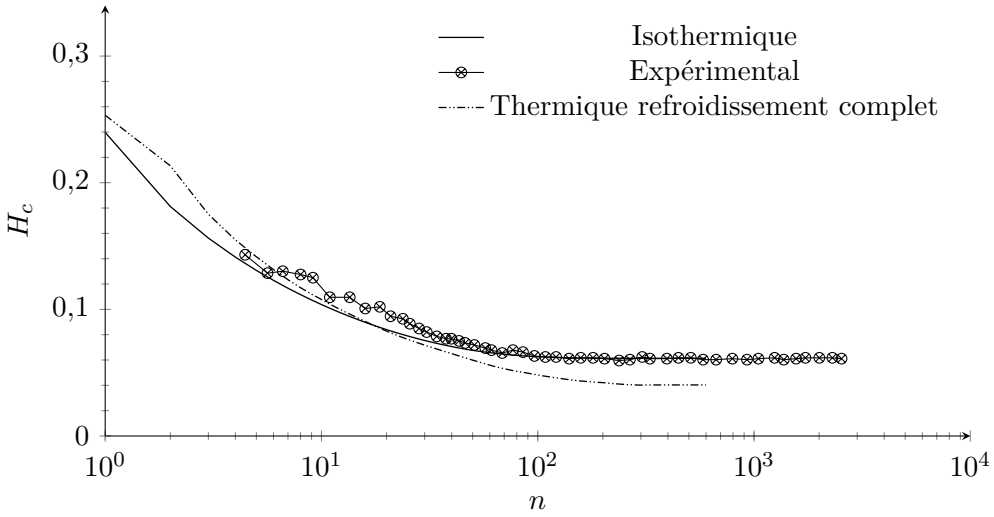

FIGURE 9 : Epaisseur de film sans dimensions en fonction du nombre de passage successif

Coefficient de frottement stabilisé

Le modèle isothermique indique une stabilisation de l'épaisseur du film d'huile après 100 passages successifs. Ce résultat est en corrélation qualitative avec les résultats expérimentaux (cf. figure 9). La position du ménisque ainsi que les débits latéraux ont été analysés afin de comprendre ce résultat. Le ménisque converge vers une valeur constante et les débits latéraux deviennent très faibles. Le fluide s'écoule donc quasiment totalement dans la direction du roulement (convection). En effet, la quantification des débits latéraux montre qu'il y en a toujours, mais ils sont extrêmement faibles.

Concernant le modèle thermique, seul le premier cas a été étudié. Ce dernier a également montré une stabilisation de l'épaisseur d'huile (cf. figure 9). Ce résultat présente ainsi une tendance qualitative similaire à celle des observations expérimentales. De même que pour le modèle isotherme, des investigations ont été menées pour comprendre cette stabilisation. La température rejoint une valeur asymptotique au cours du temps. De ce fait, le champ de température n'évolue plus et rejoint un régime stabilisé. Les débits latéraux deviennent également très faibles au cours du temps, comme pour le modèle isothermique.

Conclusion

Ce chapitre a présenté un cas d'étude tiré de la littérature. Ce cas proposait deux types de résultats différents. Le premier conduit à une stabilisation du coefficient de frottement, tandis que dans le second, celui-ci s'emballe (il croit brutalement). La différence entre les deux réside dans une vitesse d'entraînement plus élevée pour celui qui provoque un emballement du coefficient de frottement.

Ainsi, une stratégie de résolution a été mise enœuvre pour reproduire numériquement ces deux applications expérimentales. Des calculs isothermes et thermiques ont été réalisés. L'application proposant un emballement du coefficient de frottement n'a pas pu être reproduite numériquement. En effet, ni le modèle isothermique ni le modèle thermique n'ont pu proposer un résultat qualitativement proche de celui observé expérimentalement. Cependant, l'application montrant un coefficient de frottement stabilisé au cours du temps a été reproduite qualitativement par les deux modèles. En effet, les deux modèles ont rejoint un régime de fonctionnement stable. Ainsi, dans ces conditions, le contact doit opérer durant de nombreuses heures.

Conclusion générale

L'objectif de ce travail était de déterminer pendant combien de temps un roulement peut fonctionner en cas de défaillance de la lubrification.

Le fonctionnement d'un roulement a été détaillé, ce qui a mené à la conclusion qu'un seul contact (par exemple entre un élément roulant et une bague) allait être étudié lors de ce travail. La lubrification a été expliquée chronologiquement en mettant l'accent sur la lubrification EHD et la sous-alimentation. Les méthodes d'observation expérimentale et de calcul numérique d'un contact EHD ont été abordées. A travers cette observation, deux types de résultats ont été montrés lors d'études avec une quantité de lubrifiant restreinte et non renouvelée. Le premier résultat montrait que le contact rejoignait un état sable et pouvait fonctionner durant de nombreuses heures. Ce résultat a été expliqué par la présence supposée d'une réalimentation de la piste où le contact opère. Le second ne présentait pas d'état stable et l'épaisseur du film d'huile diminuait au cours du temps jusqu'à devenir tellement faible qu'un phénomène de grippage apparaissait. Finalement, le phénomène de réalimentation a été expliqué.

Par la suite, la méthode classique de résolution d'un problème EHD a été présentée. L'introduction de la sous-alimentation dans ce modèle a été

détaillée. Enfin, la procédure numérique permettant de résoudre le modèle à l'aide d'un logiciel éléments finis commercial a été abordée.

Ensuite, un travail expérimental présentant deux résultats différents a été sélectionné afin de mener une confrontation numérique qui permettrait de mieux comprendre les phénomènes intervenant dans ce cas. Pour ce faire, le modèle numérique a été adapté afin de reproduire le plus fidèlement possible le travail expérimental. En amont, le phénomène de réalimentation a été étudié et il a été prouvé que celui-ci n'intervenait pas dans l'application sélectionnée. Le cas expérimental présentant une instabilité du coefficient de frottement n'a pas pu être reproduit qualitativement par les modèles numériques isotherme et thermique. Des suggestions expliquant cet écart ont été émises. Enfin, le cas expérimental présentant une stabilisation du coefficient de frottement a été reproduit avec succès par les modèles numériques isotherme et thermique. Ainsi, un contact EHD pourrait fonctionner longtemps dans les conditions décrites.

Ainsi, le contact entre l'élément roulant et la bande de roulement au sein d'un roulement à bille est un contact proche du roulement pur. Cela signifie qu'il est très proche d'un cas isotherme. Par conséquent, le contact devrait opérer durant de nombreuses heures sans problème. Cela crée ainsi une opportunité d'optimiser la quantité de lubrifiant dans un roulement.

FOLIO ADMINISTRATIF
THESE DE L'INSA LYON, MEMBRE DE L'UNIVERSITE DE LYON

NOM : **DECOTE** DATE de SOUTENANCE : **20/11/2024**

Prénoms : **Maxence**

TITRE : **Numerical modelling of an EHL contact undergoing multiple overrollings**

NATURE : **Doctorat** Numéro d'ordre : **2024ISAL0096**

École Doctorale : **Mécanique, Énergétique , Génie Civil et Acoustique (MEGA)**

Spécialité : **Génie Mécanique**

RÉSUMÉ :
Les roulements à billes sont des éléments cruciaux pour une boîte de vitesse d'hélicoptère, car ils lui permettent de voler. En effet, une défaillance de ces éléments peut entraîner une fin dramatique de l'hélicoptère, comme un crash. Ce travail a pour but de mieux comprendre le fonctionnement d'un roulement à billes dans des conditions de défaillance de lubrification.

Afin de réaliser cela, ce travail ne va pas considérer un roulement entier (trop compliqué). Il va se focaliser sur un contact entre un élément roulant et une bande de roulement. Il constitue une première étape dans la compréhension du fonctionnement d'un roulement à billes en présence d'une panne de lubrification. L'extrapolation des résultats obtenus sur un contact à l'ensemble du roulement serait la prochaine étape.

Des travaux présentent deux comportements différents : la présence de grippage ou un fonctionnement stable. Un modèle numérique permettant de prendre en compte la sous-alimentation dans un contact ElastoHydroDynamique (EHD) (et Thermo-ElastoHydrodynamique (TEHD)) a été développé dans le but de reproduire ces travaux expérimentaux. La sous-alimentation est introduite par le biais d'une méthode innovante faisant appel au maillage mobile. Ce modèle numérique a été confronté avec succès à une référence provenant de la littérature. Par la suite, il a été comparé à des résultats expérimentaux en condition de perte de lubrifiant. Des situations stables dans lesquelles le contact fonctionne durant de nombreuses heures sans ajout de lubrifiant ont été obtenues.

MOTS-CLÉS : **Lubrification, ElastoHydroDynamique, sous-alimentation, maillage mobile, avarie de lubrifiant, perte de lubrifiant.**

Laboratoire de recherche : **Laboratoire de Mécanique des Contacts et des Structures (LaMCoS)**

Directeur de thèse : **FILLOT Nicolas**

Président du Jury : **CAYER-BARRIOZ Juliette**

Composition du Jury :
ALMQVIST Andreas
BIBOULET Nans
FILLOT Nicolas
MARIAN Max
RUELLAN Arnaud